McGill University

Doctoral Thesis

SRP-J_2-ϕ Resonances in LEO for Deorbitation of Non-Spherical Spacecraft

Author:
Catherine Massé

Supervisor:
Prof. Inna Sharf

A thesis submitted to McGill University in partial fulfillment of the requirements for the degree of Doctor of Philosophy in Mechanical Engineering

in the

Department of Mechanical Engineering
Aerospace Mechatronics Laboratory

April 2023, Montréal, QC, Canada

Abstract

It has been acknowledged for some time by the research community that the secular effect of the Solar and Thermal Radiation Pressure (STRP) is not always negligible for spacecraft in LEO. Indeed, it was observed that for certain orbits, the long-term behaviour of the spacecraft's perigee altitude is greatly affected by the SRP perturbation, whereas it usually averages out to a null secular effect for objects in other orbits. In this thesis, we first explore the resonance behaviour exhibited by the historical NASA's Echo I satellite, considering the recently published phase space theory for spherical spacecraft subject to the STRP-J_2 resonance. We then put forward a novel formulation of the resonance phenomenon that involves the attitude motion of the spacecraft. A thorough analysis of the eccentricity evolution is then performed for a rotating plate-like spacecraft subject to the STRP perturbation and the Earth's second zonal harmonic effect (J_2) in light of the newly identified resonance. Based on this analysis, we highlight the capabilities and limitations of exploiting such a phenomenon for the deorbitation of spacecraft located in Low-Earth Orbit (LEO).

The theoretical analysis of the resonance phenomenon serves as the basis on which we then propose a novel strategy to deorbit a plate-like spacecraft by enforcing an STRP-J_2 resonance in either eccentricity or semi-major axis through proper attitude control; the goal being the reduction of the altitude to enhance atmospheric drag effects to accelerate deorbitation. The feasibility of the two strategies is verified in a realistic environment modelled by the high-accuracy coupled orbit-attitude propagator D-SPOSE where the full dynamics is propagated by including STRP, gravitational and atmospheric perturbing accelerations and torques. Moreover, both the eccentricity and semi-major axis resonance strategies are compared to two alternate deorbitation solutions from prior literature that involve a bang-bang approach to either increase the orbit's eccentricity or lower its semi-major axis.

Finally, we perform a study of the effectiveness of the resonance solution in semi-major axis for a scenario where STRP is exploited to counter the loss of altitude due to atmospheric drag and track a reference in a, based on the perspective of the LightSail 2 mission. We thus highlight the flexibility of the proposed solution, and its capability to execute orbital manoeuvring. An assessment of the minimum maintainable altitude depending on solar activity is also performed, testifying to the complex relation between the threshold altitude, solar intensity and area-to-mass ratio.

Résumé

Il est connu depuis un certain temps par la communauté scientifique que l'effet séculaire de la Pression de Radiation Solaire et Thermique (PRST) n'est pas toujours négligeable pour un astronef dans l'orbite basse terrestre. Effectivement, il a été observé que, pour certaines orbites, le comportement à long terme de l'altitude au périgée de l'objet spatial est grandement affecté par la perturbation SRP, tandis qu'elle est habituellement moyennée à un effet séculaire nul pour d'autres orbites. Dans cette thèse, le comportement de la résonance précédemment mentionné est exploré pour le satellite historique Echo I de la NASA. Ceci est accompli à l'aide des données récemment publiées de théorie d'espace d'état pour les astronefs sphériques sujets à la résonance PRST-J_2. Ensuite, est fournie une analyse inédite et exhaustive du phénomène de résonance par l'excentricité due au couplage entre la PRST et le second effet harmonique de zone de la Terre (J_2), la résonance PRST-J_2-ϕ. Cette analyse est faite pour un astronef plat en rotation à vitesse constante autour d'un axe fixe. Les capacités et les limitations de l'exploitation d'un tel phénomène pour la désorbitation d'un astronef sont ainsi soulignées.

L'analyse théorique du phénomène de résonance sert comme base sur laquelle une nouvelle stratégie de désorbitation d'un astronef plaque est proposée. Par cette analyse, une réduction de l'altitude pour augmenter l'effet de la traînée atmosphérique est visée afin d'accélérer la désorbitation et ce, par l'application de la résonance PRST-J_2 sur l'excentricité ou le demi-grand axe avec une commande appropriée de l'attitude. La faisabilité des deux stratégies est vérifiée dans un environnement réaliste modélisé par le propagateur haute précision de couplage orbite-attitude D-SPOSE, où les équations dynamiques complètes sont propagées en incluant la PRST, les perturbations gravitationnelles et atmosphériques, ainsi que les couples. De plus, les stratégies de résonance sur l'excentricité et le demi-grand axe sont comparées à deux solutions de désorbitation alternatives provenant de littérature antérieure et impliquant une approche bang-bang¬ pour soit augmenter l'excentricité de l'orbite ou diminuer le demi-grand axe.

Finalement, une étude de l'efficatité de la méthode de résonance pour le demi-grand axe est effectuée dans un scénario où la PRST est exploitée afin de contrer la perte d'altitude due à la traînée atmosphérique de façon à maintenir un demi-grand axe référence. Ceci, à la lumière des résultats de la mission LightSail 2. On souligne ainsi la flexibilité offerte par la solution proposée pour effectuer des manoeuvres orbitales. Finalement, une analyse de l'altitude minimale maintenable

est effectuée et témoigne du caractère complexe de la relation entre cette limite, l'intensité solaire et le ratio aire/masse de l'astronef.

Acknowledgements

Above all, I would to thank my supervisor Inna Sharf who contributed to every aspect of the work presented in this thesis. She was a reliable guide who challenged me to always be thorough and clear in my analyses, qualities that made me a better researcher. Through her constant rigour and expertise, she greatly elevated the quality of my work. I want to also thank Florent Deleflie whose own expertise benefited numerous aspects of this research.

I would also like to acknowledge the contribution of Luc Sagnières who developed the orbital propagator D-SPOSE, which was extensively used throughout this work. The high quality of his software made it an easy-to-use and solid tool.

I want to thank as well my former supervisor David Saussié who initiated me to research along with my colleagues at the McGill Aerospace Mechatronics Lab: Mitchell, Hunter, Ehsan and Zihao.

On a more personal level, I would also like to show my appreciation to my family: my parents Andrée et Benoit who supported me mentally and, at times, financially all through my academic journey; my sister Dominique and her sweet children Léa and Mathis; but most of all, my anchor through all of this, Cédric, whom I love dearly and on whom fell the daily burden of supporting a Ph.D. student. The one who had to remind me to eat and sleep, and who carried me through my numerous life questionings and uncertainties.

The work conducted over the last four years and presented in this thesis was financially supported by the Fonds de recherche du Québec - Nature et Technologies (FRQNT), McGill Engineering Doctoral Award (MEDA), along with Professor Sharf's Nature Sciences and Engineering Research Council (NSERC) Discovery Grant.

Claims Of Originality

The main original contributions of this thesis are:

- Formulation of a fundamental eccentricity resonance model for stably rotating plate-like objects under the coupled action of the Solar and Thermal Radiation Pressure (STRP) and the geopotential second zonal harmonic (J_2):
  - Generalization of the resonance theory for a panel rotating at a constant rate, including phase space and equilibrium/stability analyses
  - Proposition of a methodology based on stability and phase plot analyses to identify the conditions for the strongest resonant effect
  - Exploration of the use of the resonance effect for a panel rotating at a constant rate for spacecraft deorbitation
- Proposition to enforce resonance effect, either in eccentricity or semi-major axis, through active attitude control in order to accelerate deorbitation:
  - Demonstration of the feasibility to deorbit a spacecraft subject to STRP, J_2 and drag perturbations, by generating a resonance either in eccentricity or semi-major axis
  - Verification of the proposed solutions in a realistic environment modelled by D-SPOSE where full dynamics is propagated by including STRP, geopotential and atmospheric perturbing accelerations and torques
  - Investigation of the special case of spacecraft in a sun-synchronous orbit to illustrate a multiple resonance scenario
  - Critical comparison of proposed schemes to previously published bang-bang type STRP-exploiting deorbitation strategies highlighting the advantages and limitations of investigated solutions
  - Investigation of the power/energy budget and compatibility of proposed solutions with solar powering
- Expansion of the applications of the resonance in semi-major axis to orbital manoeuvring:

  - Demonstration of the capability to raise or lower the semi-major axis by exploiting resonance

- Verification of most recent SRP-J_2 resonance theory for spherical spacecraft against the recorded data of Echo I balloon satellite

The source code of D-SPOSE provided by Luc Sagnières was used to generate the numerical simulation results throughout this thesis. Figures presented were generated by Catherine Massé from either MATLAB or Microsoft PowerPoint software. The document was prepared in Overleaf and compiled in LaTeX. Presented data analyses and various conclusions result from discussions between Catherine Massé and Inna Sharf. The work presented in this thesis was conducted under the guidance of Inna Sharf and has benefited from her suggestions and comments along with the contribution of Florent Deleflie and anonymous journal article reviewers. Parts of this thesis have previously appeared in the following journal article and conference papers:

- C. Massé, I. Sharf, and F. Deleflie, "SRP-J2 resonances in low earth orbits for objects with a time-variant area-to-mass ratio," in *Proceedings of the 31st AAS/AIAA Space Flight Mechanics Meeting*, AAS 21-375, Feb. 2021, pp. 3169–3187

- C. Massé, I. Sharf, and F. Deleflie, "Exploitation of SRP-J2-phi resonances for de-orbitation of space objects with time-variant area-to-mass ratio," in *Proceedings of the 72nd International Astronautical Congress*, IAC–21–C1.7.6, Oct. 2021

- C. Massé and I. Sharf, "Echo I case study of SRP effect on orbital motion," in *Proceedings of the 73rd International Astronautical Congress*, IAC–22–C1.9.9, Sep. 2022

- C. Massé and I. Sharf, "Exploitation of thermal radiation resonance for deorbitation of spacecraft through attitude control," in *Proceedings of the 73rd International Astronautical Congress*, IAC–22–A6.5.3, Sep. 2022

- C. Massé, I. Sharf, and F. Deleflie, "Exploitation of STRP and J2 perturbations for deorbitation of spacecraft through attitude control," *Acta Astronautica*, vol. 203, pp. 551–567, 2023

Contents

List of Figures

List of Tables

List of Abbreviations

ADR	Active Debris Removal
AIAA	American Institute of Aeronautics and Astronautics
DCM	Direction Cosine Matrix
ECI	Earth-Centered Inertial
ESA	European Space Agency
IADC	Inter-Agency Space Debris Coordination Committee
JAXA	Japan Aerospace eXploration Agency
LEO	Low Earth Orbits
LVLH	Local-Vertical/Local Horizontal
NASA	National Aeronautics and Space Administration
RAAN	Right Ascension of the Ascending Node
RCD	Reflectance Control Device
ReDSHIFT	Revolutionary Design of Spacecraft through Holistic Integration of Future Technologies
SRP	Solar Radiation Pressure
STRP	Solar and Thermal Radiation Pressure
TLE	Two-Line Element
TRP	Thermal Radiation Pressure

Chapter 1

Introduction

Like a sailboat extracting energy from the wind to navigate on the sea, the natural disturbances affecting the motion of an object in space can be channelled to perform orbital manoeuvres to alleviate the need for fuel, or other propellants. In the past decade, such a possibility prompted researchers to explore the effect of the Solar Radiation Pressure (SRP) on high area-to-mass ratio objects orbiting Earth, specifically, the *resonance* effect due to the coupling of SRP with the Earth's second zonal harmonic J_2. This resurgence of interest in the phenomenon leads to great advances in its characterization and in the possibility of exploiting it to accelerate the re-entry of defunct space assets. This, with the ultimate goal of mitigating the space debris generation and further pollution of the Low Earth Orbits (LEO).

1.1 The SRP-J_2 resonance

The research community has acknowledged for some time that the secular effect of solar radiation pressure is not always negligible for spacecraft in LEO. Indeed, it was observed that for certain orbits, the long-term behaviour of the spacecraft's perigee altitude is greatly affected by the SRP perturbation, whereas it usually averages out to a null secular effect for objects in other orbits. Historically, the Vanguard I satellite is the first Earth-orbiting object that was observably impacted by this phenomenon; in its 654 by 3969 km orbit, the SRP perturbation lead to a 3 km-amplitude perigee oscillation—sufficient to reduce the estimated orbital lifetime of the 0.02 m^2/kg satellite from 2000 to 240 years [6].

NASA's Echo I satellite (see Figure 1.1) is yet another spacecraft launched early in the space era that has been coined to exhibit the resonance phenomenon. For the balloon-type communication satellite launched in August 1960 at an altitude of 1600 km, the resonant oscillations in perigee altitude reached an unparalleled amplitude of 550 km, owing to its high area-to-mass ratio estimated at 11.7 m^2/kg. This ultimately led to a much faster re-entry in May 1968 due to the resulting exponential increase in atmospheric drag at low perigee altitudes [7].

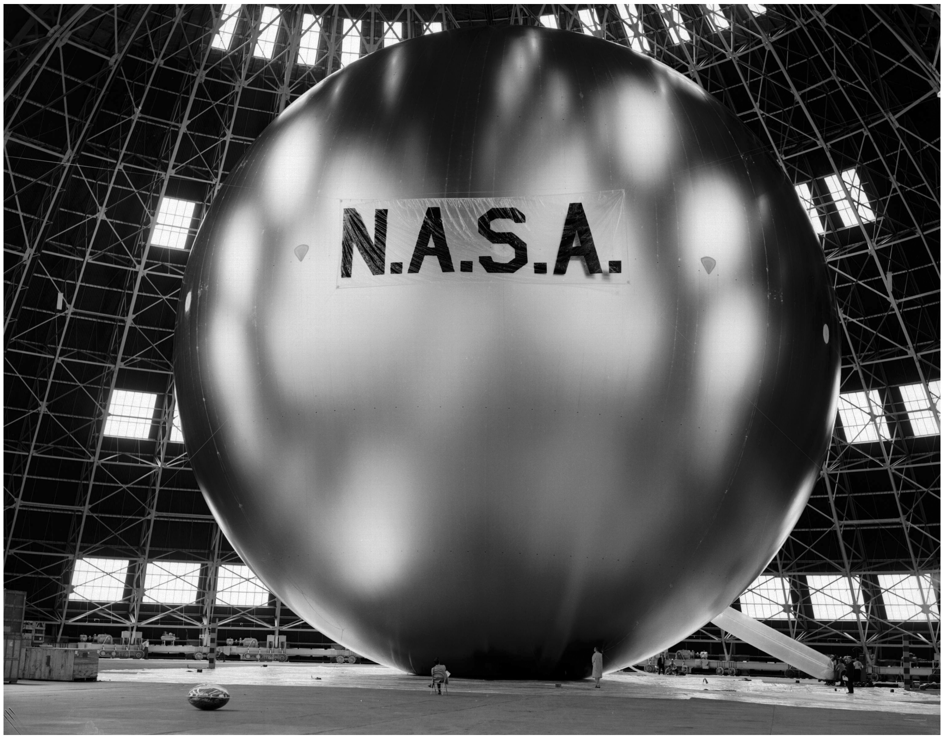

Figure 1.1: Static inflation test of Echo I satellite in Weeksville, N.C (Taken from [8])

1.1.1 Resonance identification and characterization

The unexpected behaviour of Vanguard I led Musen et al. [9] to identify the coupling between SRP and geopotential, specifically, the Earth's second zonal harmonic J_2, as the cause of the discrepancy between Vanguard's observed position and what was initially expected. Musen et al. also showed that the coupling of the two perturbations can lead, under specific conditions, to secular eccentricity oscillations of considerable amplitude, also referred to as a *resonance* effect [10]. A more detailed description of the resonance and the associated conditions was later presented by Cook [11]. More specifically, based on the averaged equations of motion, Cook identified, for a spherical body, the location of six orbital resonances in the form of a condition on the rate of change of the phase angles. The six phase angle rates are linearly dependent on the rates of the Right Ascension of the Ascending Node (RAAN, Ω) of the orbit of the spacecraft, its argument of perigee (ω) and the solar ecliptic longitude (λ_S), also referred to as the longitude of the Sun. In the literature, these conditions on the phase angle rates are also referred to as the resonance conditions or the *commensurability conditions*. Under the spherical body assumption, these resonances are limited to specific ensembles of orbits, also referred to as deorbitation corridors [12]–[14]. Notwithstanding, the characterization of the phenomenon by Cook based solely on the phase angle rate constraints is deficient.

To better understand the eccentricity resonance phenomenon, it is worthwhile to recall the existence of the 1933 Brown and Shook's Planetary Theory [15]. In fact, the possibility of resonance in celestial motion had been known for multiple decades before the first satellite launch in 1957.

In their work, Brown and Shook highlight that a parallel can be made between the resonant behaviour of celestial bodies and the motion of a simple pendulum. The relation between the orbital eccentricity of the body and a resonant phase angle resembles that of the rate and phase of the pendulum, this model is often referred to in the literature as the first fundamental resonance model [16]. Although the pendulum motion can serve as a good analogy to orbital mechanics under certain conditions, the comparison loses its validity for orbits with low eccentricity. Using the orbit-averaged Hamiltonan formulation of the equations of motions for a balloon satellite under the single resonance hypothesis, Krivov and Getino [17] derived a more precise representation of the phase space which can take five different topologies. He classified these based on the spacecraft area-to-mass ratio and orbital semi-major axis.

More recent work performed by Alessi et al. [18] presents an equilibrium and stability analysis supported with appropriate phase portraits, to evaluate and delineate the impact of the orbital inclination on a spherical spacecraft resonant dynamics. The study further shows the clear impact of the area-to-mass ratio on the location of the equilibrium points. This feature is key to the characterization of resonance since the highest-amplitude eccentricity oscillation for a particular phase plot is reached at the separatrix—in this case, a phase curve associated with an unstable equilibrium. From these results, we also infer that the width in inclination of the deorbitation corridors, i.e., the range of inclinations leading to a significant resonance effect for a specific semi-major axis, although very narrow for small area-to-mass ratio objects, is significantly larger when this ratio is high.

Gkolias et al. [19] extended the work presented by Alessi et al. [18], and provided a more detailed formulation of Hamiltonian describing the coupled dynamics of the SRP and J_2 effects. A thorough analysis of the complex resonant dynamics was performed. Their more accurate phase space description, similar to what was presented in [17], was used to determine the minimum area-to-mass ratio required to deorbit a spacecraft based on its location in space, and the resulting phase space topology.

1.1.2 Exploitation of passive SRP-J_2 resonance for deorbitation

In anticipation of a sheer increase of traffic in LEO, and to mitigate the inherent collision risks, a consortium of researchers worked at identifying passive means to minimize the environmental impact of space debris in the circumterrestrial region collaborated under the umbrella of the ReDSHIFT (Revolutionary Design of Spacecraft through Holistic Integration of Future Technologies) project [14]. As part of their mandate, the team conducted, between 2016 and 2019, extensive studies, in part, on the long-term evolution of the space population [12], [20]–[22]. Based on their findings, one the most influential factors in the evolution of the space debris environment is the post-mission disposal (deorbitation time) of spacecraft and rocket bodies [22]. Decreasing the number of threatening non-active satellites by quick end-of-life deorbitation is thus expected to reduce collision risks, hence, reduce the proliferation of space debris.

The disposal process in LEO typically involves lowering the orbital perigee to an altitude where atmospheric drag is sufficient to deorbit the debris in a timely manner. Based on the currently available technologies, this is usually achieved by a single impulsive manoeuvre executed at the apogee. This type of manoeuvres may, however, require a considerable delta-v (ΔV) impulse, i.e., high propulsion capabilities. Towards the goal of finding passive solutions to deorbitation, the ReDSHIFT team built on the idea initially put forward by Lücking et al. [23]–[25], that natural resonances could be exploited to achieve the required lowering of the perigee to ensure rapid decay. This idea became a cornerstone of their mitigation propositions.

The teamwork of ReDSHIFT on the characterization of the passive SRP-J_2 resonance corridors, among others, to be exploited as "natural highways" for end-of-life disposal of space assets in LEO is the most extensive up-to-date. It includes analytical studies, such as frequency analysis [26], eccentricity amplitude estimation [27], equilibrium and stability analysis [18], as well as numerical cartography of the resonant deorbitation corridors in the LEO region [13], [28], [29]. The objective was to provide the necessary tools for the design of a proper and cost-effective disposal strategy in compliance with the mitigation guidelines to minimize the environmental impact of a planned mission. However, the inclination width of the "natural highways" is small, a few degrees, for spacecraft with area-to-mass ratios (A/m) lower than 1 m^2/kg [30]. This means that for a spacecraft to exploit the SRP-J_2 resonance for deorbitation, the spacecraft must already be near the resonant inclination; otherwise, the ΔV required to change the orbit inclination is too costly.

1.2 Space environment in low Earth orbit

To offer broader and faster internet access, companies such as SpaceX and OneWeb have, since 2019, begun to massively populate several key orbits in the already crowded low Earth region (altitudes below 2,000 km); this marked the beginning of a new era in space exploitation. As of April 14, 2023, ESA's DISCOS database catalogues 4,004 Starlink satellites (see Figure1.2) launched by SpaceX in orbits ranging from 350 to 580 km. From this number, 301 have already re-entered the Earth's atmosphere [31]. Although Starlink satellites are placed in relatively low orbits from which a rapid natural decay is ensured by the sufficiently dense atmosphere, not all mega-constellations (actual and planned) are. OneWeb, for instance, has already placed more than 540 satellites in orbits as high as 1,230 km [31].

This sheer increase of space assets in an already compromised space environment composed of massive pieces of debris straying the low Earth region enables space debris growth by increasing the probability of collisions and explosions. Some of these, like Saturn IVB (13,500 kg) rocket stages, have been in orbit since the '60s [31], [32], and are expected to remain in orbit for many more decades. As a testimony to the threat posed by failed or uncontrolled space assets, we can cite the infamous 2009 collision involving the uncontrolled Russian Kosmos-2251 (900 kg) and the active American Iridium 33 (662 kg) satellites that occurred at an altitude of 790 km with an impact velocity of 11.6 km/s. This collision alone generated 2,368 new trackable debris, the

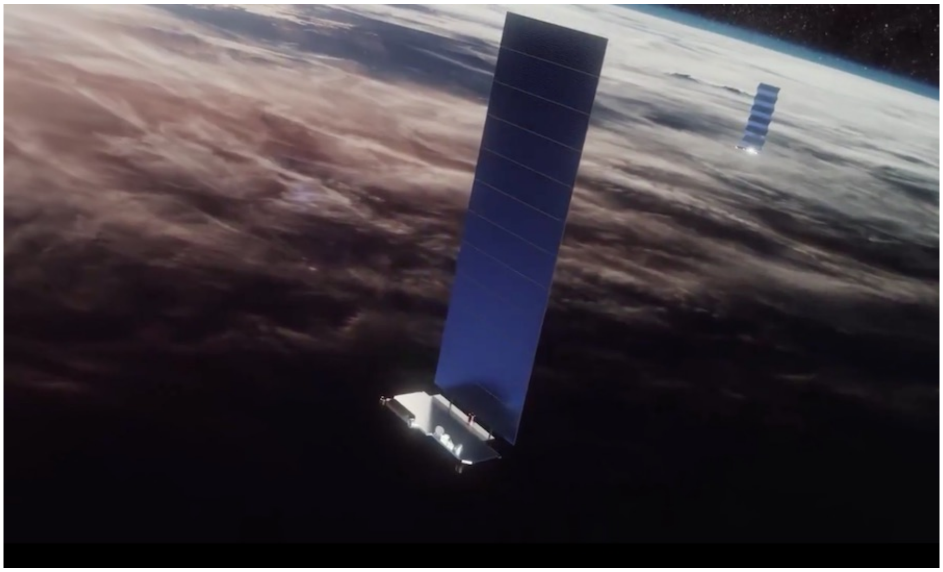

Figure 1.2: Conceptual view of Starlink satellites (Credit: SpaceX)

number representing nearly 25% of the >10 cm objects in the space population at that time [33], [34]. We can also cite numerous explosions, related to residual propellant or battery failures, that caused hundreds of trackable debris fragments to be projected chaotically (see Table 1.1 for a non-exhaustive list of debris-generating events). Fig. 1.3 shows the evolution of the space population from which we can assess the clear impact of the most critical debris-generating events listed in Table 1.1.

Table 1.1: Most critical debris generating events since 1957 and number of generated debris catalogued by DISCOS database on April 14, 2023 [31]

Year	**Object**	**Cause**	**Nb of debris**
1965	Titan IIIC Transtage	engine explosion	108
1981	Kosmos-1275	battery explosion	478
1986	Ariane 1	residual propellant explosion	502
1996	Pegasus/HAPS	residual propellant explosion	753
2007	FengYun-1C	anti-satellite missile test	3,533
2008	Kosmos-2421	disintegrated	511
2009	Kosmos-2251, Iridium 33	accidental collision	2,368
2015	NOAA-16	battery explosion	457
2021	Kosmos-1408	anti-satellite missile test	1,775

The Inter-Agency Space Debris Coordination Committee (IADC) presented, for the first time in 2002, their Space Debris Mitigation Guidelines in which they suggest certain means to minimize the impact of human activity on space exploitation; the latest revision was issued in June 2021 [36]. The main takeaways from these are the necessity to passivate the spacecraft at their end-of-life, i.e.,

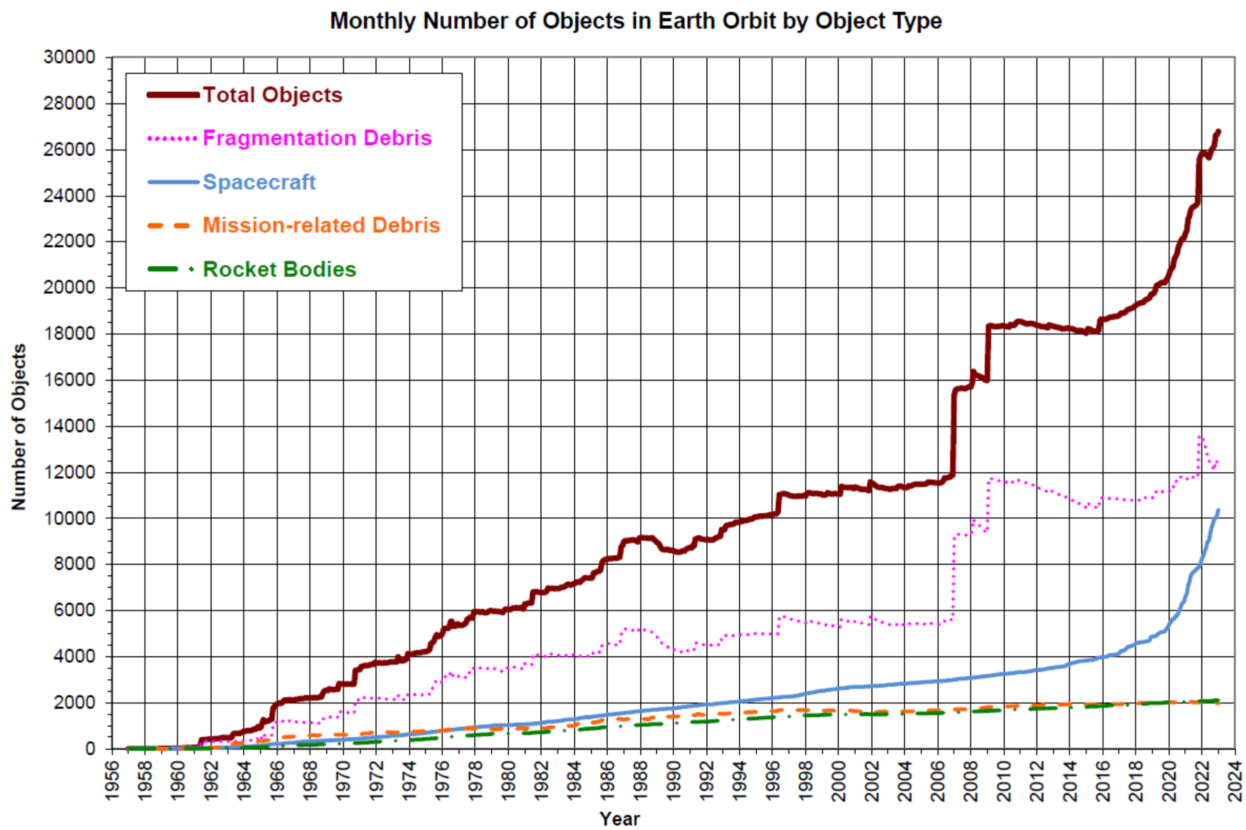

Figure 1.3: Monthly number of objects in the Earth orbit officially catalogued as of March 2023 by the U.S. Space Surveillance Network since 1957 (Taken from [35])

empty the batteries and remove any residual propellant, to prevent explosions during decay. Also, the IADC suggests a maximum end-of-life disposal time of 25 years, also referred to as the 25-year guideline, to curtail space debris proliferation. In its report on the space debris environment, the IADC however estimates that, for any given year, only between 10 and 40% of the spacecraft launched before 2017 respect the disposal guidelines [37]: the high disposal cost of space assets being a solid disincentive for spacecraft owners and operators to abide by these legally non-binding rules.

Even if no penalty is incurred for non-compliance to strict mitigation requirements, the leading telecommunication companies are aware of the dangers associated with the introduction of mega-constellations in LEO and are imposing stricter mitigation constraints than those recommended by IADC. In October 2022, the American Institute of Aeronautics and Astronautics (AIAA) facilitated the publication of a best practice reference document by Iridium, SpaceX and OneWeb. The document provides its own space debris mitigation guidelines to ensure sustainable use of space. It further states that a disposal time of less than 5 years, preferably 1 year, should be ensured. Although at altitudes below 400 km, atmospheric drag is sufficient to ensure compliance, at higher altitudes, a reliable disposal strategy is required [38]. For OneWeb satellites launched to an altitude of, 1,200 km, such active end-of-life management is imperative.

While the leading mega-constellations companies such as SpaceX and OneWeb have the means to equip their assets with efficient disposal technologies to comply with their self-imposed end-of-life requirements, not all satellite owners and operators have. Following the democratization of space access enabled by the low-cost launches offered by reusable launchers such as the falcon 9 partially reusable launch vehicle [39], a plethora of new start-ups emerged, most of them proposing low-cost solutions for a variety of space missions [40]. In this context, the rapid population of the limited naturally compliant orbits puts further pressure on the need to develop reliable and affordable disposal means. Otherwise, the ability to safely access and operate satellites in the higher low Earth orbits at reasonable costs will be jeopardized.

However, even if all new space assets abide by the strictest mitigation rules, the IADC still forecasts growth in space population. They predict an increase in catastrophic collisions from non-manoeuvrable upper stages and spacecraft even if no new object is injected into orbit. The low compliance of space assets to the suggested mitigation rules only compounds the situation. In light of this, they conclude that the sustainable management of space exploitation not only relies on good practices but also on remediation efforts [41].

1.2.1 Spacecraft remediation

The predicted increase in catastrophic collisions by the IADC is expected to become the dominant source of debris if no action is taken to remediate the problem. There is therefore a necessity to remove hazardous space assets through Active Debris Removal (ADR) [41].

Many ADR concepts were put forward by researchers over the last two decades, e.g., tether-based, dynamical system-based, sail-based, and laser-based methods to name a few [42]. However, according to the authors of [42], most of the proposed solutions lack of experimental verification phases, which are crucial for viable commercial deployment. Nonetheless, the main idea for upcoming ADR missions is to send a system into space (a chaser) that will act to capture and lower a particular debris towards its re-entry into the Earth's atmosphere to be disintegrated. The execution of a complete ADR mission is however a complex problem with diverse issues at the economic, political, legal and technological levels, although, such missions are slowly starting to materialize.

As an example of upcoming ADR missions, the ESA contracted ClearSpace team is planning to remove a Vespa rocket upper stage debris from its 750 km orbit by 2026 [43]. Another example is the End-of-Life Services by Astroscale-demonstration (ELSA-d) mission launched in March 2021 which proved the ability to perform a controlled close approach rendezvous with a small debris [44]. The lessons learned from these first steps toward complete debris removal will serve for their next planned missions, namely Active Debris Removal by Astroscale-Japan (ADRAS-J, 2023) [45], and End-of-Life Services by Astroscale-Multi-client (ELSA-M, 2024) [46].

ADR solutions are still in their infancy, and there will be many years before these technologies are thoroughly tested for widespread deployment, and before international regulations provide an adequate framework for debris removal operations. In the meantime, it is essential to limit to a minimum the impact of current human activity in space. This implies reducing as much as possible spacecraft orbiting time past their service life. To achieve this goal on a global scale, and convince spacecraft owners and operators to adopt the required measures, it is essential to develop and make available novel solutions that offer a reliable and affordable alternative to spacecraft deorbitation.

1.3 Solar sailing

As previously alluded the exploitation of the SRP-J_2 resonance for deorbitation allows to significantly lower the disposal cost for a spacecraft initially in the vicinity of a resonance orbit. It is expected that once an object is placed in a deorbitation corridor, no additional manoeuvring is required as the descent is passively driven by the effect of natural perturbations. However, to obtain the desired effect, strict conditions on the spacecraft's location must be met. For spacecraft with functional control capabilities, other end-of-life strategies involving the maximization/minimization of its sunlit area have also been suggested as potential solutions for deorbitation, particularly for plate-like spacecraft.

In December 2010, JAXA's IKAROS flew by Venus six months after it departed from Earth making it the first interplanetary solar sail voyage [47], [48]. This mission demonstrated the possibility of navigating into space by exploiting SRP propulsion. It further showed the possibility of controlling the spin axis of the spacecraft by changing the reflectance of its 200 m^2 sail using a Reflectance Control Device (RCD) [48]. The RCD allows to alternate between a specular-dominant and a diffusive-dominant surface. Synchronizing the change rate with the spinning phase allows the reorientation of the spin axis with electrical power, thus, without the use of fuel [48]. This highlights the importance of the spacecraft's surface optical properties in the study of SRP effects.

The solar sailing capabilities demonstrated by the IKAROS mission could also be applied to dispose of Earth-orbiting satellites as was suggested by Borja and Tun [49]. The authors proposed the use of a bang-bang reorientation scheme to maximize the global effect of the SRP on the semi-major axis decrease by either minimizing or maximizing the Sun exposed surface appropriately. Colombo et al. [50] developed a similar strategy to increase eccentricity. The coupling between the *attitude* and the SRP effect on orbital motion leads to a cumulative effect on the orbital parameters; such a solution can be applied to a spacecraft in any orbit as long as it possesses the ability to reorient itself with respect to the Sun: twice per orbit in the case of semi-major axis solution proposed by Borja and Tun, and every few months for the eccentricity solution proposed by Colombo et al. Such solutions aim at accelerating deorbitation by either lowering the semi-major axis or increasing the eccentricity but inverting the logic allows for the opposite effect. This possibility enables orbital manoeuvring through solar sailing and could, among other things, be used to further increase altitude as was demonstrated by the LightSail 2 mission.

LightSail 2 (see Figure 1.4) was a citizen-funded project carried by The Planetary Society, a non-profit organization with the mission to "empower the world's citizens to advance space science and exploration" [51]. The controllable solar sail was successfully put into a 720 km orbit in July

2019 and has publicly shared its telemetry data until re-entry in November 2022. Its primary objective was to demonstrate controlled solar sailing by countering the loss of energy due to drag with SRP propulsion. They did so by exploiting a bang-bang type strategy to maximize the altitude increase as suggested by Borja and Tun [49], [52]. LightSail 2 served as a testing platform for orbital manoeuvres exploiting SRP which will be useful for future NASA missions, namely ACS3, NEA Scout, Solar Cruise and NEO Surveyor with the ultimate goal of using solar sailing to orbit the Sun and detect potential threats to Earth.

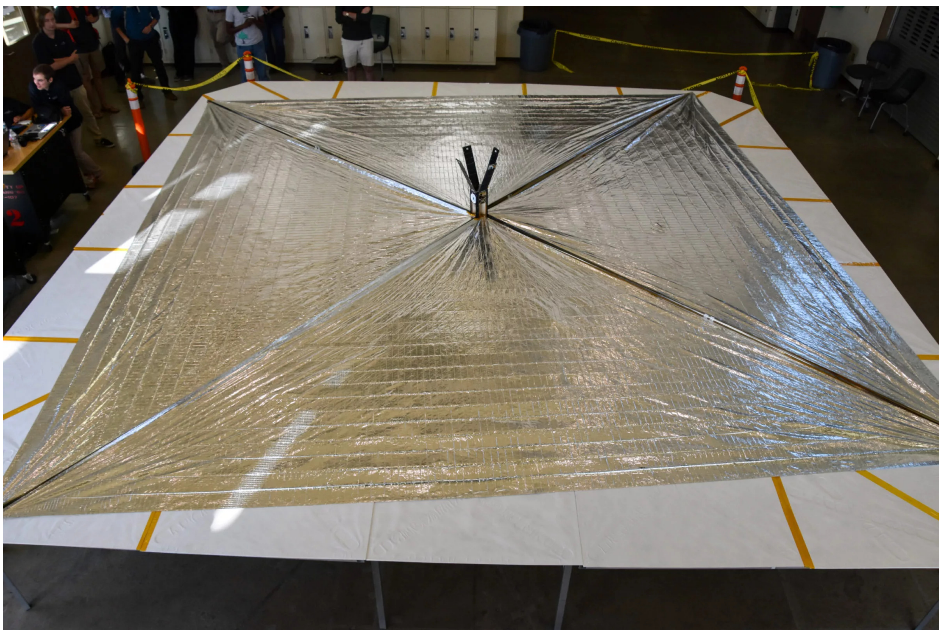

Figure 1.4: The Planetary Society's LightSail 2 spacecraft during sail deployment testing in 2016 (Taken from [53])

As previously alluded these bang-bang-type methods for reorienting the spacecraft require active control capabilities. The desire to have a fully passive deorbitation solution with no restrictions on the initial location motivated the investigation of a quasi-rhombic-pyramid sail for passive attitude stabilization to generate a substantial eccentricity increase over time [54]. The feasibility of this concept was assessed for a simplified quasi-rhombic pyramid by Miguel and Colombo [55]. The analysis showed that stable deorbiting is indeed achievable given some restrictions depending on the physical properties of the sail. Passive disposal means are of very high interest as they represent end-of-life solutions robust to spacecraft failure.

Although sail propulsion may be less time efficient than fuel propulsion, the cost savings offered by such a solution is a clear advantage, while also being safer and more robust due to a reduced dependency on fuel. Also, the possibility to perform orbital manoeuvres by exploiting natural perturbations instead of using other power sources like propellant is not only interesting for deorbitation purposes but could be further employed for collision avoidance or interplanetary travel. To make space exploitation more sustainable and reduce high mission costs, the Control for Orbit Manoeuvring Through Perturbations for Application to Space Systems (COMPASS) group is exploring the possibility of optimizing orbital manoeuvring to use external perturbations as propulsion forces instead of treating them as disturbances to counter [56].

1.4 Orbital propagation

The high costs related to building a technology demonstration spacecraft and launching it into space make physical testing expensive and difficult. Spacecraft and mission design thus rely on extensive simulation analyses, as well as accurate numerical models of the different perturbations affecting the motion of a body in space.

Great advances have been made in the field of numerical computation since the first attempts to characterize the SRP-J_2 resonance in the early ’60s. For instance, in 1962, when studying the resonant motion of Echo I, Cook resorted to analytical expressions of the averaged dynamics. This model was derived from Lagrange’s planetary equations averaged over one orbit for a spacecraft subject to SRP and J_2 effects while neglecting atmospheric drag [11], [57]. Given the limited computational resources of that era, averaging was essential to propagate complex orbital problems in a timely manner.

Since these early studies of Echo I, more accurate perturbation models have become available, particularly for atmospheric density, thus allowing for more accurate orbit propagation of spacecraft decay when subject to resonance, among other phenomena [58]. Also, with the considerable improvement in numerical computation, it is now possible to perform the full numerical integration of non-averaged equations of motion in a practical way. These capabilities enabled more precise prediction tools of more accurate perturbation models, spacecraft with complex geometries, and over longer periods, but there is still a trade-off to be made between precision and computation speed. In this light, averaged models are still of interest, particularly when performing preliminary analysis or when trying to isolate the secular tendencies from the short-period noise. Depending on the situation, certain assumptions can be made to greatly reduce calculations, thus the computation time, with only a small loss of accuracy.

1.4.1 Types of orbital propagators

Several orbital propagators exist, each more suitable for a certain type of application, but as a baseline, most of them consider the major orbital perturbation sources, namely, the geopotential and third body attraction, the atmospheric drag and the solar radiation pressure. The ReDSHIFT team whose work we discussed earlier employed, among others, the two following propagators [29]:

- FLORA (Fast, Long-term ORbit Analysis): this propagator exploits averaged analytical equations omitting short-period variations; thus, it is faster, but it is not as accurate [59];

- NEPTUNE (NPI Ephemeris Propagation Tool with Uncertainty Extrapolation): this is a high-fidelity propagator that also allows the consideration of the Earth's albedo, solid Earth tides, polar tides and ocean tides, in addition to the major perturbations sources. It numerically integrates the equations of motion yielding more accurate orbit predictions than averaged propagators [29].

LEGO [60], FOP [61], DCP [61], STELA [62], THALASSA [63] and INDEMN [64] are some of the other propagators used by the research community and there are many more.

Both FLORA and NEPTUNE were used to assess the capabilities of the propagators to identify resonance corridors. NEPTUNE (numerical integration of full equations) results showed additional SRP-J_2 resonance corridors that were invisible to FLORA (averaged analytical equations). Although not all of them could be explained, some were found to be associated with the coupling of the shadow of the Earth and the SRP [29]. The SRP is a relatively small perturbation in comparison to the geopotential or third-body attractions from the Sun or the Moon. However, as previously mentioned, in the case of resonance, the cumulative effect becomes significant over time. It is thus important to be mindful when performing the averaging as to the possibility of resonances and consider them as long-period variations, not short-period. The comparison performed in [29] shows that, although analytical models might be very useful for preliminary analysis, results should always be verified using numerical integration of the most accurate equations of motion.

1.4.2 D-SPOSE

Throughout this thesis, the settings for different deorbitation strategies exploiting the resonance phenomenon are derived from simplified mathematical models, while the efficiency of these strategies is assessed using the state-of-the-art open source simulator D-SPOSE (Debris Spin/Orbit Simulation Environment) recently developed by [65]–[67]. D-SPOSE integrates numerically the full set of equations of motions and allows for long-term motion propagation of space debris as an alternative to the propagators previously presented.

D-SPOSE distinguishes itself from the aforementioned propagators by explicitly considering the coupled attitude-orbital dynamics of a body in space, and by integrating into a single simulator the effects on both orbital and attitude motions of the most significant perturbations. While most propagators consider only the major perturbations, D-SPOSE also considers the eddy-current torque, the infrared acceleration and torque, the internal energy dissipation and the hypervelocity impacts [68]. The highly detailed modelling of attitude motion and its coupling to an equally comprehensive model of the orbital motion make D-SPOSE one of the most accurate and validated against observations propagators available to the research community [66], [67]. The interaction of a rotating object with non-conservative forces such as aerodynamic drag is of paramount importance in this work, thus the improvements in accuracy offered by D-SPOSE, combined with validation against observations, bode well for highly accurate orbital predictions of non-spherical geometries. As alluded, attitude propagation results from D-SPOSE for several debris objects have been compared to observations; good agreement overall was obtained, but some differences remained. One possible explanation for the discrepancies from observations was suggested to be the Yarkovsky/YORP effect [65]. As part of the research conducted in this thesis, D-SPOSE was therefore enhanced by the addition of the thermal radiation pressure which is the physical source of the Yarkovsky-YORP effect.

1.5 Thesis outline

In this thesis, the aim is to provide a simple strategy that would reduce the deorbitation time of a spacecraft at its end-of-life by exploiting the effect of natural perturbations; this, with the ultimate goal of mitigating the spacecraft's impact on the space debris population at a low energy cost. Thus, Chapter 2 outlines the mathematical tools used throughout this thesis to model the dynamics of a plate-like spacecraft subject to Solar and Thermal Radiation Pressure (STRP) and the Earth's second zonal harmonic J_2 perturbations. Chapter 3 builds on Alessi's phase space description of the SRP-J_2 resonance to interpret the observed behaviour of the Echo I balloon satellite and to gain further insights into its relationship to the resonance. In Chapter 4, a novel formulation of the resonance phenomenon that involves the attitude motion of rotating plate-like spacecraft, referred to as STRP-J_2-ϕ resonance, is put forward. This allows to eliminate location restrictions of the passive STRP-J_2 resonance in eccentricity. We further delineate the capabilities of this attitude-induced resonance for deorbitation. The proposed attitude-dependant resonance is further generalized in Chapter 5 for not only the eccentricity increase but the semi-major axis as well. The settings for an attitude control law are defined to enforce the STRP-J_2-ϕ resonance in both eccentricity and semi-major axis which removes the minimum attainable altitude associated with the eccentricity resonance solution of Chapter 4. The strategies thus put forward are then compared in Chapter 6 to the similar end-of-life strategies discussed in Section 1.3, relying on a bang-bang reorientation scheme to maximize the global effect of the STRP towards deorbitation. In Chapter 7, with the perspective of the LightSail 2 mission, the settings of the semi-major axis resonance solution are modified to allow for semi-major axis tracking in a region where atmospheric drag is non-negligible. Finally, Chapter 8 presents a summary, conclusions, and a few directions for future work.

Chapter 2

Dynamics of a Plate-Like Spacecraft in LEO

As discussed in Chapter 1, the main goal of this thesis is to provide a simple strategy that would reduce a spacecraft's deorbitation time at its end-of-life by exploiting the effect of natural perturbations instead of fuel propulsion; this, with the ultimate purpose of mitigating impact on the space debris population at a low fuel cost. This work particularly concentrates on plate-like spacecraft or a panel. The motivation behind this assumption stems from SpaceX's Starlink satellite, the main components of which are a large 9x3.3 m^2 solar panel attached to a 3.3x1.4 m^2 body. This specific satellite design accounts for about 3,600 of all Earth's orbiting objects as of March 31, 2023, a number that is constantly increasing. A panel also accurately models a spacecraft equipped with a drag-enhancing device such as The Planetary Society's LightSail 2 satellite. The mission of this particular spacecraft will be the motivation for the analysis presented in Chapter 7.

To deorbit a spacecraft, its altitude needs to be lowered either over its complete orbit, by reducing its orbital semi-major axis a, or near its perigee, by increasing its orbital eccentricity e. It is considered that when a spacecraft reaches an altitude of approximately 200 km, the friction exerted by the atmosphere on the structure is sufficiently high to cause it to burn down and thus disintegrate in a matter of minutes. The two deorbitation solutions put forward in this thesis and presented in Chapters 4 and 5 are based on the premise that the lowering of a plate-like spacecraft altitude can be achieved by modulating the amplitude of the sun-exposed area of the panel through active control to induce a resonance effect on either the semi-major axis or the eccentricity of the spacecraft's orbit.

A brief discussion on the different perturbations acting on a spacecraft in LEO and their importance is first presented in this chapter. This is followed by the dynamics modelling of a rotating plate-like spacecraft in LEO subject to both the Earth's second zonal harmonic (J_2) and the Solar and Thermal Radiation Pressure (STRP) perturbations, the coupled action of which can lead to resonance. The relevant equations of motion are then derived based on the Hamiltonian formalism of either the non-averaged or the averaged dynamics. These equations will serve as a basis for the study of the STRP-J_2 resonance phenomenon, both in semi-major axis and eccentricity, that will follow in subsequent chapters. One should bear in mind that the purpose of this chapter is not to develop the most accurate model of spacecraft orbital dynamics in LEO. The orbital motion is affected, to a different extent, by many external perturbations which cumulatively lead to a complex oscillating behaviour of orbital elements, not necessarily of great importance in the long term. Rather, our goal is to provide the modelling of the J_2 and STRP perturbations to demonstrate that their coupling can result in a significant impact on the secular motion of the spacecraft. This simplified model will serve as a tool for the identification of the attitude conditions required to generate a resonant effect.

2.1 Orbital perturbations in LEO

The low Earth region altitudes span from 200 km to 2000 km. In the lowest part of this range, i.e., approximately below 600 km, the descent of the spacecraft is passively driven by the atmospheric drag usually leading to deorbitation in a matter of months or a few years, depending on the solar activity and area-to-mass ratio. The decent rate owed to drag, however, considerably decreases at higher altitudes due to the exponential drop in atmospheric density, thus, extending the deorbitation time from months to years and ultimately decades or centuries for spacecraft located at the highest LEO altitudes. Still in the LEO range, the geopotential, more specifically its second zonal harmonic (J_2), has a significant impact on the orbit of the spacecraft, mainly the argument of perigee ω and RAAN Ω, because of the proximity of the orbiting object to the oblate Earth. Another important perturbation, which for a long time researchers deemed to be negligible for spacecraft in LEO, is the cumulative action of the Thermal Radiation Pressure (TRP) and the Solar Radiation Pressure (SRP). These two perturbations are intrinsically linked to the gain and loss of momentum generated by: thermal emission by the spacecraft for the TRP and either incoming or reflected luminous radiation for the SRP. As evidenced by the motion of NASA's Vanguard I, as well as those of the Echo I and II balloons, under certain conditions, the action of the STRP on the eccentricity e coupled to the J_2 action on ω and Ω can cause the spacecraft to undergo strong long-periodic oscillations in eccentricity, whereas it usually averages out to a null secular effect for most spacecraft. The specific case of Echo I will be the subject of Chapter 3. Other gravitational perturbations including the third body attraction of the Moon and the Sun, as well as other radiation perturbations such as the Earth's albedo and infrared emissions, are considered to be of very small importance in the secular evolution of a spacecraft in LEO. The secular motion of the spacecraft is therefore assumed to be governed by the atmospheric drag at low altitudes (< 600km) and by the coupling of the STRP and J_2 effects otherwise.

We recall that the goal of this work is to derive a solution exploiting natural perturbations to lower the altitude of a spacecraft initially in LEO. As previously mentioned, this is passively achieved in a timely manner by the atmospheric drag for spacecraft in the lowest part of the low Earth region. Alternate solutions become interesting for spacecraft initially located at higher altitudes where the atmospheric drag is negligible. This thesis focuses on the STRP-J_2 resonance solution as a means to lower the altitude of a spacecraft initially located in the high LEO region to the threshold altitude of 600 km where atmospheric drag becomes the driving force towards deorbitation. The idea is to exploit the STRP-J_2 resonance effect on the motion of either the semi-major axis or the eccentricity of a stably rotating plate-like spacecraft. This phenomenon can happen naturally in the vicinity of certain orbits defined by a particular combination of semi-major axis a, eccentricity e and inclination i, or it can be induced by modulating the amplitude of the sun-exposed area of the panel, or equivalently by modulating the angle between the incoming light direction and the panel's normal, through active control. The attitude condition required to enforce the resonance over the whole deorbitation process can be determined from the orbital equations of motion of either a or e for a panel subject to both STRP and the J_2 harmonic of the Earth. The derivation of the relevant equations of motion is thus presented in the following sections for later use.

2.2 Kinematics

In this section, we present the reference frames and parameters used throughout this work. As well, we provide relevant transformations and vectorial quantities that will be useful in establishing the STRP-J_2 dynamics of a plate-like spacecraft rotating about the ecliptic's normal.

2.2.1 Reference frames

In Section 2.3, we derive the perturbing potential functions associated with the STRP and the Earth's second zonal harmonic. These will later be of use when deriving Hamilton's equations of motion, but before that, we first introduce the three reference frames that are used throughout this thesis: the Earth-Centered Inertial (ECI) frame, denoted as $\mathcal{F}_{\mathrm{ECI}} = \left\{O, \underrightarrow{i}, \underrightarrow{j}, \underrightarrow{k}\right\}$, the Local-Vertical/Local Horizontal (LVLH) frame $\mathcal{F}_{\mathrm{LVLH}} = \left\{O_b, \underrightarrow{r}, \underrightarrow{s}, \underrightarrow{w}\right\}$ and the body-fixed frame $\mathcal{F}_b = \left\{O_b, \underrightarrow{x}_b, \underrightarrow{y}_b, \underrightarrow{z}_b\right\}$. These are illustrated in Figs. 2.1 and 2.2.

For $\mathcal{F}_{\mathrm{ECI}}$, O is located at the centre of the Earth, $\underrightarrow{i}$ points along the vernal equinox, $\underrightarrow{k}$ points toward the celestial north pole, while $\underrightarrow{j} = \underrightarrow{k} \times \underrightarrow{i}$ completes the triad. For $\mathcal{F}_{\mathrm{LVLH}}$, O_b is located at the spacecraft position, $\underrightarrow{r}$ is directed along $\underrightarrow{OO_b}$, $\underrightarrow{w}$ is directed along the orbital angular momentum ($\underrightarrow{h}$), normal to the orbital plane, and $\underrightarrow{s} = \underrightarrow{w} \times \underrightarrow{r}$ completes the triad. For $\mathcal{F}_b$, $\underrightarrow{x}_b$ is the outward normal to the panel's front side denoted with f, i.e., $\underrightarrow{n} = -\underrightarrow{x_b}$, $\underrightarrow{z}_b$ is along the minor axis of inertia while $\underrightarrow{y}_b = \underrightarrow{z}_b \times \underrightarrow{x}_b$ completes the triad.

Note that when deriving the equations of motion, the spacecraft is assumed to rotate at a constant angular velocity $\underrightarrow{\omega}_b$ about its $\underrightarrow{z}_b$-axis ($\underrightarrow{z}_b \parallel \underrightarrow{\omega}_b$), which is set to be aligned with the ecliptic's normal (or equivalently, the orbital angular momentum of the Sun $\underrightarrow{h_S}$) illustrated in Fig. 2.3. Under this assumption, the orientation of $\mathcal{F}_b$ with respect to $\mathcal{F}_{\mathrm{ECI}}$ is given by the attitude angle ϕ, i.e., the angle between $\underrightarrow{x}_b$ and $\underrightarrow{i}$. This constraint on the rotation axis is imposed to maximize the mean exposed area and is enforced with attitude control, as presented in Chapters 4 and 5. Fig. 2.3

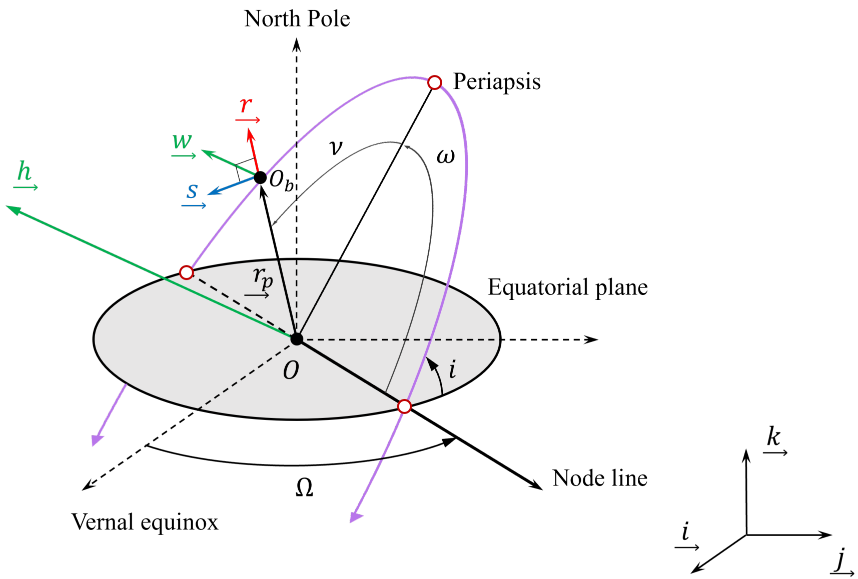

Figure 2.1: Orbital parameters representation and definitions of $\mathcal{F}_{\mathrm{ECI}}$, and $\mathcal{F}_{\mathrm{LVLH}}$

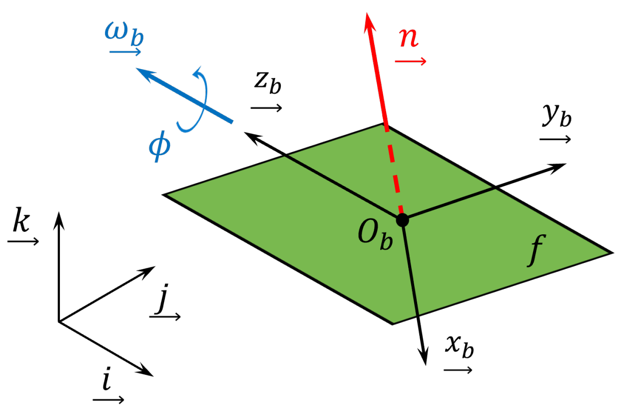

Figure 2.2: Plate spacecraft with body-fixed frame $\mathcal{F}_b$ and attitude variables ϕ and $\underset{\rightarrow}{\omega}_b$

also illustrates the longitude of the Sun λ_S and obliquity ε as well as the resulting incoming light direction vector $\underset{\rightarrow}{u}$. Note that the light perceived by the spacecraft is assumed to be identical to the light perceived by the Earth, i.e., we neglect the parallax effect. Fig. 2.1 further illustrates orbital parameters used thereafter, namely the orbital inclination, i, RAAN Ω, argument of perigee ω, and true anomaly ν.

Moreover, we introduce the spherical coordinates of the spacecraft in Fig. 2.4: r_p is the panel's geocentric distance, θ is the spherical geocentric latitude and λ is the longitude. The value of θ represents the angle between $\underset{\rightarrow}{r}_p$ and the equatorial plane as illustrated in Fig. 2.4. Based on spherical trigonometry, the following relation can be obtained:

$$\sin\theta = \sin i \sin u \tag{2.1}$$

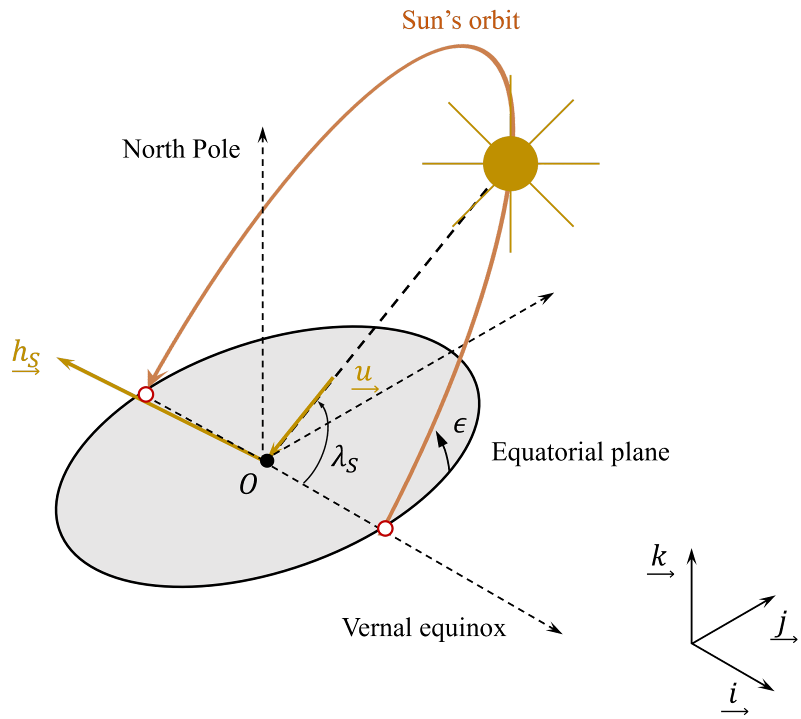

Figure 2.3: Representation of the orbital parameters of the Sun and incoming light vector $\underset{\rightarrow}{u}$

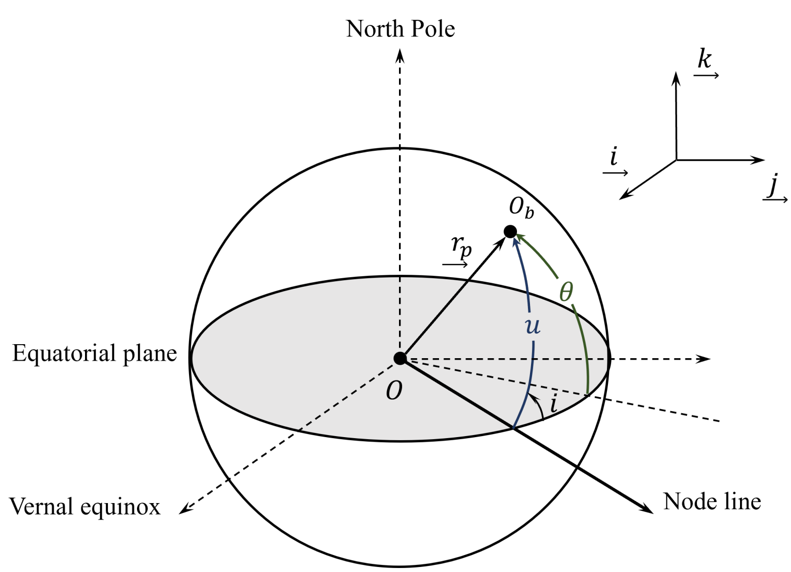

Figure 2.4: Spherical coordinates defining the spacecraft geocentric position $\underset{\rightarrow}{r}_p$

with $u = \omega + \nu$ as the argument of latitude. Eq. (2.1) will be of particular used in obtaining the geopotential expression in Section 2.3.1. Finally, the magnitude of $\underrightarrow{r}_p$ is related to the orbital elements as per:

$$r_p = a \frac{1 - e^2}{1 + e \cos \nu} \tag{2.2}$$

2.2.2 Relevant transformations

We define here the transformation from $\mathcal{F}_{\text{ECI}}$ to $\mathcal{F}_{\text{LVLH}}$ by using the following Direction Cosine Matrix (DCM):

$$\mathbf{C}_{\text{LVLH,ECI}} = \mathbf{C}_3(\omega + \nu)\, \mathbf{C}_1(i)\, \mathbf{C}_3(\Omega) \tag{2.3}$$

The notation $\mathbf{C}_{x,y}$ for DCM characterizes the orientation of the reference frame $\mathcal{F}_x$ relative to the reference frame $\mathcal{F}_y$ while $\mathbf{C}_i$ for $i = \{1, 2, 3\}$ represents the principal i DCM. Eq. (2.3) can be explicitly written in terms of the orbital parameters as:

$$\mathbf{C}_{\text{LVLH,ECI}} = \begin{bmatrix} -\sin\Omega\cos i\sin u + \cos\Omega\cos u & \cos\Omega\cos i\sin u + \sin\Omega\cos u & \sin i\sin u \\ -\sin\Omega\cos i\cos u - \cos\Omega\sin u & \cos\Omega\cos i\cos u - \sin\Omega\sin u & \sin i\cos u \\ \sin\Omega\sin i & -\cos\Omega\sin i & \cos i \end{bmatrix} \tag{2.4}$$

In a similar fashion, the $\mathcal{F}_b$ and $\mathcal{F}_{\text{ECI}}$ frames are related through the following DCM:

$$\mathbf{C}_{b,\text{ECI}} = \mathbf{C}_3(\phi)\, \mathbf{C}_1(\varepsilon) \tag{2.5}$$

which can be written in terms of the obliquity of the ecliptic ε and the attitude angle ϕ as:

$$\mathbf{C}_{b,\text{ECI}} = \begin{bmatrix} \cos\phi & \cos\varepsilon\sin\phi & \sin\varepsilon\sin\phi \\ -\sin\phi & \cos\varepsilon\cos\phi & \sin\varepsilon\cos\phi \\ 0 & -\sin\varepsilon & \cos\varepsilon \end{bmatrix} \tag{2.6}$$

Note that the obliquity of the ecliptic barely varies ($\varepsilon(t) \approx 23.43°$), and is considered constant in this work.

2.2.3 Relevant vectors in $\mathcal{F}_{\text{ECI}}$

The position vector $\underrightarrow{r}_p$ of the panel, as well as the incoming light and panel normal vectors, $\underrightarrow{u}$ and $\underrightarrow{n}$, are key in establishing the disturbing potential of the STRP and J_2 perturbations. Their components in $\mathcal{F}_{\text{ECI}}$ are denoted by $\mathbf{r}_p$, $\mathbf{u}$ and $\mathbf{n}$ respectively. The former can be explicitly written as:

$$\mathbf{r}_p = \mathbf{C}_{\text{LVLH,ECI}}^{\mathsf{T}} \begin{bmatrix} 1 \\ 0 \\ 0 \end{bmatrix} = \begin{bmatrix} -\sin\Omega\cos i\sin u + \cos\Omega\cos u \\ \cos\Omega\cos i\sin u + \sin\Omega\cos u \\ \sin i\sin u \end{bmatrix} \tag{2.7}$$

where $\mathbf{C}_{\text{LVLH,ECI}}$ is given by Eq. (2.4).

Under the previously stated assumption that the incident light vector perceived by the spacecraft is identical to the one perceived by the Earth, the incident light vector can be expressed in $\mathcal{F}_{\text{ECI}}$ as:

$$\mathbf{u} = -\begin{bmatrix} \cos\lambda_S & \sin\lambda_S\cos\varepsilon & \sin\lambda_S\sin\varepsilon \end{bmatrix}^{\mathsf{T}} \tag{2.8}$$

Since $\dot{\lambda}_S$ is almost constant ($\dot{\lambda}_S \approx 1.1408\text{e-}05°/\text{sec}$), we approximate the longitude of the Sun as: $\lambda_S(t) \approx \dot{\lambda}_S t + \lambda_{S,0}$ with $\lambda_{S,0}$ the initial value.

For the case studied in this work—a thin plate-like spacecraft rotating about the normal to the ecliptic—the panel's front side inward normal vector $\underset{\rightarrow}{n}$ can be expressed in $\mathcal{F}_{\text{ECI}}$ using Eq. (2.6) as:

$$\mathbf{n} = \mathbf{C}_{b,\text{ECI}}^{\mathsf{T}}\,\mathbf{n}_b = -\begin{bmatrix} \cos\phi & \sin\phi\cos\varepsilon & \sin\phi\sin\varepsilon \end{bmatrix}^{\mathsf{T}} \tag{2.9}$$

In Eq. (2.9), $\mathbf{n}_b = -\begin{bmatrix} 1 & 0 & 0 \end{bmatrix}^{\mathsf{T}}$ (see Figure 2.3) and $\phi(t) = \dot{\phi}\,t + \phi_0$ with $\dot{\phi} = |\underset{\rightarrow}{\omega_b}|$ and ϕ_0 depending on the initial orientation of the solar panel; it is 0 when the normal is initially opposing the vernal equinox and $\pi/2$ when it is initially along the winter solstice. From Eqs. (2.8) and (2.9), we find that the time-varying angle between $\underset{\rightarrow}{u}$ and $\underset{\rightarrow}{n}$ is:

$$\alpha(t) = \phi(t) - \lambda_S(t) = (\dot{\phi} - \dot{\lambda}_S)\,t + (\phi_0 - \lambda_{S,0}) \tag{2.10}$$

For simplicity, we will write $\alpha(t)$, $\phi(t)$ and $\lambda_S(t)$ as α, ϕ and as λ_S, but we keep in mind that these values are time-variant.

2.3 STRP-J_2 dynamics

In this section, we derive the dynamics equations of a plate-like spacecraft rotating about the ecliptic's normal when subject to the STRP and J_2 perturbations. These will be essential in establishing a deorbitation strategy exploiting the resonance due to the coupling of the two effects either in semi-major axis or in eccentricity.

2.3.1 J_2 acceleration

The geopotential perturbation due to the non-sphericity of the Earth can be expanded in terms of spherical harmonics [69]:

$$\Phi(r_p,\theta,\lambda) = -\frac{\mu}{r_p}\sum_{n=2}^{\infty}\left(\frac{R_e}{r_p}\right)^n \sum_{m=0}^{n} P_{nm}(\sin\theta)\left[C_{nm}\cos(m\lambda)+S_{nm}\sin(m\lambda)\right] \tag{2.11}$$

where μ is the gravitational constant of the Earth, R_e is the equatorial radius of the Earth, (r_p, θ, λ) are defined in Section 2.2.1, and P_{nm} are the Legendre functions evaluated at $\sin\theta$. The constants C_{nm} and S_{nm} are the so-called *Stokes coefficients* constituting the full gravity model. As it is well known that the dynamical flattening of the Earth, as represented by $J_2 = -C_{20} = 1082.6261\text{e-}6$, is nearly 500 times larger than any other term, we can approximate the perturbing geopotential function by only considering its most significant term, i.e., the J_2-term, that is:

$$\Phi(r_p,\theta,\lambda) \approx \Phi_{J_2}(r_p,\theta) = \frac{J_2\,\mu\,R_e^2}{2\,r_p^3}\left(3\,\sin^2\theta - 1\right) \tag{2.12}$$

Substituting for r_p and $\sin\theta$ into Eq. (2.12) from their expressions in Eqs. (2.2) and (2.1), we obtain:

$$\Phi(r_p,\theta,\lambda) \approx \Phi_{J_2}(r_p,\theta) = \frac{J_2\,\mu\,R_e^2}{2\,a^3}\,\frac{(1+e\cos\nu)^3}{(1-e^2)^3}\left(3\,\sin^2 i\,\sin^2 u - 1\right) \tag{2.13}$$

The above expression for the geopotential perturbation will be used in the Hamiltonian formulation of the spacecraft dynamics in Section 2.4.

2.3.2 STRP acceleration

The STRP acceleration vector of a spacecraft in direct sunlight can be expressed as [65]:

$$\underset{\rightarrow}{a}_{\text{STRP}} = P_r\,\beta\,\frac{A_{\text{nom}}}{m}\left(\frac{a_S}{r_S}\right)^2\cos\alpha\left[(\sigma_a+\sigma_{rd})\,\underset{\rightarrow}{u} + \frac{2}{3}\left(\sigma_{rd}+\sigma_a\frac{\varepsilon_l-\varepsilon_d}{\varepsilon_l+\varepsilon_d}\right)\underset{\rightarrow}{n} + 2\,\sigma_{rs}\cos\alpha\,\underset{\rightarrow}{n}\right] \tag{2.14}$$

for $\alpha \in [-\pi/2, \pi/2]$. In Eq. (2.14), P_r is the radiation pressure, β accounts for the shadow effect: it takes the value of 1 when in direct sunlight, and 0 when in the Earth's shadow; A_{nom} is the nominal area of the surface exposed to the Sun, m is the mass of the spacecraft, assumed constant, a_S and r_S are the orbital semi-major axis of the Sun and distance from Earth, while σ_a, σ_{rd} and σ_{rs} are respectively the fraction of incident photons absorbed, reflected diffusely and reflected specularly by the surface with $\sigma_a+\sigma_{rd}+\sigma_{rs}=1$. The emissivity coefficients (associated with the TRP) of the sunlit and dark sides of the panel are given by ε_l and ε_d, with $0 \le \{\varepsilon_l, \varepsilon_d\} \le 1$, and α represents the angle between $\underset{\rightarrow}{u}$ and $\underset{\rightarrow}{n}$ such that $\cos\alpha = \underset{\rightarrow}{u}\cdot\underset{\rightarrow}{n}$.

To maximize the resonant effect while requiring simple attitude motion, the plate-like spacecraft, or panel, is set to rotate, as previously mentioned, at angular velocity $\underset{\rightarrow}{\omega}_b$ about its minor axis of inertia, $\underset{\rightarrow}{z}_b$-axis, aligned parallel to the fixed axis of the orbital angular momentum of the Sun $\underset{\rightarrow}{h}_S$. Under such conditions, the STRP acceleration can be expressed, for a Lambertian surface, in terms of its component along the incident light unit vector $\underset{\rightarrow}{u}$ and the panel's normal $\underset{\rightarrow}{n}$. It was shown in [1] that the asymmetry of the optical properties between the two sides of the panel could be compensated by using symmetric mean values; hence, for this work, the optical properties are considered identical on both sides. We introduce $s = \texttt{sign}(\underset{\rightarrow}{u} \cdot \underset{\rightarrow}{n})$, so that the inward normal to the exposed surface is $s\,\underset{\rightarrow}{n}$. The STRP acceleration then takes the following form:

$$\underset{\rightarrow}{a}_{\text{STRP}} = C_{\text{STRP}} \cos\alpha \left[(\sigma_a + \sigma_{rd})\, s\, \underset{\rightarrow}{u} + \frac{2}{3}\left(\sigma_{rd} + \sigma_a \frac{\varepsilon_f - \varepsilon_b}{\varepsilon_f + \varepsilon_b} s\right) \underset{\rightarrow}{n} + 2\,\sigma_{rs} \cos\alpha\, s\, \underset{\rightarrow}{n} \right] \tag{2.15}$$

where we introduced

$$C_{\text{STRP}} = P_r\, \beta\, \frac{A_{\text{nom}}}{m} \tag{2.16}$$

and simplified for $\frac{a_S}{r_S} = 1$. It is noted that Eq. (2.15) is valid for any α under the conditions set in this section, i.e., $\underset{\rightarrow}{z}_b$ parallel to $\underset{\rightarrow}{h}_S$ and symmetrical optical properties.

The thermal radiation acceleration term appearing in Eqs. (2.14) and (2.15) was obtained from [70, pp. 47-49], where the expression for a solar sail is given, using our notation, as:

$$\underset{\rightarrow}{a}_{\text{TRP}} = C_{\text{STRP}}\, \sigma_a \frac{\varepsilon_f B_f - \varepsilon_b B_b}{\varepsilon_f + \varepsilon_b} s \cos\alpha\, \underset{\rightarrow}{n} \tag{2.17}$$

In Eq. (2.17), the emissivity coefficients of the front and back sides of the panel are given by ε_f and ε_b, while B_f and B_b represent the coefficients accounting for the non-Lambertian nature of the surface. While in writing Eq. (2.14), we substituted $2/3$ for the values of B_f and B_b to represent a Lambertian surface, i.e., a surface with isotropic luminance [70], an assumption held throughout this thesis. Also, $\frac{\varepsilon_l - \varepsilon_d}{\varepsilon_l + \varepsilon_d}$ was replaced by $\frac{\varepsilon_f - \varepsilon_b}{\varepsilon_f + \varepsilon_b} s$ in Eq. (2.15) to lift the dependency of the emissivity coefficients on the orientation of the panel with respect to the incoming light. We note that Eq. (2.17) is obtained assuming that the energy absorbed from the incoming solar flux is entirely converted into heat. In the case of a solar panel, some of the energy goes to charge batteries, therefore reducing the magnitude of the resulting TRP acceleration. This is however ignored here.

STRP potential

Since the Earth is far from the Sun, the incident light perceived by the spacecraft is considered identical to the one perceived by the Earth. Under this simplifying assumption, when the spacecraft is in direct sunlight, the STRP acceleration as given by Eq. (2.15) is independent of the spacecraft position. The STRP acceleration can therefore be expressed at a given time as the negative gradient of the following specific potential function:

$$\Phi_{\text{STRP}} = -\underset{\rightarrow}{a}_{\text{STRP}} \cdot \underset{\rightarrow}{r}_p = -\mathbf{a}_{\text{STRP}}^{\mathsf{T}} \mathbf{r}_p \tag{2.18}$$

where the STRP acceleration vector is explicitly dependent on time through the position of the Sun λ_S along with the panel's orientation ϕ (see Eq. (2.19)). Its components in $\mathcal{F}_{\text{ECI}}$ are denoted by $\mathbf{a}_{\text{STRP}}$, and can be explicitly written as:

$$\mathbf{a}_{\text{STRP}} = C_{\text{STRP}} \cos\alpha \left[(\sigma_a + \sigma_{rd})\, s\, \mathbf{u} + \frac{2}{3} \left(\sigma_{rd} + \sigma_a \frac{\varepsilon_f - \varepsilon_b}{\varepsilon_f + \varepsilon_b} s \right) \mathbf{n} + 2\, \sigma_{rs} \cos\alpha\, s\, \mathbf{n} \right] \tag{2.19}$$

where $\mathbf{u}$ and $\mathbf{n}$ are given by Eqs. (2.8) and (2.9) respectively. Eq. (2.18) can be rewritten using Eqs. (2.7) to (2.10) as:

$$\begin{aligned} \Phi_{\text{STRP}} = C_{\text{STRP}}\, r_p \cos\alpha \sum_{j=1}^{6} \mathcal{T}_j(\varepsilon, i) \Bigg[& (\sigma_a + \sigma_{rd})\, s \cos\psi_j \quad + \ldots \\ & \frac{2}{3} \left(\sigma_{rd} + \sigma_a \frac{\varepsilon_f - \varepsilon_b}{\varepsilon_f + \varepsilon_b} s \right) \cos(\psi_j + n_3\, \alpha) + 2\, \sigma_{rs} \cos\alpha\, s \cos(\psi_j + n_3\, \alpha) \Bigg] \end{aligned} \tag{2.20}$$

where we made use of the following intermediate expressions:

$$\begin{aligned} \mathbf{u}^{\mathsf{T}} \mathbf{r}_p &= -r_p \sum_{j=1}^{6} \mathcal{T}_j(\varepsilon, i) \cos\psi_j \\ \mathbf{n}^{\mathsf{T}} \mathbf{r}_p &= -r_p \sum_{j=1}^{6} \mathcal{T}_j(\varepsilon, i) \cos(\psi_j + n_3\, \alpha) \end{aligned} \tag{2.21}$$

with the sinusoidal terms argument ψ_j taking the following form:

$$\psi_j = n_1\, \Omega + n_2\, (\omega + \nu) + n_3\, \lambda_S \tag{2.22}$$

The values of n_1, n_2 and n_3 for $j = \{1, 2, ..., 6\}$ are stated in Table 2.1. Finally, the $\mathcal{T}_j(\varepsilon, i)$ functions also appearing in Eq. (2.20) are defined (dropping the dependence on ε and i) as:

$$\begin{aligned} \mathcal{T}_1 &= \cos^2\left(\frac{\varepsilon}{2}\right) \cos^2\left(\frac{i}{2}\right) & \mathcal{T}_2 &= \cos^2\left(\frac{\varepsilon}{2}\right) \sin^2\left(\frac{i}{2}\right) \\ \mathcal{T}_3 &= \frac{1}{2} \sin(\varepsilon) \sin(i) & \mathcal{T}_4 &= -\frac{1}{2} \sin(\varepsilon) \sin(i) \\ \mathcal{T}_5 &= \sin^2\left(\frac{\varepsilon}{2}\right) \cos^2\left(\frac{i}{2}\right) & \mathcal{T}_6 &= \sin^2\left(\frac{\varepsilon}{2}\right) \sin^2\left(\frac{i}{2}\right) \end{aligned} \tag{2.23}$$

Since the obliquity of the ecliptic barely varies, the $\mathcal{T}_j$ magnitude is therefore mainly governed by the orbital inclination. We find that $\mathcal{T}_1 > \mathcal{T}_j$ for all $j \neq 1$ and $i < 90°$, while $\mathcal{T}_2 > \mathcal{T}_j$ for all $j \neq 2$

and $i > 90°$. This will be of importance in Chapters 4 and 5 when identifying the specific resonant term to be exploited to induce the fastest deorbitation.

Table 2.1: Indices in the argument angle $\psi_j = n_1\,\Omega + n_2\,\omega + n_3\,\lambda_S$ of periodic terms in Eq. (2.20)

j	n_1	n_2	n_3
1	-1	-1	1
2	1	-1	-1
3	0	-1	1
4	0	-1	-1
5	-1	-1	-1
6	1	-1	1

Fourier series expansion for a rotating panel

In order to express the STRP potential given by Eq. (2.20) for a rotating panel with symmetric optical properties as a continuous function, the presence of the sign function, s, is problematic. Indeed, as can be seen from Eq. (2.20), the STRP potential function is composed of three terms that are either linear in $s\cos\alpha$ or $s\cos^2\alpha$. To work around this issue, we observe that both $s\cos\alpha$ and $s\cos^2\alpha$ are periodic of period $T = \pi$;[1] therefore, we propose to approximate these two functions by using a Fourier series expansion as a function of α.

Recall the Fourier series of a function $f(x)$:

$$f(x) = \frac{a_0}{2} + \sum_{m=1}^{\infty} \left(a_m \cos mx + b_m \sin mx\right) \tag{2.24}$$

where

$$\left.\begin{aligned} a_m &= \frac{1}{T}\int_{-T}^{T} f(x)\cos\frac{m\pi x}{T}\,\mathrm{d}x \\ b_m &= \frac{1}{T}\int_{-T}^{T} f(x)\sin\frac{m\pi x}{T}\,\mathrm{d}x \end{aligned}\right\} \qquad m = \{0,\,1,\,2,\,\ldots\} \tag{2.25}$$

Evaluating the Fourier coefficients using Eq. (2.25) for $f(\alpha) = s\cos\alpha$, we obtain the values presented in Table 2.2 up to $m = 4$. Accounting for properties of parity yields the following expansion:[2]

$$s\cos\alpha = \frac{a_0}{2} + \sum_{q=1}^{\infty} a_{(2q)}\cos(2q\,\alpha) \tag{2.26}$$

Following the same procedure, we obtain the corresponding expansion for $s\cos^2\alpha$ (Table 2.2):

$$s\cos^2\alpha = \sum_{q=1}^{\infty} a_{(2q-1)}\cos((2q-1)\,\alpha) \tag{2.27}$$

[1] $T = \pi$ when $\dot{\alpha} \neq 0$, otherwise $T = \infty$

[2] a_x coefficient represents the non-zero values from the corresponding column in Table 2.2

Table 2.2: Fourier series coefficients a_m and b_m up to $m = 4$ obtained by evaluating Eq. (2.25) for $f(\alpha)$

$f(\alpha)$	a_0	a_1	b_1	a_2	b_2	a_3	b_3	a_4	b_4
$s\cos\alpha$	$4/\pi$	0	0	$4/3\pi$	0	0	0	$-4/15\pi$	0
$s\cos^2\alpha$	0	$8/3\pi$	0	0	0	$8/15\pi$	0	0	0

Replacing $s\cos\alpha$ and $s\cos^2\alpha$ by their Fourier expansions of Eq. (2.26) and Eq. (2.27), and making use of the trigonometric identity $\cos a \cos b = \frac{1}{2}\{\cos(a-b)+\cos(a+b)\}$, Eq. (2.20) can be written in a more compact form as:

$$\Phi_{\text{STRP}} = C_{\text{STRP}}\, r_p \sum_{j=1}^{6} \mathcal{T}_j \sum_{k=-\infty}^{\infty} C_k \cos\psi_{j,k} \tag{2.28}$$

with $\psi_{j,k}$ defined as:

$$\begin{aligned}\psi_{j,k} = \psi_j + n_3\, k\, \alpha &= n_1\,\Omega + n_2\,(\omega+\nu) + n_3\,(\lambda_S + k\alpha) \\ &= n_1\,\Omega + n_2\,(\omega+\nu) + n_3\,(1-k)\,\lambda_S + n_3\, k\, \phi\end{aligned} \tag{2.29}$$

where we made use of the ψ_j expression given by Eq. (2.22). The C_k coefficient accounts for the optical and thermal properties of the surface and is defined as:

$$C_k = \begin{cases} a_{|k|}\dfrac{(\sigma_a+\sigma_{rd})}{2} + a_{|k-1|}\sigma_{rs}\,, & k \text{ even} \notin \{0,2\} \\ a_{|k|}\dfrac{(\sigma_a+\sigma_{rd})}{2} + a_{|k-1|}\sigma_{rs} + \dfrac{1}{3}\sigma_{rd}\,, & k \in \{0,2\} \\ a_{|k-1|}\dfrac{1}{3}\sigma_a\dfrac{\varepsilon_f-\varepsilon_b}{\varepsilon_f+\varepsilon_b}\,, & k \text{ odd} \end{cases} \tag{2.30}$$

Based on the definition of C_k given by Eq. (2.30), we can conclude that the k-odd terms are associated with the TRP perturbation and the k-even terms are associated with the SRP perturbation. Also, for the TRP terms, the magnitude of $C_{k-\text{odd}}$ is linearly dependent on σ_a, meaning that for a perfectly reflective body ($\sigma_a = 0$), the TRP vanishes. Indeed, for a perfectly reflective spacecraft, no energy is absorbed from the incoming solar flux, therefore no heat can be emitted. The TRP effect is however maximal for a black body ($\sigma_a = 1$).

For the case when $k = 0$, although $C_0 > C_k$ for all $k \neq 0$, the attitude angle ϕ does not have any impact on the argument $\psi_{j,0}$ or consequentially the STRP potential of Eq. (2.28), as directly deduced from Eq. (2.29). Moreover, we gather from Eq. (2.30) that $C_2 > C_k$, $k \neq \{0,2\}$ when $\left|\frac{\varepsilon_f-\varepsilon_b}{\varepsilon_f+\varepsilon_b}\right| < 0.5$ and $C_1 > C_k$, $k \neq \{0,1\}$ otherwise.

Special case of $\underrightarrow{u} \parallel \underrightarrow{n}$

In the literature, we can find a formulation similar to Eq. (2.15) for the STRP perturbing acceleration in the particular case when $\underrightarrow{u}$ and $\underrightarrow{n}$ are aligned, and hence, $\cos\alpha = 1$. The corresponding

STRP perturbation is given by:

$$\underset{\rightarrow}{a}_{\text{STRP}, \underset{\rightarrow}{u} \parallel \underset{\rightarrow}{n}} = C_{\text{STRP}} \, \sigma_{\text{eff}} \, \underset{\rightarrow}{u} \tag{2.31}$$

Note that the sign function s vanishes from the general expression of Eq. (2.15), and therefore the Fourier series expansions in k is not required; the effective STRP coefficient σ_{eff} fully accounts for the optical properties of the spacecraft, and is defined, for a panel, as:

$$\sigma_{\text{eff,plate}} = \sigma_a + \sigma_{rd} + \frac{2}{3}\left(\sigma_{rd} + \sigma_a \frac{\varepsilon_f - \varepsilon_b}{\varepsilon_f + \varepsilon_b}\right) + 2\sigma_{rs} \tag{2.32}$$

The resulting potential thus takes the form of:

$$\Phi_{\text{STRP}, \underset{\rightarrow}{u} \parallel \underset{\rightarrow}{n}} = C_{\text{STRP}} \, r_p \, \sigma_{\text{eff}} \sum_{j=1}^{6} \mathcal{T}_j \cos(\psi_j) \tag{2.33}$$

and is a summation of only six j-terms, in contrast to the infinity of (j,k)-terms in our more general formulation of Eq. (2.28). This formulation will be of particular relevance for the test scenario involving a bang-bang reorientation scheme presented in Chapter 6.

Another special case is that of a spherical spacecraft, also referred to as the cannonball case in the literature. The net STRP acceleration is obtained by integrating Eq. (2.14) over the sun-exposed hemisphere's area of the spacecraft. The net acceleration is thus found to be aligned with $\underset{\rightarrow}{u}$ and its expression is given by Eq. (2.31), with:

$$\sigma_{\text{eff,sphere}} = 1 + \frac{4}{9}\left(\sigma_{rd} + \sigma_a \frac{\varepsilon_f - \varepsilon_b}{\varepsilon_f + \varepsilon_b}\right) \tag{2.34}$$

This formulation will be of importance in the study of the Echo I balloon presented in Chapter 3.

2.4 Hamiltonian formulation

Our goal in this chapter is to obtain the dynamics effect of STRP on the semi-major axis and the eccentricity equations of motion. This can be achieved using various approaches, for example, with Lagrange planetary equations, or its alternate formulation given by Gauss variational equations. Here, we choose to use the Hamiltonian formulation for a spacecraft in a Keplerian motion around the Earth and subject to the disturbing potential of the Earth's second zonal harmonic and the STRP. The semi-major axis and eccentricity dynamics can then be directly obtained from the Hamiltonian of the problem. Finally, we will show that the averaged dynamics reduces to a single degree-of-freedom when subject to a single STRP-J_2-ϕ resonance. To the best of our knowledge, this has never been done and will be of paramount importance for the resonance study of Chapter 4 for a panel rotating at a constant rate. A simplification for the particular case of a spherical spacecraft will also be presented for later use in Chapter 3 where we will study the motion of Echo I. This simplified resonance model corresponds to that presented by Alessi et al. in [18].

2.4.1 Complete dynamics of panel subject to STRP and J_2

The Hamiltonian associated with an Earth-orbiting plate-like body subject to STRP and the J_2 harmonic perturbations is given by:

$$\mathcal{H} = \mathcal{H}_{\text{Kepler}} + \mathcal{H}_{\text{STRP}} + \mathcal{H}_{J_2} \tag{2.35}$$

where

$$\mathcal{H}_{\text{Kepler}} = -\frac{\mu}{2a} \tag{2.36}$$

is the Hamiltonian associated with the Keplerian motion of the spacecraft around Earth, while $\mathcal{H}_{J_2}$ is taken to be Φ_{J_2} from Eq. (2.13):

$$\mathcal{H}_{J_2} = \frac{J_2\,\mu\,R_e^2}{2a^3}\,\frac{(1+e\cos\nu)^3}{(1-e^2)^3}\left(3\sin^2 i\,\sin^2 u - 1\right) \tag{2.37}$$

As was emphasized in the previous section, Φ_{STRP} depends on the time-varying longitude of the Sun (λ_S) and orientation of the panel (ϕ); recall that $\underset{\rightarrow}{z}_b$ is assumed to be parallel to $\underset{\rightarrow}{h}_S$. To render the associated Hamiltonian autonomous, we introduce, as in [71], two conjugate pairs of variables, (Γ, τ) and (Λ, α), such that:

$$\dot{\tau} = \frac{\partial\mathcal{H}}{\partial\Gamma} = \dot{\lambda}_S \quad \text{and} \quad \dot{\alpha} = \frac{\partial\mathcal{H}}{\partial\Lambda} \tag{2.38}$$

to the STRP potential of Eq. (2.28) yielding the following expression for the STRP Hamiltonian:

$$\mathcal{H}_{\text{STRP}} = C_{\text{STRP}}\,r_p \sum_{j=1}^{6} \mathcal{T}_j \sum_{k=-\infty}^{\infty} C_k \cos\psi_{j,k} + \dot{\tau}\,\Gamma + \dot{\alpha}\,\Lambda \tag{2.39}$$

To obtain Hamilton's equations of motion, we need to define the corresponding Hamiltonian in terms of a canonical set of variables. We thus introduce the Delaunay variables—a set of canonical coordinates, for which, the three generalized coordinates are the mean anomaly M, the argument of perigee ω and the RAAN Ω, while the three conjugate momenta L, G and H can be expressed in terms of the Keplerian elements a, e and i as per:

$$\begin{aligned} L &= \sqrt{\mu\,a} & l &= M \\ G &= L\sqrt{1-e^2} & g &= \omega \\ H &= G\cos i & h &= \Omega \end{aligned} \tag{2.40}$$

The Hamiltonian of Eq. (2.35) can thus be expressed in terms of the canonical coordinates of Eq. (2.40) as:

$$\mathcal{H} = C_{\text{STRP}}\, r_p \sum_{j=1}^{6} \mathcal{T}_j(\varepsilon, {}^{H}/_{G}) \sum_{k=-\infty}^{\infty} C_k \cos\Big\{n_1\, h + n_2\, (g + \nu(l)) + n_3\, (\tau + k\, \alpha)\Big\} + \dot{\tau}\Gamma + \ \dots \\ \dot{\alpha}\Lambda + \frac{J_2 R_e^2 \mu^4}{2\, G^6} \left(1 + \sqrt{1-(G/L)^2} \cos(\nu(l))\right)^3 \left[3\left(1 - \frac{H^2}{G^2}\right) \sin^2(g + \nu(l)) - 1\right] - \frac{\mu^2}{2 L^2} \tag{2.41}$$

where the true anomaly ν is a function of the generalized coordinate l, i.e., the mean anomaly. It is noted that there exists no direct analytical relation for $\nu(l)$. We note the dependency of $\mathcal{T}_j$ from Eq. (2.23) on $H/G = \cos i$, which we can explicitly write as:

$$\begin{aligned} \mathcal{T}_1 &= \frac{1}{2}\cos^2\left(\frac{\varepsilon}{2}\right)\left(\frac{H}{G}+1\right) & \mathcal{T}_2 &= \frac{1}{2}\cos^2\left(\frac{\varepsilon}{2}\right)\left(1-\frac{H}{G}\right) \\ \mathcal{T}_3 &= \frac{1}{2}\sin(\varepsilon)\sqrt{1-\left(\frac{H}{G}\right)^2} & \mathcal{T}_4 &= -\frac{1}{2}\sin(\varepsilon)\sqrt{1-\left(\frac{H}{G}\right)^2} \\ \mathcal{T}_5 &= \frac{1}{2}\sin^2\left(\frac{\varepsilon}{2}\right)\left(\frac{H}{G}+1\right) & \mathcal{T}_6 &= \frac{1}{2}\sin^2\left(\frac{\varepsilon}{2}\right)\left(1-\frac{H}{G}\right) \end{aligned} \tag{2.42}$$

The final set of action-angle coordinates is defined to be $\mathbf{p} = \begin{bmatrix} L & H & G & \Gamma & \Lambda \end{bmatrix}^\top$ and $\mathbf{q} = \begin{bmatrix} l & h & g & \tau & \alpha \end{bmatrix}^\top$. The equations of motion can then be derived from the Hamiltonian of Eq. (2.41) using Hamilton's equations:

$$\dot{\mathbf{p}} = -\left(\frac{\partial \mathcal{H}}{\partial \mathbf{q}}\right)^\top \quad , \quad \dot{\mathbf{q}} = \left(\frac{\partial \mathcal{H}}{\partial \mathbf{p}}\right)^\top \tag{2.43}$$

As previously mentioned, the purpose of obtaining the equations of motion for a plate-like spacecraft subject to the J_2 and STRP perturbations is to use them as a tool for the identification of the attitude condition, i.e., condition on ϕ, required to enforce a resonant effect. Recall that the STRP-J_2 resonance is characterized by a significant cumulative effect of the STRP perturbation over time. Since we aim at exploiting resonances in e and a, the STRP dynamics for these two osculating elements are specifically of interest.

Eccentricity dynamics due to STRP

From the definition of L and G in Eq. (2.40), $e = \sqrt{1-(G/L)^2}$, and thus, the equation of motion describing the secular evolution of the eccentricity axis is therefore related to that of L and G through:

$$\frac{\mathrm{d}e}{\mathrm{d}t} = \frac{\sqrt{1-e^2}}{e\sqrt{\mu\, a}}\left[\sqrt{1-e^2}\,\frac{\mathrm{d}L}{\mathrm{d}t} - \frac{\mathrm{d}G}{\mathrm{d}t}\right] \tag{2.44}$$

From Eq. (2.43) we have:

$$\frac{\mathrm{d}L}{\mathrm{d}t} = -\frac{\partial \mathcal{H}}{\partial l} \qquad \text{and} \qquad \frac{\mathrm{d}G}{\mathrm{d}t} = -\frac{\partial \mathcal{H}}{\partial g} \tag{2.45}$$

hence, Eq. (2.44) can be rewritten as:

$$\frac{\mathrm{d}e}{\mathrm{d}t} = \frac{\sqrt{1-e^2}}{e\sqrt{\mu a}}\left[\frac{\partial \mathcal{H}}{\partial g} - \sqrt{1-e^2}\,\frac{\partial \mathcal{H}}{\partial l}\right] \tag{2.46}$$

The partial derivatives for the STRP contribution of $\mathcal{H}_{\text{STRP}}$ (see Eq. (2.39)) are given by:

$$\begin{aligned}\frac{\partial \mathcal{H}_{\text{STRP}}}{\partial g} &= C_{\text{STRP}} \sum_{j=1}^{6} \mathcal{T}_j \sum_{k=-\infty}^{\infty} C_k\, r_p \sin\left(\psi_{j,k}\right) \\ \frac{\partial \mathcal{H}_{\text{STRP}}}{\partial l} &= C_{\text{STRP}} \sum_{j=1}^{6} \mathcal{T}_j \sum_{k=-\infty}^{\infty} C_k \left(r_p \sin\left(\psi_{j,k}\right) + \cos\left(\psi_{j,k}\right)\frac{\partial r_p}{\partial \nu}\right)\frac{\partial \nu}{\partial l}\end{aligned} \tag{2.47}$$

where we made use of $n_2 = -1$ for all j (see Table 2.1). The expression for $\frac{\partial \nu}{\partial l}$ can be derived from Kepler's law of motion as shown in Appendix C for $M = l$:

$$\frac{\partial \nu}{\partial l} = \frac{(1+e\cos\nu)^2}{(1-e^2)^{3/2}} \tag{2.48}$$

and $\frac{\partial r_p}{\partial \nu}$ from the relation of Eq. (2.2) as:

$$\frac{\partial r_p}{\partial \nu} = a\,e\,\frac{1-e^2}{(1+e\cos\nu)^2}\sin\nu \tag{2.49}$$

Making use of Eqs. (2.46) to (2.49) and rearranging, we obtain the STRP contribution to the eccentricity dynamics:

$$\begin{aligned}\left.\frac{\mathrm{d}e}{\mathrm{d}t}\right|_{\text{STRP}} = -C_{\text{STRP}}\frac{\sqrt{1-e^2}}{n\,a}\sum_{j=1}^{6}\mathcal{T}_j\sum_{k=-\infty}^{\infty} C_k \Bigg[&\cos(\psi_{j,k})\sin\nu + \ldots \\ &\sin(\psi_{j,k})\left(\cos\nu + \frac{\cos\nu + e}{1+e\cos\nu}\right)\Bigg]\end{aligned} \tag{2.50}$$

which is equivalent to:

$$\begin{aligned}\left.\frac{\mathrm{d}e}{\mathrm{d}t}\right|_{\text{STRP}} = -C_{\text{STRP}}\frac{\sqrt{1-e^2}}{n\,a}\sum_{j=1}^{6}\mathcal{T}_j\sum_{k=-\infty}^{\infty} C_k \Bigg[&\sin(\widetilde{\psi}_{j,k})\left(1 + \frac{1}{2(1+e\cos\nu)}\right) + \ldots \\ &\frac{\sin(\psi_{j,k}-\nu)}{2\,(1+e\cos\nu)} + e\frac{\sin(\psi_{j,k})}{(1+e\cos\nu)}\Bigg]\end{aligned} \tag{2.51}$$

where we used the trigonometric identities: $\sin(a+b) = \sin a \cos b + \cos a \sin b$ and $\sin a \cos b = \frac{1}{2}\{\sin(a+b) + \sin(a-b)\}$. In Eq. (2.51), we introduced the (j,k) argument angle:

$$\begin{aligned} \widetilde{\psi}_{j,k} = \psi_{j,k} + \nu &= n_1\,\Omega + n_2\,\omega + n_3\,(\lambda_S + k\,\alpha) \\ &= n_1\,\Omega + n_2\,\omega + n_3\,(k\,\phi + (1-k)\,\lambda_S) \end{aligned} \tag{2.52}$$

We note that, since $n_2 = -1$ for all j, based on Eq. (2.29), the ν-term present in $\psi_{j,k}$ vanishes in $\widetilde{\psi}_{j,k}$. The $\widetilde{\psi}_{j,k}$ angle is thus slow-varying while the other argument angles of Eq. (2.51), $\psi_{j,k}$ and $(\psi_{j,k} - \nu)$, are fast-varying. This assessment is made on the basis that, in LEO, the oscillation period of the true anomaly ν is in the order of a few hours, the longitude of the Sun λ_S has a 1-year period, while the main oscillations of Ω and ω, driven by the secular effect of J_2, have periods in the order of weeks/months at the minimum.

For orbits with small eccentricities, i.e., $e \ll 1$, Eq. (2.51) can be approximated with:

$$\left.\frac{\mathrm{d}e}{\mathrm{d}t}\right|_{\mathrm{STRP}} \approx -C_{\mathrm{STRP}}\,\frac{\sqrt{1-e^2}}{n\,a}\sum_{j=1}^{6}\mathcal{T}_j\sum_{k=-\infty}^{\infty}C_k\left[\frac{3}{2}\sin(\widetilde{\psi}_{j,k}) + \frac{1}{2}\sin(\psi_{j,k} - \nu)\right] \tag{2.53}$$

This result will be used in the derivation of the attitude condition for resonance in e in Chapter 5.

Semi-major axis dynamics due to STRP

From the definition of L in Eq. (2.40), $a = L^2/\mu$, and thus, the equation of motion describing the evolution of the semi-major axis is therefore related to that of L through:

$$\frac{\mathrm{d}a}{\mathrm{d}t} = 2\sqrt{\frac{a}{\mu}}\,\frac{\mathrm{d}L}{\mathrm{d}t} = -2\sqrt{\frac{a}{\mu}}\,\frac{\partial\mathcal{H}}{\partial l} \tag{2.54}$$

where $\frac{\mathrm{d}L}{\mathrm{d}t}$ is given by Eq. (2.45). Making use of $\frac{\partial\mathcal{H}_{\mathrm{STRP}}}{\partial l}$ given in Eq. (2.47), we obtain from Eq. (2.54) the STRP contribution to the semi-major axis dynamics:

$$\left.\frac{\mathrm{d}a}{\mathrm{d}t}\right|_{\mathrm{STRP}} = -C_{\mathrm{STRP}}\,\frac{2}{n\sqrt{1-e^2}}\sum_{j=1}^{6}\mathcal{T}_j\sum_{k=-\infty}^{\infty}C_k\left[e\sin(\widetilde{\psi}_{j,k}) + \sin\psi_{j,k}\right] \tag{2.55}$$

where we made use of the $\widetilde{\psi}_{j,k}$ from Eq. (2.52). We emphasize once again that $\widetilde{\psi}_{j,k}$ (no explicit dependence on ν) is slow varying while $\psi_{j,k}$ is fast-varying (explicit dependence on ν). For orbits with small eccentricities, i.e., $e \ll 1$, Eq. (2.55) can be approximated with:

$$\left.\frac{\mathrm{d}a}{\mathrm{d}t}\right|_{\mathrm{STRP}} \approx -C_{\mathrm{STRP}}\,\frac{2}{n\sqrt{1-e^2}}\sum_{j=1}^{6}\mathcal{T}_j\sum_{k=-\infty}^{\infty}C_k\sin\psi_{j,k} \tag{2.56}$$

This result will be of use in the derivation of the attitude condition of resonance in a in Chapter 5.

2.4.2 Averaged dynamics of a panel subject to STRP and J_2

The averaged Hamiltonian is obtained by integrating the Hamiltonian of Eq. (2.35) over one complete period of the mean anomaly l as:

$$\overline{\mathcal{H}} = \frac{1}{2\pi}\int_0^{2\pi} \mathcal{H}\mathrm{d}l \tag{2.57}$$

Because the Hamiltonian is expressed as a function of the true anomaly ν and not the mean anomaly l, we make use of Eq. (2.48) to rewrite Eq. (2.57) as:

$$\overline{\mathcal{H}} = \frac{1}{2\pi}\int_0^{2\pi} \mathcal{H}\frac{(1-e^2)^{3/2}}{(1+e\cos\nu)^2}\mathrm{d}\nu \tag{2.58}$$

Performing the integration with $\mathcal{H}$ as per Eq. (2.41) yields the following averaged Hamiltonian:

$$\begin{aligned}\overline{\mathcal{H}} = -\frac{3}{2}\overline{C}_{\mathrm{STRP}}\frac{L}{\mu}\sqrt{L^2-G^2}\sum_{j=1}^{6}\mathcal{T}_j(\varepsilon, {}^{H}\!/_{G})\sum_{k=-\infty}^{\infty}C_k\cos\overline{\psi}_{j,k} + \dot{\tau}\Gamma + \dot{\alpha}\Lambda + \ldots \\ \frac{J_2R_e^2\mu^4}{4L^3}\frac{G^2-3H^2}{G^5} - \frac{\mu^2}{2L^2}\end{aligned} \tag{2.59}$$

where the averaged (j,k) argument angle is:

$$\begin{aligned}\overline{\psi}_{j,k} &= n_1 h + n_2 g + n_3(\tau + k\alpha) \\ &= n_1\Omega + n_2\omega + n_3(1-k)\lambda_S + n_3 k\phi\end{aligned} \tag{2.60}$$

and

$$\overline{C}_{\mathrm{STRP}} = P_r\overline{\beta}\frac{A_{\mathrm{nom}}}{m} \tag{2.61}$$

with $\overline{\beta}$ representing the fraction of the spacecraft orbit for which the spacecraft is in direct sunlight. It is understood that averaged quantities are used in the averaged dynamics model even if not explicitly noted.

We observe from Eq. (2.59) that L, or equivalently a (refer to Eq. (2.40)), is constant since $\overline{\mathcal{H}}$ does not depend on its canonical counterpart l, owing to the averaging of the STRP potential expansion. Thus, with l as an ignorable (cyclic) coordinate, the set of action-angle coordinates for the averaged dynamics can be reduced to $\mathbf{p} = \begin{bmatrix} H & G & \Gamma & \Lambda \end{bmatrix}^{\mathsf{T}}$ and $\mathbf{q} = \begin{bmatrix} h & g & \tau & \alpha \end{bmatrix}^{\mathsf{T}}$.

Similarly to the derivation of the non-averaged eccentricity equation of motion presented in the previous section, it is possible to derive the equation describing secular evolution of the eccentricity from the averaged Hamiltonian of Eq. (2.59).

Eccentricity averaged equation of motion

From Eq. (2.40), $e = \sqrt{1-(G/L)^2}$ and recalling that L is constant, the equation of motion describing the secular evolution of the eccentricity axis is therefore related to that of G through:

$$\frac{\mathrm{d}\overline{e}}{\mathrm{d}t} = -\frac{\sqrt{1-e^2}}{e\sqrt{\mu\,a}}\frac{\mathrm{d}G}{\mathrm{d}t} = \frac{\sqrt{1-e^2}}{e\sqrt{\mu\,a}}\frac{\partial\overline{\mathcal{H}}}{\partial g} \tag{2.62}$$

The secular evolution of the mean eccentricity is obtained from Eq. (2.59) similarly as for Eq. (2.50) thus:

$$\frac{\mathrm{d}\overline{e}}{\mathrm{d}t} = -\frac{3}{2}\overline{C}_{\text{STRP}}\frac{\sqrt{1-e^2}}{n\,a}\sum_{j=1}^{6}\mathcal{T}_j\sum_{k=-\infty}^{\infty}C_k\sin(\overline{\Psi}_{j,k}) \tag{2.63}$$

It is noted that the J_2 term in Eq. (2.59) has a null secular effect on e as it is not dependant on g (or equivalently ω). We also make a note of the close resemblance of Eq. (2.63) to Eq. (2.53). Eq. (2.63) will be used in the derivation of the attitude condition for resonance in e in Chapter 4.

2.5 Single resonance scenario for averaged dynamics

The work presented in this section is based on the assumption that for a single-resonance scenario, the dynamics is mainly governed by the resonant term of the STRP potential series expansion, whereas the contributions from other terms average out to a null long-term effect. Under such conditions, the four-degree-of-freedom averaged system presented in Section 2.4.2 further reduces to a single degree-of-freedom system. Important insights into the STRP-J_2-resonance phenomenon can then be obtained from the study of the reduced system.

Under the single-resonance assumption, the averaged Hamiltonian reduces to a single (j,k)-term of the expression in Eq. (2.59), that is:

$$\overline{\mathcal{H}}_{j,k} = -\frac{3}{2}\overline{C}_{\text{STRP}}\frac{L}{\mu}\sqrt{L^2-G^2}\,\mathcal{T}_j(\varepsilon,{}^{H}\!/{}_{G})\,C_k\cos\overline{\Psi}_{j,k} + \frac{J_2\,Re^2\,\mu^4}{4L^3}\frac{G^2-3H^2}{G^5} + \dot{\tau}\Gamma + \dot{\alpha}\Lambda - \frac{\mu^2}{2L^2} \tag{2.64}$$

where $\overline{\Psi}_{j,k}$ from Eq. (2.60) is the resonant (j,k) angle, and L is constant. Following Daquin et al. [71] and Alessi et al. [18], we apply the canonical transformation:

$$\mathfrak{T} = \begin{pmatrix} n_1 & n_2 & n_3 & n_3\,k \\ 1/n_2 & 0 & 0 & 0 \\ 0 & 0 & 1 & 0 \\ 0 & 0 & 0 & 1 \end{pmatrix} \tag{2.65}$$

to $\mathbf{p} = \begin{bmatrix} H & G & \Gamma & \Lambda \end{bmatrix}^\mathsf{T}$ and $\mathbf{q} = \begin{bmatrix} h & g & \tau & \alpha \end{bmatrix}^\mathsf{T}$ yielding the following action-angle variables:

$$\mathbf{\Sigma} = \left(\mathfrak{T}^{-1}\right)^\mathsf{T} \mathbf{p} \ , \qquad \boldsymbol{\sigma} = \mathfrak{T}\,\mathbf{q} \tag{2.66}$$

In the above, $\mathbf{\Sigma} = [\Sigma_1, \Sigma_2, \Sigma_3, \Sigma_4]^\mathsf{T}$, and $\boldsymbol{\sigma} = [\sigma_1, \sigma_2, \sigma_3, \sigma_4]^\mathsf{T}$ are defined explicitly as:

$$\begin{aligned}
\Sigma_1 &= n_2^{-1}\,G\,, & \sigma_1 &= n_1\,h + n_2\,g + n_3\,(\tau + k\alpha)\,,\\
\Sigma_2 &= -n_1\,G + n_2\,H\,, & \sigma_2 &= n_2^{-1}h\,,\\
\Sigma_3 &= -n_2^{-1}\,n_3\,G + \Gamma\,, & \sigma_3 &= \tau\,,\\
\Sigma_4 &= -n_2^{-1}\,n_3\,k\,G + \Lambda\,, & \sigma_4 &= \alpha
\end{aligned} \tag{2.67}$$

where $\sigma_1 = \overline{\psi}_{j,k}$ is the resonant (j,k) angle and Σ_2 is the constant of motion as stated in [18][3]. The averaged Hamiltonian can then be expressed explicitly as a function of the resonant (j,k) angle as in Alessi et al. [18][4]:

$$\begin{aligned}
\overline{\mathcal{H}}_{j,k} = -\frac{3}{2}\overline{C}_{\text{STRP}}\frac{L^2}{\mu}\sqrt{1-\tfrac{\Sigma_1^2}{L^2}}\,\mathcal{T}_j(\varepsilon, {}^{\Sigma_2}\!/_{\Sigma_1})\,C_k\cos\sigma_1 + \dot{\tau}\,(n_3\,\Sigma_1 + \Sigma_3) - \frac{\mu^2}{2L^2} + \ \ldots\\
\frac{J_2\,Re^2\,\mu^4}{4L^3}\,\frac{\left(-3\,n_1\,\Sigma_1^2 + \Sigma_1^2 - 6\,\Sigma_1\Sigma_2\,n_1\,n_2 - 3\,\Sigma_2^2\right)}{\Sigma_1^5\,n_2} + n_3\,\Sigma_1\,(\dot{\tau} + k\,\dot{\alpha}) + \Sigma_3\,\dot{\tau} + \Sigma_4\,\dot{\alpha}
\end{aligned} \tag{2.68}$$

We note the dependency of $\mathcal{T}_j$ from Eq. (2.42) on $\Sigma_2/\Sigma_1 = (H/G - n_1\,n_2)$. The equations of motion are then obtained with Eq. (2.68) for the new set of action-angle coordinates:

$$\dot{\Sigma}_i = -\frac{\partial\overline{\mathcal{H}}_{j,k}}{\partial\sigma_i} \quad , \qquad \dot{\sigma}_i = \frac{\partial\overline{\mathcal{H}}_{j,k}}{\partial\Sigma_i} \tag{2.69}$$

[3] The authors of [18] refer to the constant of motion denoted here with Σ_2 as Λ

[4] Since $n_1 \in \{0,\,1\}$ and $n_2 \in \{-1,\,1\}$, then $n_1^2 = n_1$ and $n_2^2 = 1$

which reduces to a one-degree-of-freedom system described by:

$$\begin{aligned}
\dot{\Sigma}_1 &= -\frac{3}{2}\overline{C}_{\text{STRP}}\frac{L^2}{\mu}\mathcal{T}_j C_k\sqrt{1-\tfrac{\Sigma_1^2}{L^2}}\sin\sigma_1 \\
\dot{\Sigma}_2 &= \dot{\Sigma}_3 = \dot{\Sigma}_4 = 0 \\
\dot{\sigma}_1 &= -\frac{3}{2}\overline{C}_{\text{STRP}}\frac{L^2}{\mu}C_k\left(\frac{\partial\mathcal{T}_j}{\partial\Sigma_1}\sqrt{1-\tfrac{\Sigma_1^2}{L^2}} - \mathcal{T}_j\frac{1}{\sqrt{1-\tfrac{\Sigma_1^2}{L^2}}}\frac{\Sigma_1}{L^2}\right)\cos\sigma_1 + \dots \\
&\quad \frac{3J_2R_e^2\mu^4}{4L^3n_2\Sigma_1^4}\left(3n_1 - 1 + 8n_1n_2\frac{\Sigma_2}{\Sigma_1} + 5\frac{\Sigma_2^2}{\Sigma_1^2}\right) + n_3(\dot{\tau} + k\dot{\alpha}) \\
\dot{\sigma}_2 &= -\frac{3}{2}\overline{C}_{\text{STRP}}\frac{L^2}{\mu}C_k\frac{\partial\mathcal{T}_j}{\partial\Sigma_2}\sqrt{1-\tfrac{\Sigma_1^2}{L^2}}\cos\sigma_1 - \frac{6J_2R_e^2\mu^4}{4L^3n_2\Sigma_1^4}\left(n_1n_2 + \frac{\Sigma_2}{\Sigma_1}\right) \\
\dot{\sigma}_3 &= \dot{\tau} \\
\dot{\sigma}_4 &= \dot{\alpha}
\end{aligned} \tag{2.70}$$

We can conclude from the system of Eq. (2.70) that Σ_2 is indeed a constant of motion as are Σ_3 and Σ_4. The spacecraft resonant dynamics is thus entirely described by $\dot{\Sigma}_1$ and $\dot{\sigma}_1$ for specific and constant values of j, a (or L), $\frac{\Sigma_2}{L}$ and $\frac{A_{\text{eff}}}{m}C_k$ for which we define effective the area-to-mass ratio as:

$$\frac{A_{\text{eff}}}{m} = \frac{A_{\text{nom}}}{m}\overline{\beta} \tag{2.71}$$

We also note here the ranges of the normalized Σ_1 and Σ_2 variables:

$$\begin{aligned}
\frac{\Sigma_1}{L} &= n_2^{-1}\sqrt{1-e^2} \quad \in \quad [0,\,1]\times n_2 \\
\frac{\Sigma_2}{L} &= (n_2\cos i - n_1)\sqrt{1-e^2} \quad \in \quad [-1,\,1] - n_1
\end{aligned} \tag{2.72}$$

which vary with n_1 and n_2 defined in Table 2.1 for a specific j.

Special case of a spherical spacecraft

In the particular case of a spherical spacecraft, $\alpha = 0$, the STRP Hamiltonian is given by Eq. (2.33) and the total averaged Hamiltonian reduces to:

$$\begin{aligned}
\overline{\mathcal{H}}_{\underset{\rightarrow}{u}\parallel\underset{\rightarrow}{n}} = -\frac{3}{2}\overline{C}_{\text{STRP}}\,\sigma_{\text{eff,sphere}}\frac{L}{\mu}\sqrt{L^2-G^2}\sum_{j=1}^{6}\mathcal{T}_j(\varepsilon, {}^{H}\!/_{G})\cos\overline{\psi}_j + \dot{\tau}\Gamma + \dots \\
\frac{J_2R_e^2\mu^4}{4L^3}\frac{G^2-3H^2}{G^5} - \frac{\mu^2}{2L^2}
\end{aligned} \tag{2.73}$$

with the set of action-angle coordinates defined as $\mathbf{p} = \begin{bmatrix} H & G & \Gamma \end{bmatrix}^\mathsf{T}$ and $\mathbf{q} = \begin{bmatrix} h & g & \tau \end{bmatrix}^\mathsf{T}$. This is equivalent to the Hamiltonian given by Alessi et al. in [18] where $\overline{\mathcal{H}}$ is omitted. In Eq. (2.73), $\overline{\psi}_j$ is defined as:

$$\overline{\psi}_j = n_1\,\Omega + n_2\,\omega + n_3\,\lambda_S \tag{2.74}$$

When subject to a single j resonance, like the Echo I balloon (see Chapter 3), the three-degree-of-freedom system reduces to a single degree-of-freedom system described by:

$$\begin{aligned}
\dot{\Sigma}_1 &= -\frac{3}{2}\overline{C}_{\text{STRP}}\,\sigma_{\text{eff,sphere}}\,\frac{L^2}{\mu}\mathcal{T}_j\sqrt{1-\tfrac{\Sigma_1^2}{L^2}}\,\sin\sigma_1 \\
\dot{\sigma}_1 &= -\frac{3}{2}\overline{C}_{\text{STRP}}\,\sigma_{\text{eff,sphere}}\,\frac{L^2}{\mu}\left(\frac{\partial\mathcal{T}_j}{\partial\Sigma_1}\sqrt{1-\tfrac{\Sigma_1^2}{L^2}} - \mathcal{T}_j\frac{1}{\sqrt{1-\tfrac{\Sigma_1^2}{L^2}}}\frac{\Sigma_1}{L^2}\right)\cos\sigma_1 + \;\dots \\
&\qquad \frac{3\,J_2\,R_e^2\,\mu^4}{4\,L^3\,n_2\,\Sigma_1^4}\left(3\,n_1 - 1 + 8\,n_1\,n_2\,\frac{\Sigma_2}{\Sigma_1} + 5\,\frac{\Sigma_2^2}{\Sigma_1^2}\right) + n_3\,\dot{\tau}
\end{aligned} \tag{2.75}$$

with

$$\begin{aligned}
\Sigma_1 &= n_2^{-1}\,G\,, \qquad & \sigma_1 &= n_1\,h + n_2\,g + n_3\,\tau \\
\Sigma_2 &= -n_1\,G + n_2\,H
\end{aligned} \tag{2.76}$$

which correspond to Eq. (2.67) with $\alpha = 0$ and $C_k = \sigma_{\text{eff,sphere}}$. Note that the definition of Σ_1 and Σ_2 is unchanged, thus Eq. (2.72) still holds. Also recall that for a spherical spacecraft, the effective STRP coefficient $\sigma_{\text{eff,sphere}}$ of Eq. (2.34) fully accounts for the optical properties of the balloon.

Chapter 3

Echo I Case Study – Passive *e*-Resonance

Through the '60s, many authors studied the case of Echo I up to a two-year period. Those studies used the orbit propagation tools limited by the computational resources of that era, and with limited fidelity of the perturbation models available at the time. Thus, Jastrow and Bryant wrongly estimated the lifetime of Echo I to be 20 years based on its orbital period rate of change [72]; Shapiro and Jones used the recorded data from Echo I to gain a better insight into the density behaviour at 1600 km altitudes [73], while Cook utilized his averaged model [11] to estimate the area-to-mass ratio of Echo I, as it was suspected to have changed over its life due to skin punctures by meteorites [57]. All of these efforts, nevertheless, confirmed the leading role of the SRP in the spacecraft dynamics.

In this Chapter, we revisit the orbital motion of Echo I, now considering its complete life span. We aim to support the resonance theory for its motion, in light of the more mature understanding and the recent findings on this phenomenon, more specifically, the equilibrium and stability theory as presented by Alessi et al. [18]. The satellite's motion is first propagated with D-SPOSE software-—a high-fidelity coupled orbital-attitude propagator developed in-house—which includes, among others, the most accurate models to date for the SRP, geopotential, and atmospheric perturbations [65]–[67]. Note, we are neglecting the TRP for this particular study as its effect was found to be negligible for Echo I. We first demonstrate that our propagation model is in very good agreement with the recorded Two-Line Element (TLE) data of the satellite [32]. We then follow the work of Alessi et al. on the SRP-J_2 phase space to model the resonant dynamics of Echo I using the previously identified propagation parameters. This model is later used to interpret the observed behaviour of the spherical spacecraft. Finally, we take the analysis further and modify the original orbit of Echo I, which we then propagate using the realistic environment modelling of D-SPOSE, to reflect: a stable equilibrium situation, and a strong resonance scenario. The results thus obtained offer several new findings and insights into the behaviour of Echo I and its relationship to the SRP-J_2-resonance.

3.1 Orbital propagation of Echo I

In this section, we compare Echo I observed position over its entire lifetime to the propagation results obtained with D-SPOSE, to verify our numerical model. This model will later be used to illustrate characteristic features of the eccentricity resonance.

3.1.1 Model of Echo I

Echo I was a 30.48-m-diameter balloon constructed with Mylar polyester film covered with vapour-deposited aluminum to allow for passive reflection of radio frequency signals [74], [75]. The satellite weighed 62.3 kg and contained an additional 13.6 kg of sublimating powders to maintain an internal pressure sufficient to preserve the geometrical integrity of the sphere [57], [76]. The authors of [77], suggested, based on the observed eccentricity evolution, that internal gas was leaking from the satellite through punctures in the skin of the balloon caused by meteorite impacts. It is assumed that only a small quantity remained inside on January 11, 1961, meaning that the area-to-mass ratio $\frac{A_{\text{nom}}}{m}$ of the satellite would have increased up to a value of 11.7 m^2/kg [57], and Echo I progressively lost its spherical shape [75].

For the propagations in D-SPOSE, since it is believed that the $\frac{A_{\text{nom}}}{m}$ of Echo I was changing over its first year due to aforementioned gas leakage, we initialize our propagation at epoch May 12, 1962, 14:23:48, with the associated orbit defined by the Keplerian elements in Table 3.1, and propagate until the re-entry of the spacecraft on May 24, 1968. Also, since the time evolution of the satellite shape is unknown, the spacecraft is modelled as a near-sphere with 224 surface elements as illustrated in Fig. 3.1. The spacecraft dimensions and parameters are presented in Table 3.2. Considering that by May 12, 1962, 14:23:48, all the gas had escaped the balloon, the nominal area-to-mass ratio was computed from the sphere cross-section (729.7 m^2) and the remaining mass of the spacecraft of 62.3 kg and thus set to 11.7 m^2/kg. Also, we found that the best fit between D-SPOSE's orbital propagation results and Echo I observed position was obtained by setting the effective reflectivity coefficient to $\sigma_{\text{eff,sphere}} = 1.08$, and the drag coefficient to $C_d = 3.46$; these values are justified as follows.

Table 3.1: Orbital conditions at initial epoch 1962/05/12 14:23:48

a (km)	e	i (°)	Ω (°)	ω (°)	ν (°)
7,892	1.255e-3	47.214	29.83	324.21	35.68

We note that $\sigma_{\text{eff,sphere}}$ can be computed, based on the shape of the object, from the optical parameters of the spacecraft σ_a, σ_{rd} and σ_{rs} which are respectively the fraction of incident photons absorbed, reflected diffusely and reflected specularly by the surface with $\sigma_a + \sigma_{rd} + \sigma_{rs} = 1$. In the special case of a spherical spacecraft, the effective reflectivity coefficient for SRP computation can

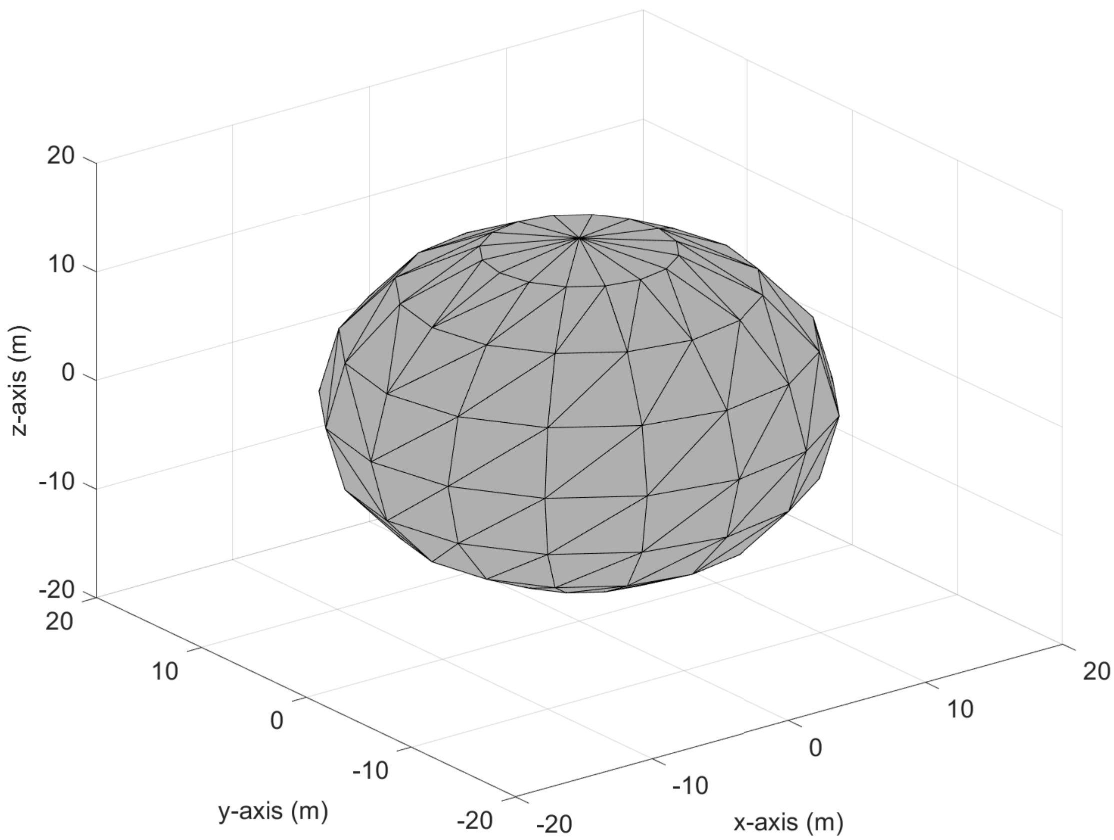

Figure 3.1: Echo I geometrical model to be used in D-SPOSE

Table 3.2: Echo I model parameters

Parameter	Description	Value	Units
d	diameter	30.48	m
$\frac{A_{\text{nom}}}{m}$	nominal area-to-mass	11.7	m^2/kg
$\sigma_{\text{eff,sphere}}$	effective reflectivity	1.08	-
C_d	drag coefficient	3.46	-
$\overline{\beta}$	mean shadow coefficient	0.77	-

be obtained from σ_{rd} only, as in [78], using Eq. (2.34):

$$\sigma_{\text{eff,sphere}} = 1 + \frac{4}{9}\sigma_{rd} \tag{3.1}$$

for a Lambertian surface. In Eq. (3.1), the emissivity contribution is neglected since we assume the heat emission to be evenly distributed around the sphere. Based on NASA's reference coefficient for aluminized coatings [79], the effective reflectivity value should lie within $\sigma_{\text{eff-sphere,NASA}} \in [1.0089, 1.0512]$ which is very close to our estimate of $\sigma_{\text{eff,sphere}} = 1.08$.

For the drag coefficient, our estimation for Echo I is uncertain, and we consider C_d constant, which is not exact. The drag coefficient is expected to vary with solar activity, and it is also expected to increase with height due to the decrease in the mean molecular weight of the atmosphere. Cook [80] evaluated that, under the most advantageous conditions—mean molecular weight of the atmosphere of 1—the drag coefficient of a sphere at altitudes ranging from 1000 km to 2000 km should be between 3.4 and 3.7 depending on the solar activity. For a more realistic mean molecular weight of 4, C_d is expected to be between 2.8 and 3.1.[1] Even though drag estimation is still a challenging problem, the fitted value of 3.46 used here tends to indicate that Echo I is not exactly spherical, as was suggested by Wilson [75], with a shape in-between the perfect sphere and a deflated balloon.

3.1.2 Propagation Results

We first verify our numerical model against the TLE data for Echo I available on Space-Track.org [32]. A propagation is thus carried out in D-SPOSE using the model of the spacecraft as described in Section 3.1.1 with a fixed time step of 30 s, and the accelerations due to the following perturbations are included:

- SRP: For a constant radiation pressure[2] $P_r = \frac{1{,}361}{c} \, \frac{\text{N}}{\text{m}^2}$
- gravitational field: EGM2008 up to degree and order 5
- atmospheric drag: NRLMSISE-00 with recorded equivalent planetary amplitude AP and solar radiation flux F10.7cm
- Moon and Sun third body interactions
- Earth shadow: geometric model with penumbra transition

The semi-major axis a and eccentricity e time responses obtained from the propagation are compared to the recorded TLEs in Fig. 3.2. A very good fit can be observed, therefore confirming the validity of our model. Also clearly observable are the oscillations in the eccentricity response, between the near-zero values and the maximum value of 0.068, these with an approximate period of 324 days. Although our results exhibit an excellent match for the eccentricity response, a discrepancy of about 10 km is observable between D-SPOSE semi-major axis prediction and the TLE data between the years 1965 and 1968. This might be explained by the constant C_d value employed to model the drag coefficient. We can deduce from this difference, in line with the discussion on the drag coefficient in Section 3.1.1, that a higher C_d should be employed at higher altitudes, and it should decrease as the altitude decreases.

[1] Cook's [80] results are based on the assumption that the mean molecular weight of the spacecraft surface is 16

[2] $c = 299{,}792{,}458$ m/s represents the speed of light

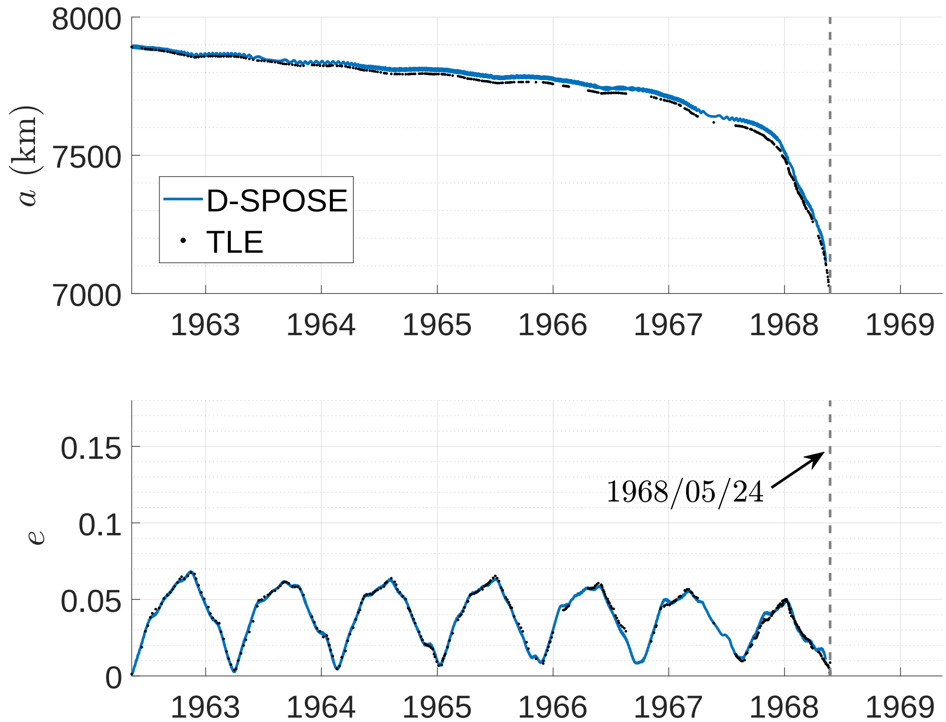

Figure 3.2: Semi-major axis and eccentricity responses for the propagation of the orbit of Table 3.1 at initial epoch 1962/05/12 14:23:48

Additional propagations with D-SPOSE—one where the SRP perturbation is excluded, and another where the J_2 perturbation is excluded—allow, by comparing the corresponding time histories to those obtained including all the perturbations (see Fig. 3.3), to partially corroborate the conclusions of the early investigations related to this satellite [57], [72], [73]: the large oscillations in eccentricity are indeed due to the action of the SRP perturbations, and they contributed to accelerating the re-entry of Echo I by about 3 years and 10 months. However, the results of Fig. 3.3 also reveal that the J_2 perturbation seems to only have a slight effect on the oscillation period, without much effect on the amplitude. This contradicts the conclusions found in the literature stating that the large oscillations in eccentricity are due to the coupling action of both the SRP and the J_2 perturbations. It will be made clear in the following sections that Echo I was indeed subject to the SRP-J_2-resonance phenomenon, although, for the specific orbit of Echo I, the J_2 action on the first ($j = 1$) resonance is small.

As partially reflected in Fig 3.3, the SRP-J_2-resonance is a multi-faceted phenomenon with several dependencies, and to adequately capture its complexity, we must resort to the analysis of the resonant phase space. We gather from [18] that the commensurability condition established by Cook [11] is deficient in the characterization of the resonance phenomenon, and that a stability analysis of the spacecraft dynamics model provides a better portrait of its resonant behaviour.

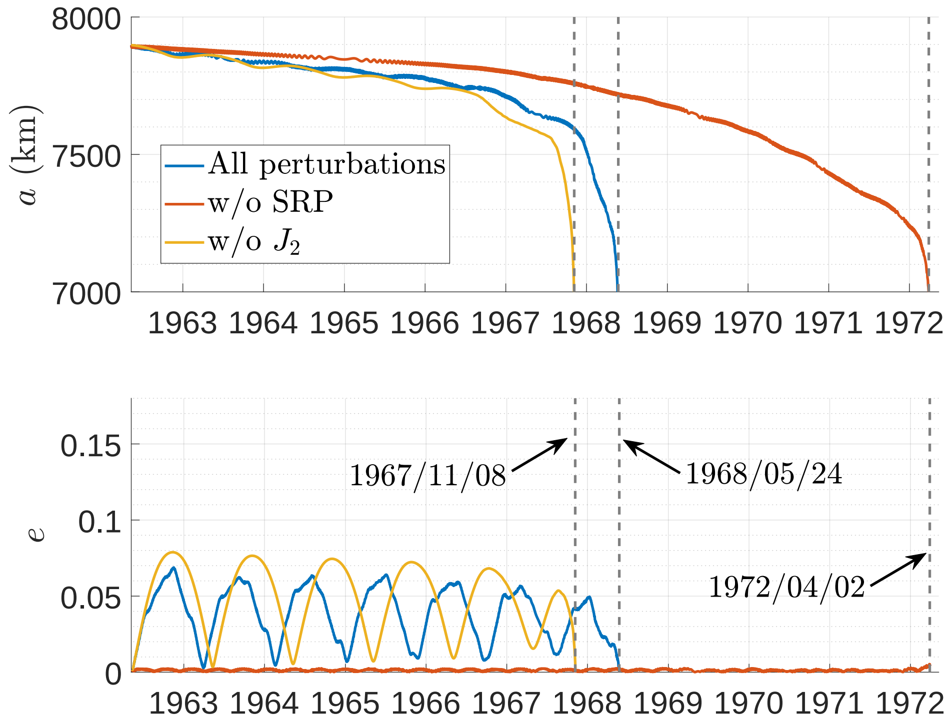

Figure 3.3: Semi-major axis and eccentricity responses for the propagation of the orbit of Table 3.1 at initial epoch 1962/05/12 14:23:48 comparing including SRP, gravitational and drag perturbations (blue), excluding SRP (orange), and excluding gravitational (yellow)

3.2 Echo I resonance study

In this section, we apply the stability theory put forward by Alessi et al. [18] for spherical spacecraft in resonance to the motion of Echo I. From the single resonance averaged Hamiltonian formulation presented in Section 2.5, we identify the equilibrium points which are key to establishing the topology of the phase portrait. We then use the theoretical model of resonance, and our understanding of it, to interpret the observed behaviour of Echo I.

3.2.1 Equilibrium identification

The normalized parameter values computed for the orbit of Table 3.1 are listed in Table 3.3 as a function of j using Eq. (2.72).

Table 3.3: $\frac{\Sigma_1}{L}$ and $\frac{\Sigma_2}{L}$ evaluated for the orbit of Table 3.1 ($e = 1.255\text{e-}3$ and $i = 47.214°$) for different j

j	Σ_1/L	Σ_2/L
1, 5	0.9999992	-0.3207
2, 6	-0.9999992	-1.6793
3, 4	0.9999992	0.6793

Also, from the one-degree-of-freedom Hamiltonian system described by Eq. (2.75), we see that the oscillation period is given by $\dot{\sigma}_1$ which can be approximated by evaluating the given expression at $\sigma_1 = \frac{\pi}{2}$:

$$\dot{\sigma}_{1,J_2} = n_3\,\dot{\tau} + \frac{3\,J_2\,R_e^2\,\mu^4}{4\,L^3\,n_2\,\Sigma_1^4}\left(3\,n_1 - 1 + 8\,n_1\,n_2\,\frac{\Sigma_2}{\Sigma_1} + 5\,\frac{\Sigma_2^2}{\Sigma_1^2}\right) \tag{3.2}$$

We note that in the particular case of Eq. (3.3), $\dot{\sigma}_1$ is only affected by the J_2 perturbation. From Eq. (3.2), we can write the commensurability condition initially expressed by Cook [11] as:

$$0 = n_3\,\dot{\tau} + \frac{3\,J_2\,R_e^2\,\mu^4}{4\,L^3\,n_2\,\Sigma_1^4}\left(3\,n_1 - 1 + 8\,n_1\,n_2\,\frac{\Sigma_2}{\Sigma_1} + 5\,\frac{\Sigma_2^2}{\Sigma_1^2}\right) \tag{3.3}$$

As will be shown in the following section, the driving term in the motion of Echo I is the $j = 1$ term. Evaluating Eq. (3.2) for $j = 1$ (i.e., $n_1 = -1$, $n_2 = -1$, $n_3 = 1$) and the orbit of Table 3.1, we find that $\dot{\sigma}_{1,J_2} = -2.237\text{e-}7$ rad/sec yielding a period of $T = 325$ days. This is consistent with the eccentricity response in Fig. 3.2 for which a period of 324 days was identified. We note here that, in this particular case, the contribution of the J_2-term in Eq. (3.2) is smaller than that of the $\dot{\tau}$-term by a factor of 10. This explains the fact that a similar resonance effect can be observed even when neglecting the geopotential (see Fig. 3.3 yellow vs. blue lines).

As established in Section 2.5, the resonant dynamics of the spacecraft is entirely defined by $\dot{\Sigma}_1$ and $\dot{\sigma}_1$ of Eq. (2.75). The equilibrium conditions are thus derived by solving:

$$\dot{\Sigma}_1 = 0 \quad , \quad \dot{\sigma}_1 = 0 \tag{3.4}$$

The equilibrium conditions can then be found for two distinct cases: the general case where $\Sigma_1 \neq L$, or equivalently $e \neq 0$ (refer to Eqs. (2.40) and (2.76)), and the specific case where $\Sigma_1 = L$ (or $e = 0$).

$\Sigma_1 \neq L$ ($e \neq 0$) case:

Here, $\dot{\Sigma}_1$ can only be null when $\sigma_1 = 0$ or $\sigma_1 = \pi$. The second condition for equilibrium in Eq. (3.4) can therefore be restated as $\dot{\sigma}_1(\sigma_1 = \{0, \pi\}) = 0$, or explicitly as:

$$\begin{aligned} 0 = \; & \pm\frac{3}{2}\overline{C}_{\text{SRP}}\,\sigma_{\text{eff,sphere}}\,\frac{L^2}{\mu}\left(\frac{\partial\mathcal{T}_j}{\partial\Sigma_1}\sqrt{1-\frac{\Sigma_1^2}{L^2}} - \mathcal{T}_j(\varepsilon, {}^{\Sigma_2}/_{\Sigma_1})\,\frac{1}{\sqrt{1-\frac{\Sigma_1^2}{L^2}}}\,\frac{\Sigma_1}{L^2}\right) + n_3\,\dot{\tau} + \ldots \\ & \frac{3\,J_2\,R_e^2\,\mu^4}{4\,L^3\,n_2\,\Sigma_1^4}\left(3\,n_1 - 1 + 8\,n_1\,n_2\,\frac{\Sigma_2}{\Sigma_1} + 5\,\frac{\Sigma_2^2}{\Sigma_1^2}\right) \end{aligned} \tag{3.5}$$

Solving Eq. (3.5) allows to identify the equilibrium values $(\Sigma_{1,\text{eq}}, \sigma_{1,\text{eq}})$ associated with a particular combination of j, a (or L), $\frac{\Sigma_2}{L}$ and $\frac{A_{\text{eff}}}{m}\sigma_{\text{eff,sphere}}$. Recall that $\frac{A_{\text{eff}}}{m}$ is given by Eq. (2.71). The nature of the equilibrium, stable or unstable, can be determined based on the Jacobian matrix eigenvalues at the equilibrium:

$$J_{\Sigma_1 \neq L} = \begin{bmatrix} 0 & \left.\frac{\partial \dot{\Sigma}_1}{\partial \sigma_1}\right|_{(\Sigma_{1,\text{eq}},\, \sigma_{1,\text{eq}})} \\ \left.\frac{\partial \dot{\sigma}_1}{\partial \Sigma_1}\right|_{(\Sigma_{1,\text{eq}},\, \sigma_{1,\text{eq}})} & 0 \end{bmatrix} \tag{3.6}$$

A negative sign for $\left.\frac{\partial \dot{\Sigma}_1}{\partial \sigma_1}\right|_{(\Sigma_{1,\text{eq}},\, \sigma_{1,\text{eq}})} \times \left.\frac{\partial \dot{\sigma}_1}{\partial \Sigma_1}\right|_{(\Sigma_{1,\text{eq}},\, \sigma_{1,\text{eq}})}$ indicates a stable equilibrium (two imaginary eigenvalues), and a positive sign implies the opposite (two real eigenvalues: one positive, one negative). A maximum of 3 equilibria can exist when $\Sigma_1 \neq L$ for a fixed combination of j, a, $\frac{\Sigma_2}{L}$ and $\frac{A_{\text{eff}}}{m}$ as can be concluded from [18].

$\Sigma_1 = L$ ($e = 0$) case:

In this special case, $\dot{\Sigma}_1$ from Eq. (2.75) is necessarily null. The equilibrium conditions of Eq. (3.4) thus reduce to $\dot{\sigma}_1 = 0$. With the use of Eq. (2.75), we find that this can only be met for:

$$0 = \frac{3}{2} \overline{C}_{\text{SRP}}\, \sigma_{\text{eff,sphere}}\, a\, \mathcal{T}_j(\varepsilon, {}^{\Sigma_2}\!/_{\Sigma_1}) \frac{\Sigma_1}{L^2} \cos \sigma_1 \tag{3.7}$$

which is only satisfied at $\sigma_1 = \frac{\pi}{2}$ (or $\sigma_1 = \frac{3\pi}{2}$). Otherwise the $\overline{C}_{\text{SRP}}$-term of the $\dot{\sigma}_1$ expression in Eq. (2.75) tends toward infinity. The resulting point, $(e, \sigma_1) = (0, \{\frac{\pi}{2}, \frac{3\pi}{2}\})$, exists for any j, a, $\frac{\Sigma_2}{L}$ and $\frac{A_{\text{eff}}}{m} \sigma_{\text{eff,sphere}}$ values.

In addition, for the equilibrium condition to hold, the summation of the J_2- and $\dot{\tau}$-terms of the $\dot{\sigma}_1$ expression in Eq. (2.75) must also be null, i.e., Cook's commensurability condition of Eq. (3.3) must be met. As alluded to in Chapter 1, for a spherical body, this condition is only met for specific orbits, and this is not the case for the orbit of Echo I. However, as alluded earlier in this section, for the particular case of Echo I and the orbit of Table 3.1 with $e = 0$ we find that $\dot{\sigma}_{1,J_2} = -2.24$e-7 rad/sec which is small. For this reason, we refer to the point $(e_{\text{q-eq}}, \sigma_{1,\text{q-eq}}) = (0, \{\frac{\pi}{2}, \frac{3\pi}{2}\})$ as a quasi-equilibrium and treat it as an unstable equilibrium in the remainder of this chapter as will be justified by the phase plot analysis.

Solving the equilibrium condition of Eq. (3.5) for the initial semi-major axis value of Echo I from Table 3.1: $a = 7{,}892$ km, constant effective area-to-mass ratio $\frac{A_{\text{eff}}}{m} \sigma_{\text{eff,sphere}} = 9.73$ m^2/kg, and initial $\frac{\Sigma_2}{L}$ from Table 3.3 allows to identify the stable and unstable equilibrium points associated with each j resonance. These equilibria are listed in Table 3.4 along with the unstable quasi-equilibria at $e = 0$ and $\sigma_1 = \{\frac{\pi}{2}, \frac{3\pi}{2}\}$ deduced from Eq. (3.7) which, as aforementioned, exist for any j, a, $\frac{\Sigma_2}{L}$ and $\frac{A_{\text{eff}}}{m} \sigma_{\text{eff,sphere}}$ combinations. The value of the effective area-to-mass ratio, $\frac{A_{\text{eff}}}{m} \sigma_{\text{eff,sphere}} = 9.73$ m^2/kg, was computed using Eqs. (2.71) with the parameters listed in Table 3.2.

The equilibrium points of Table 3.4 come in pairs (stable/unstable), and, as it will be made clear in the following section, each pair defines a libration region in its respective j resonance phase space. The stable equilibrium is located at the eye of the region bounded by the unstable

Table 3.4: Equilibrium points locations in the $i \in [0, 90]^\circ$ range for $a = 7,892$ km, $\frac{A_{\text{eff}}}{m}\sigma_{\text{eff,sphere}} = 9.73$ m^2/kg, and $\frac{\Sigma_2}{L}$ from Table 3.3

P	j	e	i (°)	σ_1	stability
1-0	1	0	N/A	$\frac{\pi}{2}, \frac{3\pi}{2}$	unstable
1-1	1	0.03345	47.23	0	stable
2-0	2	0	N/A	$\frac{\pi}{2}, \frac{3\pi}{2}$	unstable
2-1	2	9.738e-4	47.21	π	stable
3-0	3	0	N/A	$\frac{\pi}{2}, \frac{3\pi}{2}$	unstable
3-1	3	3.196e-3	47.21	π	stable
4-0	4	0	N/A	$\frac{\pi}{2}, \frac{3\pi}{2}$	unstable
4-1	4	1.650e-3	47.21	0	stable
5-0	5	0	N/A	$\frac{\pi}{2}, \frac{3\pi}{2}$	unstable
5-1	5	1.845e-3	47.21	π	stable
5-2	5	0.4744	50.53	0	stable
5-3	5	0.4735	50.52	π	unstable
6-0	6	0	N/A	$\frac{\pi}{2}, \frac{3\pi}{2}$	unstable
6-1	6	5.725e-5	47.21	π	stable

equilibrium (or quasi-equilibrium) associated phase curve. This particular phase curve, also referred to as a separatrix, represents the locations for which the resonance effect is maximal within each particular phase space, as it manifests the greatest change in eccentricity. The amplitude of this variation progressively diminishes the further the phase curve is from this limit and becomes null at the stable equilibrium.

3.2.2 Stability analysis

Following the stability analysis performed by Alessi et al. [18] and solving the equilibrium condition of Eq. (3.5) for the same semi-major axis and effective area-to-mass ratio as for the equilibria of Table 3.4, but with $\frac{\Sigma_2}{L}$ ranging from $-1-n_1$ to $1-n_1$ yields the results of Figs. 3.4 to 3.6. The three figures illustrate the location of the equilibrium points associated with, respectively, the $j = \{1, 5\}$, $j = \{2, 6\}$ and $j = \{3, 4\}$ resonances in the $[0, 90]$ deg inclination interval. We note that the equilibria initially computed in terms of Σ_1 for a range of Σ_2 were transformed into the more understandable eccentricity and inclination parameters using Eqs. (2.40) and (2.76), with $a = 7,892$ km.

The equilibrium locations for the phase spaces of the orbit in Table 3.1 are identified with black 'x's in Figs. 3.4 to 3.6. These equilibria correspond to the $\frac{\Sigma_2}{L}$ values of Table 3.3. The following observations can be made on these equilibria.

$\boldsymbol{j = \{2, 6\}}$ **resonances:** We gather from the equilibrium values listed in Table 3.4 for $j = 2$ and $j = 6$, that the equilibrium points are located at very low eccentricities ($e < 0.001$), and from

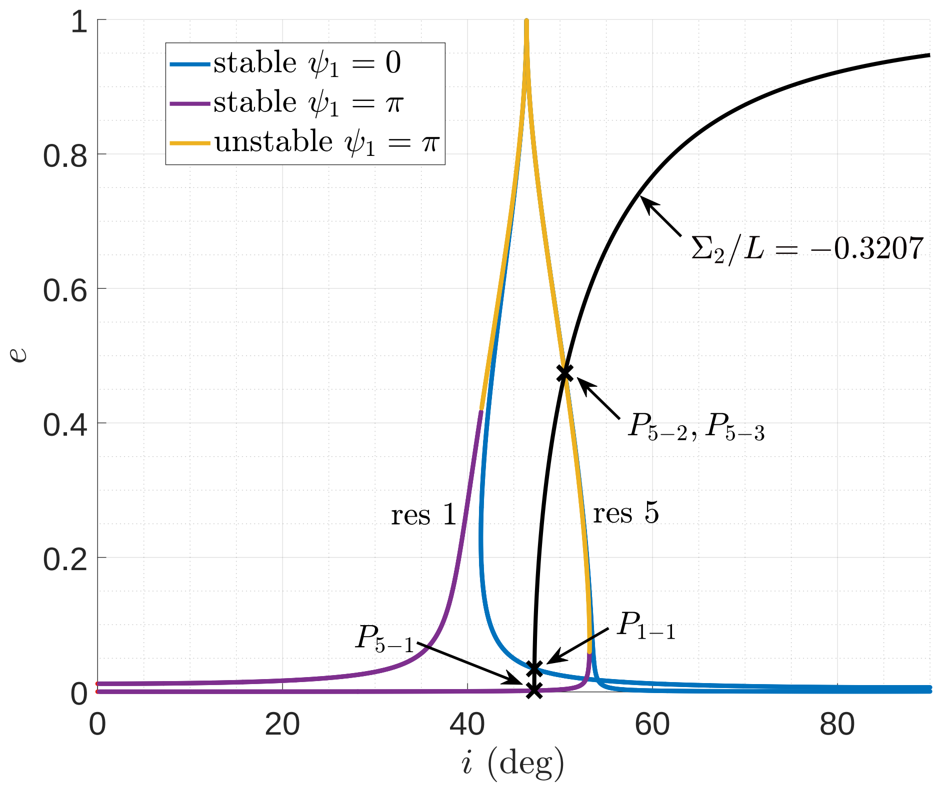

Figure 3.4: Location of the equilibrium points associated with the $j = \{1, 5\}$ resonances for $a = 7,892$ km and $\frac{A_{\text{eff}}}{m}\sigma_{\text{eff,sphere}} = 9.73$ m^2/kg. The equilibrium points associated with the orbit of Table 3.1 are marked by a 'x'

the corresponding phase plots that the effect due to both the $j = 2$ and $j = 6$ resonances is only of small significance on the orbit of Echo I. The phase plots (not included here) show libration regions of small amplitudes: $\Delta e \approx 0.002$ around P_{2-1} for $j = 2$, and $\Delta e \approx$ 1.1e-4 around P_{6-1} for $j = 6$. These plots are not presented here, but they can be obtained by propagating Eq. (2.75) at different (Σ_1, σ_1) combinations.[3]

***j* = {3, 4} resonances:** Similar conclusions can be drawn for the $j = \{3, 4\}$ resonances as for $j = \{2, 6\}$.

***j* = {1, 5} resonances:** Fig. 3.7 shows an expanded view of Fig. 3.4 to offer a clearer view of the equilibrium points locations for $j = 1$ and $j = 5$. Differently from the $j = \{2, 6\}$ resonances, Fig. 3.7 shows equilibrium values at high eccentricity locations: $e \approx 0.47$ for the pair P_{5-2}/P_{5-3} as listed in Table 3.4. From the phase plot, a libration region with an amplitude of $\Delta e \approx 0.06$ can be observed around the stable P_{5-2}. The region is bounded by the phase curve of the unstable P_{5-3}. This region does not extend to the eccentricity range of Echo I which is < 0.068. Similarly, the stable/unstable equilibrium pair P_{5-1}/P_{5-0} defines a second libration region of small amplitude

[3]Propagating Eq. (2.75) at the equilibrium points provide the most important phase curves which contain all the necessary information to establish the phase portrait topology.

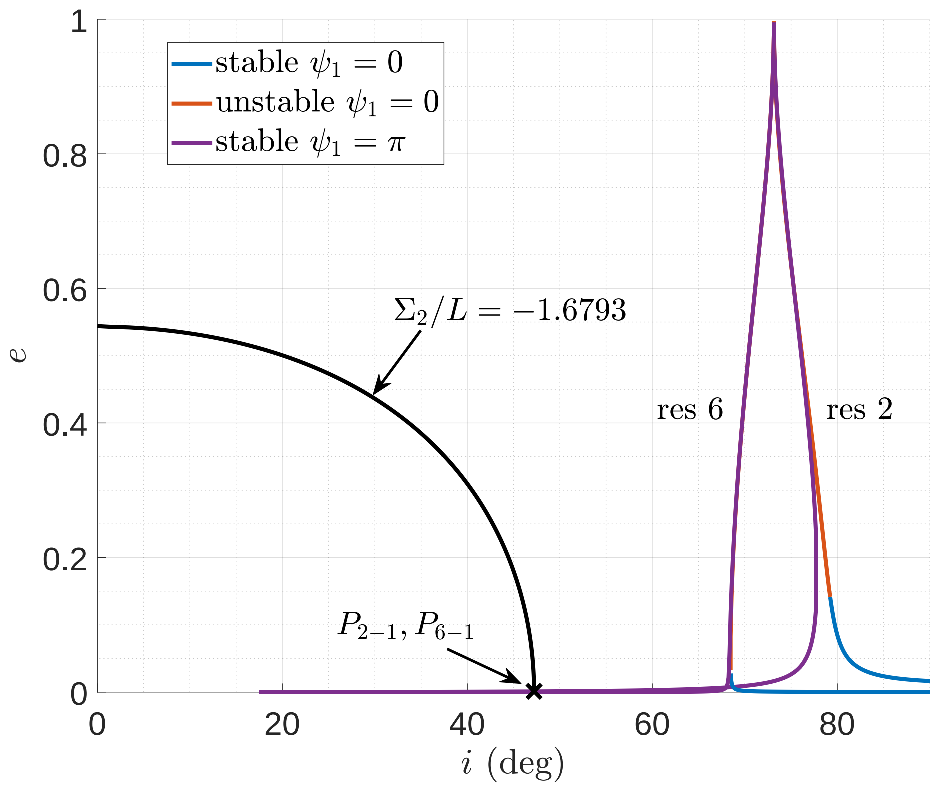

Figure 3.5: Location of the equilibrium points associated with the $j = \{2, 6\}$ resonances for $a = 7,892$ km and $\frac{A_{\text{eff}}}{m}\sigma_{\text{eff,sphere}} = 9.73$ m^2/kg. The equilibrium points associated with the orbit of Table 3.1 are marked by a 'x'

$\Delta e = 3.8$e-3 around P_{5-1}. Once again, the phase plot for $j = 5$ is not presented here, but it can be obtained from Eq. (2.75).

Finally, for the $j = 1$ resonance, we note the presence of a libration region of significant amplitude, $\Delta e \approx 0.067$, around the stable point P_{1-1} and bounded by the phase curve associated with the unstable quasi-equilibrium P_{1-0}. Fig. 3.9 illustrates the corresponding phase plot along with P_{1-0} and P_{1-1} resulting phase curves. We recall that $\sigma_1 = \psi_j$, with ψ_j as per Eq. (2.22). The amplitude and closeness of the libration region to the eccentricity range of Echo I make the $j = 1$ resonance a major contributor to the oscillations in eccentricity observed for the spacecraft. Based on the previous findings for the different resonances, we further conclude that the $j = 1$ resonance is the only one significantly affecting the secular evolution of Echo I. A deeper analysis of this specific resonance is thus conducted in the following section for the special case of Echo I.

3.2.3 Phase plot analysis

In Section 3.2.2, we identified the $j = 1$ resonance as the only major contributor to the eccentricity oscillations experienced by Echo I. In this section, to further investigate its impact, we analyze its phase portrait in comparison to observations of the orbital position of Echo I.

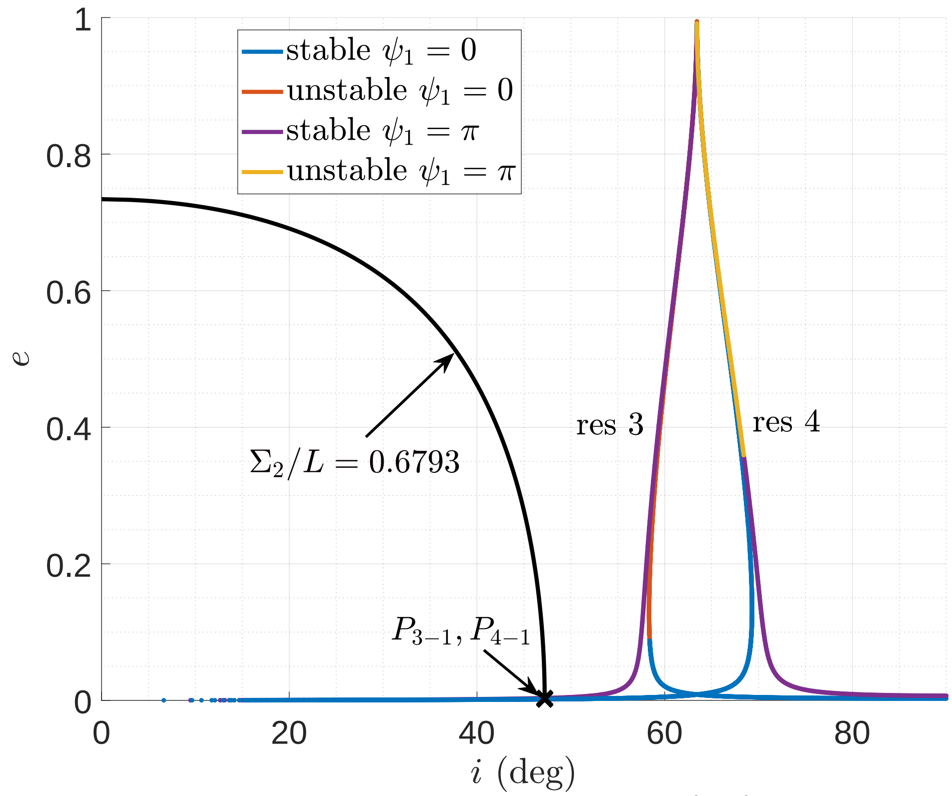

Figure 3.6: Location of the equilibrium points associated with the $j = \{3, 4\}$ resonances for $a = 7{,}892$ km and $\frac{A_{\text{eff}}}{m}\sigma_{\text{eff,sphere}} = 9.73$ m^2/kg. The equilibrium points associated with the orbit of Table 3.1 are marked by a 'x'

Table 3.5: Orbital observations of Echo I from TLEs and values of $\frac{\Sigma_2}{L}$ computed with Eq. (2.72) for $j = 1$

	date	a (km)	e	i (deg)	ψ_1 (rad)	Σ_2/L
$T_{0\text{yr}}$	1962/05/12 14:23:48	7,892	1.25e-3	47.21	5.30	-0.3207
$T_{2\text{yr}}$	1964/05/11 11:40:22	7,808	5.03e-2	47.27	0.54	-0.3210
$T_{5\text{yr}}$	1967/05/22 21:46:09	7,619	3.45e-2	47.28	5.71	-0.3213

Up to this point, the semi-major axis was considered constant as it is not secularly affected by the SRP and the J_2 perturbations. However, the lowering of the perigee (to about 550 km) because of the eccentricity increase, along with the high area-to-mass ratio of Echo I (11.7 m^2/kg), lead to considerable alterations of the Hamiltonian associated with the Keplerian motion ($\mathcal{H}_{\text{Kepler}}$) of Eq. (2.36) due to the atmospheric drag action, thus, significantly affecting the system described by the Hamiltonian of Eq. (2.41). To evaluate this impact, the $j = 1$ resonance phase plots associated with three observed orbits, recorded respectfully at about 0, 2, and 5 years from the initial epoch May 12, 1962, 14:23:48, are presented in Figs. 3.9 to 3.11. Recall from Section. 2.5 that a resonance phase plot is defined by constant a, $\frac{\Sigma_2}{L}(e,i)$ and $\frac{A_{\text{eff}}}{m}\sigma_{\text{eff,sphere}}$ for a specific j. The location

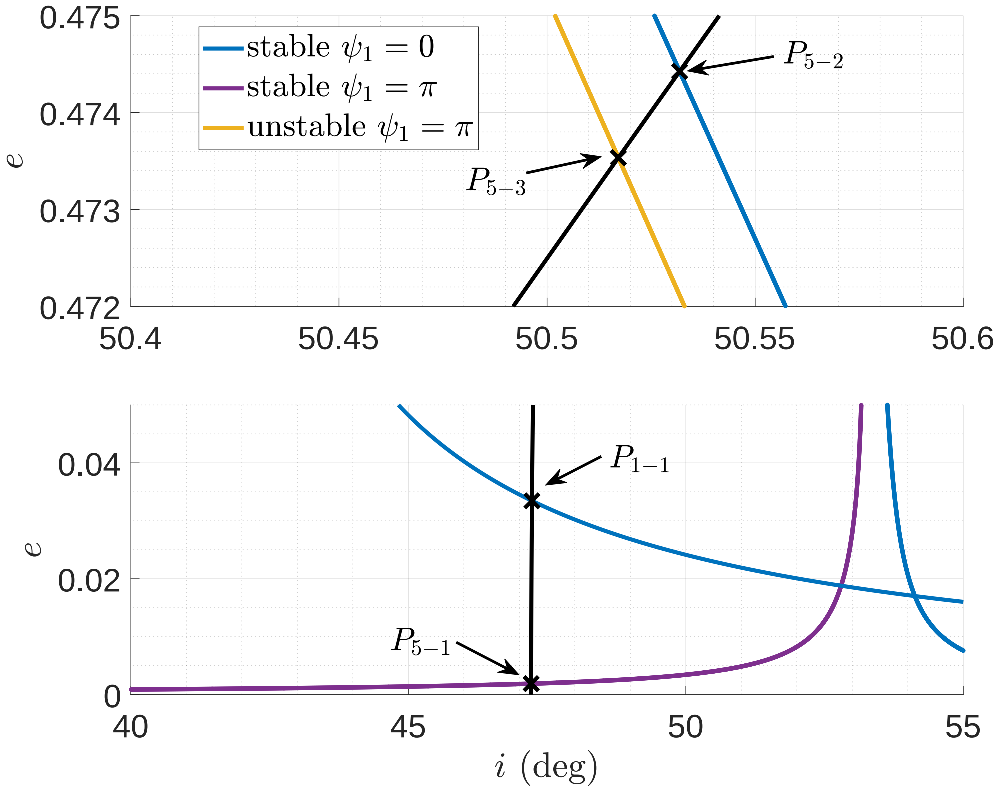

Figure 3.7: Location of the equilibrium points associated with the $j = \{1, 5\}$ resonances for $a = 7{,}892$ km and $\frac{A_{\text{eff}}}{m}\sigma_{\text{eff,sphere}} = 9.73$ m^2/kg, expanded view of Fig. 3.4. The equilibrium points associated with the orbit of Table 3.1 are marked by a 'x'

of the observed orbits on their respective phase plots is marked by a green dot and the resulting phase curve is drawn in dark red. The details of the three orbits are listed in Table 3.5, and are also identified in Fig. 3.8 which shows the recorded a and e values obtained from Echo I TLEs.

We first note from the general form of the phase plots in Figs. 3.9 to 3.11, that they do not vary much over the 5-year time frame. From Fig. 3.9, we can also assess the importance of the phase curves associated with the unstable quasi-equilibrium and stable equilibrium, respectively P_{1-0} and P_{1-1}. The former in particular, as the associated phase curve is delineating the libration region. As already mentioned, this specific phase curve, the separatrix, manifests the greatest change in eccentricity, whereas the oscillation amplitude is null at the stable equilibrium.

Still from Fig. 3.9, we note the proximity of the initial position of Echo I ($T_{0\text{yr}}$ from Table 3.1, green dot) to the separatrix, confirming the importance of the $j = 1$ resonance on the motion of Echo I. However, comparing these results to those of Figs. 3.10 and 3.11, the Echo I related phase curve changes considerably from $T_{0\text{yr}}$ to $T_{5\text{yr}}$. Generating the same figures for many more recordings of Echo I would show that the phase curve in dark red oscillates around the separatrix, sometimes even nearing the stable equilibrium. Such variation might be attributable to neglected

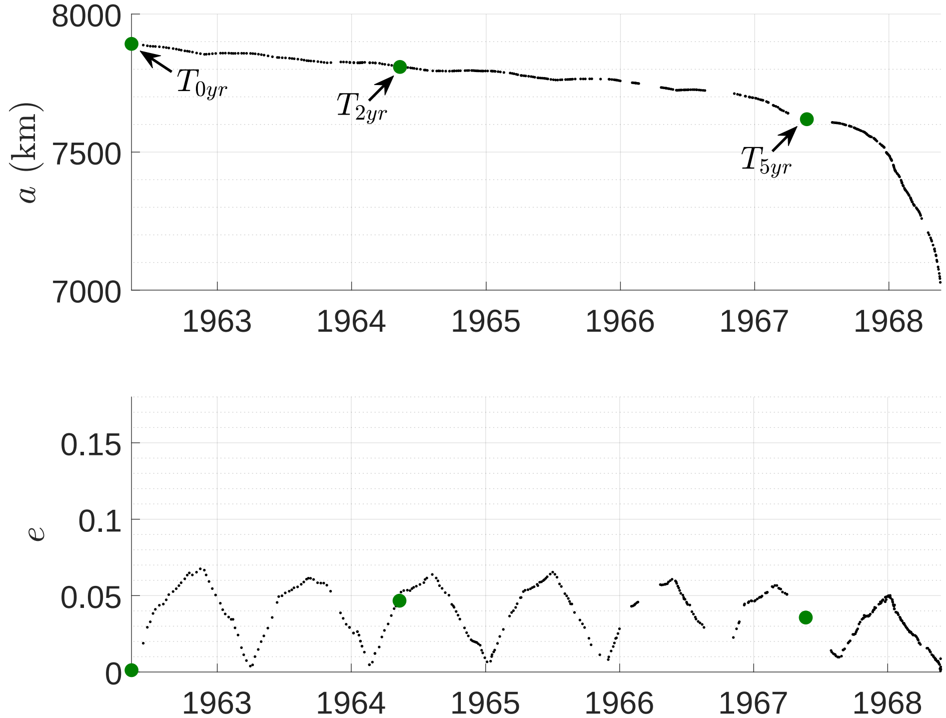

Figure 3.8: Evolution of a and e for Echo I as recorded by the TLEs, and identification of the TLEs listed in Table 3.5: $T_{0\text{yr}}$, $T_{2\text{yr}}$ and $T_{5\text{yr}}$ (green dots)

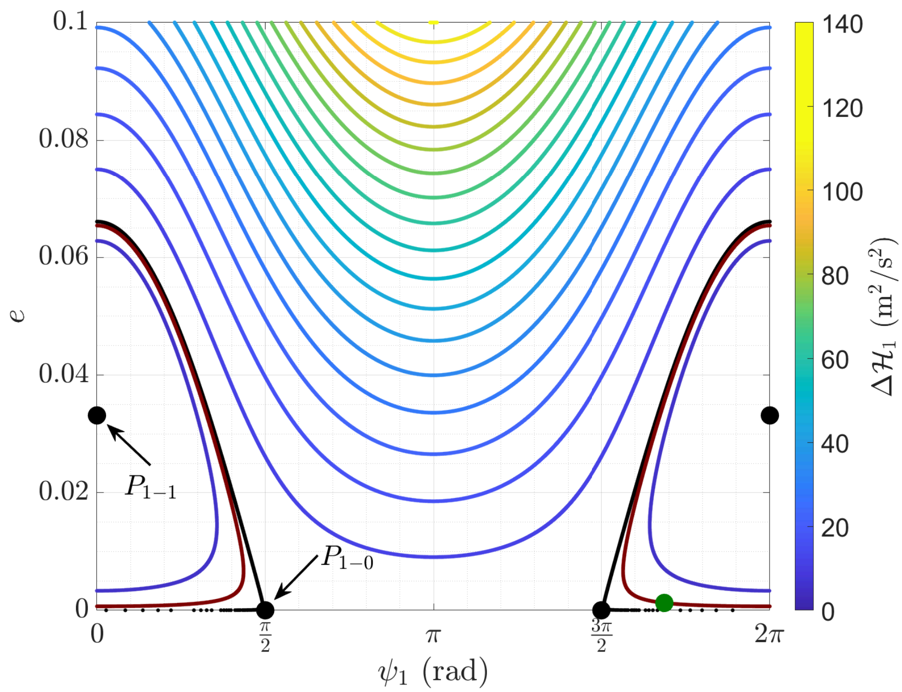

Figure 3.9: Phase plot associated with the $j = 1$ resonance, for orbit $T_{0\text{yr}}$ (green dot) as defined in Table 3.5, and $\frac{A_{\text{eff}}}{m}\sigma_{\text{eff,sphere}} = 9.73$ m^2/kg.

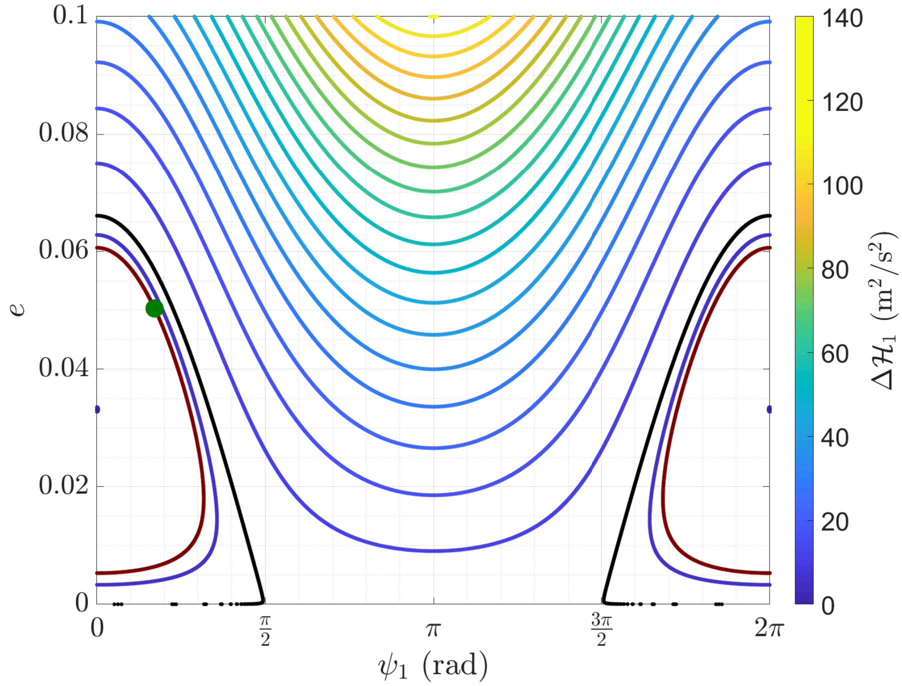

Figure 3.10: Phase plot associated with the $j = 1$ resonance, for orbit $T_{2\text{yr}}$ (green dot) as defined in Table 3.5, and $\frac{A_{\text{eff}}}{m}\sigma_{\text{eff,sphere}} = 9.73$ m^2/kg

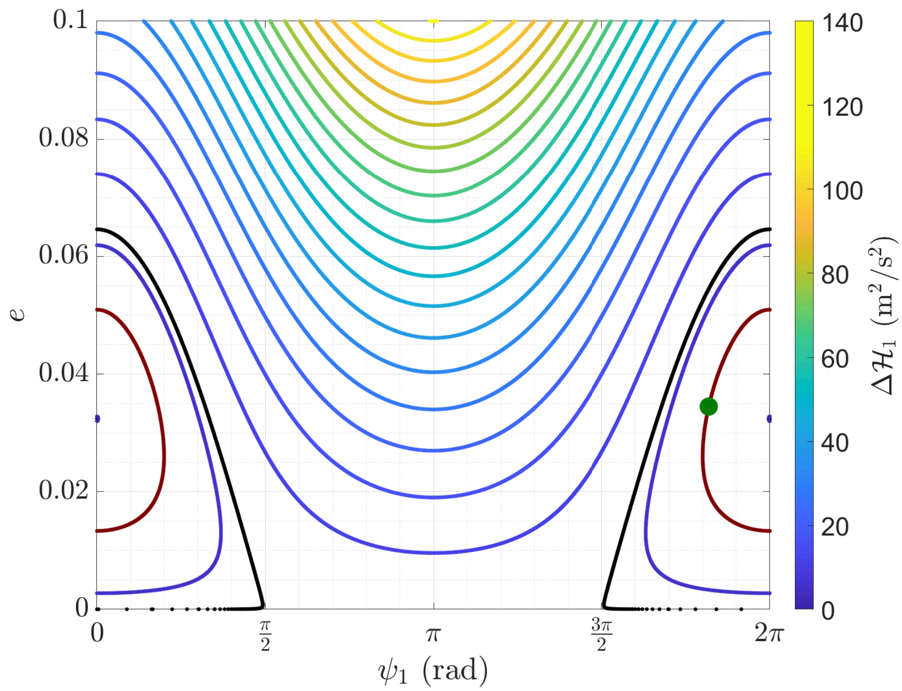

Figure 3.11: Phase plot associated with the $j = 1$ resonance, for orbit $T_{5\text{yr}}$ (green dot) as defined in Table 3.5, and $\frac{A_{\text{eff}}}{m}\sigma_{\text{eff,sphere}} = 9.73$ m^2/kg

external perturbations, short-period effects of the SRP, or non-resonant SRP terms, all of which are neglected when generating the phase plots.

As can be seen from the equidistant (in $\Delta\mathcal{H}_1$) phase curves of Figs. 3.9 to 3.11, only a small difference in the Hamiltonian distinguishes the stable and unstable equilibria. Thus, even small perturbations might lead to a critical alteration of the phase curve. We must also bear in mind the limited accuracy of the recorded TLEs which might also explain these variations.

We can conclude from the analysis performed in this section that the resonance phase plots allow us to illustrate the *leading* behaviour of the spacecraft dynamics when in resonance. It is however a simplified model and the contribution of the omitted dynamics, although small, should be considered. Particular attention must be paid to objects in the vicinity of the separatrix, as small variations in $\mathcal{H}_j$ can lead to a change of regime, libration vs circulation. This is even more important for dynamics similar to that represented by the phase plot topology of Fig. 3.15 (presented in the following section) for which a change of regime represents a drastic change in the amplitude of the eccentricity oscillations.

3.3 Echo I resonance test cases

In this section, we extrapolate the Echo I resonance model presented in the previous section for two extreme scenarios: the motion near a stable equilibrium for which we expect e to remain constant, and the motion under the strongest possible resonance for which we expect e to be subject to the fastest increase. For this analysis, we first employ the resonance model of the previous section to identify the initial orbital conditions for each aforementioned scenario. The corresponding fictitious orbits of the satellite are then propagated using D-SPOSE. The results thus obtained offer new findings and insights into the behaviour of Echo I and the SRP-J_2-resonance.

3.3.1 Echo I placed in stable equilibrium orbit

In Section 3.2.1, we identified for a $j = 1$ resonance the equilibria associated with the phase space defined by the effective area-to-mass ratio of Echo I $\frac{A_{\text{eff}}}{m}\sigma_{\text{eff,sphere}} = 9.73$ m^2/kg, and Echo I initial orbit of Table 3.1, more specifically: $a = 7{,}892$ km and $\frac{\Sigma_2}{L} = -0.3207$. For our analysis, we modify the initial orbit to that of Table 3.6 so that the new orbit is located at the stable equilibrium P_{1-1} of Table 3.4, still with $a = 7{,}892$ km and $\frac{\Sigma_2}{L} = -0.3207$. We note that on May 12, 1962, at 14:23:48, the longitude of the Sun is $\lambda_S = 51.4°$. The values of Ω and ω are thus set so that $\psi_1 = 0$ for the modified orbit (see Eq. (2.22) for $j = 1$).

Table 3.6: Fictitious orbital initial conditions of stable equilibrium at initial epoch 1962/05/12 14:23:48 ($\lambda_S = 51.4°$)

a (km)	e	i (°)	Ω (°)	ω (°)	ν (°)
7,892	0.03345	47.23	51.4	0	35.68

Propagating the orbit of Table 3.6 under the same conditions as in Section 3.1.2, we obtain the semi-major axis and eccentricity time responses presented in Fig. 3.12. The associated phase response of the eccentricity is shown in Fig. 3.13 for the first four years. We note from these results that the eccentricity oscillates between 0.0294 and 0.0447 while ψ_1 remains within -0.157 rad and 0.215 rad (-8.95° and 12.3°) over the first four years. Although we observe some small oscillations in e and ψ_1 resulting from the action of the external perturbations and non-resonant terms neglected when generating the phase plot, we conclude that the motion of the spacecraft remains in the vicinity of the stable equilibrium location, as was expected.

We further observe from Fig. 3.12, that even without reaching the highest eccentricity values of Echo I, the higher eccentricity average, $e \approx 0.03345$, for the stable equilibrium test case decreases the perigee sufficiently (about 260 km) to deorbit the spacecraft within seven years starting at the initial epoch of May 12, 1962, 14:23:48 used for our propagations.

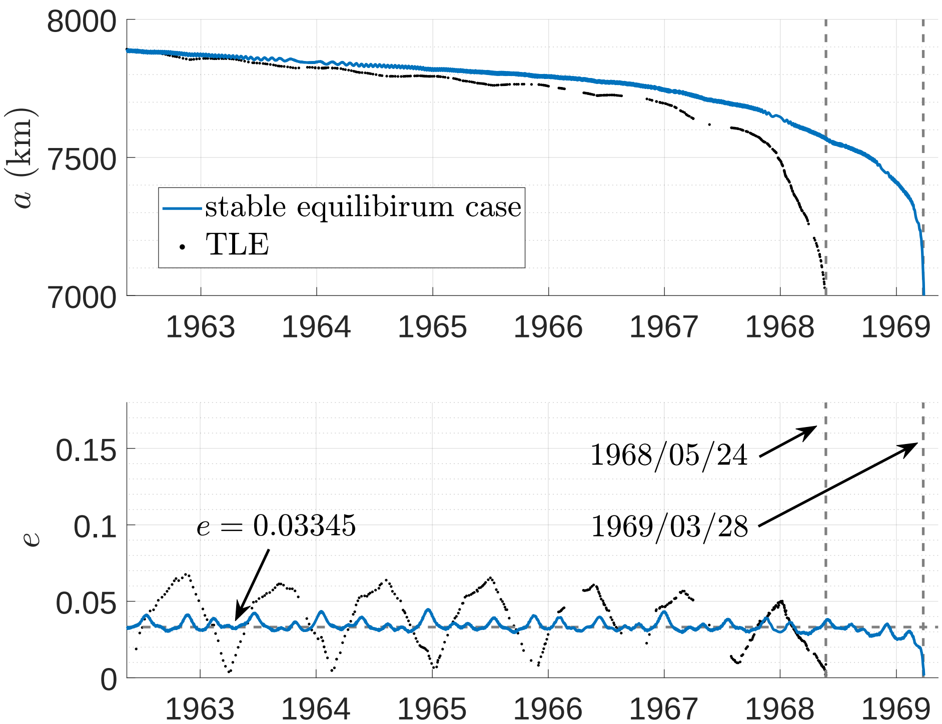

Figure 3.12: Semi-major axis and eccentricity responses for the propagation of the orbit of Table 3.6 in D-SPOSE at initial epoch 1962/05/12 14:23:48 (blue) in comparison to the observed TLEs (black dots)

3.3.2 Echo I placed in strongest resonance

As mentioned in Section 1.1.2, for an orbit defined by specific a and e, the range of inclinations leading to a significant resonance effect is usually very narrow for objects with area-to-mass ratios smaller than 1 m^2/kg. For large area-to-mass ratio objects, like Echo I, the width of this corridor becomes much larger. Indeed, even though Echo I orbit was located about 8° from the inclination leading to the strongest resonance, it still experienced eccentricity variations on the order of 0.068.

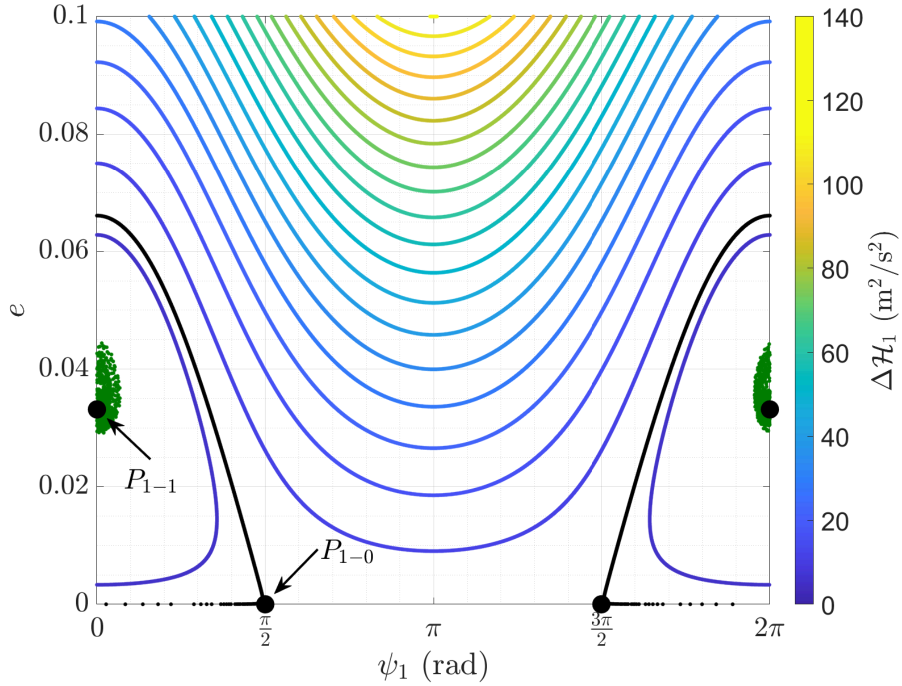

Figure 3.13: Phase response for the 4-year propagation of the orbit of Table 3.6 in D-SPOSE at initial epoch 1962/05/12 14:23:48 (green dots around the P_{1-1} equilibrium) superimposed over the phase plot associated with the $j=1$ resonance for $a = 7982$ km, $\frac{\Sigma_2}{L} = -0.3207$ and $\frac{A_{\text{eff}}}{m}\sigma_{\text{eff,sphere}} = 9.73$ m^2/kg

This was enough to significantly vary its perigee height (about 550 km oscillations), and thus reduce its lifetime by nearly four years as was concluded in Section 3.1.2. Had Echo I been located at the resonant inclination, however, its lifetime would have been even shorter, in fact, shorter than 7 months, as we will see from the results presented in this section.

The condition for a resonance as presented by Cook [11] and given by Eq. (3.3) allows to identify, for the actual orbital a and e of Echo I, as listed in Table 3.1, the inclination expected to yield the strongest resonant effect:

$$i_{\text{res, Cook}} = 39.766^\circ \quad \leftrightarrow \quad \left.\frac{\Sigma_2}{L}\right|_{\text{res, Cook}} = -0.23134 \tag{3.8}$$

However, as alluded in Section 3.1, and made clear by the resonance analysis performed by Alessi et al. in [18], this condition is deficient in characterizing the resonance phenomenon. This is further confirmed by the results of Figs. 3.14 and 3.15. Fig. 3.14 presents the phase plot associated with $\left.\frac{\Sigma_2}{L}\right|_{\text{res, Cook}}$ while Fig. 3.15 presents the phase plot for which the eccentricity is subject to the highest variation. The latter corresponds to:

$$i_{\max\,\Delta e} = 39.143^\circ \quad \leftrightarrow \quad \left.\frac{\Sigma_2}{L}\right|_{\max\,\Delta e} = -0.22442 \tag{3.9}$$

still for a and e from Table 3.1. We note that the inclination values of Eqs. (3.8) and (3.9) are very close. However, in the vicinity of $\frac{\Sigma_2}{L}\Big|_{\text{res, Cook}}$ and $\frac{\Sigma_2}{L}\Big|_{\max \Delta e}$, small differences lead to significant discrepancies in the phase plots, as clearly evident from Figs. 3.14 and 3.15. Comparing the two phase portraits separatrices (black curves), we observe that the maximum variation in eccentricity is $\Delta e = 0.632$ for Cook's resonance while a maximum $\Delta e = 0.699$ is reached for $\frac{\Sigma_2}{L}\Big|_{\max \Delta e}$.

The resulting $j = 1$ equilibrium points for the latter scenario obtained from Eqs. (3.5) and (3.7) for the orbit defined by a and e from Table 3.1 and $i_{\max \Delta e}$ from Eq. (3.9) are presented in Table 3.7 and identified in Fig. 3.15. We note that the maximum possible Δe is reached for the case where the Hamiltonian of the unstable quasi-equilibrium P_{1-0} and unstable equilibrium P_{1-2}, coincide.

Table 3.7: Equilibrium points locations associated with the $j = 1$ resonance, for $a = 7982$ km, $\frac{\Sigma_2}{L}\big|_{\max \Delta e} = -0.22442$ and $\frac{A_{\text{eff}}}{m}\sigma_{\text{eff,sphere}} = 9.73$ m^2/kg

P	j	e	i (°)	σ_1	stability	$\Delta\mathcal{H}_1$ (m^2/s^2)
1-0	1	0	N/A	$\frac{\pi}{2}, \frac{3\pi}{2}$	unstable	490
1-1	1	0.2751	39.95	π	stable	561
1-2	1	0.5432	42.89	π	unstable	490
1-3	1	0.5816	43.60	0	stable	0

Propagating the initial conditions of Table 3.1 in D-SPOSE, but with $i = \{i_{\text{res, Cook}}, i_{\max \Delta e}\}$ from Eqs. (3.8) and (3.9), and under the same conditions as in Section 3.1.2, we obtain the results of Fig. 3.16 shown in comparison to the observed motion of Echo I. For these orbits, Echo I would have been expected to be deorbited within only seven months instead of > 6 years, once again, about the initial epoch of May 12, 1962, 14:23:48.

We also note by comparing Figs. 3.14 and 3.15 that, in the case of $\frac{\Sigma_2}{L}\Big|_{\text{res, Cook}}$, the separatrix remains near $\psi_1 = \frac{\pi}{2}$ for $e \in [0, 0.5]$ while for $\frac{\Sigma_2}{L}\Big|_{\max \Delta e}$ it does not. Moreover, from Eq. (2.75), we gather that the maximum rate of change in Σ_1, equivalently in e, is achieved at $\psi_1 = \frac{\pi}{2}$. The case of $\frac{\Sigma_2}{L}\Big|_{\text{res, Cook}}$ might thus lead to a faster increase in eccentricity in the $e \in [0, 0.5]$ range. The difference is, however, not significant in the scenario of Fig. 3.16 (orange vs. blue curves) for which the spacecraft evolves from $e = 0.0125$ to a maximum eccentricity of $e = 0.11$ before it is deorbited. Within this range, $\psi_1 \approx \frac{\pi}{2}$ for both cases as can be seen from Figs. 3.14 and 3.15, therefore leading to a similar increase rate in e.

3.4 Concluding remarks

In this Chapter, we analyzed the orbital motion of Echo I in light of the SRP-J_2-resonance phase space theory recently published by Alessi et al. [18] for spherical spacecraft. It was found that even though Echo I was located far from the theoretical resonant orbit given by Cook's commensurability condition [11], the satellite's eccentricity still exhibited a resonant behaviour due to its

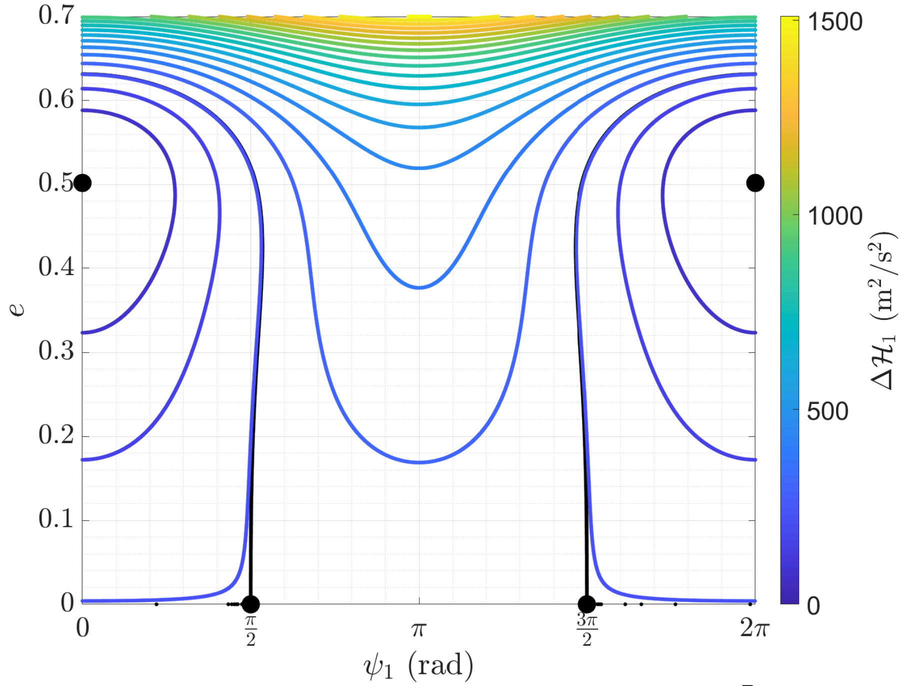

Figure 3.14: Phase plot associated with the $j = 1$ resonance, for $a = 7982$ km, $\frac{\Sigma_2}{L}\big|_{\text{res, Cook}} = -0.23134$ and $\frac{A_{\text{eff}}}{m}\sigma_{\text{eff,sphere}} = 9.73$ m^2/kg

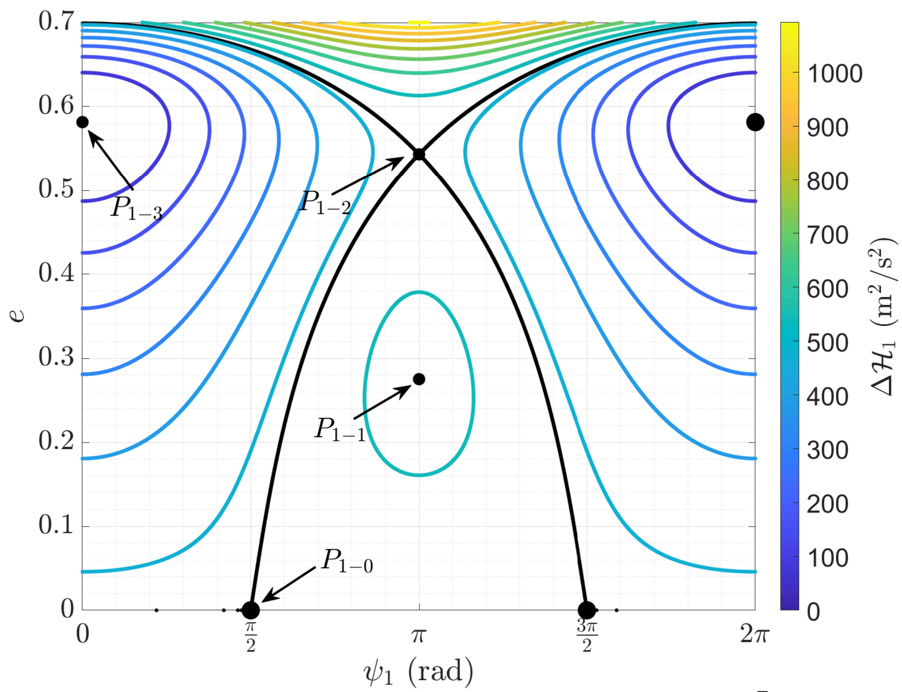

Figure 3.15: Phase plot associated with the $j = 1$ resonance, for $a = 7982$ km, $\frac{\Sigma_2}{L}\big|_{\max\,\Delta e} = -0.22442$ and $\frac{A_{\text{eff}}}{m}\sigma_{\text{eff,sphere}} = 9.73$ m^2/kg

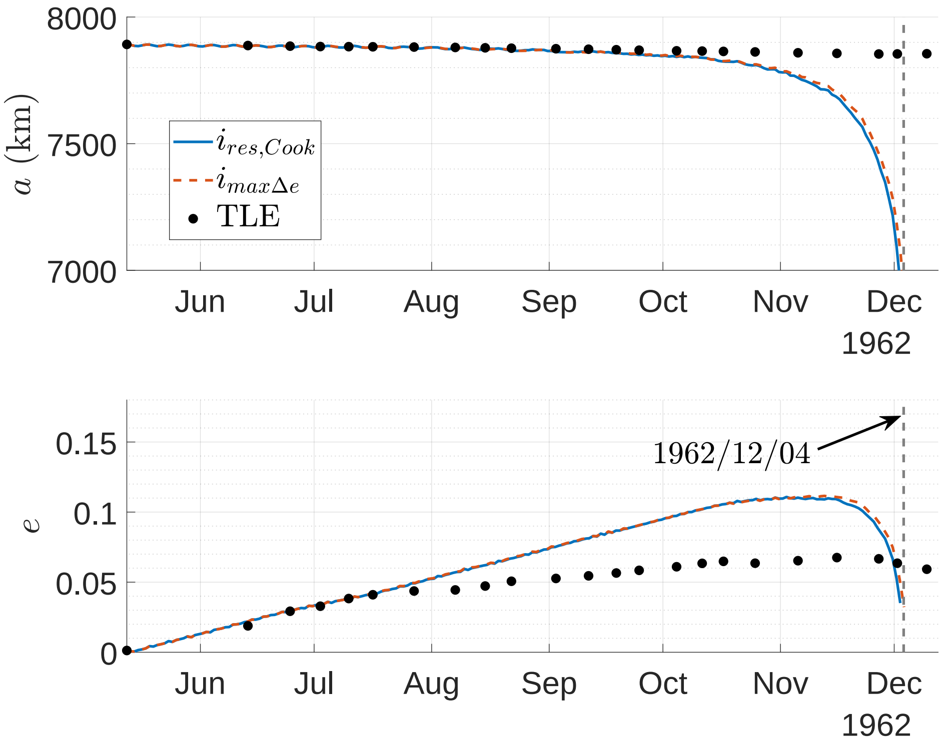

Figure 3.16: Semi-major axis and eccentricity responses for the propagation of the orbit $T_{0\text{yr}}$ of Table 3.5 with $i = \{i_{\text{res, Cook}}, i_{\text{max }\Delta e}\}$ in D-SPOSE at initial epoch 1962/05/12 14:23:48 in comparison to the observed TLEs (black dots)

proximity to the separatrix, i.e., the phase curve associated with an unstable equilibrium point, in the phase space of the first ($j = 1$) resonance. The separatrix, in this particular case, has an amplitude in eccentricity of $\Delta e \approx 0.067$ owing to the high area-to-mass ratio of Echo I (11.7 m^2/kg), which is consistent with the recorded TLEs for Echo I.

We also deepened the resonance analysis of Echo I by placing the satellite in two extreme fictitious orbits, which we then propagated using the realistic environment modelled by D-SPOSE. We thus confirmed that, in the vicinity of a stable equilibrium, both the phase angle and the eccentricity remain nearly constant. We also concluded that, although the fastest eccentricity increase is obtained for the orbit given by solving Cook's commensurability condition for small e, the highest eccentricity variation is reached for the case where the Hamiltonian of the unstable quasi-equilibrium and unstable equilibrium, exist and coincide. The propagation of the latter fictitious orbit showed that, had the inclination of Echo I been $i = 39.766°$ instead of $i = 47.214°$ on May 12, 1962, 14:23:48, then it would have deorbited in less than 7 months, instead of > 6 years as was its finale.

As was demonstrated in this chapter, the coupling of the SRP and J_2 perturbations can have a strong resonance effect in eccentricity that acts to passively deorbit the spacecraft. As well, the magnitude of the effect is highly dependent on the location of the spacecraft and the effective area-to-mass ratio. In the next chapter, we aim to lift this limitation of the spacecraft position and show that a strong resonance in eccentricity can be generated for a plate-like spacecraft by orienting it properly.

Chapter 4

e-Resonance for Constant Rotation Rate

As suggested by Lücking et al. [23]–[25], the STRP-J_2 resonance can be used to accelerate the deorbitation time of a spacecraft by increasing the eccentricity of its orbit, thus reducing the perigee's altitude to a point where the atmospheric drag becomes non-negligible. Existing analyses of this phenomenon are, however, based on the limiting cannonball assumption, whereby the STRP perturbing acceleration is aligned with the incoming light ($\underset{\rightarrow}{u}$) and the effective STRP coefficient (σ_{eff}) of the object in question is a constant, as highlighted in Chapter 2. Although the ensuing conclusions adequately apply to balloon spacecraft, as Echo I discussed in Chapter 3, they fail to characterize the resonant behaviour of a rotating *non-spherical* spacecraft. It has been argued that the cannonball results also hold for non-spherical spacecraft, although, if an averaged effective STRP coefficient is employed, resonance can only occur at very specific locations. The cannonball resonances, inherently restricted to only a few specific orbits, severely confine the possibility of deorbitation exploiting the STRP-J_2 resonance. Indeed, the spacecraft is required to already be near one of these specific locations; otherwise, the ΔV required to change the orbit at end-of-life is too costly.

In this chapter, we explore the effect of *rotational* motion of the spacecraft/debris on the resonance phenomenon. We suggest that a resonance effect of considerable strength can be achieved for non-spherical spacecraft in *any* orbit, by adopting an appropriate rotational motion scenario. We refer to this type of resonance, i.e., resonance involving attitude changes, as a ϕ-resonance. In this way, a spacecraft can exploit the STRP-J_2-ϕ resonance to accelerate its deorbitation, without any restrictions on its initial orbital inclination. More specifically, this chapter focuses on the case of a thin planar spacecraft—a panel—rotating at a constant rate $\dot{\phi}$ about the ecliptic's normal for which the dynamics was established in Chapter 2. The suggested approach, however, shows some limitations as it will be made clear by the analysis of the relevant phase plots.

4.1 Resonance study for plate-like spacecraft

In this section, we study the STRP-J_2 resonance for a plate-like spacecraft modelled with the parameters of Table 4.1, and rotating at a constant rate $\dot{\phi}$ about the normal to the ecliptic. We first derive the resonance condition analogue to the condition derived by Cook under the cannonball assumption. We then perform a stability analysis to provide more insight into the eccentricity evolution as a function of the resonant angle and rotation rate. Finally, we highlight the limitations of exploiting this phenomenon for deorbitation.

Table 4.1: Spacecraft Model Parameters

Parameter	Description	Value	Units
m	mass	variable	-
l_y	length along $\underset{\rightarrow}{y}_b$	3.3	m
l_z	length along $\underset{\rightarrow}{z}_b$	9	m
A_{nom}	nominal area	$l_y l_z = 29.7$	m^2
C_d	drag coefficient	2.2	-
σ_a	absorptivity	1	-
σ_{rs}	specular reflectivity	0	-
σ_{rd}	diffuse reflectivity	0	-

4.1.1 Resonance condition derivation

There is a strong similarity between the equations describing the STRP-J_2-ϕ single-resonance dynamics of a panel rotating a constant rate ($\dot{\phi}$) and that of a sphere. As can be gathered from the Echo I resonance study in Chapter 3, for a spherical spacecraft, the resonance dynamics is dictated by the combination of a, e and i (or $\frac{\Sigma_2}{L}$), in other words, the only way to influence the strength of the resonance is to modify the orbit of the spacecraft. In Section 3.3.2, this was achieved by modifying the orbit's inclination. Performing orbital manoeuvres can, however, be very costly in terms of fuel requirements, especially for inclination changes. The introduction of the $\dot{\alpha}$ parameter in the plate-like system dynamics offers more flexibility. It is assumed that $\dot{\alpha}$ can be fixed by setting $\dot{\phi}$ accordingly (see Eq. (2.10)) using the attitude control system of the spacecraft. Recall that α corresponds to the angle between the incoming light $\underset{\rightarrow}{u}$ and the inward normal of the panel front side $\underset{\rightarrow}{n}$.

As alluded to in the previous chapters, a resonance occurs when one of the periodic terms in the equation of motion of an osculating element—here we are interested in the eccentricity e—has a nearly null frequency. In such a case, the long-term behaviour of the element is governed by the associated resonant term. In light of this, the condition for a resonance to occur can be identified directly from the eccentricity equation of motion. The criterion for a resonance can therefore be derived from Eq. (2.63), which we rewrite here:

$$\frac{\mathrm{d}\bar{e}}{\mathrm{d}t} = -\frac{3}{2}\overline{C}_{\mathrm{STRP}}\frac{\sqrt{1-e^2}}{n\,a}\sum_{j=1}^{6}\mathcal{T}_j\sum_{k=-\infty}^{\infty}C_k\sin(\overline{\psi}_{j,k}) \tag{4.1}$$

For the analysis presented in this chapter, we will refer to the one degree-of-freedom system derived in Section. 2.5 based on the averaged Hamiltonian dynamics. For consistency, the eccentricity equation of motion averaged over one revolution of the spacecraft is employed to derive the resonance condition, that is $\dot{\overline{\psi}}_{j,k} \approx 0$, and it takes the form of:

$$\begin{aligned}\frac{\mathrm{d}\overline{\psi}_{j,k}}{\mathrm{d}t} &= n_1\,\dot{\Omega} + n_2\,\dot{\omega} + n_3\,(\dot{\lambda}_S + k\,\dot{\alpha}_{j,k})\\ &= n_1\,\dot{\Omega} + n_2\,\dot{\omega} + n_3\,(1-k)\,\dot{\lambda}_S + n_3\,k\,\dot{\phi}_{j,k} \approx 0\end{aligned} \tag{4.2}$$

where $\psi_{j,k}$ is as per Eq. (2.29). As stated in Section 2.5, under the single-resonance assumption, the dynamics of the rotating panel is given by the one-degree-of-freedom averaged Hamiltonian system of Eq. (2.70) with $\dot{\sigma}_1 = \dot{\overline{\psi}}_{j,k}$. The commensurability condition thus takes the form:

$$\begin{aligned}\dot{\sigma}_1 = &-\frac{3}{2}\overline{C}_{\mathrm{STRP}}\,C_k\,\frac{L^2}{\mu}\left(\frac{\partial\mathcal{T}_j}{\partial\Sigma_1}\sqrt{1-\tfrac{\Sigma_1^2}{L^2}} - \mathcal{T}_j(\varepsilon,{}^{\Sigma_2}/_{\Sigma_1})\frac{1}{\sqrt{1-\frac{\Sigma_1^2}{L^2}}}\frac{\Sigma_1}{L^2}\right)\cos\sigma_1 + \ \ldots\\ &n_3\,(\dot{\tau}+k\dot{\alpha}) + \frac{3\,J_2\,R_e^2\,\mu^4}{4\,L^3\,n_2\,\Sigma_1^4}\left(3\,n_1 - 1 + 8\,n_1\,n_2\frac{\Sigma_2}{\Sigma_1} + 5\,\frac{\Sigma_2^2}{\Sigma_1^2}\right) \approx 0\end{aligned} \tag{4.3}$$

which can be approximated by evaluating the given expression at $\sigma_1 = \frac{\pi}{2}$ (as in [11]) where the STRP term vanishes:

$$\dot{\sigma}_{1,J_2} = n_3\,(\dot{\tau}+k\dot{\alpha}) + \frac{3\,J_2\,R_e^2\,\mu^4}{4\,L^3\,n_2\,\Sigma_1^4}\left(3\,n_1 - 1 + 8\,n_1\,n_2\frac{\Sigma_2}{\Sigma_1} + 5\,\frac{\Sigma_2^2}{\Sigma_1^2}\right) \approx 0 \tag{4.4}$$

We recall that $\dot{\tau} = \dot{\lambda}_S$ and $L = \sqrt{\mu\,a}$ from Eq. (2.40) are considered constant, $\frac{\Sigma_2}{L} = (n_2\cos i - n_1)\sqrt{1-e^2}$ from Eq. (2.72) is a constant of motion, while the value of $\Sigma_1 = L\sqrt{1-e^2}$ oscillates under the resonance action: the stronger the resonance, the larger the amplitude $\Delta\Sigma_1$, and equivalently Δe.

We reiterate here that the attitude angle ϕ, equivalently α (see Eq. (2.10)), has an effect on the resonant rate only if $k \neq 0$; in which case, it is possible to solve the commensurability condition of Eq. (4.4) for $\dot{\alpha}$ given any combination of a, e and $\frac{\Sigma_2}{L}$, that is for any orbit. This expands the possibility of exploiting a resonance phenomenon in any orbit instead of a very specific ensemble of orbits, as is the case for a spherical spacecraft. Solving Eq. (4.4) for $\dot{\alpha}$ yields the resonant-(j,k)

α rate:

$$\frac{\mathrm{d}\alpha_{j,k}}{\mathrm{d}t}\left(a,\,e,\,\frac{\Sigma_2}{L}\right) = -\frac{1}{k}\,\dot{\lambda}_S + \frac{3\,J_2\,R_e^2\,n}{4\,k\,n_2\,n_3\,\mu\,a^3\,(1-e^2)^3}\left[-5\,\Sigma_2^2 - 8\,n_1\,\Sigma_2\,\sqrt{\mu\,a\,(1-e^2)}\right.$$
$$\left.(1-3n_1)\,\mu\,a\,(1-e^2)\right] \tag{4.5}$$

and ultimately, using Eq. (2.10), the resonant-(j,k) rotation rate of the panel:

$$\frac{\mathrm{d}\phi_{j,k}}{\mathrm{d}t}\left(a,\,e,\,\frac{\Sigma_2}{L}\right) = \frac{\mathrm{d}\alpha_{j,k}}{\mathrm{d}t}\left(a,\,e,\,\frac{\Sigma_2}{L}\right) + \dot{\lambda}_S \tag{4.6}$$

This means that to generate a ϕ-resonance, the panel needs to rotate at a rate of $\dot{\phi} \approx \dot{\phi}_{j,k}$ computed for the values of a, e and $\frac{\Sigma_2}{L}$ associated with its orbit. Bear in mind that while a and $\frac{\Sigma_2}{L}$ are constant over time, e oscillates due to the resonance. For the purpose of our analysis, $\dot{\phi}_{j,k}$, or equivalently $\dot{\alpha}_{j,k}$, is defined for the eccentricity value of the initial orbit.

It was shown in Chapter 3 that the condition expressed by Eq. (4.4)—equivalent to Cook's commensurability condition derived under the cannonball assumption (see Eq. (3.3))—is deficient in characterizing the resonant behaviour; a phase plot/stability analysis is necessary to paint a proper portrait of the resonance. Nonetheless, solving $\dot{\sigma}_{1,J_2} = 0$ for $\dot{\phi}$ at a specific orbit still gives a good approximation of the rotation rate that would yield the strongest (j,k)-resonance effect in the vicinity of this orbit.

In the following sections, we investigate the effect of the rotation rate on the (1,2)-resonance dynamics of a panel initially located in the orbit of Table 4.2, O2. We further show, through the study of the relevant phase plots, that small variations in $\dot{\phi}$—on the order of a few percent from the computed $\dot{\phi}_{1,2} = -3.9432\text{e-}6°$/sec—may have a determining effect on the long term evolution of the eccentricity. We note that orbit O2 is chosen because $\dot{\phi}_{1,2}$ associated with this orbit is well separated from $\dot{\phi}_{j,2}$ for $j \in \{2,\ldots,6\}$ so that there is no coupling between the first and other resonances.

Table 4.2: Orbital elements of O2 and resonance parameters for $j = 1$ and $k = 2$

	a (km)	e	i (°)	$\overline{\beta}$	Ω (°)	ω (°)	ν (°)	$\frac{\Sigma_2}{L}$	$\dot{\phi}_{1,2}$ (°/sec)
O2	8,078	0.01	60	0.78	0	0	45	-0.49997	-3.9432e-6

We note that there exists an infinity of possible resonances, each modulated by the associated $\mathcal{T}_j$ and C_k coefficients. In the remainder of this section, we restrict our analysis to the (1,2)-resonance since, based on our observations previously stated in Section 2.3, for $\left|\frac{\varepsilon_f-\varepsilon_b}{\varepsilon_f+\varepsilon_b}\right| < 0.5$ and $i < 90°$, it is the one with the strongest effect, i.e., $\mathcal{T}_1 C_2 > \mathcal{T}_j C_k$ for all $j \neq 1$ and $k \neq \{0,2\}$. We also emphasize the fact that the $(j,0)$ resonances are associated with specific orbits and, therefore, cannot be exploited in a ϕ-resonance deorbitation scenario. In the literature, these are referred to as the resonant orbits and were identified under the cannonball assumption [11], [27].

4.1.2 Equilibrium identification

Recall from the previous chapter that the form of the phase plot is intrinsically linked to the locations of the equilibria. We subsequently show how these are derived from the (Σ_1, σ_1)-system of Eq. (2.70). Due to the close similarity between the rotating panel case and the cannonball case previously addressed, only the main results are briefly provided here. For more details, the reader may refer to Section 3.2.1.

The equilibria are obtained by solving:

$$\dot{\Sigma}_1 = 0 \quad , \quad \dot{\sigma}_1 = 0 \tag{4.7}$$

where, in the case of a rotating panel, $\dot{\Sigma}_1$ and $\dot{\sigma}_1$ are given by Eq. (2.70) for which we note an explicit dependency on $\dot{\alpha}$. Solving Eq. (4.7), we conclude that for $e \neq 0$ (or $\Sigma_1 \neq 1$), an equilibrium ($\Sigma_{1,\text{eq}}$,$\sigma_{1,\text{eq}}$) exists only if $\sigma_1 \in \{0, \pi\}$ and:

$$\begin{aligned} 0 = & -\frac{3}{2}\overline{C}_{\text{SRP}} C_k \frac{L^2}{\mu}\left(\frac{\partial \mathcal{T}_j}{\partial \Sigma_1}\sqrt{1-\frac{\Sigma_1^2}{L^2}} - \mathcal{T}_j(\varepsilon, {}^{\Sigma_2}/_{\Sigma_1})\frac{1}{\sqrt{1-\frac{\Sigma_1^2}{L^2}}}\frac{\Sigma_1}{L^2}\right)\cos\sigma_1 + n_3\,(\dot{\tau}+k\dot{\alpha}) + \dots \\ & \frac{3J_2R_e^2\mu^4}{4L^3n_2\Sigma_1^4}\left(3n_1 - 1 + 8n_1n_2\frac{\Sigma_2}{\Sigma_1} + 5\frac{\Sigma_2^2}{\Sigma_1^2}\right) \end{aligned} \tag{4.8}$$

in which case, the stability of the equilibrium point is deduced from the product $\left.\frac{\partial \dot{\Sigma}_1}{\partial \sigma_1}\right|_{(\Sigma_{1,\text{eq}},\sigma_{1,\text{eq}})} \times \left.\frac{\partial \dot{\sigma}_1}{\partial \Sigma_1}\right|_{(\Sigma_{1,\text{eq}},\sigma_{1,\text{eq}})}$: a negative sign indicates that the point is stable, otherwise it is unstable. Fig. 4.1 illustrates the eccentricity locations of the equilibrium points associated with the (1,2)-resonance in the vicinity of $\dot{\phi}_{1,2}$ for a $\frac{A_{\text{eff}}}{m} = 1$ m^2/kg panel modelled as a black body ($\sigma_a = 1$), and located in O2 orbit of Table 4.2. The equilibrium associated with $\dot{\phi}_{1,2}$ computed for O2 (see Table 4.2 for $\dot{\phi}_{1,2}$ value) is identified with a black 'x' in Fig. 4.1.

Another point of interest is the quasi-equilibrium, $(e_{\text{q-eq}}, \sigma_{1,\text{q-eq}}) = (0, \{\frac{\pi}{2}, \frac{3\pi}{2}\})$[1], that exists for any j, a, $\frac{\Sigma_2}{L}$, $\dot{\alpha}$ (or $\dot{\phi}$) and $\frac{A_{\text{eff}}}{m}C_k$ values. This point is always unstable since, even though $\dot{\Sigma}_1 = 0$, $\dot{\sigma}_1 = \pm\infty$ whenever $\dot{\sigma}_{1,J_2}(e=0) \neq 0$ (see Eqs. (2.70) and (4.4)).

From Fig. 4.1, we gather that for O2, there exist three equilibria when $\dot{\phi} < -3.9070\text{e-}6°$/sec and only one otherwise. Together with the quasi-equilibrium, we come to the same conclusion as in Section 3.2.1: the equilibria come in pairs (stable/unstable). Each pair defines a libration region bounded by the unstable equilibrium phase curve, the separatrix, with the stable equilibrium at its centre. This will be confirmed by the phase plot analysis presented in the following section. We also conclude from Fig. 4.1, that small variations in $\dot{\phi}$, on the order of a few percent (-4e-6°/sec to -3.6e-6°/sec), significantly change the locations of the equilibria, ultimately affecting the number

[1] $\dot{\alpha}$ is finite

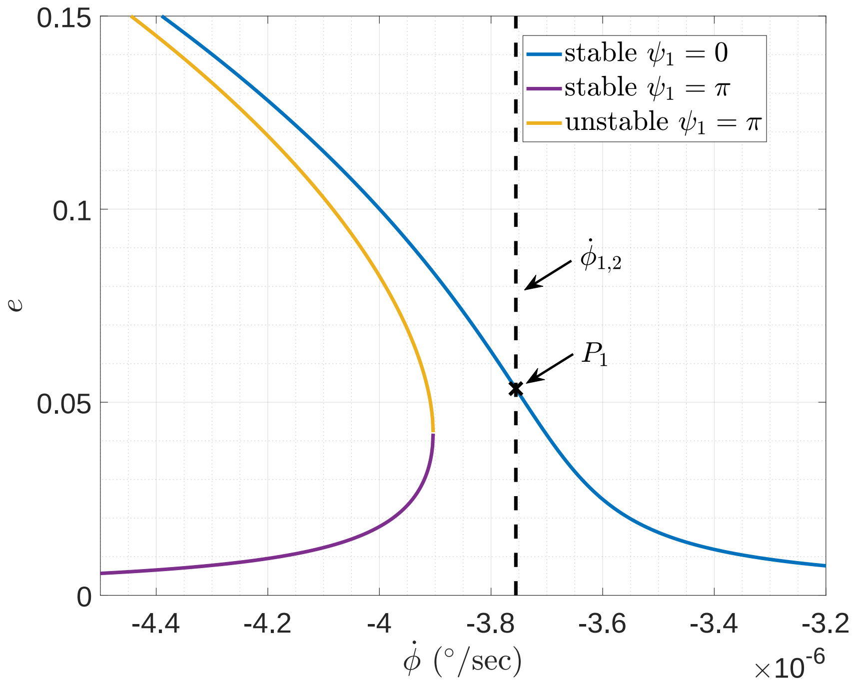

Figure 4.1: Equilibrium location for O2 assuming $\frac{A_{\text{eff}}}{m} = 1$ m^2/kg and $\sigma_a = 1$ obtained by solving Eq. (2.70)

of equilibrium points and the form of the phase portrait. This supports our previous statement that $\dot{\phi}$ has a determining effect on the long-term evolution of the eccentricity.

It is worth mentioning that the coupling of the different (j,k)-resonances that may arise for certain orbits might lead to a more complex phase portrait with more equilibria. In particular, there is coupling between the $j = 1$ and $j = 2$ resonances at Sun-synchronous orbits since $\dot{\bar{\Omega}} = \dot{\lambda}_S$. There is also coupling when generating a ϕ-resonance ($k \neq 0$) in the vicinity of a resonant orbit, i.e., an orbit for which the commensurability condition of Eq. (4.2) with $k = 0$ is passively met. Even though resonance coupling is not covered by the analysis presented in this chapter, the possibility of coupling exists and must be assessed beforehand since the results presented in this chapter are obtained under the generally, but not always, admissible single-resonance assumption.

4.1.3 Phase plot analysis

In the remainder of this section, we investigate how the change in the equilibria affects the phase plots. Recall that the phase curves associated with the stable and unstable equilibria/quasi-equilibria contain all the necessary information to establish the phase portrait topology. The information contained in Fig. 4.1 is thus sufficient to generate the 2D phase plots associated with values of $\dot{\phi}$ ranging from -4.5e-6°/sec to -3.2e-6°/sec. We draw in Figs. 4.2 to 4.6 five (1,2)-resonance phase plots for a 1 m^2/kg black panel initially in O2 and rotating at five selected rotation rates, respectively. Table 4.3 lists the resulting equilibrium locations for all five $\dot{\phi}$ values. We note that Fig. 4.3 represents the special case for which the Hamiltonian of the unstable quasi-equilibrium P_0 and unstable equilibrium P_2 coincide, i.e., the associated separatrices coincide.[2] This corresponds to the case for which the maximum Δe is reached as was stated in Section 3.3.2 for the spherical case, and we denote the generating $\dot{\phi}$ value as $\dot{\phi}_{1,2\text{-max}\,\Delta e}$. Also, Fig. 4.6 represents the special case for which $\dot{\phi} = \dot{\phi}_{1,2\text{-O2}}$. Figs. 4.2, 4.4 and 4.5 are intermediate cases selected to depict the possible topologies of the phase portraits.

For our analysis, we define:

- P_0 as the unstable quasi-equilibrium located at $e = 0$ and $\psi_{1,2} = \{\frac{\pi}{2}, \frac{3\pi}{2}\}$;
- P_1 as the stable equilibrium at $\psi_{1,2} = 0$, blue line in Figs. 4.2(b) to 4.6(b);
- P_2 as the unstable equilibrium at $\psi_{1,2} = \pi$, yellow line in Figs. 4.2(b) to 4.6(b);
- P_3 as the stable equilibrium at $\psi_{1,2} = \pi$, purple line in Figs. 4.2(b) to 4.6(b).

Note that points P_2 and P_3 do not exist for $\dot{\phi} > -3.9070\text{e-}6°/\text{sec}$.

Table 4.3: Equilibrium points locations for a (1,2)-resonance obtained by solving Eq. (2.70) for $\frac{A_{\text{eff}}}{m} = 1$ m^2/kg, $\sigma_a = 1$, with a and $\frac{\Sigma_2}{L}$ from Table 4.2

P	$\dot{\phi}$ (°/sec)	e	i (°)	σ_1	stability	$\Delta\overline{\mathcal{H}}_{1,2}$ (m^2/s^2)
1-0	-4.3920e-6	0	N/A	$\frac{\pi}{2}, \frac{3\pi}{2}$	unstable	8.217
1-1	-4.3920e-6	0.15022	60.38	0	stable	0
1-2	-4.3920e-6	0.14397	60.35	π	unstable	2.462
1-3	-4.3920e-6	0.00664	60.00	π	stable	8.245
2-0	-3.9432e-6	0	N/A	$\frac{\pi}{2}, \frac{3\pi}{2}$	unstable	1.352
2-1	-3.9432e-6	0.09069	60.14	0	stable	0
2-2	-3.9432e-6	0.06668	60.07	π	unstable	1.352
2-3	-3.9432e-6	0.02441	60.01	π	stable	1.450
3-0	-3.9170e-6	0	N/A	$\frac{\pi}{2}, \frac{3\pi}{2}$	unstable	1.149
3-1	-3.9170e-6	0.08609	60.12	0	stable	0
3-2	-3.9170e-6	0.05563	60.05	π	unstable	1.247
3-3	-3.9170e-6	0.03087	60.01	π	stable	1.266
4-0	-3.9020e-6	0	N/A	$\frac{\pi}{2}, \frac{3\pi}{2}$	unstable	1.042
4-1	-3.9020e-6	0.08338	60.11	0	stable	0
5-0	-3.7555e-6	0	N/A	$\frac{\pi}{2}, \frac{3\pi}{2}$	unstable	0.341
5-1	-3.7555e-6	0.05352	60.05	π	stable	0

Figs. 4.2 to 4.4 each shows two libration regions. In the phase plot of Fig. 4.2, the two regions are defined by the P_3/P_0 and P_1/P_2 stable/unstable pairs while in the phase plot of Fig. 4.4 the pairs P_1/P_0 and P_3/P_2 define the libration zones. The change in the pairing occurs at the limit case of Fig. 4.3 for which the P_0 and P_1 phase curves coincide when $\dot{\phi} = \dot{\phi}_{1,2\text{-max}\,\Delta e} = -3.9432\text{e-}6°/\text{sec}$

[2] The averaged Hamiltonian given by Eq. (2.59) remains constant along each phase curve.

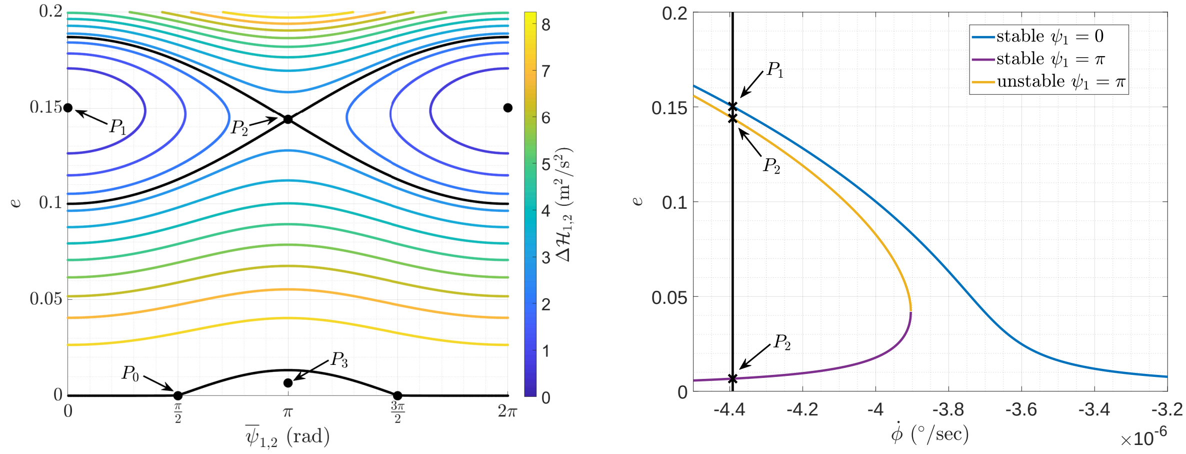

(a) Phase plot (b) Equilibrium location

Figure 4.2: Phase plot and equilibria for a (1,2)-resonance obtained by solving Eq. (2.70) for $\frac{A_{\text{eff}}}{m} = 1$ m^2/kg, $\sigma_a = 1$, with a and $\frac{\Sigma_2}{L}$ from Table 4.2, and rotating at $\dot{\phi} = -4.3920\text{e-}6°$/sec about the ecliptic normal

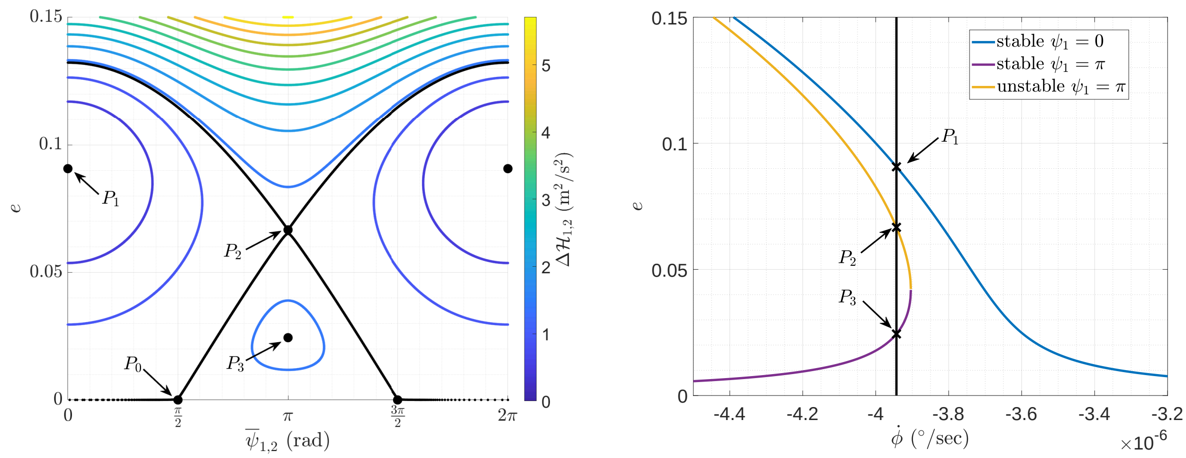

(a) Phase plot (b) Equilibrium location

Figure 4.3: Phase plot and equilibria for a (1,2)-resonance obtained by solving Eq. (2.70) for $\frac{A_{\text{eff}}}{m} = 1$ m^2/kg, $\sigma_a = 1$, with a and $\frac{\Sigma_2}{L}$ from Table 4.2, and rotating at $\dot{\phi} = \dot{\phi}_{1,2\text{-max}\,\Delta e} = -3.9432\text{e-}6°$/sec about the ecliptic normal

(from Table 4.3: $\Delta\overline{\mathcal{H}}_{1,2} = 1.352$ m^2/s^2 for both P_0 and P_2). The maximum eccentricity variation, $\Delta e = 0.1323$ is reached at the separatrix of Fig. 4.3(a) as compared to $\Delta e = 0.1263$ for Fig. 4.4(a), $\Delta e = 0.1227$ for Fig. 4.5(a), $\Delta e = 0.0871$ for Fig. 4.2(a) and $\Delta e = 0.0674$ for Fig. 4.6(a). This is in line with the conclusions of Section 3.3.2.

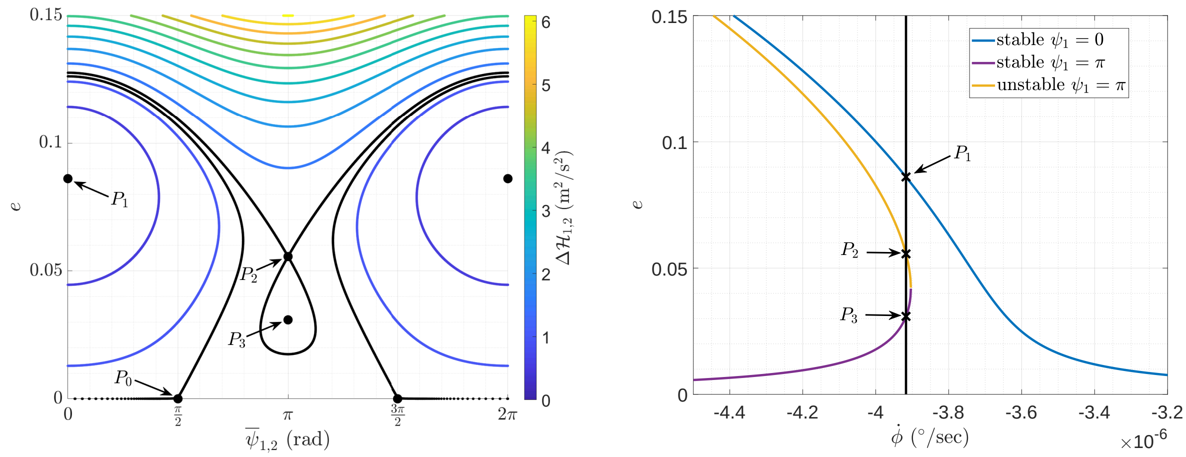

(a) Phase plot (b) Equilibrium location

Figure 4.4: Phase plot and equilibria for a (1,2)-resonance obtained by solving Eq. (2.70) for $\frac{A_{\text{eff}}}{m} = 1$ m^2/kg, $\sigma_a = 1$, with a and $\frac{\Sigma_2}{L}$ from Table 4.2, and rotating at $\dot{\phi} = -3.9170\text{e-}6°$/sec about the ecliptic normal

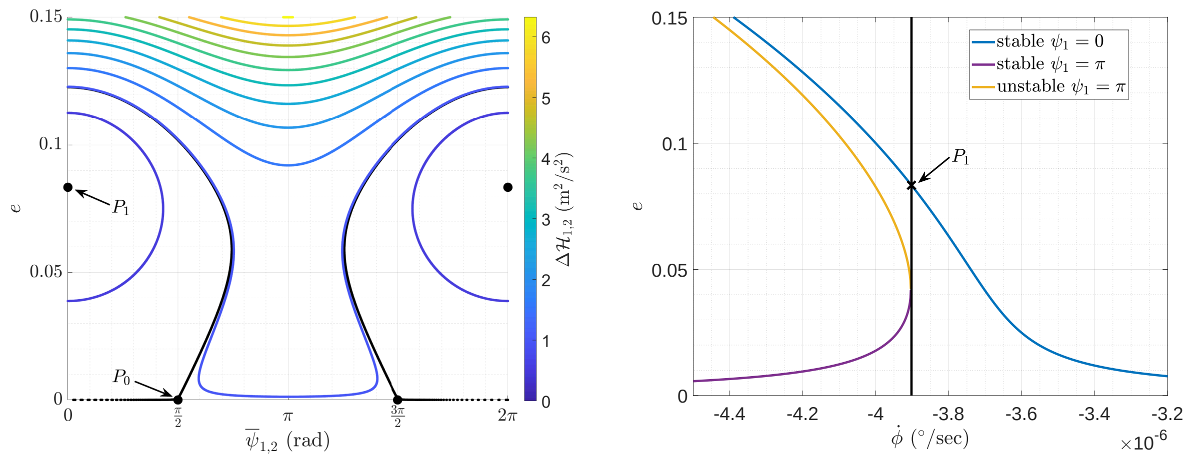

(a) Phase plot (b) Equilibrium location

Figure 4.5: Phase plot and equilibria for a (1,2)-resonance obtained by solving Eq. (2.70) for $\frac{A_{\text{eff}}}{m} = 1$ m^2/kg, $\sigma_a = 1$, with a and $\frac{\Sigma_2}{L}$ from Table 4.2, and rotating at $\dot{\phi} = -3.9020\text{e-}6°$/sec about the ecliptic normal

In the following section, we assess the validity of the phase plots analysis, and the possibility of exploiting the ϕ-resonance to deorbit a spacecraft initially in O2, based on the assumption that the maximum Δe is reached at the separatrix.

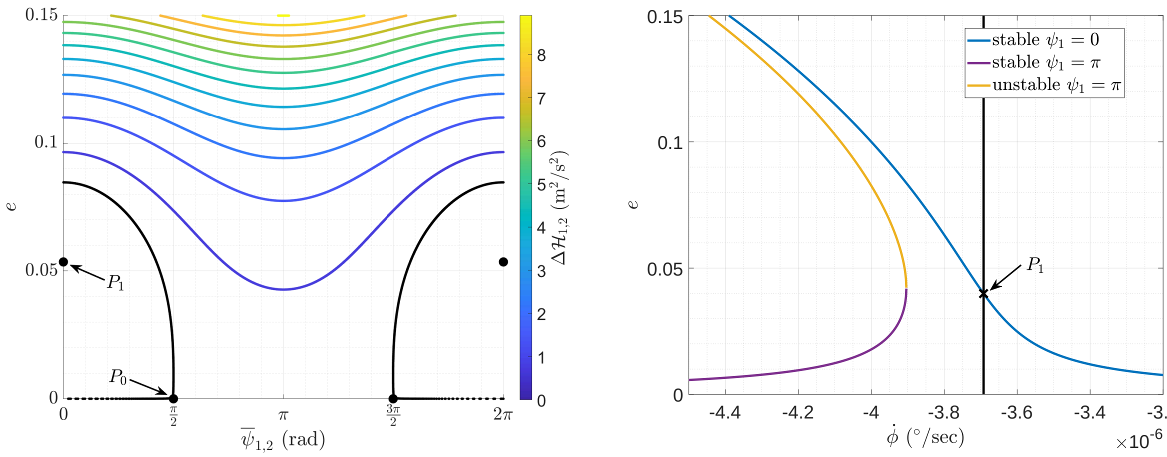

(a) Phase plot (b) Equilibrium location

Figure 4.6: Phase plot and equilibria for a (1,2)-resonance obtained by solving Eq. (2.70) for $\frac{A_{\text{eff}}}{m} = 1$ m^2/kg, $\sigma_a = 1$, with a and $\frac{\Sigma_2}{L}$ from Table 4.2, and rotating at $\dot{\phi} = \dot{\phi}_{1,2\text{-O2}} = -3.7555\text{e-}6°$/sec about the ecliptic normal

4.2 Deorbitation with constant rotation rate

The phase plots presented in the previous section describe the averaged single-resonance system of Eq. (2.70), meaning that only the $j = 1$ and $k = 2$ term, $\overline{\mathcal{H}}_{1,2}$, of the averaged Hamiltonian $\overline{\mathcal{H}}$ (Eq. (2.59)) is considered. In a more realistic environment, the non-averaged short-period oscillations of $\mathcal{H}_{1,2}$ as well as the other $\mathcal{H}_{j,k}$ terms along with the omitted (n,m)-terms of the geopotential (see Eqs. (2.11) and (2.12)) would also contribute to the dynamics of the spacecraft. Another very important perturbation that was omitted so far is the atmospheric drag. As was concluded in Section. 3.2.3, its effect can drastically alter the dynamics of a spacecraft at low altitudes.

To evaluate the impact of the neglected dynamics and perturbing accelerations on the spacecraft resonance dynamics when rotating at a constant rate, a 60-year propagation is carried out in D-SPOSE including the STRP, the geopotential up to degree and order 2, and this, with and without the inclusion of atmospheric drag and/or the Earth shadow. The perturbing torques were excluded to allow a constant rotation rate without requiring active control. The perturbing accelerations in D-SPOSE are implemented using the following models [65]–[67]:

- STRP: Eq. (2.14) for a constant radiation pressure[3] $P_r = \frac{1{,}361}{c}\ \frac{\text{N}}{\text{m}^2}$
- gravitational field: EGM2008 up to degree and order 2
- drag: NRLMSISE-00 with constant equivalent planetary amplitude Ap = 15 and solar radio flux F10.7 cm = 140 sfu
- Earth shadow: geometric model with penumbra transition as implemented in D-SPOSE [65]

[3] $c = 299{,}792{,}458$ m/s represents the speed of light

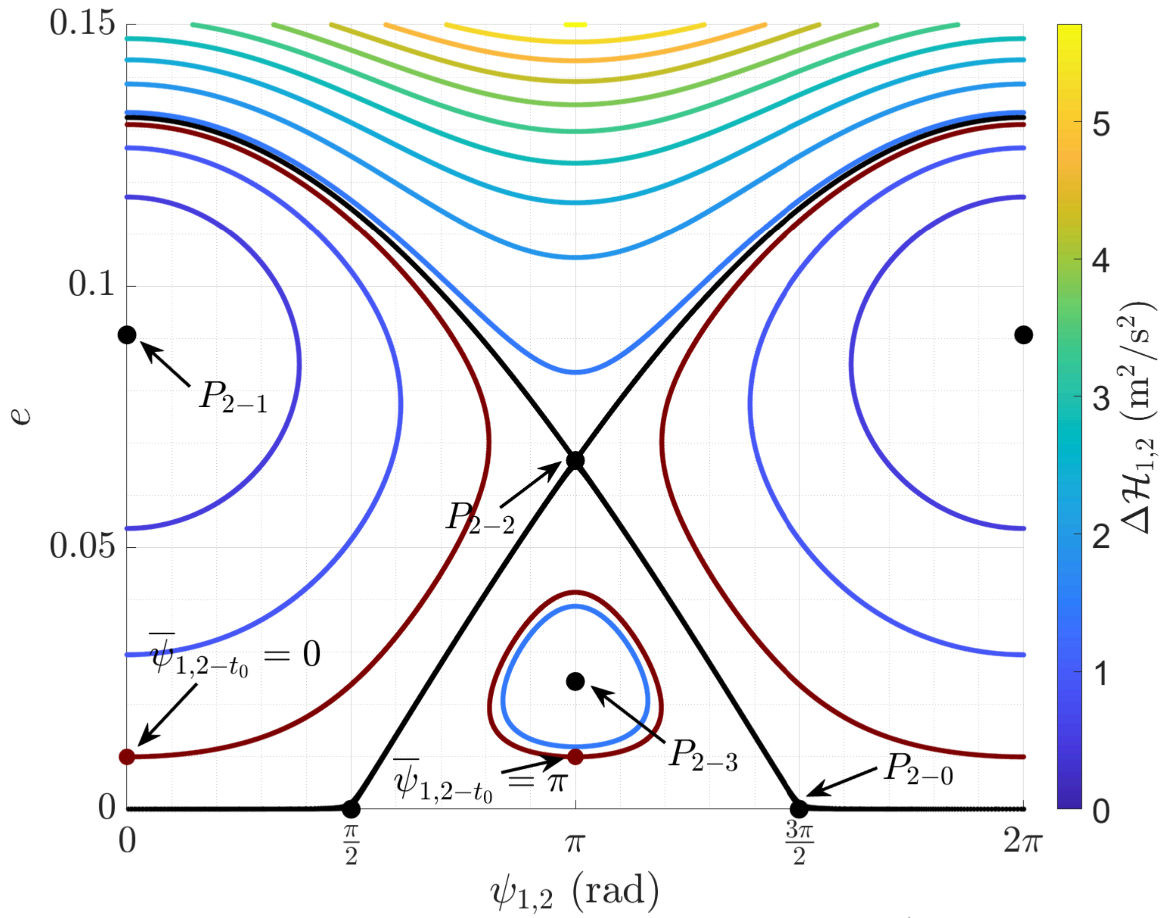

Figure 4.7: Phase plot for a (1,2)-resonance obtained by solving Eq. (2.70) for $\frac{A_{\text{eff}}}{m} = 1$ m^2/kg, $\sigma_a = 1$, with a and $\frac{\Sigma_2}{L}$ from Table 4.2, and rotating at $\dot{\phi} = \dot{\phi}_{1,2\text{-max}\,\Delta e} = -3.9432\text{e-}6°$/sec about the ecliptic normal. The phase curves associated with the O2 orbit for initial $\overline{\psi}_{1,2} = 0$ and $\overline{\psi}_{1,2} = \pi$ are shown in dark red

For all investigated perturbation cases, the initial orbit O2 is defined in Table 4.2, with the panel modelled by the parameters of Table 4.1. The mass is adjusted to yield an effective area-to-mass ratio of $\frac{A_{\text{nom}}}{m} = 1$ m^2/kg (see Eq. (2.71)). All propagations are initialized at epoch 2000-01-01T00:00:00 ($\lambda_S = 280°$) with a fixed time step of 30 sec. For these simulations, a rotation rate of $\dot{\phi} = \dot{\phi}_{1,2\text{-max}\,\Delta e} = -3.9432\text{e-}06°$/sec is chosen as it is expected to yield the maximum eccentricity increase for orbits with nearly null e.

In Fig. 4.7, we draw over the phase plot of Fig. 4.3(a) (obtained for $\dot{\phi} = \dot{\phi}_{1,2\text{-max}\,\Delta e}$), the phase curves associated with the O2 orbit, for initial $\overline{\psi}_{1,2} = 0$ and $\overline{\psi}_{1,2} = \pi$, to highlight the effect of the initial phase angle on the eccentricity evolution. Indeed, the initial ϕ value must be carefully selected as the phase curves associated with $\overline{\psi}_{1,2} = 0$ and $\overline{\psi}_{1,2} = \pi$, for $\dot{\phi} = -3.9432\text{e-}06°$/sec, yield very different maximum values of e: 0.1309 and 0.0414 respectively as can be seen from Fig. 4.7.

We make a note that, although in theory, the greatest eccentricity increase is observed at the separatrix, in a realistic case, the effect of neglected perturbations might lead to an unwanted change of regime that would prevent this. For instance, in the particular case of Fig. 4.7, a panel initially located at the separatrix could, under the action of neglected perturbations, be pushed to the libration region defined by the P_{2-3}/P_{2-0} stable/unstable equilibrium pair, for which the maximum attainable eccentricity is much smaller. In light of this, when setting the initial attitude angle ϕ, it is better to distance the $(\overline{\psi}_{1,2}, e)$ location from the separatrix so that the panel is more likely to remain within the high-amplitude libration region defined by the P_{2-1}/P_{2-2} pair. For the simulations presented in this section, the panel is thus set to be initially oriented at $\phi = 140°$ so that $\overline{\psi}_{1,2} = 0$ (see Eq. (2.60)). The time responses of a, e and perigee height h_p—where the perigee height $h_p = a(1-e) - R_e$ with R_e the Earth's equatorial radius—as well as e vs. $\overline{\psi}_{1,2}$ are shown in Fig. 4.8. Additionally, the reference responses obtained from the averaged system of Eq. (2.70) for O2 are also shown in dark red in Fig. 4.8.

We subsequently analyze the results for the three perturbation cases: the first one excluding both the Earth shadow and atmospheric drag, the second one including the Earth shadow but excluding atmospheric drag, and the final one including both the Earth shadow and atmospheric drag. We note that in all three cases, the STRP and geopotential up to degree and order 2 are always included.

4.2.1 Without Earth shadow and atmospheric drag

For this case, $\overline{\beta} = 1$ and $\frac{A_{\text{nom}}}{m}$ is set to 1 m^2/kg for the propagation in D-SPOSE. We observe from the e vs. $\overline{\psi}_{1,2}$ response of Fig. 4.8, that the results obtained in D-SPOSE (blue curve) follow the expected results obtained from the averaged single-resonance system of Eq. (2.70) for O2 (dark red curve). Also, from the semi-major axis a time response of Fig. 4.8 (blue curve), we confirm that the mean value of a remains constant over time, an assumption that was fundamental to obtaining Eq. (2.70), and consequentially the phase plots of section 4.1.3 for O2. We conclude from these results that for the case of O2, the contribution of the short-period dynamics along with the non-resonant term in the system Hamiltonian $\mathcal{H}$ and omitted (n,m) geopotential terms are negligible as far as the long-term behaviour of the panel when rotating at a constant rate of $\dot{\phi} = \dot{\phi}_{1,2\text{-max}\,\Delta e}$. The single-resonance assumption holds.

We also note from the eccentricity time response and phase plot of Fig. 4.8 (two bottom figures) the decrease in the magnitude of the eccentricity time rate, $|\dot{e}|$, as the averaged resonant phase angle $\overline{\psi}_{1,2}$ nears 0 (or 2π) and π. This will be further discussed shortly.

4.2.2 With Earth shadow and without atmospheric drag:

For this case, the Earth shadow is not ignored, therefore $\overline{\beta} = 0.78$ and $\frac{A_{\text{nom}}}{m}$ is set to 1.28 m^2/kg for the propagation in D-SPOSE, so that $\frac{A_{\text{eff}}}{m} = 1$ m^2/kg. An important observation we can make from

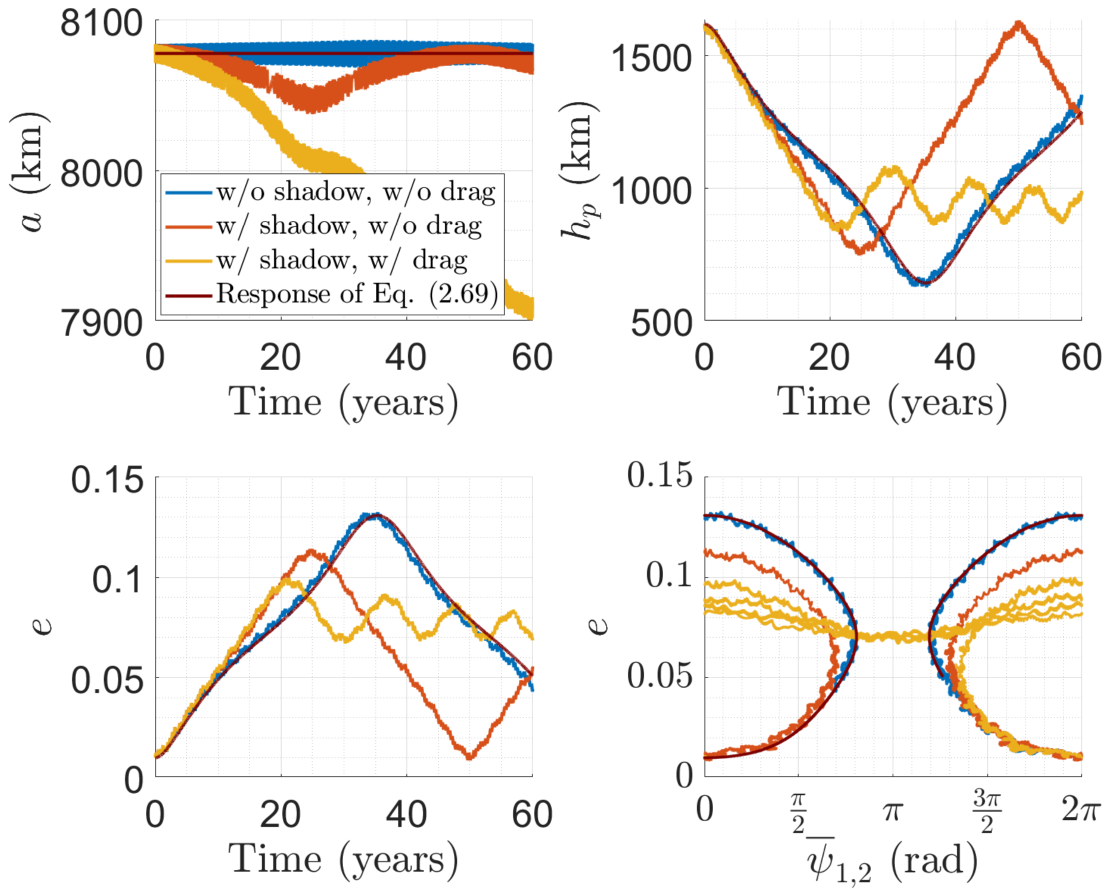

Figure 4.8: Time response of a (1,2) resonance when propagating O2 over 60 years in D-SPOSE with and without the Earth shadow and/or the atmospheric drag and with $\dot{\phi} = -3.9432\text{e-}06°/\text{sec}$

the semi-major axis time response of Fig. 4.8 is that the mean value of a is not constant over time; it varies in the range 8,078-8,046 km. Apart from including the shadow effect, the perturbation conditions are identical to the previous case. This indicates that the coupled effect of the Earth shadow and STRP perturbation is at play in the secular variation of a.[4] Recall that the explicit dependence of β on the true anomaly ν was not considered in the averaging of $\mathcal{H}$ to obtain $\overline{\mathcal{H}}$ (see Eqs. (2.57) to (2.61)). Rather, an approximate mean value representing the sunlight period vs. orbital period ratio was used, $\overline{\beta}$. As noted earlier, the assumption that a remains constant is fundamental to obtaining the averaged dynamics of the reference model, but it does not hold for this case. Indeed, a small change in the semi-major axis has an important impact on the form of the phase plot, especially near the heart of the resonance, i.e., where the effect is the strongest. The variation in a due to the shadow effect thus explains the discrepancy between the eccentricity time responses of Fig. 4.8 with (orange curves) and without (blue curves) the inclusion of the Earth

[4]The geopotential is not affected by the Sun, thus the inclusion or exclusion of the Earth shadow has no effect on this perturbation.

shadow. The former reaches a maximum eccentricity of $e = 0.113$, which is less than the latter, which reaches a maximum eccentricity of $e = 0.131$.

4.2.3 With Earth shadow and atmospheric drag

As for the previous case, the Earth shadow is not ignored, therefore $\overline{\beta} = 0.78$ and $\frac{A_{\text{nom}}}{m}$ is set to 1.28 m^2/kg for this case as well, and similar conclusions can be drawn. Although, in the present case, the change in the semi-major axis is accentuated by the effect of the atmospheric drag.

We can further observe, from the eccentricity responses in Fig. 4.8 (yellow curves), the change from a libration to a circulation regime after about 20 years. The reduction of the mean value of a from 8,078 km to 8,020 km during these first 20 years considerably impacts the shape of the resonance. The amplitude of the eccentricity oscillations in the circulation regime further reduces as a decreases, along with the amplitude of the libration region (the maximum eccentricity amplitude), which we recall is given by the phase curve associated with the quasi-equilibrium at $e = 0$ and $\overline{\psi}_{1,2} = \{\frac{\pi}{2}, \frac{3\pi}{2}\}$, P_0, see Fig. 4.4(a). Although the resonance significantly lowers the altitude of the perigee —it reaches a minimum value of $h_p = 805$ km after 20 years—this is not enough to deorbit the spacecraft initially in O2.

In the absence of perturbations for O2, the minimum attainable perigee altitude is 585 km (dark red curves in Fig. 4.8), but with the inclusion of atmospheric drag and Earth shadow, this minimum h_p value increases to 805 km (yellow curve in Fig. 4.8). This is counterintuitive as atmospheric drag normally acts towards lowering an orbiting body.

4.3 Concluding remarks

We can first conclude that it is not necessarily possible to deorbit a panel initially located in a high LEO orbit in a reasonable time frame by exploiting the eccentricity resonance under a constant rotational rate assumption. Indeed the resonance effect might not be sufficiently strong to lower the perigee enough for the atmospheric drag to ensure the spacecraft's re-entry. We further showed that the change in the semi-major axis resulting from the atmospheric drag can considerably weaken the resonance. Recall that we set $\dot{\phi}$ so that the resonance is at its strongest, i.e., the phase curve is collocated with the separatrix of the libration region for the initial orbit. There are no provisions to maintain this condition as orbital parameters vary under the action of neglected disturbances.

Also, we can conclude that for a constant rotation rate, the amplitude of the eccentricity oscillations is necessarily bounded, therefore, there is a minimum attainable altitude of perigee. This minimum is likely to increase as the semi-major axis changes.

Finally, the stability and phase plot analyses allow us to identify the conditions that would yield the highest increase in eccentricity. The separatrix indeed leads to the highest amplitude in e, but this, is regardless of the rate. As previously noted, the O2 propagation results showed that the rate at which the eccentricity varies, $|\dot{e}|$, diminishes as $\overline{\psi}_{1,2}$ approaches 0 (or 2π) or π. This is in line with Eq. (4.1) which shows that the resonant (j,k)-term of the eccentricity rate does not explicitly depend on $\dot{\overline{\psi}}_{j,k}$, but rather on $\overline{\psi}_{j,k}$.

These insights motivate the implementation, in Chapter 5, of an attitude tracking control law over ϕ, rather than maintaining a constant $\dot{\phi}$, so as to maximize the rate of increase in eccentricity over the whole deorbitation process. This approach will further allow to overcome the minimum attainable h_p limitation. Moreover, a similar procedure will be employed to generate a resonance directly in the semi-major axis by also tracking ϕ.

Chapter 5

STRP-J_2-ϕ Resonance Deorbitation Strategies

In Chapter 4, we concluded that when exploiting a resonance in eccentricity with a constant rotation rate $\dot{\phi}$, the variation in e is necessarily bounded and, therefore, there is a minimum attainable altitude which may not be low enough for efficient deorbitation. Also, we concluded that the weakening of the resonance due to the change in a further rises this minimum altitude. In this chapter, we put forward a solution to overcome this limitation through a systematic approach to identify the optimal deorbitation strategy. The method exploits attitude control to enforce a STRP-J_2-ϕ resonance in eccentricity of a plate-like spacecraft rotating about the ecliptic's normal.

A similar approach is also applied to generate a STRP-J_2-ϕ resonance in the semi-major axis. The motivation for this alternate strategy stems from the fact that increasing the orbital eccentricity produces the desired lowering of the orbit only near the perigee, whereas decreasing the semi-major axis has this effect over the whole orbit. Even though it is not possible to enforce a ϕ-resonance in a with a constant rotation rate $\dot{\phi}$ as was done in Chapter 4 for a resonance in e, it is possible to do so by tracking the rotation angle ϕ instead.

In order to evaluate the robustness of the suggested deorbitation strategies, the feasibility of a complete spacecraft deorbitation exploiting both the eccentricity and the semi-major axis resonances is verified using the state-of-the-art coupled orbit-attitude propagator, D-SPOSE presented in Section 1.4.2. The high-accuracy modelling of atmospheric drag effects enabled by D-SPOSE is of paramount importance to establishing a deorbitation strategy by prescribing attitude motion. Consequently, we implemented active attitude control [81] in D-SPOSE to enforce the resonance condition that would otherwise drift.

5.1 ϕ-tracking criteria for orbital resonance

As concluded in Section 4.3, under the single resonance assumption, the secular eccentricity rate is governed by its resonant (j,k)-term, whereas the contributions from other terms average out to a null long-term effect. Therefore, the maximum increase rate is achieved by appropriately modulating the rotation angle ϕ. A similar resonant effect can also be produced to decrease the semi-major axis by using the same approach. In this light, we subsequently present the derivation of the tracking criterion on ϕ to generate a resonance in eccentricity and the tracking criterion to produce a resonance in semi-major axis.

5.1.1 Eccentricity resonance tracking criterion

The non-averaged eccentricity dynamics is dictated by Eq. (2.51) as stated in Section 2.4:

$$\left.\frac{\mathrm{d}e}{\mathrm{d}t}\right|_{\mathrm{STRP}} = -C_{\mathrm{STRP}}\frac{\sqrt{1-e^2}}{n\,a}\sum_{j=1}^{6}\mathcal{T}_j\sum_{k=-\infty}^{\infty}C_k\left[\sin(\widetilde{\psi}_{j,k})\left(1+\frac{1}{2(1+e\cos\nu)}\right)+\dots\right.$$
$$\left.\frac{\sin(\psi_{j,k}-\nu)}{2\,(1+e\cos\nu)}+e\frac{\sin(\psi_{j,k})}{(1+e\cos\nu)}\right] \tag{5.1}$$

where the argument angle $\widetilde{\psi}_{j,k}$ is given by Eq. (2.52). For orbits with small eccentricities, i.e., $e \ll 1$, Eq. (5.1) can be approximated by:

$$\left.\frac{\mathrm{d}e}{\mathrm{d}t}\right|_{\mathrm{STRP}} \approx -C_{\mathrm{STRP}}\frac{\sqrt{1-e^2}}{n\,a}\sum_{j=1}^{6}\mathcal{T}_j\sum_{k=-\infty}^{\infty}C_k\left[\frac{3}{2}\sin(\widetilde{\psi}_{j,k})+\frac{1}{2}\sin(\psi_{j,k}-\nu)\right] \tag{5.2}$$

Recall from Section 2.4.1, that $\widetilde{\psi}_{j,k}$ is slow-varying while $\psi_{j,k}-\nu$ is fast-varying. Based on Eq. (5.2), both terms could be made resonant. However, since the amplitude of a $\sin(\widetilde{\psi}_{j,k})$-term is three times that of the associated $\sin(\psi_{j,k}-\nu)$-term, the former is selected as a candidate for the resonance. We reiterate once again that, under the single-resonance assumption, the secular evolution of the eccentricity is governed by its resonant STRP (j,k)-term, therefore:

$$\left.\frac{\mathrm{d}e}{\mathrm{d}t}\right|_{\mathrm{STRP}} \approx \dot{e}_{j,k} = -\frac{3}{2}C_{\mathrm{STRP}}\frac{\sqrt{1-e^2}}{n\,a}\mathcal{T}_j C_k\sin(\widetilde{\psi}_{j,k}) \tag{5.3}$$

The resonance condition, or the commensurability condition, can then be deduced from Eqs. (5.3) and Eq. (2.52) as:

$$\begin{aligned}\frac{\mathrm{d}\widetilde{\psi}_{j,k}}{\mathrm{d}t} &= n_1\,\dot{\Omega}+n_2\,\dot{\omega}+n_3\,(\dot{\lambda}_S+k\,\dot{\alpha})\\ &= n_1\,\dot{\Omega}+n_2\,\dot{\omega}+n_3\,(k\,\dot{\phi}+(1-k)\,\dot{\lambda}_S)=0\end{aligned} \tag{5.4}$$

Based on Eq. (5.3), the maximum eccentricity increase rate is achieved for $\widetilde{\psi}_{1,2}=-\frac{\pi}{2}$. The $(1,2)$-resonance is chosen since, as already noted in Chapter 4, from Section 2.3, we have for $\left|\frac{\varepsilon_f-\varepsilon_b}{\varepsilon_f+\varepsilon_b}\right| < 0.5$ and $i<90°$, $\mathcal{T}_1 C_2 > \mathcal{T}_j C_k$ for all $j\neq 1$ and $k\neq\{0,2\}$, while for $k=0$, ϕ has no effect on $\widetilde{\psi}_{j,0}$. When $i>90°$, the (2,2)-resonance should be chosen instead. It is important to mention that the $\widetilde{\psi}_{1,2}=-\frac{\pi}{2}$ condition also enforces $\dot{\widetilde{\psi}}_{1,2}=0$, so that the necessary condition for resonance, i.e., the commensurability condition of Eq. (5.4), is implicitly satisfied. In this light, we choose to implement an attitude controller to track:

$$\widetilde{\psi}_{1,2} = -\Omega - \omega - \lambda_S + 2\,\phi_{r,e\text{-resonance}} = -\frac{\pi}{2} \tag{5.5}$$

where $\widetilde{\psi}_{1,2}$ is obtained from Eq. (2.52) with $j = 1$ and $k = 2$. From Eq. (5.5), the reference attitude to be tracked, specifically the angle $\phi_{r,e\text{-resonance}}$, is evaluated based on the observed values of Ω, ω and λ_S as:

$$\phi_{r,e\text{-resonance}} = \frac{\Omega + \omega + \lambda_S - \frac{\pi}{2}}{2} \tag{5.6}$$

In Eq. (5.6), Ω, ω and λ_S are slow-varying angles with $\dot{\lambda}_S$ almost constant, while the rates of Ω and ω are mainly governed by the Earth's J_2 harmonics, and are respectively given by $\dot{\Omega}_{J_2}$ and $\dot{\omega}_{J_2}$ from Eq. (B.2) in Appendix B. These depend on the values of a, e and i. For orbits in LEO, the combination of $\dot{\Omega}$, $\dot{\omega}$ and $\dot{\lambda}_S$ leads to periods on the order of weeks/months at the minimum as noted in Section. 2.4.1; the resulting $\phi_{r,e\text{-resonance}}$ oscillations should therefore have a similar period.

5.1.2 Semi-major axis resonance tracking criterion

The non-averaged semi-major axis dynamics is dictated by Eq. (2.55) as stated in Section 2.4:

$$\left.\frac{\mathrm{d}a}{\mathrm{d}t}\right|_{\mathrm{STRP}} = -C_{\mathrm{STRP}}\,\frac{2}{n\sqrt{1-e^2}}\sum_{j=1}^{6}\mathcal{T}_j\sum_{k=-\infty}^{\infty}C_k\left[e\sin(\widetilde{\psi}_{j,k}) + \sin(\psi_{j,k})\right] \tag{5.7}$$

The subsequent derivation proceeds analogously to that of Section 5.1.1. Thus, for orbits with small eccentricities, i.e., $e \ll 1$, Eq. (5.7) can be approximated by:

$$\left.\frac{\mathrm{d}a}{\mathrm{d}t}\right|_{\mathrm{STRP}} \approx -C_{\mathrm{STRP}}\,\frac{2}{n\sqrt{1-e^2}}\sum_{j=1}^{6}\mathcal{T}_j\sum_{k=-\infty}^{\infty}C_k\,\sin(\psi_{j,k}) \tag{5.8}$$

Under the single-resonance assumption, the secular evolution of the semi-major axis is governed by its resonant STRP (j,k)-term, therefore:

$$\frac{\mathrm{d}a}{\mathrm{d}t} \approx \dot{a}_{j,k} = -C_{\mathrm{STRP}}\,\frac{2}{n\sqrt{1-e^2}}\,\mathcal{T}_j C_k\,\sin(\psi_{j,k}) \tag{5.9}$$

The resonance condition, or the commensurability condition, can then be deduced from Eq. (5.9), and using Eq. (2.29) we can write it as:

$$\begin{aligned}\frac{\mathrm{d}\psi_{j,k}}{\mathrm{d}t} &= n_1\,\dot{\Omega} + n_2\,(\dot{\omega} + \dot{\nu}) + n_3\,(\dot{\lambda}_S + k\,\dot{\alpha}) \\ &= n_1\,\dot{\Omega} + n_2\,(\dot{\omega} + \dot{\nu}) + n_3\,(k\,\dot{\phi} + (1-k)\,\dot{\lambda}_S) = 0\end{aligned} \tag{5.10}$$

Based on Eq. (5.9), the maximum semi-major axis decrease rate is achieved for $\psi_{1,2} = \frac{\pi}{2}$. As for the eccentricity resonance, enforcing $\psi_{1,2} = \frac{\pi}{2}$ also implicitly enforces the resonance condition of Eq. (5.10). In light of this, we choose to track:

$$\psi_{1,2} = -\Omega - \omega - \nu - \lambda_S + 2\,\phi_{r,a\text{-resonance}} = \frac{\pi}{2} \tag{5.11}$$

where we made use of Eq. (2.29). From Eq. (5.11), the reference attitude to be tracked, $\phi_{r,a\text{-resonance}}$, is evaluated based on the observed values of Ω, ω, ν and λ_S as:

$$\phi_{r,a\text{-resonance}} = \frac{\Omega + \omega + \nu + \lambda_S + \frac{\pi}{2}}{2} \tag{5.12}$$

where ν is a fast-varying angle with $\dot{\nu}$ on the order of n ($\dot{\nu} \approx n$ for $e \ll 1$), the mean motion, while Ω, ω and λ_S, as previously mentioned, are slow-varying angles. We then conclude using Eq. (5.12), that the panel rotation rate magnitude is approximately:

$$\left| \frac{\mathrm{d}\phi_{r,a\text{-resonance}}}{\mathrm{d}t}(a) \right| \approx \frac{n}{2} = \sqrt{\frac{\mu}{a^3}}\frac{1}{2} \tag{5.13}$$

where we made use of $n = \sqrt{\mu/a^3}$. When tracking $\phi_{r,a\text{-resonance}}$, the spacecraft completes one rotation about every two orbits.

It is worth noting that, in theory, the $\sin(\widetilde{\psi}_{j,k})$-terms in Eq. (5.7) could also be made resonant by tracking $\widetilde{\psi}_{j,k} = \pm\frac{\pi}{2}$, as is the case when enforcing an e-resonance (see Eq. (5.5)). However, for small eccentricities, the magnitude of the effect is also small. These terms are therefore not considered for a ϕ-resonance in a. It is also important to mention that, as previously noted, $\widetilde{\psi}_{j,k}$ is slow-varying. The required rotation rate to make any of the $\sin(\widetilde{\psi}_{j,k})$-terms resonant is equally slow. Coupling between these and the $\sin(\psi_{j,k})$-terms is therefore not possible when enforcing a particular resonance in a. This conclusion is also valid regarding the impact of tracking $\psi_{j,k} = \pm\frac{\pi}{2}$, as is the case when enforcing an a-resonance (see Eq. (5.11)), on the $\sin(\psi_{j,k})$-terms in the eccentricity equation of motion, Eq. (5.2).

5.2 Implementation in D-SPOSE

The objective of this section is to numerically verify, using the high-fidelity propagator D-SPOSE [65]–[67], that a STRP-J_2-ϕ resonance in both e and a is achievable in a realistic orbital environment, and can lead to deorbitation of a plate-like spacecraft notwithstanding the simplifying assumptions made when deriving the resonance criteria in the previous section. We first describe how the tracking criteria for both an e-resonance and an a-resonance are computed in D-SPOSE. Then, the implementation of the tracking control law is outlined, and finally, numerical results confirming the validity of the resonance strategies for deorbitation are presented.

5.2.1 Tracking criteria computation

Recalling from Chapter 1, D-SPOSE explicitly propagates, with high accuracy, the coupled orbital-attitude dynamics of a body in space. Specifically, D-SPOSE propagates, for a fixed time step, the absolute position and velocity vectors expressed in $\mathcal{F}_{\text{ECI}}$ ($\mathbf{r}$ and $\mathbf{v}$) as well as the quaternion representation of $\mathcal{F}_b$'s orientation with respect to $\mathcal{F}_{\text{ECI}}$ ($\mathbf{q}$) and its absolute angular velocity expressed in the $\mathcal{F}_{\text{ECI}}$ frame ($\boldsymbol{\omega}_b$).

In order to implement a control law to track $\phi = \{\phi_{r,e\text{-resonance}}, \phi_{r,a\text{-resonance}}\}$ from Eqs. (5.6) and (5.12), the RAAN, Ω, and the argument of perigee, ω, must be computed from $\mathbf{r}$ and $\mathbf{v}$. However, the singularity of ω, when the eccentricity tends to 0, may become problematic [82]. To work around this issue, we employ the equinoctial elements presented in Appendix A. In particular, with the equinoctial parameters h and k computed from the values of $\mathbf{r}$ and $\mathbf{v}$, the reference angle in Eq. (5.6) for an e-resonance is rewritten as:

$$\phi_{r,e\text{-resonance}} = \frac{\text{arctan2}(h,k) + \lambda_S - \frac{\pi}{2}}{2} \tag{5.14}$$

where $\text{arctan2}(h,k) = \Omega + \omega$, and λ_S is obtained from the ephemeris for a specific epoch.

The reference angle in Eq. (5.12) for an a-resonance is rewritten in terms of the true longitude L as:

$$\phi_{r,a\text{-resonance}} = \frac{L + \lambda_S + \frac{\pi}{2}}{2} \tag{5.15}$$

where $L = \Omega + \omega + \nu$ is computed from $\mathbf{r}$ and $\mathbf{v}$ as per Curtis [69].

5.2.2 Tracking control law

In an unperturbed environment, the spacecraft's rotation, initially set to be about a single body-fixed axis, $\underset{\rightarrow}{z}_b$, can be parameterized by a single angle, ϕ, about that axis. The consideration of the complete 3-axis rotation of the spacecraft is, however, inevitable under the action of the perturbing torques, and a different representation of the reference attitude is required. We choose to use the Direction Cosine Matrix (DCM) and design the Proportional-Integral-Derivative (PID) control law accordingly. This yields the following expression for the computation of the control torques [81]:

$$\boldsymbol{\tau}_c = \mathbf{K}_p \left(\mathbf{C}_{b,r} - \mathbf{C}_{b,r}^{\mathsf{T}}\right)^{\mathrm{V}} - \mathbf{K}_d\, \boldsymbol{\omega}_b + \mathbf{K}_i \int_0^t \left(\mathbf{C}_{b,r} - \mathbf{C}_{b,r}^{\mathsf{T}}\right)^{\mathrm{V}} \mathrm{d}t \tag{5.16}$$

The notation $\mathbf{C}_{b,r}$ characterizes the DCM orientation of the body-fixed frame $\mathcal{F}_b$ relative to the reference attitude frame $\mathcal{F}_r$. The control gain matrices are such that $\mathbf{K}_p = \mathtt{diag}\{K_{p1}, K_{p2}, K_{p3}\}$, $\mathbf{K}_d = \mathtt{diag}\{K_{d1}, K_{d2}, K_{d3}\}$ and $\mathbf{K}_i = \mathtt{diag}\{K_{i1}, K_{i2}, K_{i3}\}$. The uncross operator $[\cdot]^V$ appearing in

Eq. (5.16) is defined for a skew-symmetric matrix as:

$$\begin{bmatrix} 0 & -a_3 & a_2 \\ a_3 & 0 & -a_1 \\ -a_2 & a_1 & 0 \end{bmatrix}^{\vee} = \begin{bmatrix} a_1 \\ a_2 \\ a_3 \end{bmatrix} \tag{5.17}$$

The attitude error between $\mathcal{F}_b$ and $\mathcal{F}_r$ is obtained as follows:

$$\mathbf{C}_{b,r} = \mathbf{C}_{b,\text{ECI}}\,\mathbf{C}_{\text{ECI},r} \tag{5.18}$$

The DCM representing the orientation of the inertial frame $\mathcal{F}_{\text{ECI}}$ relative to $\mathcal{F}_r$ is computed from the reference rotation angle ϕ_r with:

$$\begin{aligned} \mathbf{C}_{\text{ECI},r} &= \mathbf{C}_1(-\bar{\varepsilon})\,\mathbf{C}_3(-\phi_r) \\ &= \begin{bmatrix} \cos\phi_r & -\sin\phi_r & 0 \\ \cos\bar{\varepsilon}\sin\phi_r & \cos\bar{\varepsilon}\cos\phi_r & -\sin\bar{\varepsilon} \\ \sin\bar{\varepsilon}\sin\phi_r & \sin\bar{\varepsilon}\cos\phi_r & \cos\bar{\varepsilon} \end{bmatrix} \end{aligned} \tag{5.19}$$

where $\mathbf{C}_x$ for $x = \{1, 2, 3\}$ represents the principal x DCM and $\bar{\varepsilon} = 23.43°$ is the mean obliquity of the ecliptic. The DCM representing the attitude of the body frame $\mathcal{F}_b$ relative to $\mathcal{F}_{\text{ECI}}$ of Eq. (2.6) is computed from the quaternion $\mathbf{q} = [q_0\ \mathbf{q}_{1:3}^{\mathsf{T}}]^{\mathsf{T}}$ with $\mathbf{q}_{1:3} = [q_1\ q_2\ q_3]^{\mathsf{T}}$ using:

$$\mathbf{C}_{b,\text{ECI}} = \begin{bmatrix} q_0^2+q_1^2-q_2^2-q_3^2 & 2\,(q_1 q_2 + q_0 q_3) & 2\,(q_1 q_3 - q_0 q_2) \\ 2\,(q_1 q_2 - q_0 q_3) & q_0^2-q_1^2+q_2^2-q_3^2 & 2\,(q_0 q_1 + q_2 q_3) \\ 2\,(q_0 q_2 + q_1 q_3) & 2\,(q_2 q_3 - q_0 q_1) & q_0^2-q_1^2-q_2^2+q_3^2 \end{bmatrix} \tag{5.20}$$

The control torque of Eq. (5.16) is applied in the rotational equations of motion implemented in D-SPOSE for the propagation duration.

5.2.3 Numerical verification

With the attitude tracking controller defined, we can now verify that a STRP-J_2-ϕ resonance in e and in a can lead to the deorbitation, i.e., a final altitude lower than 200 km, of a plate-like spacecraft in a realistic environment. Propagations are thus carried out in D-SPOSE under the attitude control law of Eq. (5.16) for $\phi_r = \{\phi_{r,e\text{-resonance}}, \phi_{r,a\text{-resonance}}\}$ where the accelerations and torques due to the following perturbations are included:

- STRP: Eq. (2.14) for a constant radiation pressure[1] $P_r = \frac{1{,}361}{c}\ \frac{\text{N}}{\text{m}^2}$

[1] $c = 299{,}792{,}458$ m/s represents the speed of light

- gravitational field: EGM2008 up to degree and order 5
- drag: NRLMSISE-00 with constant equivalent planetary amplitude Ap = 15 and solar radio flux F10.7 cm = 140 sfu
- Earth shadow: geometric model with penumbra transition as implemented in D-SPOSE [65]

The above are the same perturbations as included in the simulations of Section 4.2, but in this section, the torques are also considered along with higher order geopotential terms.

The O2 orbit introduced in Chapter 4 is used to initialize the simulations, and the propagations are carried out using the spacecraft model of Chapter 4 as well. The orbital parameters of O2 are recalled in Table 5.1 (same orbit as in Table 4.2), and the parameters employed to model the panel are recalled in Table 5.2 (same parameters as in Table 4.1 for $\frac{A_{\text{eff}}}{m} = 1$ m^2/kg).

Table 5.1: Orbital initial conditions for O2 (as per Table 4.2)

	a (km)	e	i ($^\circ$)	β	Ω ($^\circ$)	ω ($^\circ$)	ν ($^\circ$)
O2	8,078	0.01	60	0.78	0	0	45

Table 5.2: Spacecraft model parameters

Parameter	Description	Value	Units
m	mass	23.166	kg
l_y	length along $\underset{\rightarrow}{y}_b$	3.3	m
l_z	length along $\underset{\rightarrow}{z}_b$	9	m
A_{nom}	nominal area	$l_y l_z = 29.7$	m^2
I_{xx}	moment of inertia in x	$\frac{m}{12}\left(l_y^2 + l_z^2\right) = 177.4$	kg.m^2
I_{yy}	moment of inertia in y	$\frac{m}{12} l_z^2 = 156.4$	kg.m^2
I_{zz}	moment of inertia in z	$\frac{m}{12} l_y^2 = 21.02$	kg.m^2
C_d	drag coefficient	2.2	-
σ_a	absorptivity	1	-
σ_{rs}	specular reflectivity	0	-
σ_{rd}	diffuse reflectivity	0	-
ε_f	front side emissivity	0.81	-
ε_b	back side emissivity	0.85	-

Recall that the O2 orbit is selected as a test case and is not associated with any specific known spacecraft. The spacecraft is modelled as a black body ($\sigma_a = 1$), but with the emissivity parameters of the GOES-8 solar panel ($\varepsilon_f = 0.81$ and $\varepsilon_b = 0.85$) [83]. Given these thermal properties, we conclude that the thermal radiation has a negligible effect on the spacecraft dynamics with $\frac{\varepsilon_f - \varepsilon_b}{\varepsilon_f + \varepsilon_b} = 0.0241$. The spacecraft dimensions are taken to be those of Starlink's solar panel; a 9 m x 3.3 m rectangular plate [31]. The propagation is initialized for a rotation angle $\phi = 0°$ at epoch T1: 2000-01-01T00:00:00. It is carried out with a fixed time step of 30 sec, and $\mathbf{K}_p = 0.0047\,\mathbf{I}_3$, $\mathbf{K}_d = 1.56\,\mathbf{I}_3$ and $\mathbf{K}_i = 3.90\text{e-}5\,\mathbf{I}_3$ as control gains. A small time step of 30 sec is required due to the attitude modelling and attitude control during the propagation.

The results for the orbital time responses obtained when implementing $\phi_r = \{\phi_{r,e\text{-resonance}}, \phi_{r,a\text{-resonance}}\}$ are presented in Fig. 5.1 (purple curves for e-resonance and green curves for a-resonance) where they are compared to the equivalent results of Fig. 4.8 (yellow curves) obtained for a constant $\dot{\phi} = -3.9645\text{e-}06°/\text{sec}$. It is noted that these latter results were obtained by neglecting perturbing torques and higher geopotential terms. The results for the attitude time responses are presented in Figs. 5.2 and 5.3 for the eccentricity and the semi-major axis resonances respectively.

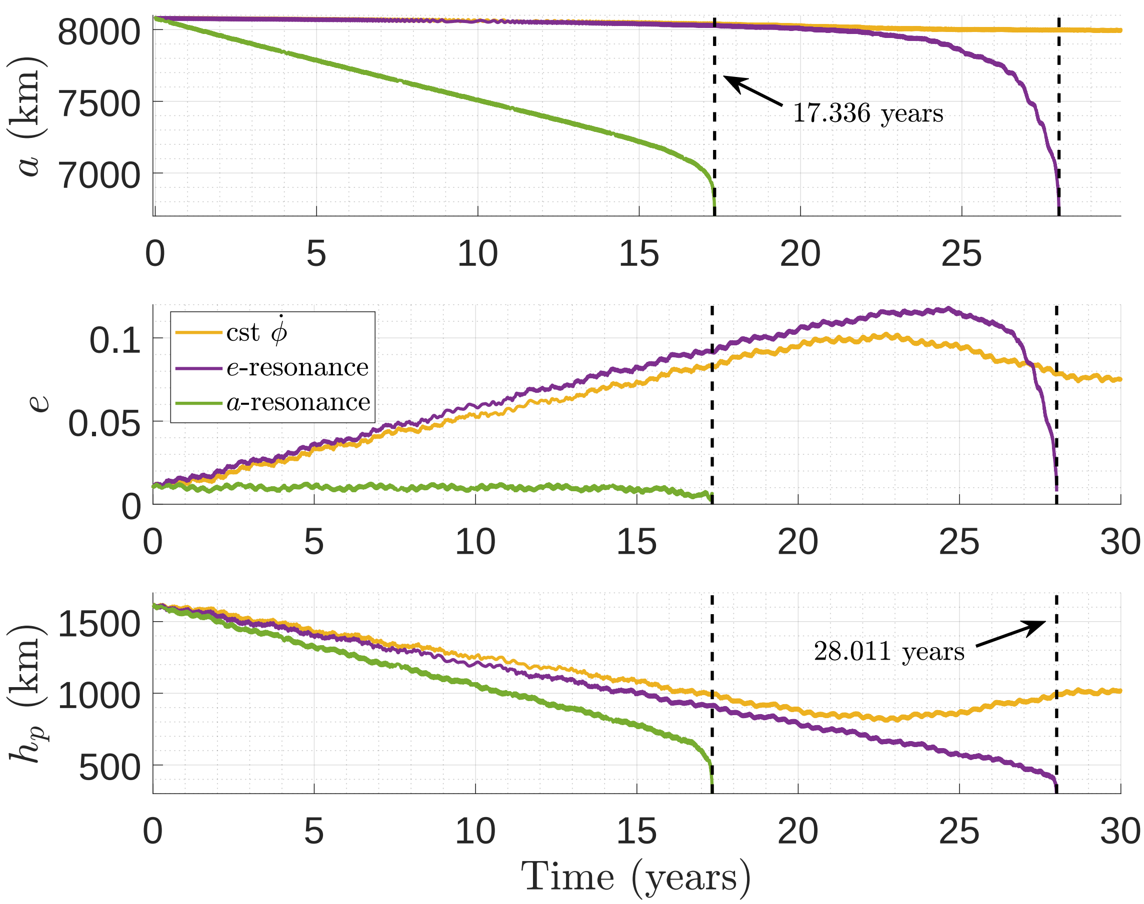

Figure 5.1: Orbital time response with tracking of $\phi_r = \{\phi_{r,e\text{-resonance}}, \phi_{r,a\text{-resonance}}\}$ when propagating O2 in D-SPOSE (purple and green curves) under STRP, J_2 and drag perturbing accelerations and torques for a time step of 30 sec compared to the results with constant $\dot{\phi}$ of Fig. 4.8 (yellow curves)

From Fig. 5.1, we can conclude that for the e-resonance (purple curves), a complete deorbitation is achievable within 28 years and 5 days. Also, at a threshold perigee altitude of around 600 km which is reached after 24 years, the drag perturbation becomes the driving force toward

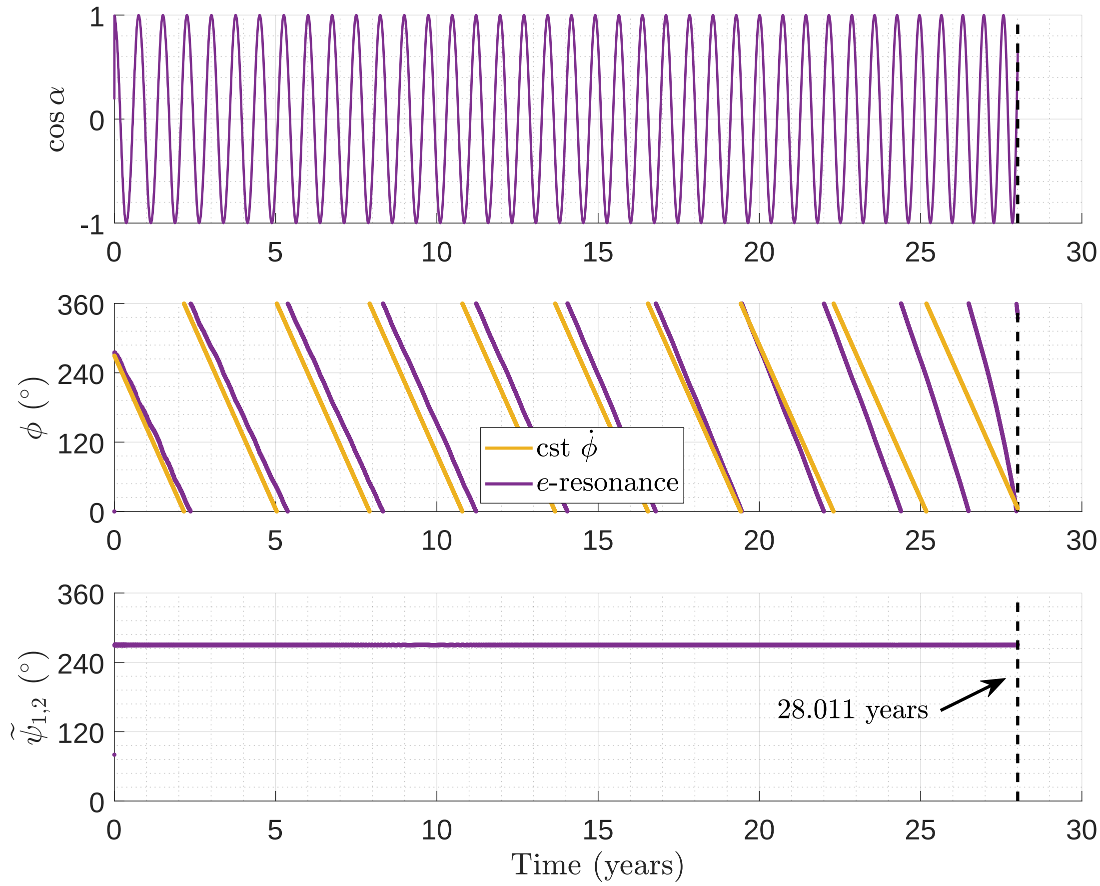

Figure 5.2: Attitude and resonant angle $\widetilde{\psi}_{1,2}$ time responses when propagating O2 in D-SPOSE with tracking of $\phi_r = \phi_{r,e\text{-resonance}}$ under STRP, J_2 and drag perturbing accelerations and torques for a time step of 30 sec with $\mathbf{K}_p = 0.006\mathbf{I}_3$, $\mathbf{K}_d = 2\mathbf{I}_3$, $\mathbf{K}_i = 5\text{e-}5\mathbf{I}_3$ compared to attitude response for $\dot{\phi} = -3.9645\text{e-}06°/\text{sec}$ (yellow curve)

the spacecraft's re-entry, as shown by the drastic decrease in semi-major axis after this time. We can also observe that, in the region where the drag effect is small and the eccentricity dynamics is mainly governed by the STRP disturbance ($t \in [0, 24]$ yr), the amplitude of the eccentricity variation is not bounded. This is in line with the resonant $\widetilde{\psi}_{1,2}$ angle response of Fig. 5.2 remaining in the vicinity of 270° ($-\frac{\pi}{2}$) throughout the propagation. From Fig. 5.2, we further conclude that, for the e-resonance with ϕ tracking, the slight variation in the rotation angle rate ($\dot{\phi}$, the slope of the ϕ response) is sufficient to deorbit the spacecraft completely, and that, with only a small control torque τ_c on the order of 10^{-5} N·m.

Fig. 5.1 also shows that when enforcing full attitude control to track $\phi_r = \phi_{r,a\text{-resonance}}$ (green curves) on a spacecraft initially in O2 and subject to perturbing accelerations and torques, the STRP-J_2-ϕ resonance in semi-major axis can lead to deorbitation within 17 years and 123 days. This is about 1.6 times faster than when tracking $\phi_r = \phi_{r,e\text{-resonance}}$ under the same conditions (purple curves). Moreover, Fig. 5.3 confirms the result of Eq. (5.13), stating that the magnitude

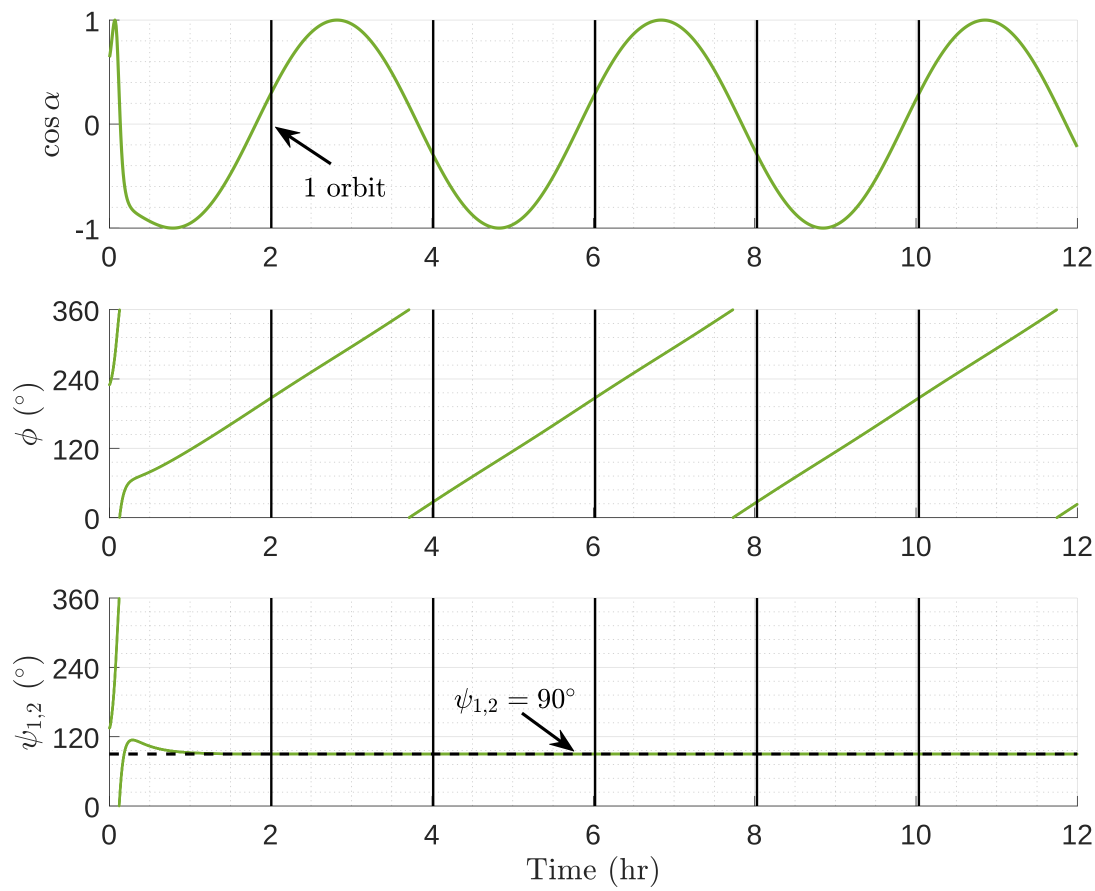

Figure 5.3: Attitude and resonant angle $\psi_{1,2}$ time responses when propagating O2 in D-SPOSE with tracking of $\phi_r = \phi_{r,a\text{-resonance}}$ under STRP, J_2 and drag perturbing accelerations and torques for a time step of 30 sec with $\mathbf{K}_p = 0.006\,\mathbf{I}_3$, $\mathbf{K}_d = 2\,\mathbf{I}_3$, $\mathbf{K}_i = 5\text{e-}5\,\mathbf{I}_3$. Note, the horizontal scale is in hours

of the rate of change of the attitude angle ϕ is half the orbital rate. Indeed the panel executes a complete revolution about its $\underset{\rightarrow}{z}_b$ axis in two orbital periods as indicated by the vertical solid black lines in the figure.

In the following section, we present an estimation method for the maximum descent rate associated with the STRP-J_2-ϕ resonance in eccentricity and semi-major axis.

5.3 Resonance descent rate estimation

The fundamental idea of this study is to exploit the resonance effect to increase the orbital eccentricity or decrease the semi-major axis of a spacecraft initially located at a high LEO altitude (>1000 km), with the ultimate goal of lowering its altitude to a threshold altitude of 600 km, at which, the atmosphere is sufficiently thick for the atmospheric drag to deorbit the spacecraft in a short period of time—few years or even months depending on the ballistic coefficient and the environment. In this context, as already mentioned, the parameter of interest for the deorbitation of a spacecraft is its altitude, or more specifically the altitude of its orbit perigee h_p—the point of the orbit at which the magnitude of the atmospheric drag is the most significant. The perigee altitude is related to the eccentricity and semi-major axis through:

$$h_p = a\,(1-e) - R_e \tag{5.21}$$

Its time rate can thereby be expressed as:

$$\frac{\mathrm{d}h_p}{\mathrm{d}t} = (1-e)\,\frac{\mathrm{d}a}{\mathrm{d}t} - a\,\frac{\mathrm{d}e}{\mathrm{d}t} \tag{5.22}$$

In LEO, only orbits with low eccentricities are realistic, typically $e < 0.2$, thus Eq. (5.22) can be approximated by:

$$\frac{\mathrm{d}h_p}{\mathrm{d}t} \approx \frac{\mathrm{d}a}{\mathrm{d}t} - a\,\frac{\mathrm{d}e}{\mathrm{d}t} \tag{5.23}$$

Descent rate for *e*-resonance: The proposed solution aims at exploiting the STRP-J_2-ϕ resonance in e in the region where drag effects are either small or almost non-existent. We defined this region as any altitude above 600 km, and we assume that, in this zone, the semi-major axis changes slowly enough so that $\dot{a} \approx 0$, yielding the estimated perigee descent rate from Eq. (5.23):

$$\dot{h}_{p,e\text{-resonance}} \approx -a\,\dot{e} \tag{5.24}$$

for small eccentricity orbits. Eq. (5.24) can be further approximated for a $(1,2)$-resonance with $\widetilde{\psi}_{1,2} = -\frac{\pi}{2}$ by making use of Eq. (5.3). Dropping the e^2-term and using $n = \sqrt{\mu/a^3}$, the altitude of perigee for a panel subject to a $(1,2)$-resonance in e thus varies at a rate of approximately:

$$\dot{h}_{p,e\text{-resonance}} \approx -\frac{3}{2}\,C_{\mathrm{STRP}}\sqrt{\frac{a^3}{\mu}}\,\mathcal{T}_1(\varepsilon, i)\,C_2 \tag{5.25}$$

where we recall $C_{\mathrm{STRP}} = P_r\,\beta\,\frac{A_{\mathrm{nom}}}{m}$, with the constant radiation pressure $P_r = \frac{1{,}361}{299{,}792{,}458}\ \frac{\mathrm{N}}{\mathrm{m}^2}$.

Fig. 5.4 illustrates Eq. (5.25) in terms of a and i for a $(1,2)$-resonance, $\beta = 1$ and $\frac{A_{\mathrm{nom}}}{m}\,C_2 = 1\,\frac{\mathrm{m}^2}{\mathrm{kg}}\,C_{2,\mathrm{bb}}$ where $C_{2,\mathrm{bb}} = 0.2122$ (see Eq. (2.30) for $\sigma_a = 1$) is the optical coefficient of a black body. From the results in Fig. 5.4, the maximum descent rate in LEO can be approximately bounded, for an e-resonance, by:[2]

$$\dot{h}_{p,e\text{-resonance}} \in [-53,\,-19]\ {}^{\mathrm{km}}\!/\!_{\mathrm{yr}} \times \beta\,\frac{A_{\mathrm{nom}}}{m}\,({}^{\mathrm{m}^2}\!/\!_{\mathrm{kg}})\,\frac{C_2}{C_{2,\mathrm{bb}}} \tag{5.26}$$

[2]Based on Eq. (2.30), $1 \le \frac{C_2}{C_{2,\mathrm{bb}}} \le 4$

It is important to note that $\mathcal{T}_2(\varepsilon, i) = \mathcal{T}_1(\varepsilon, \pi - i)$, therefore, if $i > 90°$, the maximum descent rate is obtained for a $(2,2)$-resonance, in which case, it can be deduced from Fig. 5.4 by substituting $\pi - i$ for i.

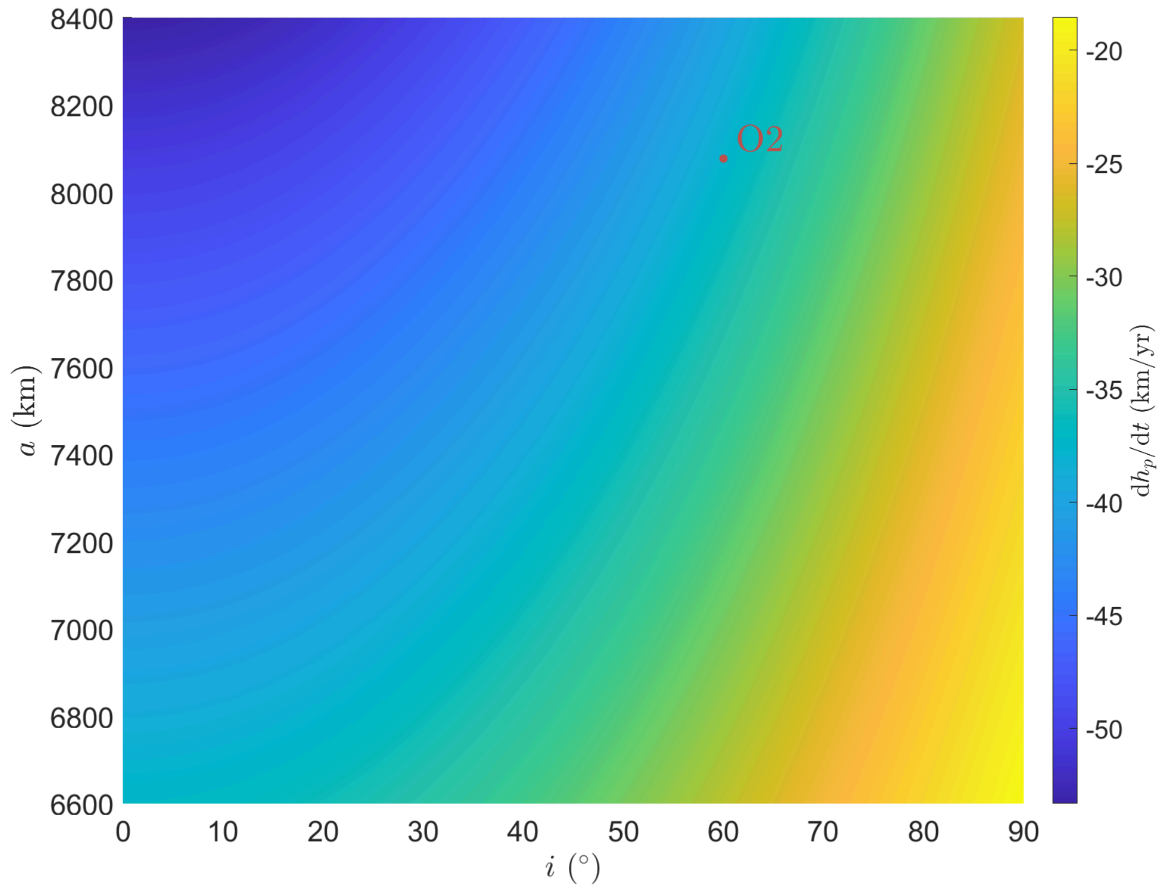

Figure 5.4: Estimated perigee descent rate given by Eq. (5.25) as a function of i and a for a $(1,2)$-resonance with $\beta = 1$ and $\frac{A_{\mathrm{nom}}}{m} C_2 = 1\,\frac{\mathrm{m}^2}{\mathrm{kg}}\, C_{2,\mathrm{bb}}$

Descent rate for *a*-resonance: As reflected by the simulation results of Section 5.2.3, when exploiting the a-resonance for deorbitation, the eccentricity remains almost constant. It is therefore reasonable to assume $\dot{e} \approx 0$, yielding the estimated perigee descent rate from Eq. (5.23):

$$\dot{h}_{p,a\text{-resonance}} \approx \dot{a} \tag{5.27}$$

for small eccentricity orbits. Similarly as for Eq. (5.24), Eq. (5.27) can be approximated for a $(1,2)$-resonance with $\psi_{1,2} = \frac{\pi}{2}$ by making use of Eq. (5.7):

$$\dot{h}_{p,a\text{-resonance}} \approx -2C_{\mathrm{STRP}}(1-e)\sqrt{\frac{a^3}{\mu}}\,\mathcal{T}_1(\varepsilon, i)\, C_2 \tag{5.28}$$

Comparing Eq. (5.28) to Eq. (5.25), we find that, for identical initial conditions, the expected descent rate of h_p when exploiting a a-resonance is about $\frac{4}{3}$ times larger than when exploiting a e-resonance. We can thus deduce from Fig. 5.4 the boundaries on the perigee altitude descent rate for an a-resonance in LEO. These are:

$$\dot{h}_{p,a\text{-resonance}} \in [-71, -26]\ {}^{\mathrm{km}}\!/\!_{\mathrm{yr}} \times (1-e)\,\beta\,\frac{A_{\mathrm{nom}}}{m}\,({}^{\mathrm{m}^2}\!/\!_{\mathrm{kg}})\,\frac{C_2}{C_{2,\mathrm{bb}}} \tag{5.29}$$

The $\dot{h}_p$ estimates obtained here indicate that the feasibility of deorbitation within a reasonable time frame depends on the spacecraft $\frac{A_{\mathrm{nom}}}{m}$ and optical properties, and which strategy is employed—the e-resonance or the a-resonance. It is important to mention that the results obtained in this section serve as an approximation of the descent rate, and hold only under the single resonance assumption. In the following section, we evaluate different scenarios associated with several orbits for which deorbitation is achieved within the 25-year IADC guideline.

5.4 Deorbitation test cases with ϕ-tracking

In this section, the three cases of Table 5.3 are simulated to illustrate how the deorbitation solutions exploiting the STRP-J_2-ϕ resonances in e and a can be used to fully deorbit a spacecraft within 25 years, given different initial conditions and spacecraft properties. For each orbit case, the two methods are defined with the corresponding reference angles, in particular, $\phi_r = \{\phi_{r,e\text{-resonance}}, \phi_{r,a\text{-resonance}}\}$ given by Eqs. (5.14) and (5.15). The propagations are initialized for a rotation angle $\phi = 0°$ at epoch T1: 2000-01-01T00:00:00. The model parameters of Table 5.2 are still used but with the masses and optical coefficients as per last columns of Table 5.3.[3] The control gains are adjusted based on the spacecraft mass m for each propagation case as:

$$\mathbf{K}_p = 0.006\,\frac{m}{29.7\ \mathrm{kg}}\,\mathbf{I}_3 \quad , \quad \mathbf{K}_d = 2\,\frac{m}{29.7\ \mathrm{kg}}\,\mathbf{I}_3 \quad , \quad \mathbf{K}_i = 5\text{e-}5\,\frac{m}{29.7\ \mathrm{kg}}\,\mathbf{I}_3 \tag{5.30}$$

Table 5.3: Orbital initial conditions and associated spacecraft model parameters

	a (km)	e	i (°)	Ω (°)	ω (°)	ν (°)	m (kg)	$(\sigma_{rs}, \sigma_{rd}, \sigma_a)$
O3	7,200	0.001	20	0	0	45	227	(0.16, 0.25, 0.59)
O4	8,400	0.001	20	0	0	45	29.7	(1, 0, 0)
O5	7,400	0.001	45	0	0	45	56	(0, 0, 1)

It is noted that the O3 parameters in Table 5.3 were chosen to represent a plausible case scenario for a mega-constellation satellite:

- initial altitude in mid-LEO, about 800 km;

[3] The parameters $I_{xx} = \frac{m}{12}\left(l_y^2 + l_z^2\right)$, $I_{yy} = \frac{m}{12} l_z^2$ and $I_{zz} = \frac{m}{12} l_y^2$ are adjusted as well as per the new value of m.

- realistic optical properties for a solar panel, in this case, the mean values of Envisat's solar array [84];
- realistic area and mass properties, taken to be those of the first Starlink satellites: $m = 227$ kg and $A_{\text{nom}} = 29.7\ \text{m}^2$ [31].

The nominal area-to-mass ratio and optical coefficients of case O4 is representative of a spacecraft equipped with a perfectly reflective area-augmentation device ($\frac{A_{\text{nom}}}{m} = 1\ \text{m}^2/\text{kg}$ and $\sigma_{rs} = 1$). The case of O5 represents nothing in particular: it was selected as an intermediate test case.

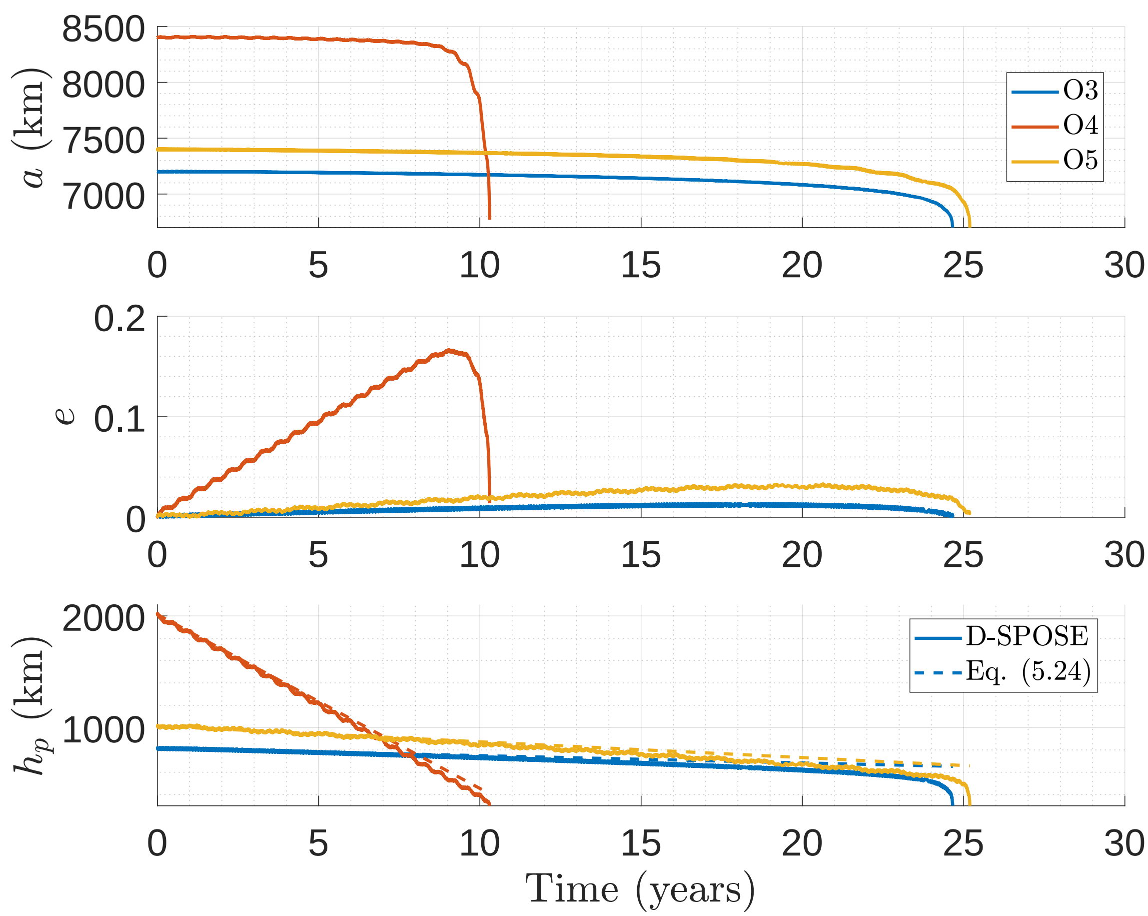

Figure 5.5: Propagation results for cases O3 to O5 of Table 5.3 in D-SPOSE with tracking of $\phi_{r,e\text{-resonance}}$ under STRP, J_2 and drag perturbing accelerations and torques for a time step of 30 sec

Figs. 5.5 and 5.6 show the propagation results for cases O3 to O5 of Table 5.3 exploiting a STRP-J_2-ϕ resonance in e and in a respectively. The slopes of the dashed lines in Figs. 5.5 and 5.6, $\dot{h}_{p,e\text{-res.}}$ from Eq. (5.25) and $\dot{h}_{p,a\text{-res.}}$ from Eq. (5.28) respectively, are given in Table 5.4 along with the respective deorbitation times for all three cases. We make a note that the initial value of semi-major axis, $a = a(t = 0)$, was used to approximate $\dot{h}_{p,e\text{-res.}}$, while a median value of $a = \frac{1}{2}(a(t = 0) + a_{\text{lim}})$ was used to approximate $\dot{h}_{p,a\text{-res.}}$ with $a_{\text{lim}} = 600\ \text{km} + R_e$ representing the

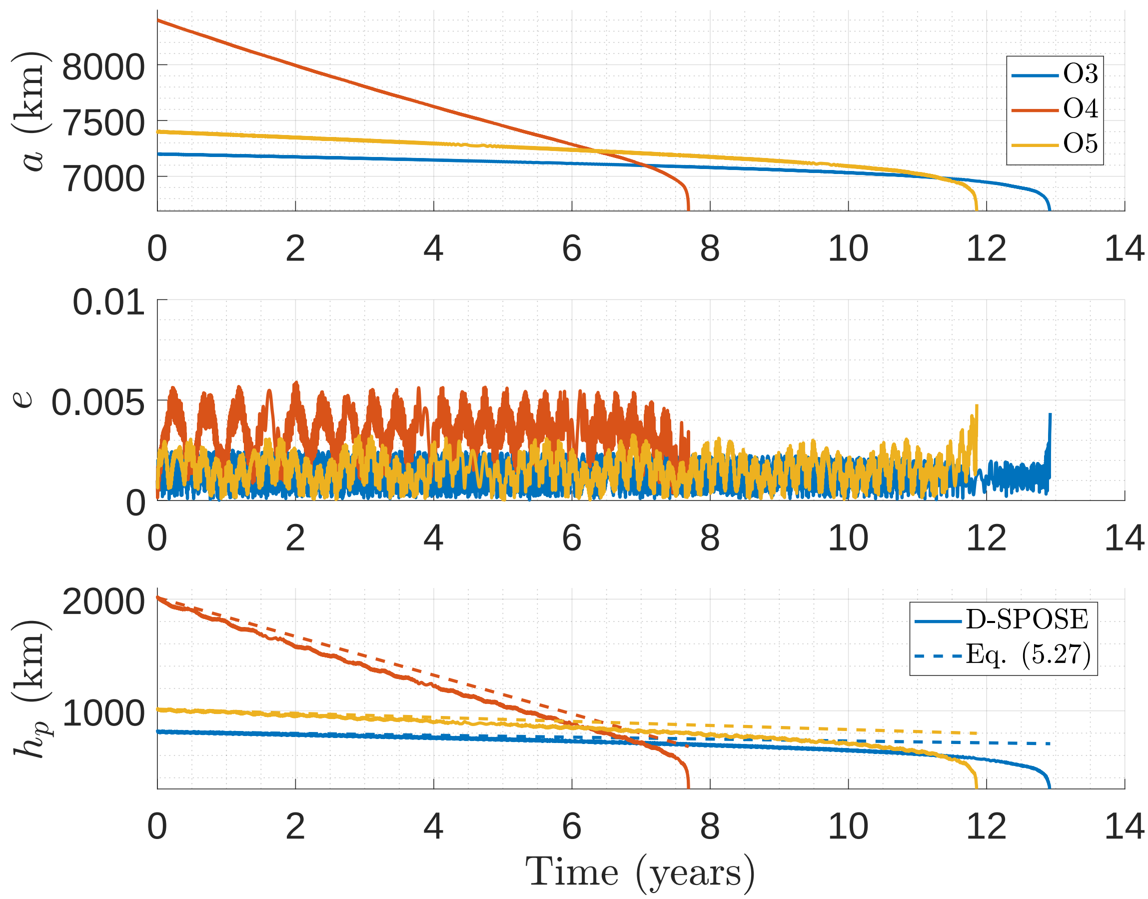

Figure 5.6: Propagation results for cases O3 to O5 of Table 5.3 in D-SPOSE with tracking of $\phi_{r,a\text{-resonance}}$ under STRP, J_2 and drag perturbing accelerations and torques for a time step of 30 sec

Table 5.4: Estimated descent rate (from Eqs. (5.25) and (5.28)) and deorbitation times for the propagations of the three initial orbits and spacecraft properties of Table 5.3

	β	$\frac{C_2}{C_{2,\text{bb}}}$	$\frac{A_{\text{nom}}}{m}$ (kg/m²)	$\dot{h}_{p,e\text{-res.}}$ (km/yr)	$\dot{h}_{p,a\text{-res.}}$ (km/yr)	$T_{e-\text{res.}}$ (yr)	$T_{a-\text{res.}}$ (yr)
O3	0.67	1.873	0.13	-6.66	-8.67	24.7	12.9
O4	0.74	4	1.00	-153	-179	10.3	7.69
O5	0.73	1	0.53	-14.6	-18.6	25.2	11.9

limit at which drag becomes the driving force towards the re-entry. This is justified by the fact that, in the region where the atmospheric drag is negligible—altitudes above 600 km—the semi-major axis remains almost constant for an e-resonance, while it decreases at an almost constant rate for an a-resonance.

The results of Figs. 5.5 and 5.6 confirm that the exploitation of the STRP-J_2-ϕ single resonance can enable the deorbitation of the spacecraft within 25 years for certain orbits and spacecraft properties. The results confirm the validity of $\dot{h}_{p,e\text{-res.}}$ from Eq. (5.25) and $\dot{h}_{p,a\text{-res.}}$ from Eq. (5.28) (dashed lines) to approximate the descent rate of a plate-like spacecraft subject to a ϕ-resonance above 600 km. We can therefore extrapolate from these results and conclude that the higher the area-to-mass ratio, $\frac{A_{\text{nom}}}{m}$, and/or the optical coefficient, C_2, the faster the decay. This was highlighted by the considerably steeper descent—both for the e-resonance and the a-resonance—of the 1 m^2/kg perfectly reflective spacecraft of the O4 case in comparison to that of the O3 and O5 cases. We can further confirm that, still under single-resonance conditions, the descent rate for a semi-major axis resonance is considerably faster than for an eccentricity resonance.

The results presented in this section are all obtained for a spacecraft subject to a single resonance. Coupling is however possible and specifically arises between the $(1,k)$ and the $(2,-k)$-terms for any Sun-synchronous orbit. In the following section, we investigate the impact of such coupling between two e-resonant terms.

Deorbitation from Sun-synchronous orbit

A Sun-synchronous orbit is defined as an orbit for which $\dot{\Omega} = \dot{\lambda}_S$. Since $\dot{\Omega}$ is mainly governed by the secular effect of the Earth's second zonal harmonics, an orbit is Sun-synchronous when:

$$\dot{\Omega}_{J_2} = -\frac{3}{2}\frac{J_2 R_e^2 n}{a^2 (1-e^2)^2} \cos i = \dot{\lambda}_S \tag{5.31}$$

The expression for $\dot{\Omega}_{J_2}$ comes from Appendix B. For Sun-synchronous orbits, the commensurability condition of Eq. (5.4) for a $(1,k)$-resonance and a $(2,-k)$-resonance become identical:

$$\frac{\mathrm{d}\widetilde{\psi}_{2,-k}}{\mathrm{d}t} = -\dot{\omega} + k\dot{\alpha} = \frac{\mathrm{d}\widetilde{\psi}_{1,k}}{\mathrm{d}t} = 0 \tag{5.32}$$

Since the commensurability condition is met for both the $(1,k)$-term and the $(2,-k)$-term, both are resonant and both are likely to have a non-negligible long-term effect. If $\widetilde{\psi}_{1,k} = -\frac{\pi}{2}$ is tracked, as in Eq. (5.5) for a $(1,2)$-resonance in eccentricity, then the second resonant angle takes the following value:

$$\widetilde{\psi}_{2,-k} = 2\,(\Omega - \lambda_S) - \frac{\pi}{2} \tag{5.33}$$

We recall that the impact of a resonant angle on the eccentricity rate is modulated by the sine function of this resonant angle, as can be gathered from Eq. (5.3). We thus conclude from Eq. (5.33) that, when tracking $\widetilde{\psi}_{1,k} = -\frac{\pi}{2}$, the contribution of the second resonant term, the $(2,-k)$-term, depends on the RAAN, Ω, and the longitude of the Sun λ_S. In light of this, we propagate, under the exact same conditions as before, the motion of a $\frac{A_{\text{nom}}}{m} = 1$ m^2/kg black body ($\sigma_a = 1$) initially in the Sun-synchronous orbits of Table 5.5, starting at epoch T1: 2000-01-01T00:00:00 ($\lambda_S = 280.9°$) and rotation angle $\phi = 0°$. The propagations are carried out for a $(1,2)$-resonance in eccentricity by tracking $\phi_{r,e\text{-resonance}}$ as given in Eq. (5.14). Based on the values of $\psi_{2,-2}$, computed with Eq. (5.33) and given in Table 5.5 for the initial conditions of cases O6.1 to O6.3, the resonant-$(2,-2)$ term is expected to either contribute to the increase in eccentricity generated by the $(1,2)$-resonance (case

O6.3, with $\sin(270°) < 0$), oppose it (case O6.1, with $\sin(68.2°) > 0$), or leave it unaffected (case O6.2, with $\sin(0°) = 0$). This will be further discussed shortly.

Table 5.5: Orbital initial conditions for a Sun-synchronous orbit with varied RAAN starting at epoch T1: 2000-01-01T00:00:00 ($\lambda_S = 280.9°$)

	a (km)	e	i (°)	Ω (°)	ω (°)	ν (°)	$\widetilde{\psi}_{1,2}$ (°)	$\widetilde{\psi}_{2,-2}$ (°)
O6.1	8,059	0.001	103	0	0	45	270	68.2
O6.2	8,059	0.001	103	325.9	0	45	270	0
O6.3	8,059	0.001	103	280.9	0	45	270	270

Figs. 5.7 and 5.8 show the orbital time responses for a, e and h_p, and the resonant angle time responses for $\widetilde{\psi}_{1,2}$ and $\widetilde{\psi}_{2,-2}$ to be compared to the eccentricity response. We gather from Fig. 5.8 that, although the initial settings are such that $\dot{\widetilde{\psi}}_{2,-2} = 0$, this condition does not firmly hold as the orbit of the spacecraft evolves under the action of external perturbations. Since the tracking law is set to enforce the (1,2)-resonance, these perturbations cause the (2,-2) resonant angle $\widetilde{\psi}_{2,-2}$ to drift over time. We can also observe from the angle responses of case O6.1 (blue curves) that it is difficult to track precisely $\widetilde{\psi}_{1,2} = -\frac{\pi}{2}$ when the eccentricity is almost null.

Furthermore, for the particular case of O6.1, because $\sin(\widetilde{\psi}_{2,-2}) > 0$ initially, and because $i = 103° > 90°$ and $\sigma_a = 1$, $C_{-2}\mathcal{T}_2 > C_2\mathcal{T}_1$ (see Eqs. (2.30) and (2.23)); the contribution of the $\sin(\widetilde{\psi}_{2,-2})$-term to the decrease in eccentricity is thus stronger than the contribution of the $\sin(\widetilde{\psi}_{1,2})$-term to its increase leading e to remain near zero all through the first 18 years of the propagation. The effect reduces as $\sin(\widetilde{\psi}_{2,-2})$ diminishes, and is reversed when $\widetilde{\psi}_{2,-2}$ crosses the 180° threshold at which point $\sin(\widetilde{\psi}_{2,-2})$ becomes negative. Similar conclusions to these presented for O6.1 can be drawn from the results of cases O6.2 (orange curves) and O6.3 (yellow curves) based on the values of $\sin(\widetilde{\psi}_{2,-2})$ over time. Particular attention must thus be paid to the initial conditions for Ω and λ_S when evaluating the possibility of exploiting STRP-J_2-ϕ resonances for deorbitation. Indeed, depending on these, the effect could be completely cancelled or, on the contrary, it could be greatly enhanced.

The same conclusions can be drawn for an a-resonance; however, because of the larger change in semi-major axis when exploiting this resonance, the rate of the second resonant angle—$\dot{\psi}_{2,-2}$ in the case of an a-resonance—diverges more quickly from 0, thus breaking the commensurability condition.

5.5 Concluding Remarks

To conclude, we demonstrated in this chapter that, it is feasible to deorbit a spacecraft subject to STRP, J_2 and drag perturbations, by generating a resonance either in eccentricity or semi-major axis. This was achieved by tracking ϕ_r to enforce: $\widetilde{\psi}_{1,2} = -\frac{\pi}{2}$ for an e-resonance, or $\psi_{1,2} = \frac{\pi}{2}$ for an a-resonance. This particular strategy was shown to overcome the limitation on the reso-

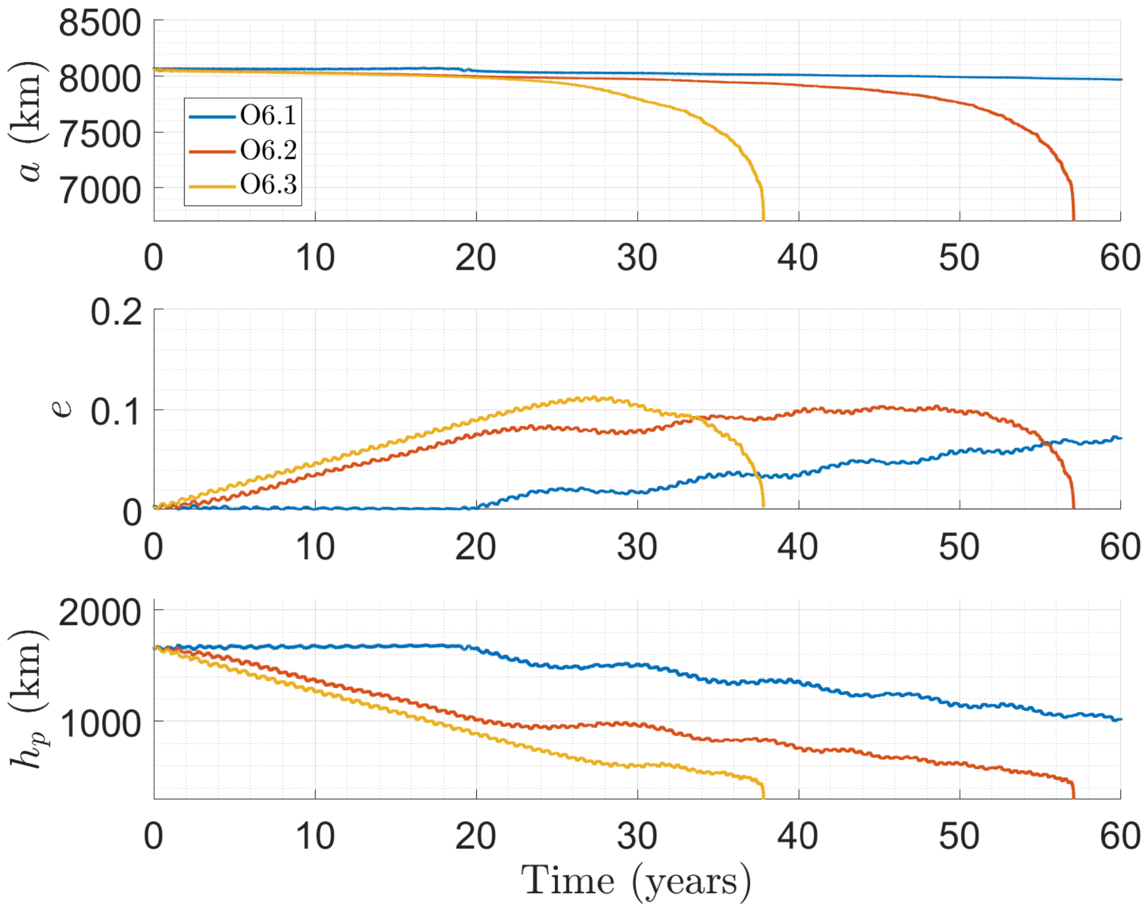

Figure 5.7: Orbital results over for cases O6.1 to O6.3 of Table 5.5 in D-SPOSE with tracking of $\phi_{r,e\text{-resonance}}$ under STRP, J_2 and drag perturbing accelerations and torques for a time step of 30 sec

nance strength and amplitude when $\dot{\phi}$ is constant, therefore allowing the spacecraft to descend to a sufficiently low altitude (~ 600 km) to be deorbited by the action of atmospheric drag.

These findings were also verified in a realistic environment modelled by D-SPOSE where the full dynamics was propagated while including STRP, geopotential and atmospheric perturbing accelerations as well as torques. The PID control law employed was shown to be robust to perturbing torques. The deorbitation strategy suggested was applied to four distinct simulation scenarios from which we can conclude that, in order to deorbit a satellite from a high LEO altitude, the nominal area-to-mass ratio must be significantly high $\frac{A_{\text{nom}}}{m} > 0.5$ m^2/kg, i.e., the spacecraft must be equipped with an area-augmentation device.

Finally, investigation of the special case of a spacecraft in a Sun-synchronous orbit for which there is an inherent coupling between the $(1,k)$-resonance and the $(2,-k)$-resonance highlighted the importance of the initial RAAN and longitude of the Sun values on the secular evolution of the eccentricity for this particular scenario, whereas these are of small significance for a single-resonance scenario.

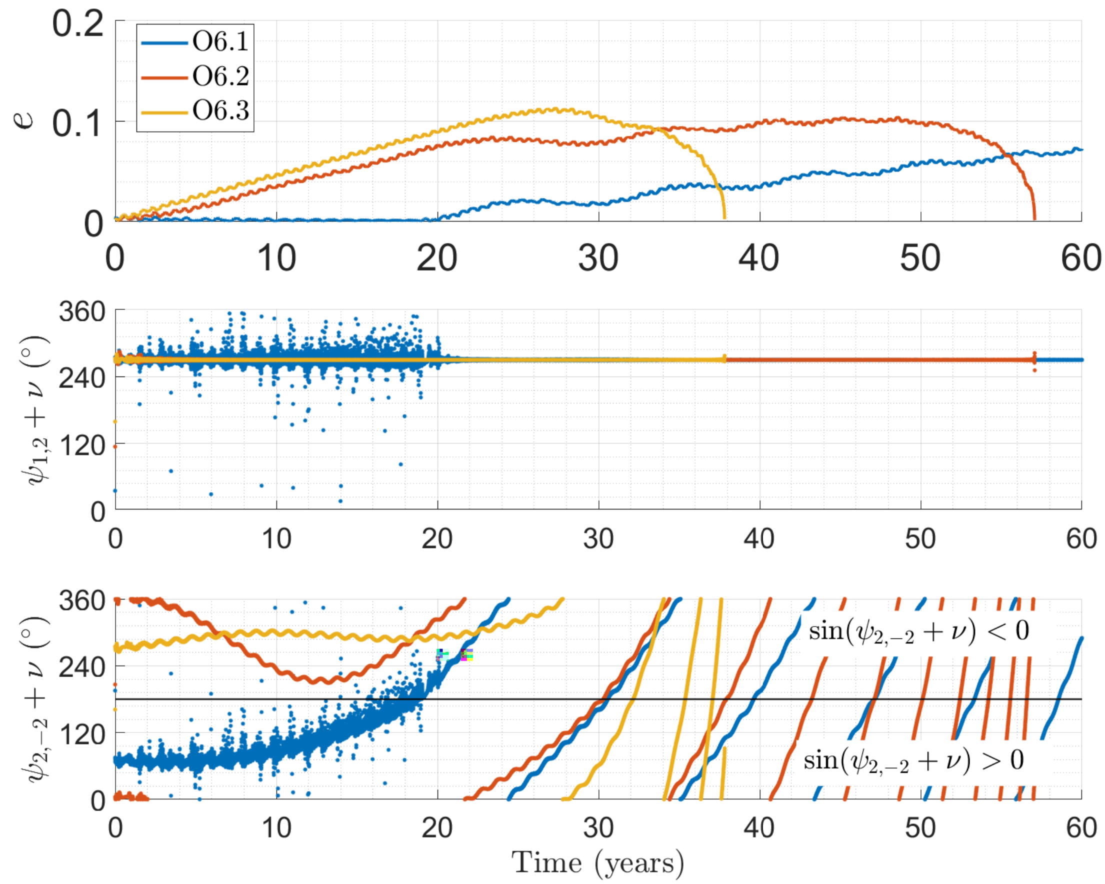

Figure 5.8: Resonant angles results for cases O6.1 to O6.3 of Table 5.5 in D-SPOSE with tracking of $\phi_{r,e\text{-resonance}}$ under STRP, J_2 and drag perturbing accelerations and torques for a time step of 30 sec

Chapter 6

Comparison to Other Deorbitation Strategies

In Chapter 5, we demonstrated that it is possible to generate a resonance of considerable strength either in semi-major axis or eccentricity, referred to as the ϕ-resonance, for a plate-like spacecraft, in arbitrary orbit. This requires adopting a specific rotational motion of the spacecraft, i.e., prescribing the attitude angle ϕ appropriately which is enforced through controlled rotational motion.

Other end-of-life strategies involving rotating the spacecraft have also been suggested in the literature as potential solutions for the deorbitation of plate-like spacecraft. Borja and Tun [49] proposed the use of a bang-bang reorientation scheme to maximize the global effect of the STRP on the semi-major axis decrease by either minimizing or maximizing the Sun exposed surface appropriately. Colombo et al. [50] developed a similar strategy to increase eccentricity. Solutions aiming to change the orbit's semi-major axis were also developed for spacecraft equipped with a perfectly reflective solar sail. One may refer to [85], [86] for more information, specifically on end-of-life strategies proposed for solar sails.

To assess the effectiveness of the deorbitation strategies proposed in Chapter 5, the solutions are evaluated and a comparison is made to the two different deorbitation strategies proposed by Colombo et al. [50], and Borja and Tun [49] for five distinct use cases. A computation of the energy budget is finally performed to evaluate and compare the feasibility of deorbitation strategies exploiting the semi-major axis variation; these are shown to be much more efficient than those exploiting the eccentricity variation when not in the vicinity of a deorbitation corridor.

6.1 Bang-bang approaches to deorbitation exploiting STRP

In this section, we present two alternate deorbitation methods which are based on a similar principle: to prescribe the attitude of a plate-like spacecraft, or a sail, to amplify the secular effect of the STRP on the altitude. The first method from [50], referred to here as e-bang-bang, exploits the STRP to increase the eccentricity by employing a bang-bang approach, or on-off approach, to attitude change. The second scheme from [49], a-bang-bang, also uses a bang-bang strategy, but to reduce the semi-major axis instead. We briefly summarize both solutions and derive the reference attitude angle using the same formalism as in Chapter 5.

6.1.1 e-Bang-bang

Colombo et al. [50] propose to modulate the projected effective area-to-mass ratio $\left(\frac{A_{\text{eff}}}{m}\cos\alpha,\right.$ with $\left.\frac{A_{\text{eff}}}{m}\text{ as per Eq. (2.71)}\right)$ either to maximize or to minimize the SRP acceleration depending on its effect on the eccentricity. For consistency, we also account for the thermal acceleration in our implementation of their deorbitation solution. The logic for the modulation of the STRP acceleration magnitude is therefore defined as:

$$a_{\text{STRP}} = \begin{cases} a_{\text{STRP,max}} & \text{if} \quad \texttt{sign}\left(\left.\dfrac{\mathrm{d}\bar{e}}{\mathrm{d}t}\right|_{\text{STRP}}\right) \geq 0 \\ a_{\text{STRP,min}} & \phantom{\text{if}} \quad \texttt{sign}\left(\left.\dfrac{\mathrm{d}\bar{e}}{\mathrm{d}t}\right|_{\text{STRP}}\right) < 0 \end{cases} \tag{6.1}$$

Recall that $\bar{e}$ refers to the orbit-averaged eccentricity.

Colombo et al. [50] further claim that for a sail, equivalent to a plate-like spacecraft, one way to modulate the effective area-to-mass ratio is by changing the sail attitude so that it is either in face-on mode or edge-on mode with respect to the Sun.

Face-on mode: The panel is fully facing the Sun so that $\underset{\rightarrow}{u} \parallel \underset{\rightarrow}{n}$ ($\cos\alpha = 1$), the STRP acceleration is maximal, and the eccentricity secular rate is governed by [17]:

$$\left.\frac{\mathrm{d}\bar{e}}{\mathrm{d}t}\right|_{\text{STRP,face-on}} = \frac{1}{n a^2 \bar{e}}\left(-\sqrt{1-\bar{e}^2}\frac{\partial \bar{R}_{\text{SRP}}}{\partial \omega}\right) \tag{6.2}$$

where

$$\begin{aligned} \frac{\partial \bar{R}_{\text{SRP}}}{\partial \omega} = \frac{3}{2} P_r c_R \frac{A_{\text{nom}}}{m} \frac{a^4 n^2 \bar{e}}{\mu} \{ & \cos\bar{\varpi}\left(\cos\bar{\Omega}\cos\lambda_S + \sin\bar{\Omega}\sin\lambda_S\cos\varepsilon\right) + \ldots \\ & \sin\bar{\varpi}\left(\cos\bar{\Omega}\cos i\sin\lambda_S\cos\varepsilon + \sin i\sin\lambda_S\sin\varepsilon - \sin\bar{\Omega}\cos i\cos\lambda_S\right)\} \end{aligned} \tag{6.3}$$

with c_R the reflectivity coefficient. For consistency with the formulation of eccentricity dynamics used in this thesis and to account for the TRP, we rewrite Eq. (6.2) in the following form:

$$\left.\frac{\mathrm{d}\bar{e}}{\mathrm{d}t}\right|_{\text{STRP,face-on}} = -\frac{3}{2} P_r \frac{A_{\text{nom}}}{m} \sigma_{\text{eff}} \frac{\sqrt{1-e^2}}{n a} \sum_{j=1}^{6} \mathcal{T}_j \sin\bar{\psi}_j \tag{6.4}$$

with $\bar{\psi}_j = n_1\bar{\Omega} + n_2\bar{\varpi} + n_3\lambda_S$ and the effective STRP coefficient of Eq. (2.32) employed in lieu of the reflectivity coefficient c_R from [17]. We notice here that the magnitude of the STRP for the bang-bang strategy is modulated by the effective STRP coefficient, σ_{eff} of Eq. (2.32), instead of the C_k coefficient of Eq. (2.30) (compare equations of motion (5.2) and (6.4)). As well, all six j-terms are included instead of only a single (resonant) term in the resonance strategy, which implies that the efficacy of the two solutions cannot be compared solely on the basis of C_k and σ_{eff} values.

Edge-on mode: The panel's normal is exactly perpendicular to the Earth-Sun line so that $\underset{\rightarrow}{n} \perp \underset{\rightarrow}{u}$ ($\cos\alpha = 0$) which yields a null scenario:

$$\left.\frac{\mathrm{d}\bar{e}}{\mathrm{d}t}\right|_{\text{STRP,edge-on}} = 0 \tag{6.5}$$

In this mode, the surface of the panel exposed to the Sun is null. Therefore, the STRP acceleration is also null as per Eq (2.14) and has no effect on the eccentricity.

As for the e-resonance method, only the eccentricity secular evolution is considered in [50]. Its sign can be obtained from the eccentricity averaged equation of motion Eq. (6.4):

$$\texttt{sign}\left(\left.\frac{\mathrm{d}\bar{e}}{\mathrm{d}t}\right|_{\text{STRP}}\right) = \texttt{sign}\left(-\sum_{j=1}^{6} \mathcal{T}_j \sin\overline{\psi}_j\right) \tag{6.6}$$

We note here that if the component of the STRP acceleration along-track (see $a_{s,\text{STRP}}$ from Eq. (B.3) in Appendix B) is positive, then the averaged eccentricity increases; otherwise it decreases. As mentioned in Section 2.2.1, the $\underset{\rightarrow}{z}_b$-axis of the panel is set to be aligned with the Sun's angular momentum $\underset{\rightarrow}{h}_S$. Then, based on Eq. (2.10), $\underset{\rightarrow}{u}$ is aligned with $\underset{\rightarrow}{n}$ when $\phi = \lambda_S$, and, $\underset{\rightarrow}{u}$ is perpendicular to $\underset{\rightarrow}{n}$ when $\phi = \lambda_S \pm \pi/2$. Following the logic of Eq. (6.1) along with Eq. (6.6), we thus define the reference angle of the panel required to increase the eccentricity as:[1]

$$\phi_{r,e-\text{bang-bang}} = \begin{cases} \lambda_S & \text{if} \quad \texttt{sign}\left(-\sum_{j=1}^{6} \mathcal{T}_j \sin\overline{\psi}_j\right) \geq 0 \\ \lambda_S + \dfrac{\pi}{2} & \phantom{\text{if}} \quad \texttt{sign}\left(-\sum_{j=1}^{6} \mathcal{T}_j \sin\overline{\psi}_j\right) < 0 \end{cases} \tag{6.7}$$

The results presented in [50] were obtained in an environment subject to the SRP acceleration only by using the averaged eccentricity equation of motion. Bearing this in mind, in Fig. 6.1, we compare the eccentricity e and perigee altitude h_p responses for the propagation of O2 in D-SPOSE with the tracking of $\phi_{r,e-\text{bang-bang}}$ including both the SRP and the geopotential (GP) (up to degree and order 2) accelerations to those obtained with only the SRP acceleration. We are neglecting the thermal radiation and shadow effects for this comparison since they were ignored in [50]. From Fig. 6.1, we notice a significant loss of efficiency ($\sim$20%) over 12 years caused by including the geopotential perturbations. Also, the higher number of steps, clearly visible in the e and h_p responses of Fig. 6.1, when including the geopotential perturbation (orange curve)

[1] For the edge-on case, $\phi_r = \lambda_S + \pi/2$ was chosen arbitrarily. Choosing $\phi_r = \lambda_S - \pi/2$ would yield the same results

indicates a considerable increase in the rate at which the panel switches from its $a_{\text{STRP,max}}$ mode to its $a_{\text{STRP,min}}$ mode. We thus conclude that the efficiency claim made by Colombo et al. [50] may be considerably degraded by additional perturbations, but overall, the solution is successful in generating an increase in eccentricity.

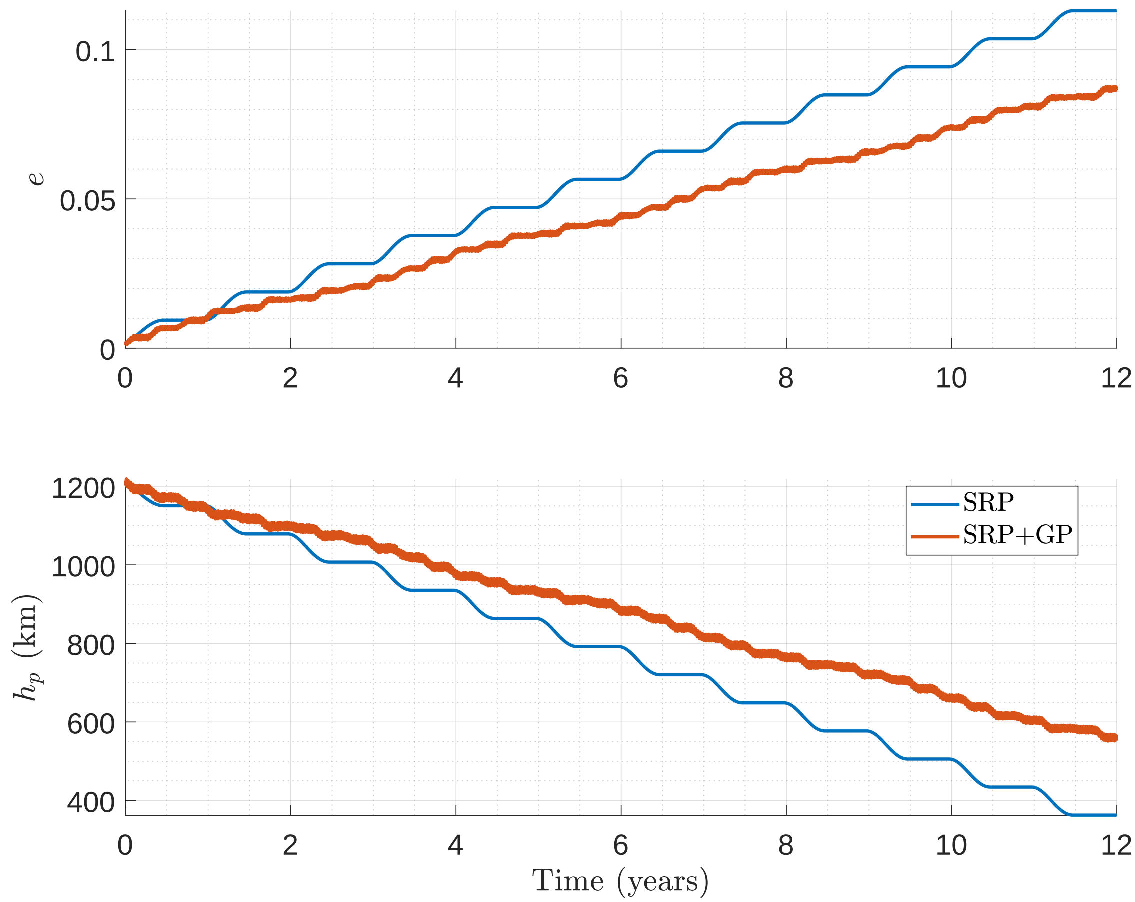

Figure 6.1: 12-year propagation of O2 with tracking of $\phi_{r,e-\text{bang-bang}}$ obtained using D-SPOSE including SRP only (blue) vs. SRP and geopotential accelerations (orange)

6.1.2 a-bang-bang

For this next deorbitation method, we are following Borja and Tun [49] who suggested that it is possible to obtain a net change in the semi-major axis by reorienting a spacecraft's solar panels twice per orbit, either to maximize or to minimize the SRP acceleration according to its effect on a. In our implementation, we use the following logic for the modulation of the STRP acceleration magnitude:

$$a_{\text{STRP}} = \begin{cases} a_{\text{STRP,max}} & \text{if} \quad \underset{\rightarrow}{s} \cdot \underset{\rightarrow}{u} \leq 0 \\ a_{\text{STRP,min}} & \phantom{\text{if}} \quad \underset{\rightarrow}{s} \cdot \underset{\rightarrow}{u} > 0 \end{cases} \tag{6.8}$$

where we recall from Section 2.2.1, $\underset{\rightarrow}{s}$ is the along-track vector aligned with the spacecraft velocity. For this solution, as for the e-bang-bang solution, the plate-like spacecraft is either in face-on mode ($\underset{\rightarrow}{n} \parallel \underset{\rightarrow}{u}$) or in edge-on mode ($\underset{\rightarrow}{n} \perp \underset{\rightarrow}{u}$).

Face-on mode: The panel is fully facing the Sun so that $\underset{\rightarrow}{u} \parallel \underset{\rightarrow}{n}$ yielding the maximum STRP acceleration as given by Eq. (2.31). Resolving it in the local vertical/local horizontal frame $\mathcal{F}_{\text{LVLH}}$, we get:

$$\begin{Bmatrix} a_{r,\text{STRP}} \\ a_{s,\text{STRP}} \end{Bmatrix}_{\text{face-on}} = -C_{\text{STRP}}\, \sigma_{\text{eff}} \sum_{j=1}^{6} \mathcal{T}_j \begin{Bmatrix} \cos \psi_j \\ \sin \psi_j \end{Bmatrix} \tag{6.9}$$

where $a_{r,\text{STRP}}$ is the radial component of the STRP acceleration and $a_{s,\text{STRP}}$ is the along-track component. In Eq. (6.9), σ_{eff} is as per Eq. (2.32), and:

$$\psi_j = n_1\, \Omega + n_2\, (\omega + \nu) + n_3\, \lambda_S \tag{6.10}$$

is as per Eq. (2.22). From the semi-major axis equation of motion approximated for $e \ll 1$ and given by Eq. (2.56), we thus obtain in face-on mode:

$$\left.\frac{\mathrm{d}a}{\mathrm{d}t}\right|_{\text{STRP,face-on}} \approx -C_{\text{STRP}} \frac{2}{n\sqrt{1-e^2}}\, \sigma_{\text{eff}} \sum_{j=1}^{6} \mathcal{T}_j \sin(\psi_j) \tag{6.11}$$

We note that, in this mode, the perturbing acceleration is aligned with $\underset{\rightarrow}{u}$ (see Eq. (2.31)), therefore its component along $\underset{\rightarrow}{s}$ in $\mathcal{F}_{\text{LVLH}}$ ($a_{s,\text{STRP}}$) acts to reduce a when $\underset{\rightarrow}{s} \cdot \underset{\rightarrow}{u}$ is negative. This confirms the settings of the a-bang-bang solution in Eq. (6.8).

Edge-on mode: The panel's normal is exactly perpendicular to the Earth-Sun line so that $\underset{\rightarrow}{n} \perp \underset{\rightarrow}{u}$ and $\cos \alpha = 0$ which yields a null scenario:

$$\left.\frac{\mathrm{d}a}{\mathrm{d}t}\right|_{\text{STRP,edge-on}} = 0 \tag{6.12}$$

As for the e-bang-bang solution, in this mode, the surface of the panel exposed to the Sun is null, therefore, the STRP has no effect on the semi-major axis.

Similar to the eccentricity maximization, we can define a condition to decrease the semi-major axis based on the logic of Eq. (6.8):

$$\phi_{r,a-\text{bang-bang}} = \begin{cases} \lambda_S & \text{if} \quad \underset{\rightarrow}{s} \cdot \underset{\rightarrow}{u} \leq 0 \\ \lambda_S + \dfrac{\pi}{2} & \quad\quad\; \underset{\rightarrow}{s} \cdot \underset{\rightarrow}{u} > 0 \end{cases} \tag{6.13}$$

which defines the reference attitude angle for the a-bang-bang scheme.

6.2 Numerical comparison

In this section, we compare, in a realistic environment, the efficiency of the four previously introduced deorbiting strategies, namely a-resonance (Section 5.1.2), e-resonance (Section 5.1.1), a-bang-bang (Section 6.1.2) and e-bang-bang (Section 6.1.1), and we do so for orbit test-cases defined in Table 6.1. The simulation conditions are as before (Section 5.2.3)

For each orbit case, the four methods are defined with the corresponding reference angles, in particular, $\phi_r = \{\phi_{r,a-\text{resonance}},\ \ \phi_{r,e-\text{resonance}}, \phi_{r,a-\text{bang-bang}}, \phi_{r,e-\text{bang-bang}}\}$ given by Eqs. (5.12), (5.6), (6.13) and (6.7). Table 5.2 model parameters are still used but with the masses and optical coefficients as per the last columns of Table 6.1. The control gains are adjusted based on the spacecraft mass m for each propagation case, based on Eq. (5.30).

Recall that the O3 parameters in Table 6.1 were chosen to represent a plausible case scenario for a mega-constellation satellite and that the O4 parameters were selected to represent a spacecraft equipped with a perfectly reflective area-augmentation device. Cases O2 and O5 were chosen to highlight the effect of relevant parameters on the descent rate of the spacecraft for the four methods; they do not represent any particular scenario. Finally, case O7 was defined to lie within the $j = 1$ passive eccentricity resonance corridor (or deorbitation corridor) associated with the values of $a = 7,600$ km and $e = 0.001$. The resonant inclination $i = 40.58°$ was computed by solving Cook's commensurability condition $\dot{\overline{\psi}}_1 = 0$, at $\overline{\psi}_1 = \frac{\pi}{2}$ (see Eq. (2.74)) as per [13]. This is equivalent to solving Eq. (3.3) for which the Σ_i are related to the Keplerian parameters through Eqs. (2.40) and (2.76). As mentioned in Chapter 1, this particular resonance leads to a passively accelerated re-entry, and the resonance condition does not depend on the rotation rate of the spacecraft $\dot{\phi}$.

Table 6.1: Orbital initial conditions and associated spacecraft model parameters

	a (km)	e	i (°)	Ω (°)	ω (°)	ν (°)	m (kg)	$(\sigma_{rs}, \sigma_{rd}, \sigma_a)$
O2	8,078	0.01	60	0	0	45	23.2	(0, 0, 1)
O3	7,200	0.001	20	0	0	45	227	(0.16, 0.25, 0.59)
O4	8,400	0.001	20	0	0	45	29.7	(1, 0, 0)
O5	7,400	0.001	45	0	0	45	56.0	(0, 0, 1)
O7	7,600	0.001	40.58	0	0	45	29.7	(0, 0, 1)

The a, e and h_p time responses for O2, O3 and O7 are presented in Figs. 6.2 to 6.4 while few cycles of the attitude responses for case O3 propagations are presented in Figs. 6.5 and 6.6, for the a and e methods respectively. A summary of the propagation results for O2 to O7 is presented in Table 6.2.

The first conclusion to draw from Figs. 6.2 and 6.3 is that when outside the passive resonance corridor, exploiting the solar radiation pressure to decrease the semi-major axis is more effective than exploiting it to increase the orbital eccentricity. Comparing the case of a-resonance to e-resonance, the deorbitation time is reduced by a factor ranging from 1.3 to 2.1 for the considered orbits. Also, outside the deorbiting corridor, i.e., excluding the O7 case, the bang-bang methods

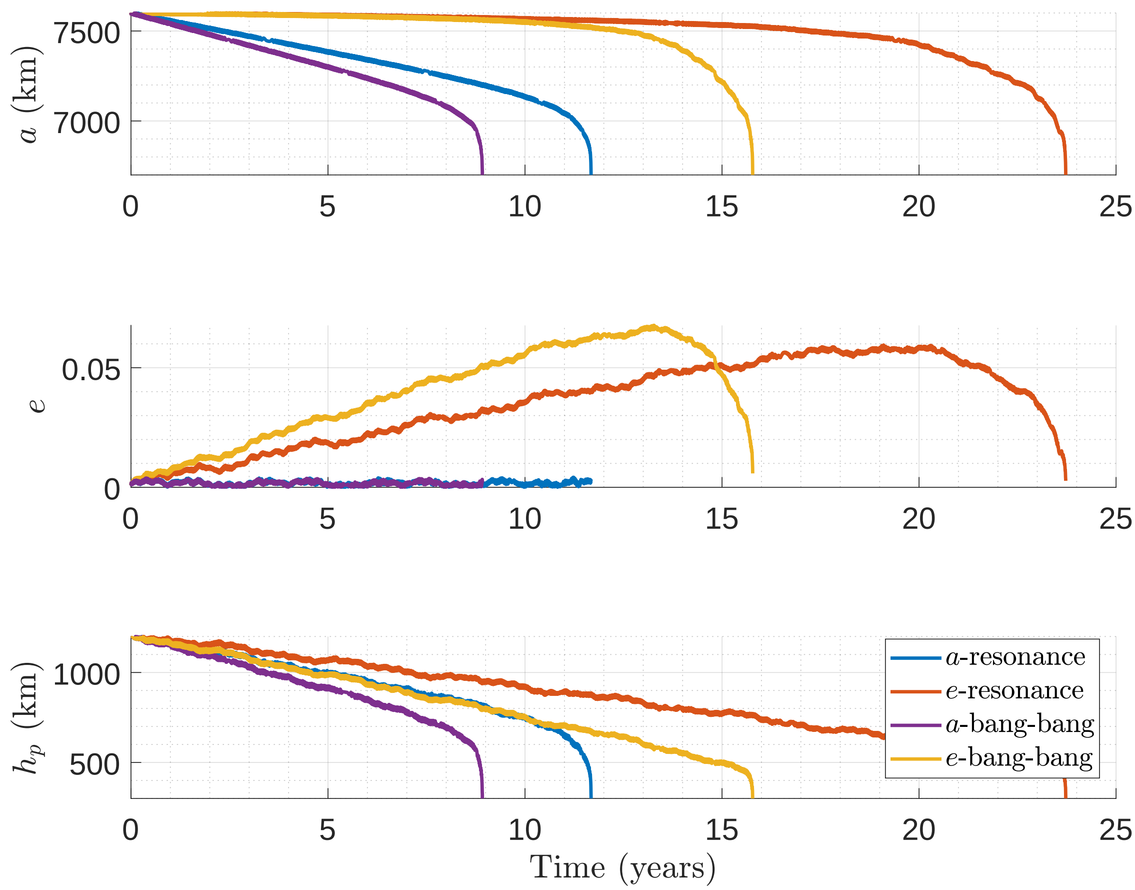

Figure 6.2: Orbital response for the propagation of O2 in D-SPOSE with $\phi_r = \{\phi_{r,a-\text{resonance}}, \phi_{r,e-\text{resonance}}, \phi_{r,a-\text{bang-bang}}, \phi_{r,e-\text{bang-bang}}\}$ including STRP, geopotential and drag perturbing accelerations and torques

are more efficient than their associated resonance methods, leading to faster deorbitation. While the bang-bang solutions maximize the effect of all the oscillating terms, that is, for the semi-major axis case, all the terms in Eq. (2.56) (respectively all the terms in Eq. (5.2) for the eccentricity case), the resonance methods aim to maximize only the effect of a single resonant term.

For the particular case of O7, the different strategies lead to different deorbitation times, as can be gathered from Fig. 6.4, and the e methods appear to be more efficient. We can also observe from this figure that, for the a methods, in the passive eccentricity resonance corridor, the resonant effects in a and e are superimposed, i.e., the semi-major axis and eccentricity decreases and increases respectively leading to a cumulative effect on the altitude of the perigee h_p. The eccentricity increase, however, is not as large as for the e methods. This is in direct correlation to the $\cos\alpha$ evolution: taking its mean value over the whole propagation for the 4 different strategies, we find that $\texttt{mean}(\cos\alpha(t)) \lesssim 1$ for the e-methods, whereas it is only $\texttt{mean}(\cos\alpha(t)) \approx 0.65$ for the a-resonance scheme and $\texttt{mean}(\cos\alpha(t)) \approx 0.55$ for the a-bang-bang scheme. The two latter values also explain why the eccentricity increase is slightly smaller for the a-bang-bang strategy than for the a-resonance. However, this is insufficient to compensate for the faster decrease in a achieved

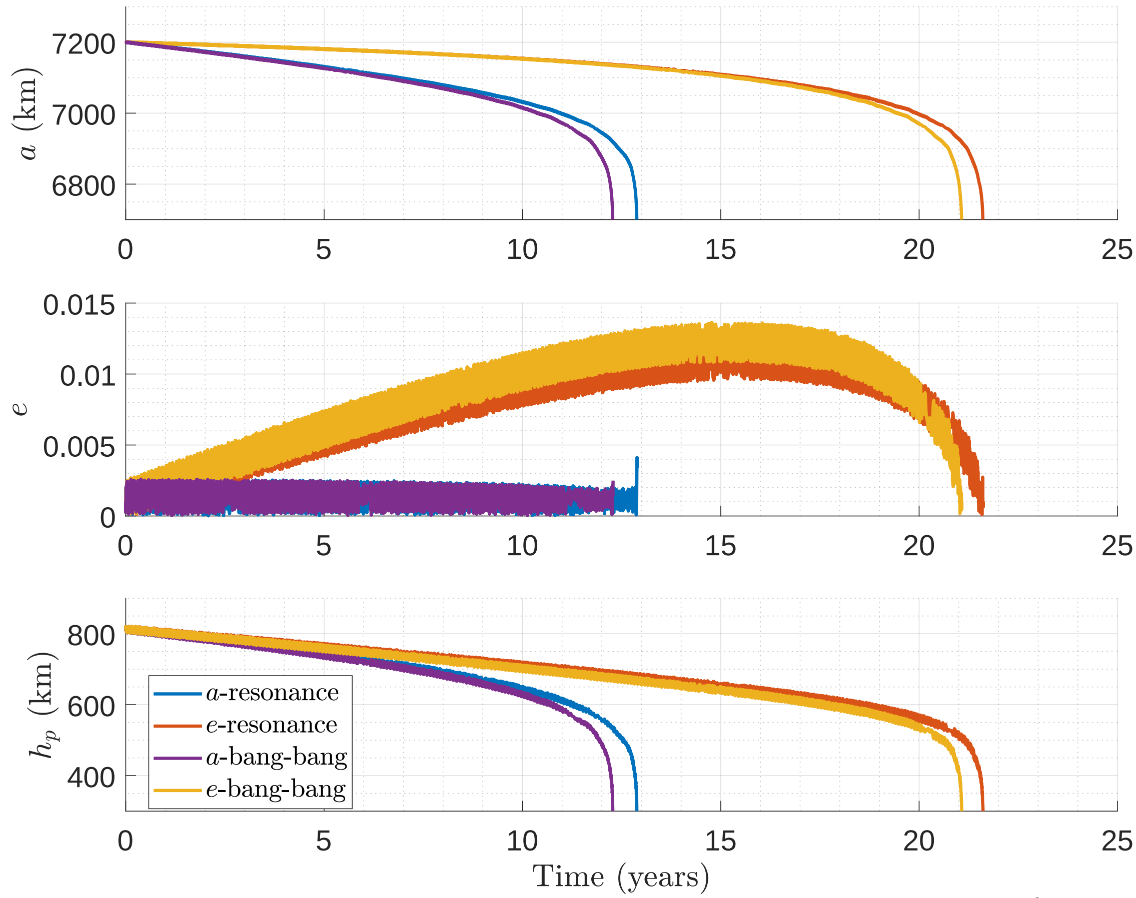

Figure 6.3: Orbital response for the propagation of O3 in D-SPOSE with $\phi_r = \{\phi_{r,a-\text{resonance}}, \phi_{r,e-\text{resonance}}, \phi_{r,a-\text{bang-bang}}, \phi_{r,e-\text{bang-bang}}\}$ including STRP, geopotential and drag perturbing accelerations and torques

with the bang-bang solution, which ultimately leads to faster deorbitation than for the a-resonance scheme.

Fig. 6.4 also illustrates a similar behaviour for the e-resonance and the e-bang-bang strategies: for both solutions, the spacecraft is fully facing the Sun as is confirmed by the resulting $\mathtt{mean}(\cos\alpha(t)) \lesssim 1$ value. Although, when the semi-major axis decreases considerably, $\cos\alpha$ starts to diverge from 1 for the e-resonance solution but not for the e-bang-bang. This difference in the panel orientation at low altitudes leads to a higher descent rate for the e-resonance case when the atmospheric drag becomes the main driver for deorbitation. This highlights the coupling effect between the spacecraft's attitude and atmospheric drag and suggests that, in the low LEO region (<600 km), a drag-enhancing solution might be favourable to our solutions exploiting STRP.

Still for the particular case of O7, when the panel is constantly facing the Sun, as is the case here for the e solutions, the resonance effect is identical to what has been published previously in [13], [26], assuming a spherical spacecraft with equivalent area-to-mass ratio and effective STRP

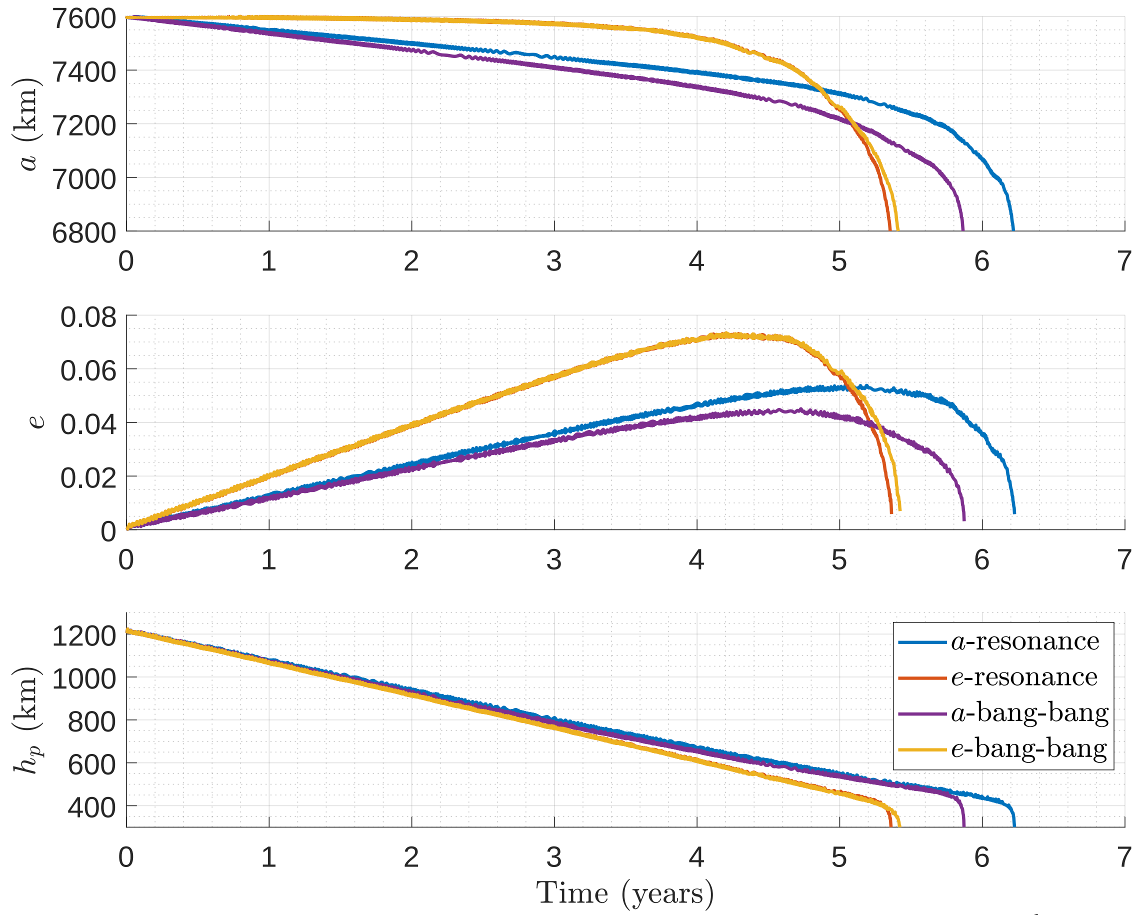

Figure 6.4: Orbital response for the propagation of O7 in D-SPOSE with $\phi_r = \{\phi_{r,a-\text{resonance}}, \phi_{r,e-\text{resonance}}, \phi_{r,a-\text{bang-bang}}, \phi_{r,e-\text{bang-bang}}\}$ including STRP, geopotential and drag perturbing accelerations and torques

coefficient.[2] We note that the atmospheric drag effect would, however, be of lesser importance since, for a plate-like spacecraft, if $\underset{\rightarrow}{u} \parallel \underset{\rightarrow}{n}$, then $\underset{\rightarrow}{n}$ is not necessarily opposing the velocity, thus leading to a smaller deceleration than for an equivalent sphere. We further note that active control is required to maintain $\cos\alpha(t) = 1$ for a plate-like spacecraft. Without active control, a passive resonance in eccentricity would still occur as confirmed by the a strategies responses in e presented in Fig. 6.4, but it would be weaker and would depend on $\mathtt{mean}(\cos\alpha(t))$.

Comparing the deorbitation times obtained for the bang-bang methods $T_{\text{x-bang-bang}}$ to their associated resonance methods $T_{\text{x-resonance}}$ presented in Table. 6.2, we notice that the deorbitation times obtained by exploiting either strategy for a and e are similar for case O3, for which recall, the mean optical properties of Envisat's solar panel are employed [84]. Moreover, the resonance methods outperform the bang-bang methods for case O4 with the optical properties characterizing a perfect mirror ($\sigma_{rs} = 1$). On the other hand, the bang-bang method is clearly superior for the black body panel (cases O2 and O5, $\sigma_a = 1$). This can be explained by the fact that the osculating element

[2]For a sphere with a Lambertian surface: $\sigma_{\text{eff}} = 1 + \frac{4}{9}\left(\sigma_{rd} + \sigma_a \frac{\varepsilon_f - \varepsilon_b}{\varepsilon_f + \varepsilon_b}\right)$

Table 6.2: Deorbitation times T in years

	a (km)	i (°)	m (kg)	$\frac{C_2}{C_{2,\text{bb}}}$	σ_{eff}	$T_{a-\text{resonance}}$	$T_{a-\text{bang-bang}}$	$T_{e-\text{resonance}}$	$T_{e-\text{bang-bang}}$
O2	7,600	60	29.7	1	1	11.7	**8.91**	23.8	**15.8**
O3	7,200	20	227	1.873	1.357	12.9	**12.3**	21.6	**21.1**
O4	8,400	20	29.7	4	2	**7.68**	8.85	**10.2**	12.8
O5	7,400	45	56	1	1	11.9	**9.72**	24.6	**18.8**
O7	7,600	40.58	29.7	1	1	6.23	**5.87**	**5.36**	5.42

rates are sensitive to the optical coefficients, as can be deduced from Eqs. (2.56), (5.2), (6.4) and (6.11). Indeed, while the effect of the bang-bang approach on the time rate of either a or e scales with the effective optical coefficient σ_{eff} given by Eq. (2.32), it scales with the optical coefficient C_2 for the resonance methods, as given by Eq. (2.30). Comparing the scaling coefficients to their limiting values for the black body (x_{bb}), we can establish the following bounds:

$$\begin{aligned} 1 \le \frac{\sigma_{\text{eff}}}{\sigma_{\text{eff,bb}}} \le 2 = \frac{\sigma_{\text{eff}}(\sigma_{rs}=1)}{\sigma_{\text{eff,bb}}} \\ 1 \le \frac{C_2}{C_{2,\text{bb}}} \le 4 = \frac{C_2(\sigma_{rs}=1)}{C_{2,\text{bb}}} \end{aligned} \tag{6.14}$$

The upper bounds on the non-dimensional optical coefficients correspond to the case of a perfect mirror ($\sigma_{rs}=1$). As can be seen from Eq. (6.14), for such a body, the effectiveness of the resonance method is increased by a factor of 4 while only by a factor of 2 for the bang-bang method. This difference explains the smaller deorbitation time for the former, as shown by the results in Table 6.2 for O4. For the propagation of O3, the scaling coefficients are $\frac{C_2}{C_{2,\text{bb}}}=1.873$ and $\frac{\sigma_{\text{eff}}}{\sigma_{\text{eff,bb}}}=1.357$ respectively; thus, explaining the smaller difference in deorbitation times for O3 as compared to those for O2 and O5.

From Fig. 6.2, we observe that a-resonance and e-bang-bang methods have a similar altitude of perigee descent rate; however, for a-resonance, the semi-major axis decreases faster than for e-bang-bang yielding a more continuous drag effect over the whole orbit. This is sufficient to accelerate the deorbitation by a few years.

The ϕ-plots and $\psi_{1,2}$-plots of Figs. 6.5 and 6.6 show proper tracking of $\psi_{1,2}=90^\circ$ and $\widetilde{\psi}_{1,2}=-90^\circ$ for the resonance methods as per Eqs. (5.11) and (5.5) respectively, and $\phi=\begin{cases}\lambda_S \\ \lambda_S+90^\circ\end{cases}$ for the bang-bang methods as per Eqs. (6.13) and (6.7). We further notice from the ϕ-plots in Figs. 6.5 and 6.6 that the two resonance methods require an almost constant panel's angular rate while the bang-bang solutions, a-bang-bang and e-bang-bang, require sudden changes in the orientation: only about once every two months for the e-bang-bang, but twice per orbital period for the a-bang-bang, therefore, requiring more active control. Moreover, we notice from the $\cos\alpha$-plot of Fig. 6.5 that for the a-resonance strategy, the panel's backside is facing the Sun once every other orbit, in which case the panel's power generation is null.

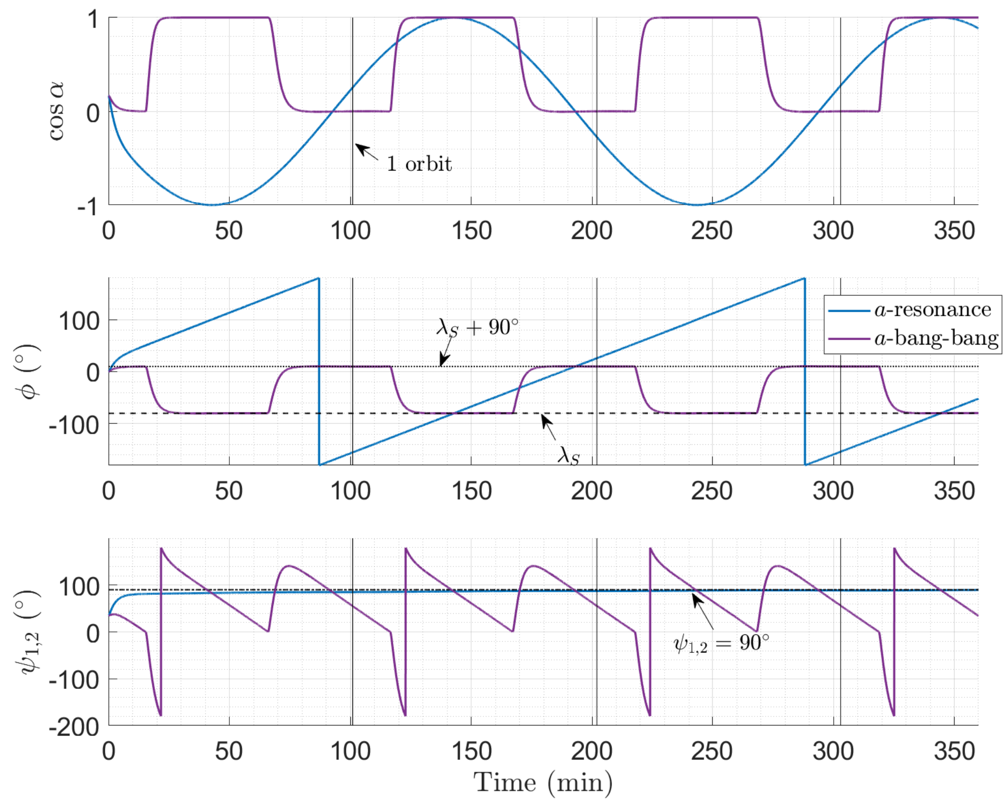

Figure 6.5: Attitude response for the propagation of O3 in D-SPOSE with $\phi_r = \{\phi_{r,a-\text{resonance}}, \phi_{r,a-\text{bang-bang}}\}$ including STRP, geopotential and drag perturbing accelerations and torques

Finally, the results for the e methods in Fig. 6.6 show that for periods of about 45 days, either the panel's backside is facing the Sun (e-resonance, $\cos\alpha < 0$) or the exposed area is almost null (e-bang-bang, $\cos\alpha = 0$). If the system had to be powered by its solar panel, these solutions would be clearly inoperable. Therefore, in the following section, we only study the energy cost of the two a methods and simulate the power and energy requirements for a specific case scenario.

6.3 Power Analysis

In this section, we compare the resonance and bang-bang semi-major axis deorbitation strategies on the basis of their power generation, energy storage and depletion responses. We compare, for both methods, the propagation results of O3 given in Fig. 6.3 and 6.5 with particular attention on the rotational motion over the initial cycles since it has direct implications for the power generation. We recall that the orbital parameters for O3 are presented in Table 6.1 as well as the associated spacecraft model parameters.

Propagating over 12 hours for the spacecraft initially in O3 with $\phi_r = \{\phi_{r,a-\text{resonance}}, \phi_{r,a-\text{bang-bang}}\}$ and under the same perturbations as in the previous sections for a fixed time step

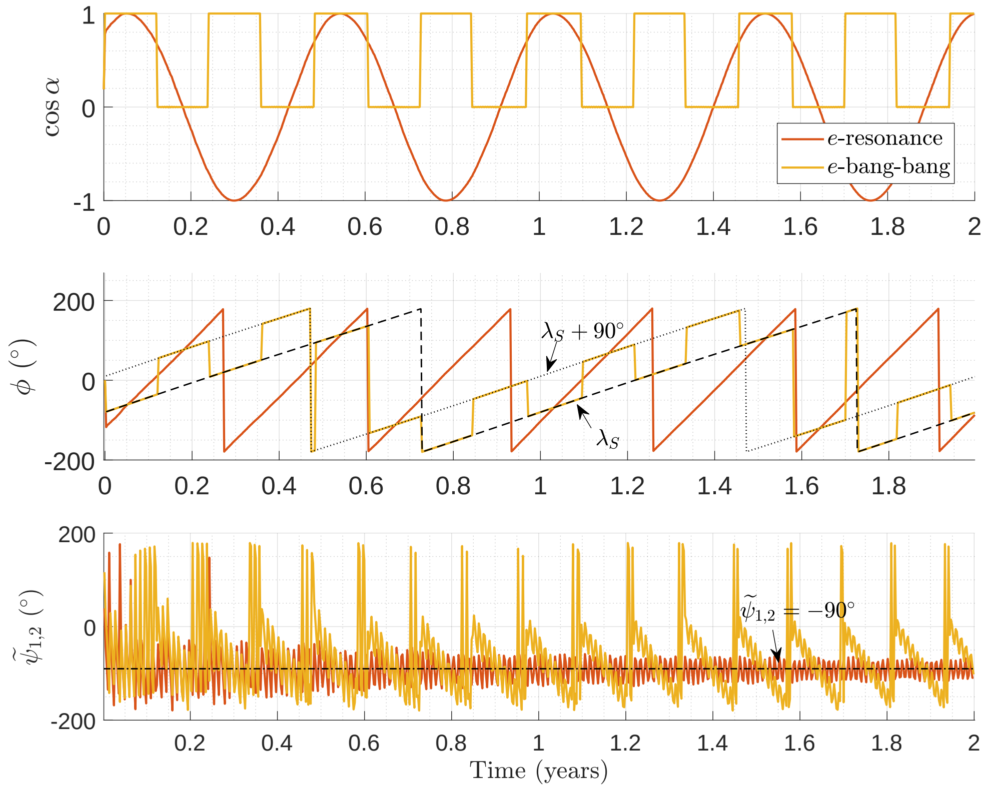

Figure 6.6: Attitude response for the propagation of O3 in D-SPOSE with $\phi_r = \{\phi_{r,e-\text{resonance}}, \phi_{r,e-\text{bang-bang}}\}$ including STRP, geopotential and drag perturbing accelerations and torques

of 0.01 sec yields the attitude responses shown in Fig. 6.7. In Fig. 6.7, we plot the z-body-fixed component of the angular velocity and control torque. The x and y components are not presented since they are too small in comparison to the corresponding z component: $<$ 1e-5 rad/s for $\omega_{b,x}$ and $\omega_{b,y}$, and $<$ 1e-4 N·m for $\tau_{c,x}$ and $\tau_{c,y}$.

As noted in Section 6.2, for the O3 use-case, a faster deorbiting time is obtained for the bang-bang method (for which the panel has to reorient twice per orbital period) than for the resonance method (for which the panel rotates at an almost constant rate). However, higher control torques are required for the bang-bang attitude changes as can be seen from the $\tau_{c,z}$ response in Fig. 6.7. The power required to rotate the panel when tracking either $\phi_{r,a-\text{bang-bang}}$ or $\phi_{r,a-\text{resonance}}$ is however very small, on the order of 0.1 mW, and is thus neglected in the power consumption.

6.3.1 Power generation and energy storage

An important aspect when evaluating the feasibility of deorbitation strategies is the power source as well as power generation vs. power consumption. In this research, we have considered plate-like spacecraft on the basis that a spacecraft solar panel is typically subject to a much stronger STRP acceleration than the spacecraft body due to its large area. It is then natural to assume that,

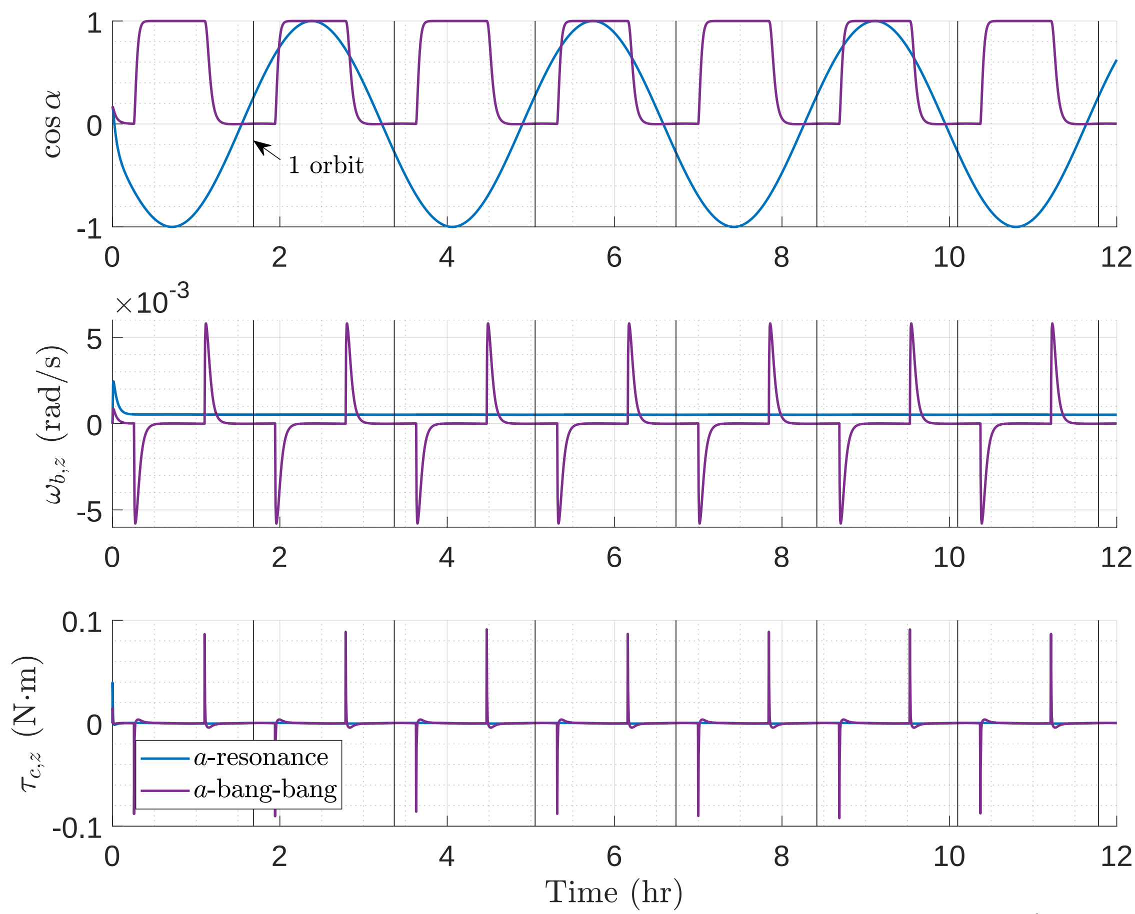

Figure 6.7: Attitude response for the propagation of O3 in D-SPOSE with $\phi_r = \{\phi_{r,a-\text{resonance}}, \phi_{r,a-\text{bang-bang}}\}$ including STRP, geopotential and drag perturbing accelerations and torques

for such a spacecraft, power should come from the solar array employed alongside batteries for energy storage and power generation when in the Earth's shadow.

Based on Table 6.2, the time required to deorbit the spacecraft using the a-schemes is on the order of 12 years which is significantly longer than the typical 5-year lifetime of small spacecraft in LEO. Proper power management is therefore of utmost importance. Fig. 6.8 shows the power income from the solar panel P_s (solid lines) along with the battery energy storage E_s for the simulation results for O3 use-case over the initial 12 hours of deorbiting with a-resonance and a-bang-bang schemes. The power income response computed by neglecting the Earth's shadow is also shown in Fig. 6.8 with dashed lines for reference. The power and energy responses were obtained using the parameters of Table 6.3 and:

$$
\begin{aligned}
P_s &= \begin{cases} P_{\text{max}}\,(1-\beta)\cos\alpha\,, & \cos\alpha >= 0 \\ 0\,, & \cos\alpha < 0 \end{cases} \\
E_s &= \frac{1}{E_{\text{max}}}\int \{P_s(t) - P_{\text{eol}}\,(t)\}\,\mathrm{d}t
\end{aligned}
\tag{6.15}
$$

with $\beta = 0$ when the spacecraft is completely in the Earth's shadow; $\beta = 1$ when it is in complete sunlight; and $0 < \beta < 1$ when in-between [65]. The stored energy E_s is bounded by maximum battery capacity (at 100%). The solar cell and power management system efficiencies of Table 6.3, η_c and η_m, are estimated based on the currently available technologies. An overview of the current state-of-the-art technologies for power generation, management and distribution systems is provided in Chapter 3 of [87]. We assume the end-of-life power consumption of the spacecraft P_{eol} to be 2 kW and the maximum battery capacity, $E_{\max}$, to be 8 kWh.

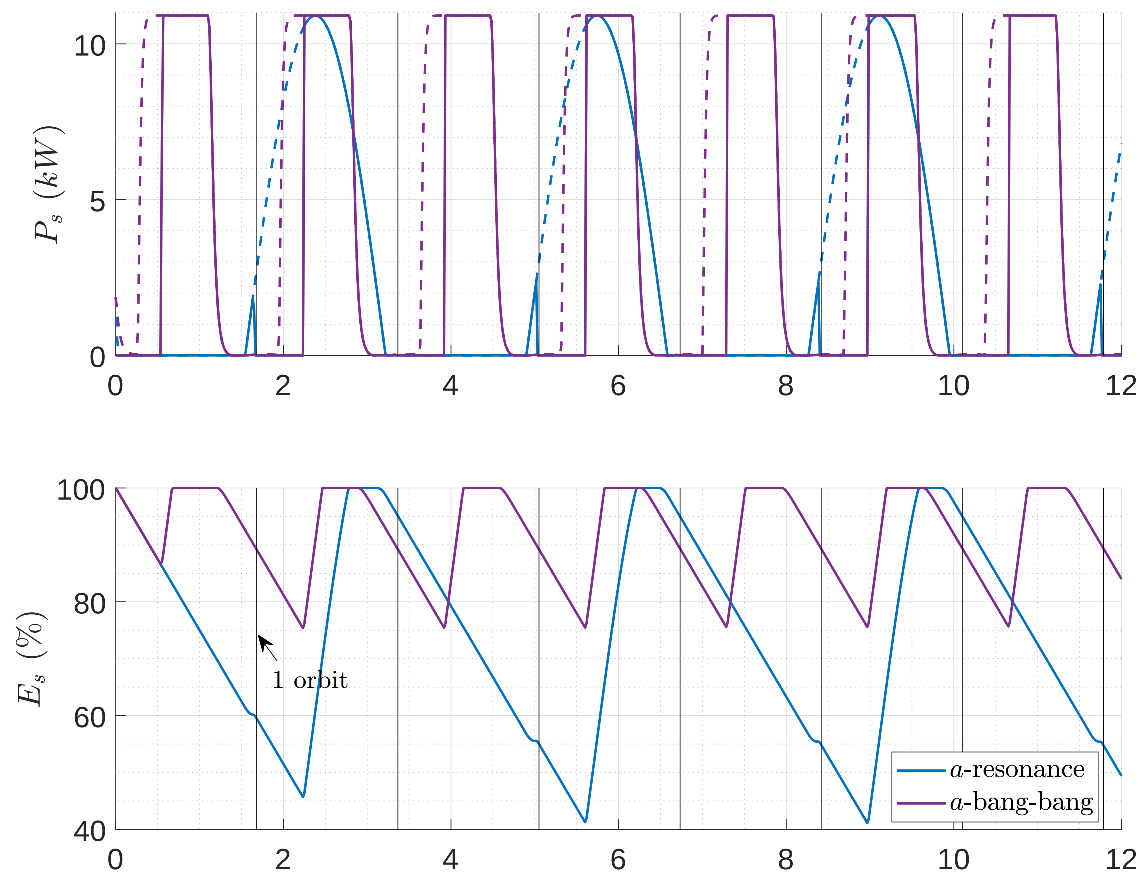

Figure 6.8: Power income with Earth's shadow (solid line) and without Earth's shadow (dashed line), and energy storing analysis for the first cycles of Fig. 6.7 propagations

The power income response from Fig. 6.8 shows that for O3, about 35% of the orbit is in Earth's shadow (∼35 minutes of the ∼101-minute period). As a reference, the power income, if the spacecraft was in constant sunlight, is given in Fig. 6.8 by the dashed line. During that time, the energy from the battery is used to power the system. For the bang-bang method, the panel completely faces the Sun long enough to completely recharge the battery every orbit, the maximum depth of discharge is therefore smaller than for the resonance strategy, for which the panel faces the Sun once every other orbit (see $\cos\alpha$-plot in Fig. 6.7). The maximum depths of discharge for the a-bang-bang and a-resonance methods are, respectively, ∼ 25% against ∼60%. The battery is however subject to half the number of charge/discharge cycles for the latter solution,

Table 6.3: Power Parameters

Parameter	Description	Value	Units
$E_{\max}$	maximum capacity	8	kWh
P_{eol}	end-of-life power consumption	2	kW
A_c	cell surface area	29.7	m^2
η_c	solar cell efficiency	0.3	-
η_m	power management system efficiency	0.9	-
S_r	solar constant	1360.8	W/m^2
$P_{\max}$	maximum available power	$A_c\,\eta_c\,\eta_m\,S_r = 10.912$	kW

which may have a non-negligible effect on the battery life expectancy. Nevertheless, the results presented here indicate that both a deorbitation strategies are power-feasible.

6.4 Concluding remarks

The deorbitation strategies proposed in Chapter 5 were compared to two previously proposed deorbitation strategies aiming to lower the altitude of perigee by either lowering the semi-major axis or increasing the eccentricity. The semi-major axis schemes were shown to be more efficient than the eccentricity solutions when not in the vicinity of the $j = 1$ deorbitation corridor, otherwise the passive increase in e leads to a faster descent. Moreover, the bang-bang strategies lead to shorter deorbitation times than their associated resonance solutions for a black body, but vice-versa when the optical coefficients are nearing those of a perfectly reflective mirror.

Finally, an investigation of the power/energy budget was conducted considering a spacecraft for which the greatest exposed area is that of its solar panel. In this context, the eccentricity strategies are not viable since the solar panel would have to face away from the Sun for long periods of time, up to a few months. The analysis however showed that the semi-major axis deorbitation schemes are compatible with solar power. It also revealed that the control power required to deorbit a spacecraft by exploiting either the resonance or the bang-bang solution is not sufficient to justify the choice of one strategy over the other. However, the difference in the Sun exposure over time for the two methods might have a non-negligible effect on the lifetime of the batteries. While the bang-bang solution led to a maximum depth of discharge of $\sim$25% and a number of cycles equal to the number of orbits, the resonance solution led to a maximum depth of discharge of $\sim$60% with half the number of cycles.

The final choice of deorbitation strategy among those proposed and evaluated in this work would require simulations and analysis for the specific mission scenario.

Chapter 7

Exploiting a-resonance for Drag Compensation in Low Earth Orbits

We showed in Chapter 6 that, for a plate-like spacecraft, the resonance effect produced by the coupling between rotational motion and STRP could be exploited to accelerate the descent of a spacecraft in LEO from arbitrary orbital conditions. The efficiency of the phenomenon as an end-of-life solution was assessed in comparison to bang-bang-type strategies previously published. For the purpose of deorbitation, these solutions aimed to either increase the orbital eccentricity in order to lower the altitude of perigee (e-resonance or e-bang-bang), or to lower the altitude by decreasing the semi-major axis (a-resonance or a-bang-bang). Besides, by choosing the specific settings of the a-schemes combined with appropriate tracking conditions, it is possible to raise the orbit by increasing the semi-major axis.

To demonstrate how STRP can be exploited in LEO, the LightSail 2 mission, introduced in Chapter 1, was launched in 2019. The LightSail was a CubeSat equipped with a controllable reflective solar sail initially launched to an altitude of 720 km. The ability of the spacecraft to orient its sail allowed the implementation of a a-bang-bang control logic to compensate for the loss of altitude induced by atmospheric drag.

In Chapter 6, we concluded that for a perfectly reflective panel or sail, the exploitation of the a-resonance leads to a faster descent than the a-bang-bang solution. With that in mind, we expand, in this chapter, the spectrum of applications of the a-resonance solution to semi-major axis tracking. We first present an overview of the LightSail 2 three-year mission, which motivated our a-tracking study, highlighting the capabilities and limitations of the suggested approach.

7.1 Overview of LightSail 2 mission

As described in Chapter 1, LightSail 2 is a citizen-funded project executed by The Planetary Society that successfully put into a 720 km orbit, a 3U CubeSat of 5 kg equipped with a controllable 32 m^2 Mylar solar sail, in July 2019. Until its re-entry in November 2022, LightSail 2 demonstrated controlled solar sailing as a means to counter orbital energy loss due to atmospheric drag by exploiting Borja and Tun's suggested bang-bang type approach [49], [52].

Even though LightSail 2 showed rather poor Sun pointing accuracy, with angular error ranging from 20° to 45°, it was able to achieve substantial drag compensation in a region where drag is non-negligible.[1] This strategy extended the lifetime of the spacecraft, initially expected to re-enter by the end of 2021, to longer than three years [52]. For reference, Fig. 7.1 shows the recorded semi-major axis, eccentricity, and perigee altitude data of LightSail 2 obtained from the Space-Track TLE database [32]. The presented data starts with the first recorded position on July 7, 2019, to its re-entry on November 17, 2022, and include the recorded solar radio flux F10.7 cm over the same time frame. From this information, we can infer that the increasing trend in the solar flux precipitated the re-entry of the solar sail. It is assumed that the drag generated by the resulting atmospheric density increase exceeded the STRP propulsion capacity of the sail.

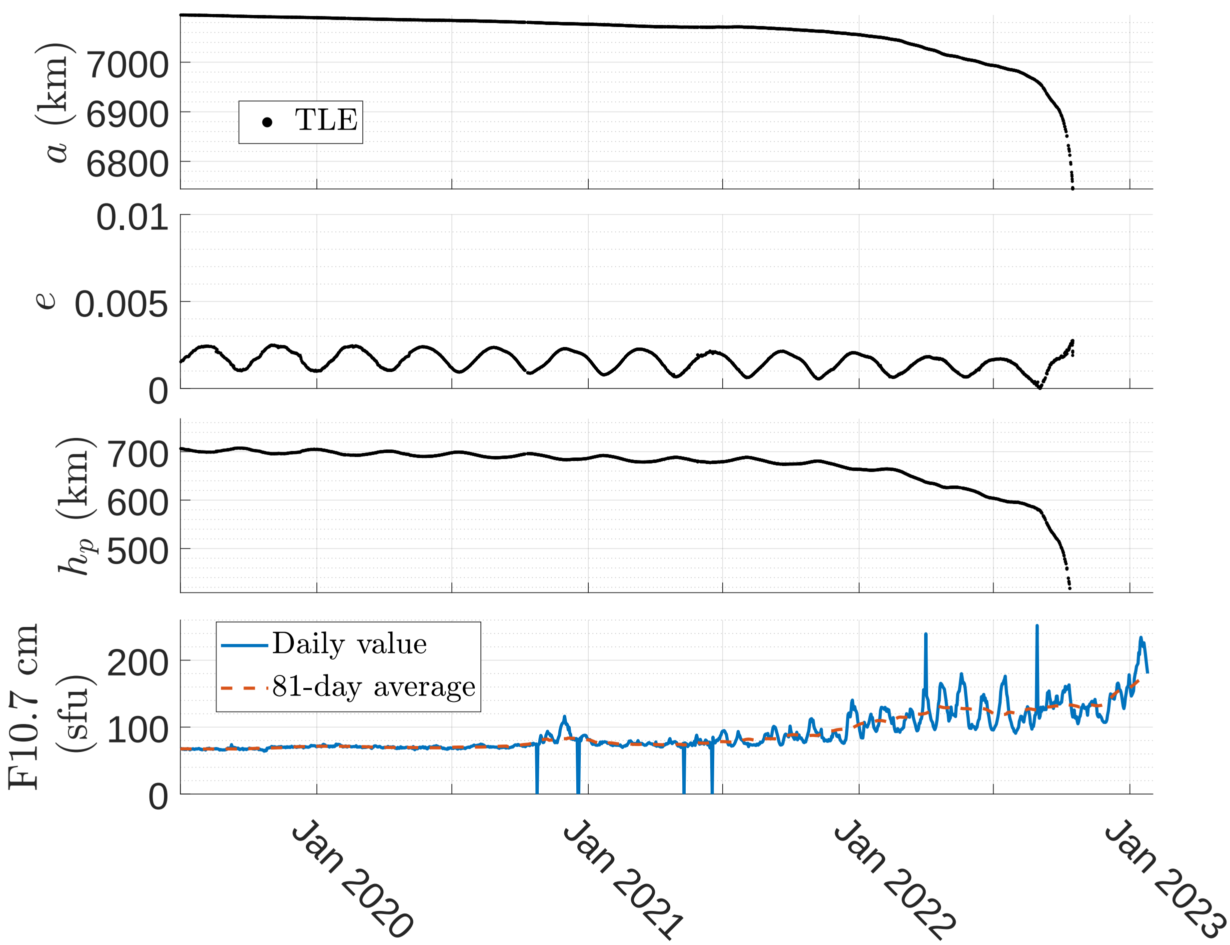

Figure 7.1: Recorded TLE data of LightSail 2 from July 7, 2019, to its re-entry on November 17, 2022, obtained in [32] compared to the recorded solar radio flux over the same period

[1]At different points, the operators of LightSail 2 changed the control parameters for testing purposes. This impacted the pointing accuracy during the mission.

It is important to note that the propulsion capacity of the spacecraft must have been reduced by the poor pointing accuracy, ranging from a 20° to 45°-error, as previously mentioned, but also the need to desaturate the momentum wheel. Based on [52], the drag compensation mode of LightSail 2, which re-orients the panel twice per orbit, relies on a momentum wheel-based control system that cannot be used indefinitely; it requires periodic desaturation during which the accumulated momentum is dumped to restore manoeuvrability and allow for adequate attitude control. The authors of [52] approximate the ON/OFF ratio of the drag compensation mode at 80% for LightSail 2.

The outcome of the Lightsail 2 mission motivates the analysis presented in the following section where we show how the previously presented resonance solution can be applied for semi-major axis tracking by exploiting STRP propulsion to compensate for the loss of altitude induced by the atmospheric drag in the low end of the LEO region.

7.2 Semi-major axis tracking criterion

Based on the results of Chapter 5, under the single-resonance assumption, the secular evolution of the semi-major axis a is governed by its resonant STRP (j,k)-term given by Eq. (5.9) from which we can deduce the extreme decrease and increase rates given for $\psi_{j,k} = \frac{\pi}{2}$ and $\psi_{j,k} = -\frac{\pi}{2}$ respectively:

$$\begin{aligned} \dot{a}_{j,k\text{-min}} &= -\tau_{\text{desat}} C_{\text{STRP}} \frac{2}{n\sqrt{1-e^2}} \mathcal{T}_j C_k \\ \dot{a}_{j,k\text{-max}} &= \tau_{\text{desat}} C_{\text{STRP}} \frac{2}{n\sqrt{1-e^2}} \mathcal{T}_j C_k \end{aligned} \tag{7.1}$$

where $C_{\text{STRP}} = P_r \beta \frac{A_{\text{nom}}}{m}$ as per Eq. (2.16). Note that τ_{desat} was introduced in Eq. (7.1) to account for the required desaturation periods, and hence, it represents the fraction of the time for which the tracking is active.

The magnitude of the semi-major axis rate is the greatest for maximal values of $\mathcal{T}_j$ and C_k given by Eqs. (2.23) and (2.30) respectively. As noted previously throughout the thesis, notwithstanding the $k = 0$ passive resonance corridor, these are maximal for a (1,2)-resonance (when $i < 90°$). Moreover, the C_k value is at its peak for $\sigma_{rs} = 1$, i.e., a perfectly reflective surface similar to the Mylar sail of LightSail 2. Thereupon, we define the following control setpoint for tracking of the semi-major axis reference a_{ref}:

$$\psi_{1,2\text{ ref}} = \arctan\left\{K_p\left(a_{\text{ref}} - \overline{a}\right)\right\} \tag{7.2}$$

Because we are interested in the secular evolution of the semi-major axis, we filter the short-period oscillations in a over an orbit to obtain $\overline{a}$ used in the computation of the reference resonant angle $\psi_{1,2\text{ ref}}$. In Eq. (7.2), the proportional gain K_p is computed, based on Eq. (7.1), as a function of the desired response time τ_r as:

$$K_p = \tau_{\text{desat}} C_{\text{STRP}} \frac{2}{n\sqrt{1-e^2}} \mathcal{T}_j C_k \tau_r \tag{7.3}$$

The reference attitude $\phi_{r,a\text{-tracking}}$ is therefore obtained similarly to Eq. (5.12) as:

$$\phi_{r,a\text{-tracking}} = \frac{\Omega + \omega + \nu + \lambda_S + \arctan\left\{K_p\left(a_{\text{ref}} - \overline{a}\right)\right\}}{2} \tag{7.4}$$

In the following section, we implement this tracking criterion in D-SPOSE and generate results for various semi-major axis references.

7.3 Numerical verification

The goal of this section is to verify in D-SPOSE that a STRP-J_2-ϕ resonance in a allows the tracking of a_{ref} by a reflective sail ($\sigma_{rs} = 1$). We first generate results for a 1 m^2/kg sail, and compare them to propagation results obtained for a 6.4 m^2/kg sail, which is more representative of the LightSail 2. As for the previous simulations, propagations are carried out under the attitude control law of Eq. (5.16) for $\phi_r = \phi_{r,a\text{-tracking}}$ of Eq. (7.4) where the accelerations and torques due to the following perturbations are included:

- STRP: Eq. (2.14) for a constant radiation pressure $P_r = \frac{1{,}361}{c}\ \frac{\text{N}}{\text{m}^2}$
- gravitational field: EGM2008 up to degree and order 5
- drag: NRLMSISE-00 with *recorded* equivalent planetary amplitude Ap and solar radio flux F10.7 cm
- Earth shadow: geometric model with penumbra transition as implemented in D-SPOSE [65]

Note that, differently from the simulations of Section 5.2.3, we use here the recorded equivalent planetary amplitude Ap and solar radio flux F10.7 cm since the time variation of the latter is of critical importance for this analysis. The O8 and O9 orbits defined in Table 7.1 are used to initialize the simulations. The O9 orbit, employed for the propagation of the 6.4 m^2/kg sail, corresponds to the recorded position of LightSail 2 at epoch T2: 2019-09-21T20:13:56. This epoch is used to initialize all simulations. For the $\frac{A_{\text{nom}}}{m} = 1$ m^2/kg sail case, the initial conditions are set to be those of the O8 orbit. It corresponds to O9 but with $i = 60°$ instead. Desaturation periods of 2.4 hours for which active control is turned off ($\tau_c = 0$ see Eq. (5.16)) were also included in D-SPOSE twice per day ($\tau_{\text{desat}} = 0.80$). For the propagations presented in this section, K_p is set to 1,800 so that the response time τ_r is on the order of a few hours. The drag coefficient is set to $C_d = 2.2$ for the simulations.

Table 7.2 compares the deorbitation dates of the various test cases presented in this section.

Table 7.1: Orbital initial conditions for a-tracking analysis and associated area-to-mass ratio

	a (km)	e	i (°)	Ω (°)	ω (°)	ν (°)	ϕ (°)	$\frac{A_{\text{nom}}}{m}$ (m^2/kg)
O8	7,093	0.0010	60.00	172.8	47.38	312.8	0	1
O9	7,093	0.0010	24.00	172.8	47.38	312.8	0	6.4

Table 7.2: Re-entry date for propagation test-cases of Section 7.3

Fig.	a_{ref} (km)	ϕ_{ref} (°)	$\frac{A_{\text{nom}}}{m}$ (m^2/kg)	Re-entry date
7.2, 7.3	N/A	0	1	Feb. 10, 2023
7.2	7,093	N/A	1	N/A
7.2	7,200	N/A	1	N/A
7.3	7,000	N/A	1	Nov. 22, 2022
7.3	7,050	N/A	1	N/A
7.5	N/A	0	6.4	Jan. 11, 2021
7.5	7,093	N/A	6.4	Feb. 24, 2023
7.6	7,000	N/A	6.4	Mar. 31, 2022

7.3.1 1 m^2/kg sail test case

For this first test case, the sail is modelled as a 32 m^2 square as per LightSail 2 dimensions, but with a mass of $m = 32$ kg yielding an area-to-mass ratio of $\frac{A_{\text{nom}}}{m} = 1$ m^2/kg. The control gains are adjusted as per the spacecraft mass, based on Eq. (5.30).

Fig. 7.2 shows the orbital a, e and h_p as well as the (1,2)-resonant angle responses when tracking $a_{\text{ref}} = 7,093$ km so as to maintain the initial semi-major axis (yellow curves), and when tracking the higher $a_{\text{ref}} = 7,200$ km (orange curves). This last setpoint is chosen to assess the capabilities of the a-resonance strategy for orbit raising. For comparison, the results obtained for the constant value of $\phi_r = 0°$, i.e., where the spacecraft maintains a constant attitude in inertial space, are also shown in Fig. 7.2 (blue curves).

The ability to maintain altitude is clearly demonstrated by the results of Fig. 7.2. The reflective 1 m^2/kg panel in O8 at epoch T2 would deorbit by February 2023 when a constant attitude setpoint is used (blue curves). However, under active a_{ref} tracking, results indicate the maintenance of the semi-major axis within ±10 km passed that date. The ±10 km variations are due to the short-period oscillations which we do not account for in the suggested tracking law. Indeed, only the secular evolution of a is of interest here.

Moreover, until December 2022, the semi-major axis tracking at $a = 7,093$ km is achieved while keeping the resonant angle $\psi_{1,2}$ between $-65°$ and $10°$. This is well within the limits of maximal propulsion: $\psi_{1,2} = \pm 90°$ (see yellow curves in Fig. 7.2). However, due to the increase in solar activity passed that date, the resonant angle $\psi_{1,2}$ saturates at the $-90°$ limit after December 2022. The increase in atmospheric density resulting from higher solar activity becomes too important, and the maximum STRP propulsion capabilities of the sail are insufficient to completely compensate for the atmospheric drag. A prolonged period of intense solar activity would cause

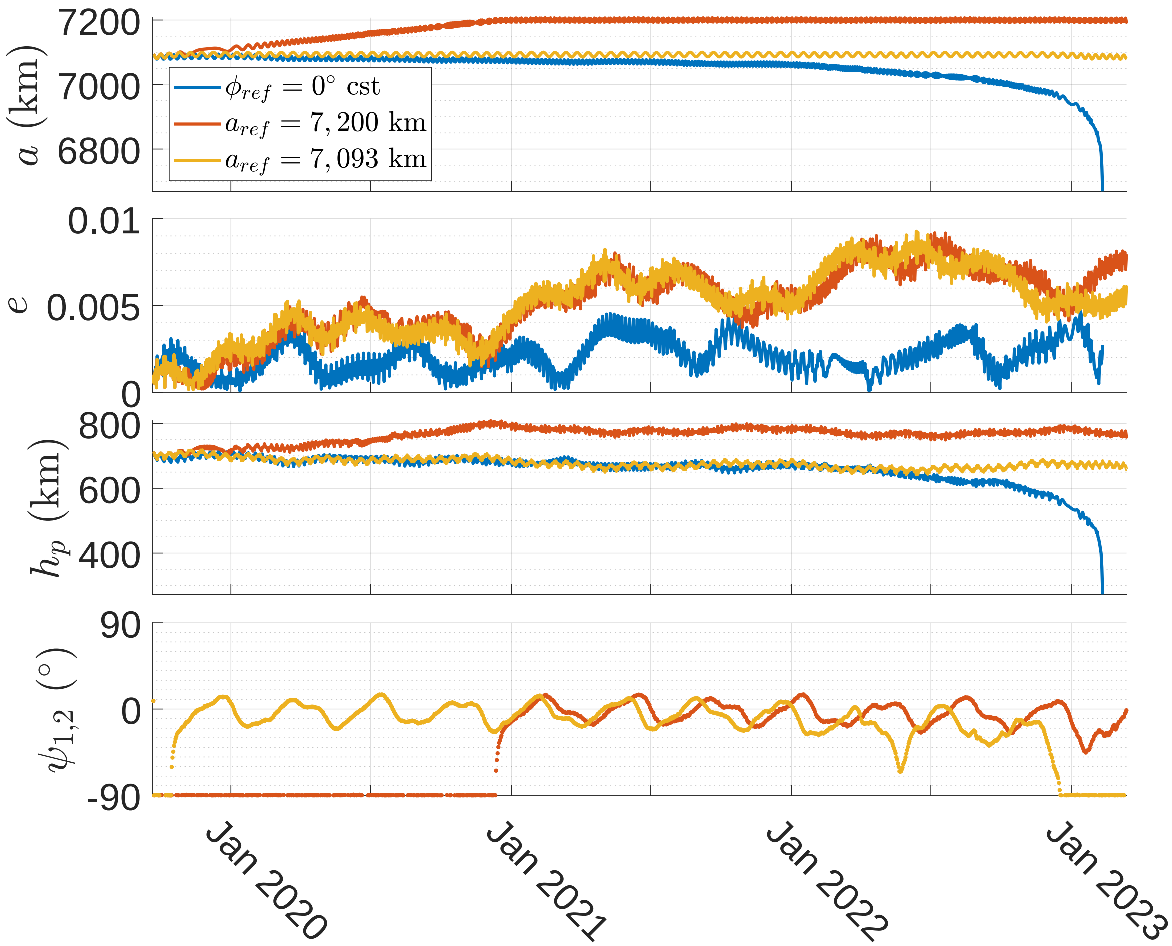

Figure 7.2: Orbital and resonant angle responses for propagation of 1 m^2/kg panel in D-SPOSE with semi-major axis tracking control

the sail to descend further. To better illustrate the correlation between the solar activity and the required propulsion efforts, Fig. 7.4 compares the recorded solar radio flux F10.7 cm to the $\psi_{1,2}$ evolution for the tracking of $a_{\text{ref}} = 7,093$ km setpoint.

An increase in eccentricity, from 0.001 to 0.009 for the tracking of $a_{\text{ref}} = 7,093$ km (yellow curves) and $a_{\text{ref}} = 7,200$ km (orange curves), is also observed in Fig. 7.2. The increase is sufficiently high after three years to reduce the altitude of the perigee by ~ 65 km, which, for these orbits, is significant vis-a-vis the resulting increase in atmospheric drag. The tracking criterion of Eq. (7.4) is designed to track a, but contains no provision for maintaining a constant eccentricity. Future investigations should consider the trade-off of maintaining a vs. e.

The ability to raise the semi-major axis to a reference value is also established by the propagation results of Fig. 7.2 (orange curves) where the spacecraft is set to reach a reference a value of 7,200 km. As presented in Section 7.2, the rate at which the spacecraft is able to raise its orbit is limited by the value $\dot{a}_{1,2\text{-max}}$ achieved at $\psi_{1,2} = -90°$ (see Eq. (7.1)). This is confirmed by the resonant angle response over the first year and the constant slope in a over that same period. We make a note that for a given (j,k)-resonance and specific optical properties, the increase/decrease rates of a are mainly limited by the nominal area-to-mass ratio of the spacecraft.

Semi-major axis tracking at low altitudes

Fig. 7.3 shows the orbital a, e and h_p as well as the (1,2)-resonant angle responses when tracking low semi-major axis reference values of $a_{\text{ref}} = \{7000; 7050\}$ km. For comparison, the results obtained for $\phi_r = 0°$ are shown as well (blue curves).

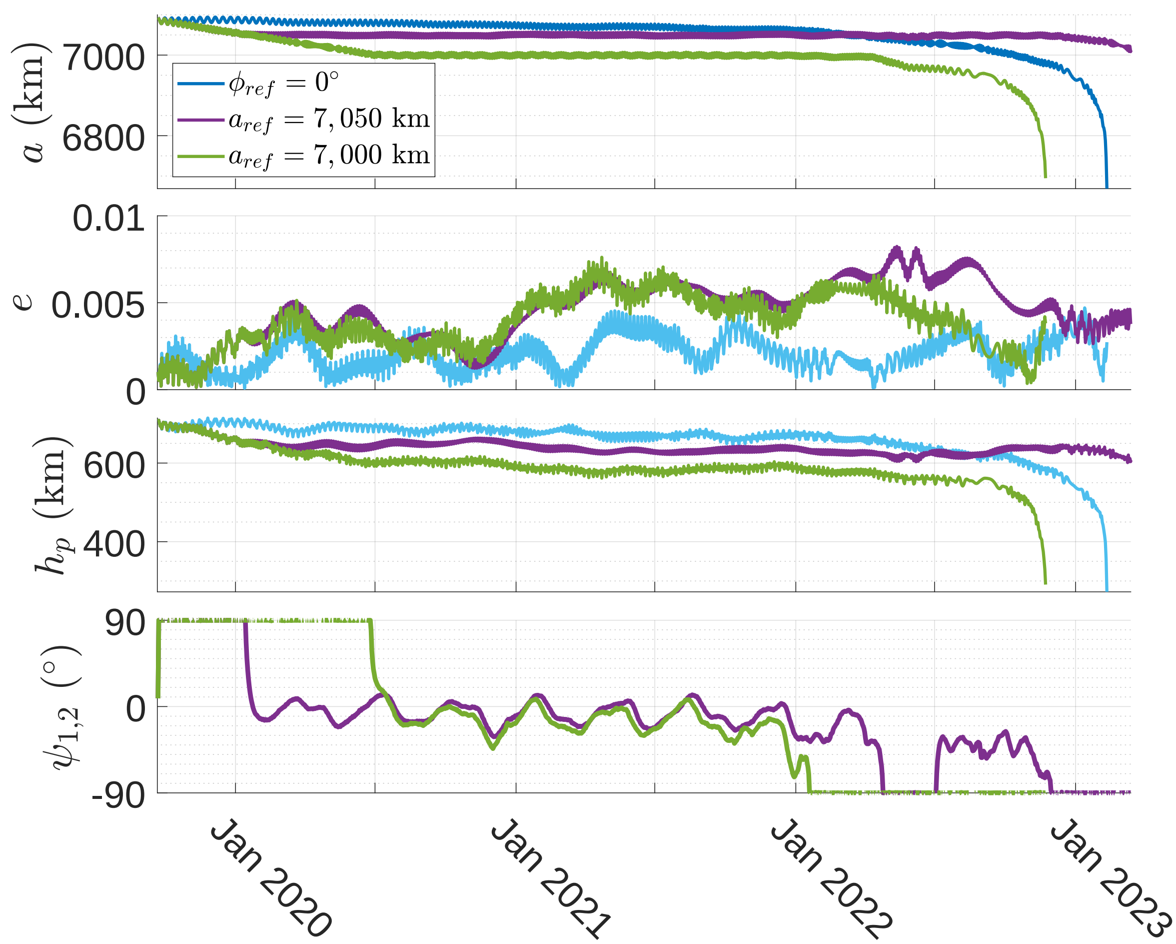

Figure 7.3: Orbital and resonant angle responses for propagation of 1 m^2/kg panel in D-SPOSE with semi-major axis tracking control

In Fig. 7.3, we explore the ability of the solar sail to maintain its semi-major axis in a region where atmospheric drag is substantial, i.e., under 700 km altitudes. These results further show the sensitivity of the a-resonance scheme to solar flux intensity and altitude. To support this, Fig. 7.4 compares the recorded solar radio flux F10.7 cm to the $\psi_{1,2}$ evolution for the tracking of $a_{\text{ref}} = \{7,050; 7,000\}$ km. These semi-major axis values correspond to perigee altitudes of ~ 675 km and ~ 625 km, respectively. As we can see from Fig. 7.4, the solar flux increases in the second part of 2021 and the trend continues through 2022. As a result, in January 2022, the atmospheric drag at ~ 625 km is too large for altitude maintenance and causes the 1 m^2/kg sail to re-enter Earth's atmosphere in November 2022 (green curves in Figs. 7.3 and 7.4).

Although the high solar intensity observed during that period is not sufficient to trigger the decay of the slightly higher sail (~ 675 km), the even stronger increase in solar activity passed November 2022 is (purple curves in Figs. 7.3 and 7.4). In Fig. 7.3, we can see the decrease in semi-major axis from $a = 7{,}050$ km in December 2022 to $a = 7{,}000$ km in April 2023.

Finally, from the $\psi_{1,2}$ time responses in Figs. 7.2 and 7.3, we can observe that, the higher the altitude, the closer the mean $\psi_{1,2}$ value is to 0 indicating that less propulsion power is required. This is in line with the reduction of atmospheric drag at higher altitudes, thus, this strategy shows better altitude manoeuvring capabilities at higher orbits.

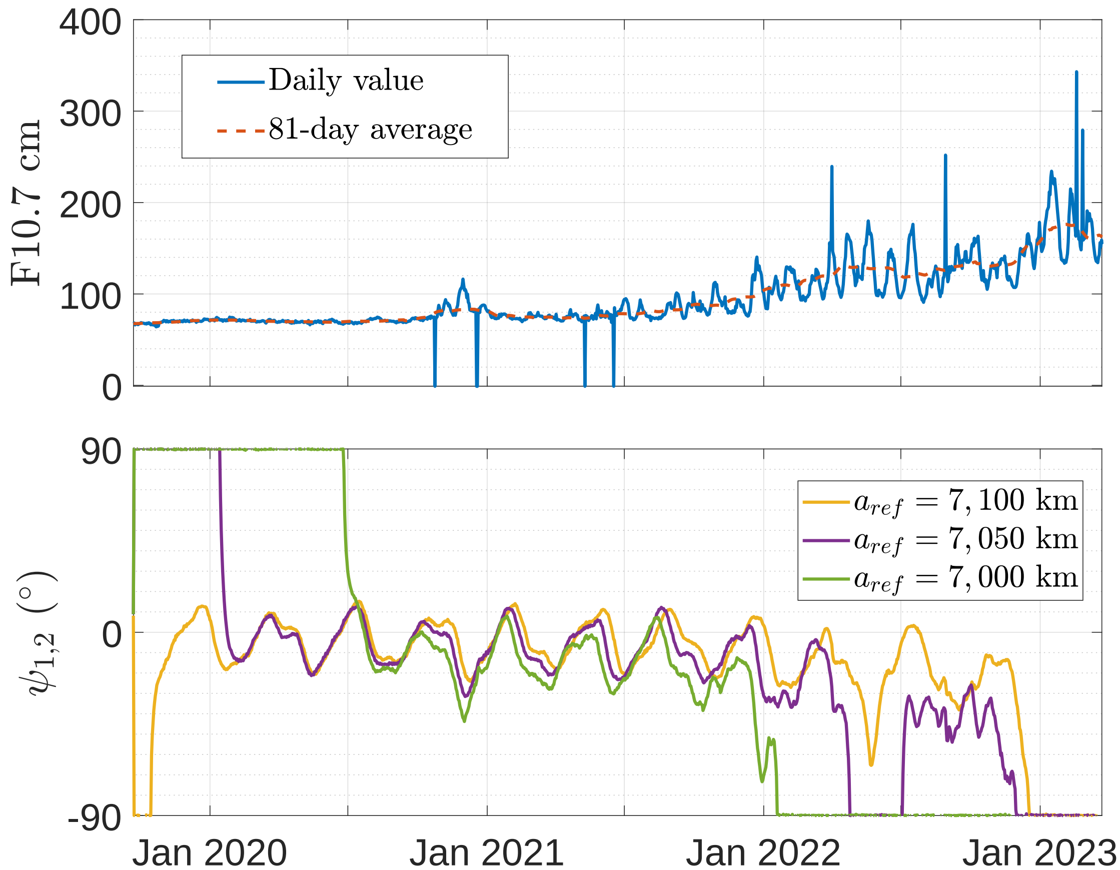

Figure 7.4: Solar radio flux impact on resonant angle (from Fig. 7.5) for propagation of 1 m^2/kg panel in D-SPOSE with semi-major axis tracking control

7.3.2 6.4 m^2/kg sail test case

For this second test case, the sail parameters are set to represent those of the LightSail 2 spacecraft. The sail is still modelled as a 32 m^2 square, but with a mass equal to that of LightSail 2, i.e.,

$m = 5$ kg, yielding an area-to-mass ratio of $\frac{A_{\text{nom}}}{m} = 6.4$ m^2/kg. The control gains are adjusted as per the spacecraft mass, based on Eq.(5.30). Propagations are carried out under the same conditions as for Figs. 7.2 and 7.3. The resulting orbital a, e and h_p as well as the (1,2)-resonant angle responses when tracking semi-major axis reference values of $a_{\text{ref}} = 7,093$ km and $a_{\text{ref}} = 7,000$ km are presented in Figs. 7.5 and 7.6 respectively. The results obtained for $\phi_r = 0°$ (blue curves) are also shown as reference in the first figure. Note that the semi-major axis response of the 1 m^2/kg sail for $a_{\text{ref}} = 7,093$ km setpoint presented in Fig. 7.2 is included in Fig. 7.5 for comparison. The same for the a response of Fig. 7.3 when tracking $a_{\text{ref}} = 7,000$ km which we included in Fig. 7.6.

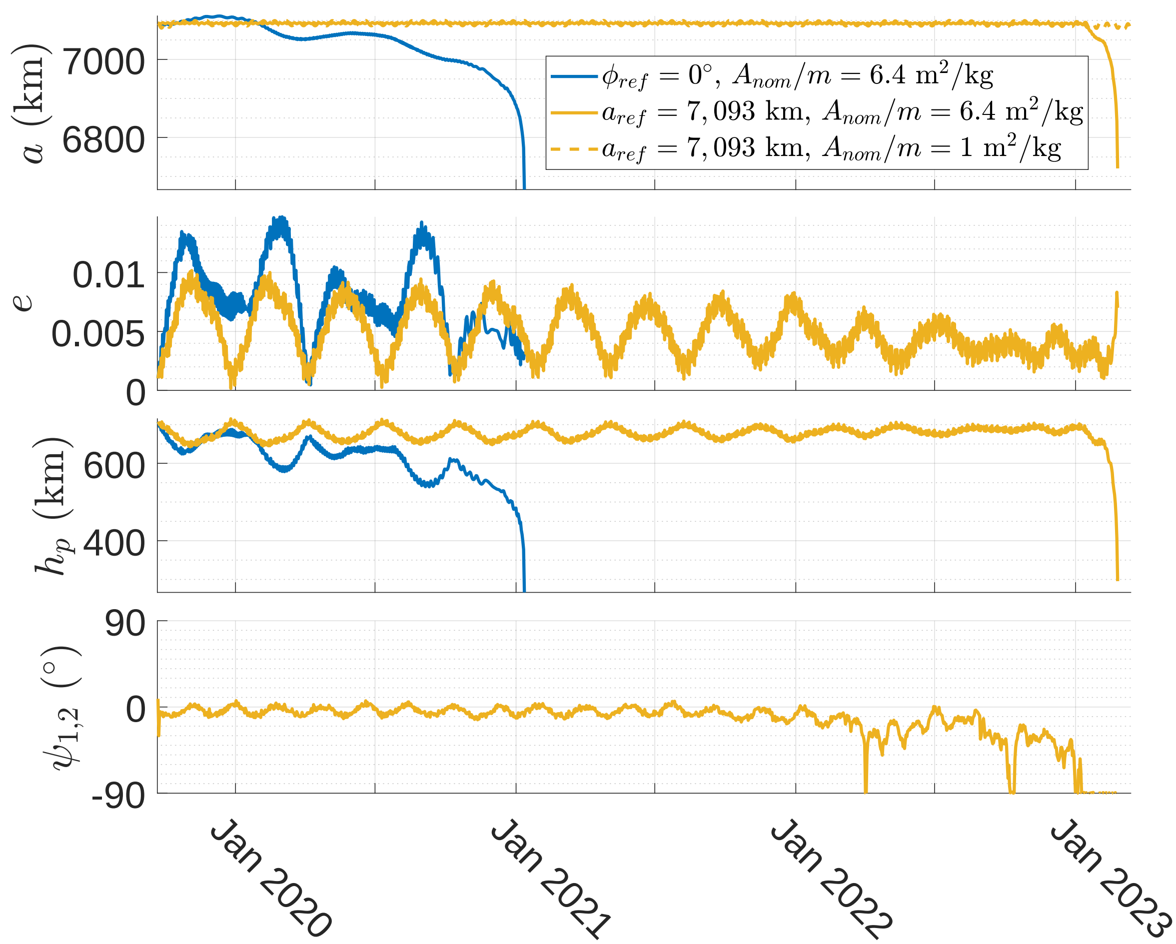

Figure 7.5: Orbital and resonant angle responses for propagation of 6.4 m^2/kg panel in D-SPOSE with semi-major axis tracking control for $a_{\text{ref}} = 7,093$ km

As observed for the 1 m^2/kg sail, using the proposed tracking criterion allows the spacecraft to maintain the orbit significantly longer than when $\phi_r = 0°$ (yellow vs. blue curves in Fig. 7.5). We can also observe from the results of Fig. 7.6, a steeper decrease in a at $\psi_{1,2} = -90°$ limit value due to the 6.4 times higher area-to-mass ratio compared to the sail of Fig. 7.3 (solid vs. dashed purple curves). This increase in $\frac{A_{\text{nom}}}{m}$ allows for stronger STRP propulsion which accelerates the descent from a 7,093 km to a 7,000 km semi-major axis.

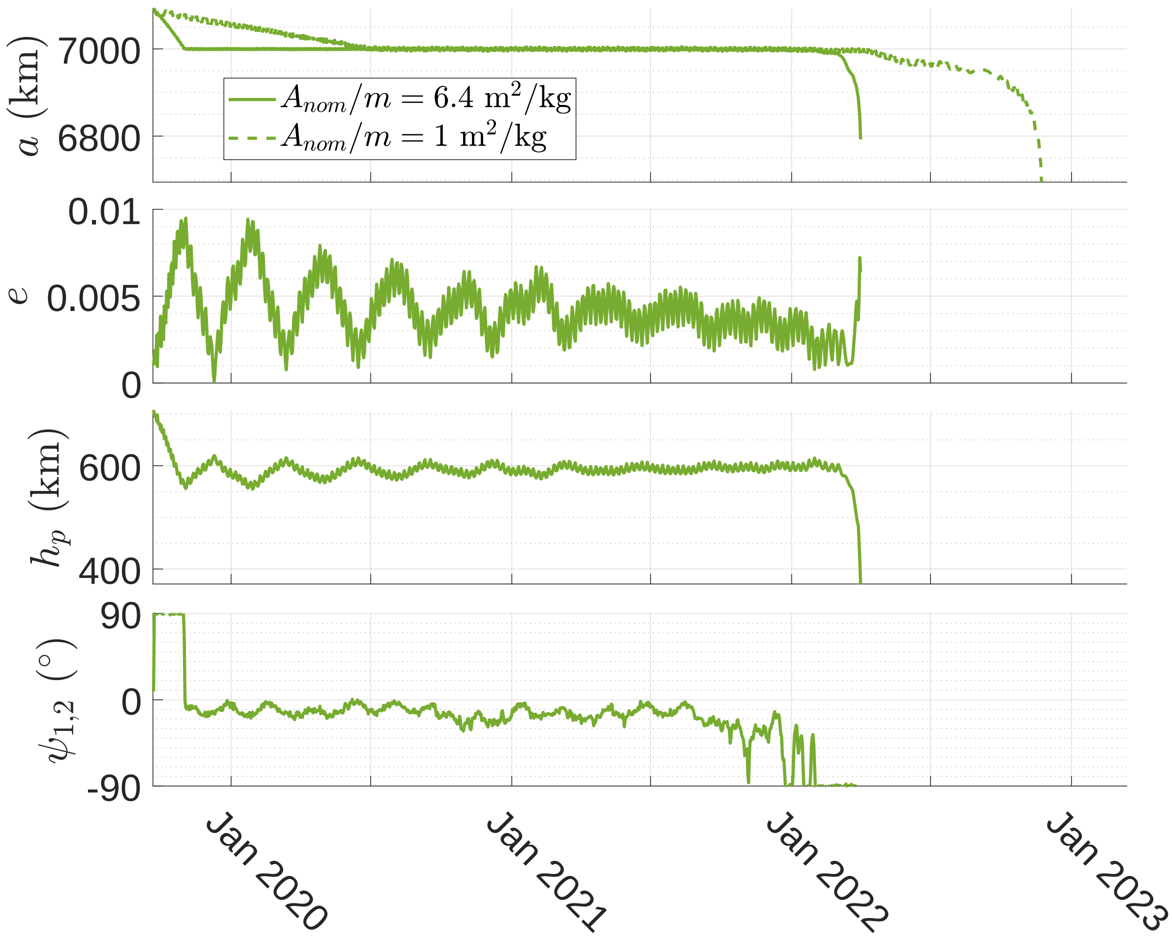

Figure 7.6: Orbital and resonant angle responses for propagation of 6.4 m^2/kg panel in D-SPOSE with semi-major axis tracking control for $a_{\text{ref}} = 7,000$ km

Although the high-area-to-mass ratio of the spacecraft improves the STRP propulsion, it makes it even more sensitive to atmospheric drag and fluctuations in solar flux. According to the propagation data presented in this section, the 1 m^2/kg sail was able to properly track a semi-major axis reference of 7,093 km passed April 2023, while the 6.4 m^2/kg sail was not, and this, under the exact same conditions (solid vs. dashed curves in Fig. 7.5). The same was observed when tracking the 7,000 km setpoint, for which the lower $\frac{A_{\text{nom}}}{m}$ sail remained in orbit longer, and this, even with the higher STRP propulsion capabilities of the 6.4 m^2/kg sail, enabled by the larger area-to-mass ratio (solid vs. dashed curves in Fig. 7.6).

7.4 Concluding remarks

With the perspective of the LightSail 2 mission, we expanded the application of the a-resonance strategy to semi-major axis tracking. The key takeaway from the analysis presented in this chapter is the high sensitivity of the minimum maintainable altitude to solar activity. This threshold altitude is highly dependent on the relative propulsion power extracted from STRP vs. the strength of the atmospheric drag.

A higher $\frac{A_{\text{nom}}}{m}$ has a positive effect on the former, but also increases the latter through raising the atmospheric drag. Therefore, the interplay of these factors should be evaluated on a case-by-case basis to establish the feasibility of a-tracking and hence, orbit maintenance through the exploitation of a-resonance for a particular mission.

Chapter 8

Conclusion

This thesis focused on the case of spacecraft in LEO where the main perturbations at play are the STRP, the geopotential (mainly its second zonal harmonic) and atmospheric drag. More specifically, this work investigated the possibility of exploiting STRP-J_2-ϕ resonances for end-of-life disposal of spacecraft; the main objective was to propose a low-cost, reliable deorbitation alternative to mitigate the spacecraft impact on space debris proliferation.

8.1 Fundamental theory of the STRP-J_2-ϕ resonance

To this end, we built on the most up-to-date analysis of the SRP-J_2 resonance of spherical spacecraft provided in the literature. Alessi's phase space equilibrium/stability theory was verified against the recorded motion of NASA's '60s Echo I balloon spacecraft. Results allowed us to draw general conclusions regarding the impact on the resonance magnitude of the spacecraft area-to-mass ratio, its proximity to the resonant inclination (as identified in the literature) and the phase angle. The main takeaway from this study is that, for typical area-to-mass ratio values, the intensity of the resonance is directly constrained by the location of the spacecraft and its proximity to the resonant inclination, also referred to as a passive deorbitation corridor. This is however not the case for non-spherical rotating spacecraft for which this theory is deficient.

Whereas state-of-the-art research falls short in terms of the resonant behaviour of a rotating object with a stable spin, a similar development to what is found in the literature was applied to generalize the resonant dynamics model. For this derivation, we considered a stably rotating panel as a fundamental model instead of the previously used cannonball assumption. Based on our formulation of the STRP-J_2-ϕ resonance model, a resonance effect can be generated at any point around Earth and is enabled by the coupling of the STRP, geopotential and periodic rotational motion. In this new scenario, the main factor influencing the state of the resonance is the rotation rate. Although the magnitude of a STRP-J_2-ϕ resonance is of smaller intensity than for the passive STRP-J_2 resonance, the potential of applications is much wider.

The case of a panel subject to STRP and J_2 perturbations, rotating at a constant rate about a fixed axis normal to the ecliptic plane acts as a proof for the possibility of coupled attitude-orbit resonances. These conditions were selected as they generate the strongest resonance for a given area-to-mass ratio to be used for spacecraft deorbitation. However, such a resonance scenario does not only apply to panels in this rotating state. The motion of an object of a more complex shape with periodic attitude variation could also lead to a resonance effect of considerable strength. As long as one can use a Fourier series expansion to express the spacecraft attitude with respect to the Sun (we used the α angle in this thesis) by a Fourier series expansion, the same approach can be employed, and similar conclusions can be drawn. Essentially, the higher the amplitude of the term associated with the fundamental frequency, the stronger can the effect be. The potential of resonant coupling between attitude and orbital motion is extremely important. Whereas attitude and orbital motions are two problems usually tackled independently, the work presented in this thesis confirmed the importance of seeing the two in combination.

In the case of eccentricity resonance for which the fundamental frequency is low (periods on the order of hundreds of days in LEO), the average dynamics was found to adequately characterize the resonant motion. This simplification however predicts a constant semi-major axis over time, which might not hold in resonance. As was shown in this thesis, the fundamental frequency characterizing the semi-major axis dynamics is fast varying, on the order of the mean motion n. When the rate of attitude change with respect to the incoming light direction is commensurate with the mean motion n, then short-period oscillations become secular. Averaged models are very useful to isolate main secular tendencies, and in the field of orbital propagation, are very convenient to quickly predict long-term motion. The strict assumptions made in developing the averaged models found in the literature, however, limit the applications of such models. With complex oscillatory motion, one needs to be mindful of the possibility of having frequencies that are commensurate. The takeaways from this could be used to develop more accurate averaged orbital models, that would account for coupling to rotational motion, for better fast predictions.

8.2 STRP-J_2-ϕ resonances for deorbitation

The newly developed theory, based on the assumption that the only perturbations at play are STRP and the geopotential J_2 harmonic, was used to assess the ability to exploit this phenomenon to induce re-entry. The conclusions were verified in the numerical environment modelled by D-SPOSE. Although the eccentricity resonance for constant rotation speed could lead to a great increase in e, this might not be sufficient to ensure the complete decay of the spacecraft. Under certain conditions, it may even have the opposite effect. It was shown that the neglected perturbations can have a substantial impact on the resonance dynamics by affecting the regime—libration or circulation—and the proximity to either a stable or unstable equilibrium, in turn, affecting the minimum attainable altitude.

Building on the theoretical analysis put forward for a rotating plate-like spacecraft, we thus proposed a novel strategy relying on attitude control to lift the minimum attainable altitude limitation associated with a constant rotation rate, to achieve full spacecraft decay at end-of-life. The goal is the reduction of the altitude to enhance atmospheric drag effects to accelerate deorbitation. Through proper attitude control, we demonstrated that it is possible to exploit the resonant action of the STRP to produce a change in eccentricity, then further extended the solution to semi-major axis resonance as well. The latter was also shown to allow for semi-major axis tracking, which testifies to the applicability of such a solution to orbital manoeuvring, assuming active attitude control of the spacecraft. A thorough analysis of the resonance solution, in eccentricity or in semi-major axis, was provided based on simulation results obtained in D-SPOSE.

A critical comparison of the proposed schemes to previously published bang-bang type STRP-exploiting deorbitation strategies was performed, from which we highlighted the advantages and limitations of the different solutions. The first takeaway from this analysis is that, for an object in the vicinity of a deorbitation corridor, the fastest way towards deorbitation by exploiting STRP propulsion is to exploit the passive deorbitation corridor. Not only is the resonance effect stronger, but it is also robust to spacecraft failure. However, this solution can only be employed if the satellite is already near such a deorbitation corridor so that the delta-v required to change the initial orbit is small. When not in the vicinity of such a corridor, solutions aiming to decrease the semi-major axis are more efficient than those aiming to increase the eccentricity. And, in the case of a perfectly reflective panel, it is the resonance in the semi-major axis that produces a slightly faster decay than the bang-bang approach. However, we suggest that, in light of the much simpler attitude requirements of the resonance solution, i.e., maintaining an almost constant rate of rotation about a fixed axis, makes it a more practical solution than the bang-bang scheme. The latter solution requires the spacecraft to perform 90° changes in its orientation twice per orbit.

8.3 Possible application of STRP-J_2-ϕ resonances for ADR

The majority of hazardous debris is not orbiting in the vicinity of the very specific passive deorbitation corridors. To eliminate this limitation on the orbit, the proposed deorbitation solutions exploiting resonance in either semi-major axis or eccentricity were suggested as end-of-life disposal means. They are particularly suitable for spacecraft equipped with a large and controllable surface (e.g. a sail) relative to their mass. As well, these strategies rely on the ability of the spacecraft to orient itself with respect to the Sun. Although, in the analysis provided, it was assumed that control capabilities had to come from the internal satellite control system, i.e., that the spacecraft be operable, this is not essential. The proposed solution could be applied to uncontrolled debris if external control of its attitude can be implemented.

The first phase of the Astroscale ADR mission objective, the ELSA-d mission, carried out from 2021 to 2022, proved the feasibility of a close approach between a chaser and debris. This is the first step towards a complete ADR mission. Although, to the best of our knowledge, Astroscale has not yet divulged how the chaser will provoke the re-entry of the debris in their future missions, one can expect that they will use a strategical delta-v (ΔV) impulse generated by propulsion means still undetermined. For the Astroscale mission, the debris is small. However, in the case of large and massive debris, such a strategy turns out to be very onerous as the required power to generate the desired ΔV increases with mass. In these cases, STRP propulsion could be an advantageous alternative. Furthermore, the possibility of exploiting the own area of the debris to enhance the propulsion power of STRP with strategies discussed in this thesis, makes it an interesting option. Also, using the resonance greatly reduces the power requirements for the chaser as it only requires enforcing an almost constant rotation rate contrary to the bang-bang type solutions that would require large periodic reorientation manoeuvres. STRP-J_2-ϕ resonances thus appear like a suitable option for the disposal of large orbiting debris, with reasonable area-to-mass ratios. The possibilities enabled by this approach could greatly reduce the cost of future ADR missions, which will become essential in the near future, as predicted by the IADC for the mega-constellation era.

Appendix A

Equinoctial Elements

We present in this appendix the equinoctial elements used to work around the singularity arising when using the Keplerian element ω based on [82].

Several sets of equinoctial elements exist including the retrograde and the direct sets. Here we use the latter. It is important to note that this set of equations presents singularities when the inclination tends to π for equatorial satellites.

In order to define the equinoctial elements, we first introduce the equinoctial frame $\mathcal{F}_E = \{O, \underset{\rightarrow}{f}, \underset{\rightarrow}{g}, \underset{\rightarrow}{w}\}$ illustrated in Fig. A.1. The direct equinoctial elements expressed in terms of the Keplerian elements are:

$$\begin{aligned}
a &= a \\
h &= e\sin(\omega + \Omega) \\
k &= e\cos(\omega + \Omega) \\
p &= \tan\left(\frac{i}{2}\right)\sin\Omega \\
q &= \tan\left(\frac{i}{2}\right)\cos\Omega \\
L &= \nu + \omega + \Omega
\end{aligned} \tag{A.1}$$

Based on Eqs. (5.14) and (5.15), the parameters of interest in Eq. (A.1) are h, k, and the true longitude L.

D-SPOSE propagates the position and velocity vectors expressed in the Earth-Centred-Inertial (ECI) frame, $\mathcal{F}_{\text{ECI}}$ denoted by $\mathbf{r}$, $\mathbf{v}$ respectively. The first step in determining the equinoctial elements from the position and velocity vectors expressed in $\mathcal{F}_{\text{ECI}}$ is to compute the $\mathcal{F}_E$ basis

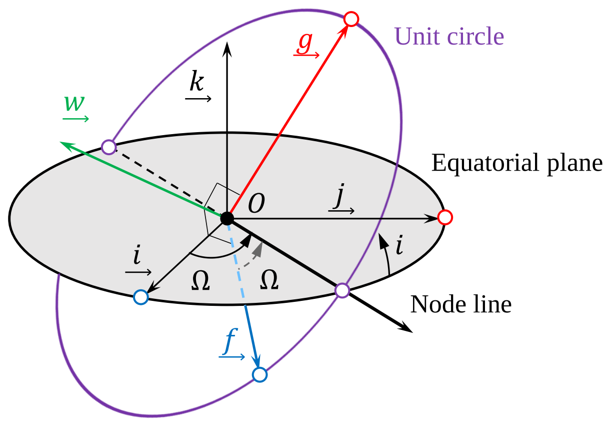

Figure A.1: Direct equinoctial reference frame reproduced from [82]

vectors also expressed in $\mathcal{F}_{\text{ECI}}$ ($\mathbf{f}$, $\mathbf{g}$, $\mathbf{w}$) as follows:

$$\begin{aligned}\mathbf{w} &= \frac{\mathbf{r}\times\mathbf{v}}{|\mathbf{r}\times\mathbf{v}|} \\ \mathbf{f} &= \frac{1}{1+p^2+q^2}\begin{bmatrix}1-p^2+q^2 \\ 2pq \\ -2p\end{bmatrix} \\ \mathbf{g} &= \frac{1}{1+p^2+q^2}\begin{bmatrix}2pq \\ 1+p^2-q^2 \\ 2q\end{bmatrix}\end{aligned} \tag{A.2}$$

where the elements p and q are given by:

$$\begin{aligned}p &= \frac{w_x}{1+w_z} \\ q &= -\frac{w_y}{1+w_z}\end{aligned} \tag{A.3}$$

and $\mathbf{w} = [w_x,\, w_y\, w_z]$. The eccentricity vector expressed in $\mathcal{F}_E$ is given by:

$$\mathbf{e} = -\frac{\mathbf{r}}{\mathbf{v}} + \frac{\mathbf{v}\times(\mathbf{r}\times\mathbf{v})}{\mu} \tag{A.4}$$

The equinoctial elements h and k are then:

$$\begin{aligned}h &= \mathbf{e}\cdot\mathbf{g} \\ k &= \mathbf{e}\cdot\mathbf{f}\end{aligned} \tag{A.5}$$

In order to obtain the true longitude L, we still need to compute the position coordinates in $\mathcal{F}_E$:

$$\begin{aligned} X &= \mathbf{r} \cdot \mathbf{f} \\ Y &= \mathbf{r} \cdot \mathbf{g} \end{aligned} \tag{A.6}$$

which are employed to obtain the eccentric longitude F:

$$\begin{aligned} \sin F &= h + \frac{(1-h^2 b)\,Y - h\,k\,b\,X}{a\sqrt{1-h^2-k^2}} \\ \cos F &= k + \frac{(1-k^2 b)\,X - h\,k\,b\,Y}{a\sqrt{1-h^2-k^2}} \end{aligned} \tag{A.7}$$

where:

$$b = \frac{1}{1+\sqrt{1-h^2-k^2}} \tag{A.8}$$

Finally, the true longitude $L = \arctan 2(\sin L, \cos L)$ can be computed from:

$$\begin{aligned} \sin L &= \frac{(1-k^2 b)\,\sin F + h\,k\,b\,\cos F - h}{1 - h\,\sin F - k\,\cos F} \\ \cos L &= \frac{(1-h^2 b)\,\cos F + h\,k\,b\,\sin F - k}{1 - h\,\sin F - k\,\cos F} \end{aligned} \tag{A.9}$$

Appendix B

Gauss' Singly-Averaged Equations of Motion

Gauss' equations of motion averaged over one orbit of the spacecraft ($\nu \in [0, 2\pi]$) for an object subject to STRP and J_2 perturbations are [11], [18]:

$$
\begin{aligned}
\frac{\mathrm{d}a}{\mathrm{d}t} &= 0 \\
\frac{\mathrm{d}e}{\mathrm{d}t} &= \frac{3}{2}\frac{(1-e^2)^{\frac{1}{2}}}{n\,a}\,a^*_{s,\,\mathrm{SRP}} \\
\frac{\mathrm{d}i}{\mathrm{d}t} &= -\frac{3}{2}\frac{e\cos\omega}{n\,a\,(1-e^2)^{\frac{1}{2}}}\,a_{w,\,\mathrm{SRP}} \\
\frac{\mathrm{d}\Omega}{\mathrm{d}t} &= \dot{\Omega}_{J_2} + \dot{\Omega}_{\mathrm{SRP}} \\
\frac{\mathrm{d}\omega}{\mathrm{d}t} &= \dot{\omega}_{J_2} + \dot{\omega}_{\mathrm{SRP}}
\end{aligned}
\tag{B.1}
$$

where $n = \sqrt{\mu/a^3}$ is the spacecraft mean motion. In the last two equations, the contributions to $\dot{\Omega}$ and $\dot{\omega}$ from the SRP and J_2 effects can be independently expressed as:

$$
\begin{aligned}
\dot{\Omega}_{\mathrm{SRP}} &= -\frac{3}{2}\frac{e\sin\omega}{n\,a\,(1-e^2)^{\frac{1}{2}}\sin i}\,a_{w,\,\mathrm{SRP}} \\
\dot{\Omega}_{J_2} &= -\frac{3}{2}\frac{J_2\,R_e^2\,n}{a^2\,(1-e^2)^2}\cos i \\
\dot{\omega}_{\mathrm{SRP}} &= -\frac{3}{2}\frac{(1-e^2)^{\frac{1}{2}}}{n\,a\,e}\,a^*_{r,\,\mathrm{SRP}} - \dot{\Omega}_{\mathrm{SRP}}\cos i \\
\dot{\omega}_{J_2} &= \frac{3}{2}\frac{J_2\,R_e^2\,n}{a^2\,(1-e^2)^2}\left(\frac{5}{2}\cos^2 i - \frac{1}{2}\right)
\end{aligned}
\tag{B.2}
$$

In Eqs. (B.1) and (B.2), $a_{r,\,\mathrm{SRP}}$, $a_{s,\,\mathrm{SRP}}$ and $a_{w,\,\mathrm{SRP}}$ are the components of the STRP acceleration (see Eq. (2.14)) in $\mathcal{F}_{\mathrm{LVLH}}$ ($\underset{\rightarrow}{a}_{\mathrm{SRP}} = a_{r,\mathrm{SRP}}\,\underset{\rightarrow}{r} + a_{s,\mathrm{SRP}}\,\underset{\rightarrow}{s} + a_{w,\mathrm{SRP}}\,\underset{\rightarrow}{w}$). Their, values are given in Eq. (B.3) for a black-body ($\sigma_a = 1$) [11]. The * notation used in Eqs. (B.1) and (B.2) represents the value at perigee, i.e., at $\nu = 0$.

$$
\begin{aligned}
\begin{Bmatrix} a^*_{r,\mathrm{SRP}} \\ a^*_{s,\mathrm{SRP}} \end{Bmatrix} &= P_r\,\beta\,\frac{A_p(t)}{m}\sum_{j=1}^{6}\mathcal{T}_j \begin{Bmatrix} \cos\psi_j \\ -\sin\psi_j \end{Bmatrix} \\
a_{w,\mathrm{SRP}} \begin{Bmatrix} \sin\omega \\ \cos\omega \end{Bmatrix} &= P_r\,\beta\,\frac{A_p(t)}{m}\sum_{j=1}^{6}\frac{\partial\mathcal{T}_j}{\partial i} \begin{Bmatrix} \cos\psi_j \\ -\sin\psi_j \end{Bmatrix}
\end{aligned}
\tag{B.3}
$$

with the time-variant projected area $A_p(t) = \cos\alpha(t)\,A_{\mathrm{nom}}$. The argument ψ_j employed in (B.3) can be expressed as $\psi_j = n_1\,\Omega + n_2\,\omega + n_3\,\lambda_S$ where the values of n_1, n_2 and n_3 for $j = \{1,2,...,6\}$ are stated in Table 2.1.

Appendix C

Differential Equation of True vs. Mean Anomaly

From Kepler's law of motion the mean anomaly M can be expressed in terms of the eccentric anomaly E, and the eccentricity e as:

$$M = E - e \sin E \tag{C.1}$$

Differentiating this equation with respect to E yields:

$$\frac{\mathrm{d}M}{\mathrm{d}E} = 1 - e \cos E \tag{C.2}$$

Also, still from Kepler's law of motion, we have:

$$\nu = \arccos\left[\frac{\cos E - e}{1 - e \cos E}\right] \tag{C.3}$$

Differentiating this equation and simplifying yields:

$$\frac{\mathrm{d}\nu}{\mathrm{d}E} = \frac{(1-e^2)^{1/2}}{1 - e \cos E} \tag{C.4}$$

Then, from Eqs. (C.2) and (C.4), we have:

$$\frac{\mathrm{d}M}{\mathrm{d}\nu} = \frac{(1 - e \cos E)^2}{(1-e^2)^{1/2}} \tag{C.5}$$

Making use of

$$1 - e \cos E = \frac{1-e^2}{1 + e \cos \nu} \tag{C.6}$$

along with Eq. (C.5), we finally have:

$$\frac{\mathrm{d}M}{\mathrm{d}\nu} = \frac{(1-e^2)^{3/2}}{(1+e\cos\nu)^2} \tag{C.7}$$

and inversely

$$\frac{\mathrm{d}\nu}{\mathrm{d}M} = \frac{(1+e\cos\nu)^2}{(1-e^2)^{3/2}} \tag{C.8}$$

Bibliography

[1] C. Massé, I. Sharf, and F. Deleflie, "SRP-J2 resonances in low earth orbits for objects with a time-variant area-to-mass ratio," in *Proceedings of the 31st AAS/AIAA Space Flight Mechanics Meeting*, AAS 21-375, Feb. 2021, pp. 3169–3187.

[2] C. Massé, I. Sharf, and F. Deleflie, "Exploitation of SRP-J2-phi resonances for de-orbitation of space objects with time-variant area-to-mass ratio," in *Proceedings of the 72nd International Astronautical Congress*, IAC–21–C1.7.6, Oct. 2021.

[3] C. Massé and I. Sharf, "Echo I case study of SRP effect on orbital motion," in *Proceedings of the 73rd International Astronautical Congress*, IAC–22–C1.9.9, Sep. 2022.

[4] C. Massé and I. Sharf, "Exploitation of thermal radiation resonance for deorbitation of spacecraft through attitude control," in *Proceedings of the 73rd International Astronautical Congress*, IAC–22–A6.5.3, Sep. 2022.

[5] C. Massé, I. Sharf, and F. Deleflie, "Exploitation of STRP and J2 perturbations for deorbitation of spacecraft through attitude control," *Acta Astronautica*, vol. 203, pp. 551–567, 2023.

[6] C. McLaughlin Green and M. Lomask, "Vanguard-a history.," *NASA Special Publication*, vol. 4202, 1970.

[7] R. Parkinson, H. Jones, and I. Shapiro, "Effects of solar radiation pressure on earth satellite orbits," *Science*, vol. 131, no. 3404, pp. 920–921, 1960.

[8] NASA, *August 1960 - project echo launched*, https://www.nasa.gov/directorates/heo/scan/images/history/August1960.html, Sep. 2018.

[9] P. Musen, R. Bryant, and A. Bailie, "Perturbations in perigee height of Vanguard I," *Science*, vol. 131, no. 3404, pp. 935–936, 1960.

[10] P. Musen, "The influence of the solar radiation pressure on the motion of an artificial satellite," *Journal of Geophysical Research*, vol. 65, no. 5, pp. 1391–1396, 1960.

[11] G. Cook, "Luni-solar perturbations of the orbit of an earth satellite," *Geophysical Journal International*, vol. 6, no. 3, pp. 271–291, 1962.

[12] V. Schaus, J. Radtke, E. Stoll, *et al.*, “Results of reference long-term simulations focussing on passive means to reduce the impact of space debris,” in *7th European Conference on Space Debris, ESA/ESOC*, ESA, 2017, pp. 1–10.

[13] E. M. Alessi, G. Schettino, A. Rossi, and G. B. Valsecchi, “Natural highways for end-of-life solutions in the LEO region,” *Celestial Mechanics and Dynamical Astronomy*, vol. 130, no. 5, p. 34, 2018.

[14] A. Rossi, E. M. Alessi, G. Schettino, V. Schaus, and G. B. Valsecchi, “How an aware usage of the long-term dynamics can improve the long-term situation in the LEO region,” *Acta Astronautica*, 2020.

[15] E. Brown and C. Shook, *Planetary Theory* (Harvard College Library history of science project). University Press, 1933. [Online]. Available: https://books.google.ca/books?id=isy7AAAAIAAJ.

[16] S. Breiter, “Fundamental models of resonance,” *Monografias de la Real Academia de Ciencias de Zaragoza*, vol. 22, pp. 83–92, 2003.

[17] A. V. Krivov and J. Getino, “Orbital evolution of high-altitude balloon satellites.,” *Astronomy and Astrophysics*, vol. 318, pp. 308–314, 1997.

[18] E. M. Alessi, C. Colombo, and A. Rossi, “Phase space description of the dynamics due to the coupled effect of the planetary oblateness and the solar radiation pressure perturbations,” *Celestial Mechanics and Dynamical Astronomy*, vol. 131, no. 9, p. 43, 2019.

[19] I. Gkolias, E. M. Alessi, and C. Colombo, “Dynamical taxonomy of the coupled solar radiation pressure and oblateness problem and analytical deorbiting configurations,” *Celestial Mechanics and Dynamical Astronomy*, vol. 132, pp. 1–18, 2020.

[20] J. Radtke, C. Kebschull, and E. Stoll, “Interactions of the space debris environment with mega constellations—using the example of the OneWeb constellation,” *Acta Astronautica*, vol. 131, pp. 55–68, 2017.

[21] H. Lewis, J. Radtke, A. Rossi, *et al.*, “Sensitivity of the space debris environment to large constellations and small satellites,” *Journal of the British Interplanetary Society*, vol. 70, pp. 105–117, 2017.

[22] A. Rossi, E. Alessi, G. Valsecchi, *et al.*, “A quantitative evaluation of the environmental impact of the mega constellations,” 2017.

[23] C. Lücking, C. Colombo, and C. McInnes, “A passive de-orbiting strategy for high altitude cubesat missions using a deployable reflective balloon,” in *8th IAA Symposium on Small Satellites*, 2011.

[24] C. Lücking, C. Colombo, and C. R. McInnes, “A passive satellite deorbiting strategy for medium earth orbit using solar radiation pressure and the J2 effect,” *Acta Astronautica*, vol. 77, pp. 197–206, 2012.

[25] C. Lücking, C. Colombo, and C. R. McInnes, "Solar radiation pressure-augmented deorbiting: Passive end-of-life disposal from high-altitude orbits," *Journal of Spacecraft and Rockets*, vol. 50, no. 6, pp. 1256–1267, 2013.

[26] G. Schettino, E. M. Alessi, A. Rossi, and G. B. Valsecchi, "A frequency portrait of low earth orbits," *Celestial Mechanics and Dynamical Astronomy*, vol. 131, no. 8, p. 35, 2019.

[27] E. M. Alessi, G. Schettino, A. Rossi, and G. B. Valsecchi, "Solar radiation pressure resonances in low earth orbits," *Monthly Notices of the Royal Astronomical Society*, vol. 473, no. 2, pp. 2407–2414, 2018.

[28] A. J. Rosengren, D. K. Skoulidou, K. Tsiganis, and G. Voyatzis, "Dynamical cartography of earth satellite orbits," *Advances in Space Research*, vol. 63, no. 1, pp. 443–460, 2019.

[29] V. Schaus, E. M. Alessi, G. Schettino, A. Rossi, and E. Stoll, "On the practical exploitation of perturbative effects in low earth orbit for space debris mitigation," *Advances in Space Research*, vol. 63, no. 7, pp. 1979–1991, 2019.

[30] G. Schettino, E. Alessi, A. Rossi, and G. Valsecchi, "Characterization of low earth orbit dynamics by perturbation frequency analysis," in *68th International Astronautical Congress, Adelaide, Australia, Paper Number IAC-17-C1*, vol. 9, 2017.

[31] ESA, *Discosweb*, 2022. [Online]. Available: `https://discosweb.esoc.esa.int/objects`.

[32] USSPACECOM, *Historical elset*, 2022. [Online]. Available: `https://www.space-track.org`.

[33] C. Pardini and L. Anselmo, "Review of past on-orbit collisions among cataloged objects and examination of the catastrophic fragmentation concept," *Acta Astronautica*, vol. 100, pp. 30–39, 2014.

[34] T. Kelso *et al.*, "Analysis of the Iridium 33 Cosmos 2251 collision," 2009.

[35] N. Aeronautics and S. A. (NASA), *Orbital debris quarterly news*, `https://orbitaldebris.jsc.nasa.gov/quarterly-news/pdfs/odqnv27i1.pdf`, Volume 27, Issue 1, May 2023.

[36] "IADC space debris mitigation guidelines," IADC Working Group 4/Steering Group, Tech. Rep. IADC-02-01 Rev. 3, Jun. 2021.

[37] "IADC report on the status of the space debris environment," IADC Working Group 2/Steering Group, Tech. Rep. IADC-23-01, Jan. 2023.

[38] "Satellite orbital safety best practices," AIAA, Iridium, OneWeb, SpaceX, Tech. Rep. Version 2.0, Oct. 2022.

[39] SpaceX, *Falcon 9 - first orbital class rocket capable of reflight*, 2023. [Online]. Available: `https://www.spacex.com/vehicles/falcon-9`.

[40] M. Weinzierl and M. Sarang, *The commercial space age is here*, B. Harvard Business Review and Society, Eds., [Online; posted 12-February-2021], Feb. 2021. [Online]. Available: https://hbr.org/2021/02/the-commercial-space-age-is-here.

[41] "IADC statement on active debris removal," IADC Steering Group, Tech. Rep. IADC-22-02, Dec. 2022.

[42] C. P. Mark and S. Kamath, "Review of active space debris removal methods," *Space Policy*, vol. 47, pp. 194–206, 2019.

[43] ESA, *Clearspace-1*, 2023. [Online]. Available: https://www.esa.int/Space_Safety/ClearSpace-1.

[44] Astroscale, *Astroscale's ELSA-d mission successfully completes complex rendezvous operation*, [Online; posted 4-May-2022], 2022. [Online]. Available: https://astroscale.com/astroscales-elsa-d-mission-successfully-completes-complex-rendezvous-operation/.

[45] Astroscale, *ADRAS-J*, 2023. [Online]. Available: https://astroscale.com/missions/adras-j/.

[46] Astroscale, *ELSA-M*, 2023. [Online]. Available: https://astroscale.com/elsa-m/.

[47] Y. Tsuda, O. Mori, R. Funase, *et al.*, "Flight status of ikaros deep space solar sail demonstrator," *Acta astronautica*, vol. 69, no. 9-10, pp. 833–840, 2011.

[48] Y. Tsuda, O. Mori, R. Funase, *et al.*, "Achievement of IKAROS—Japanese deep space solar sail demonstration mission," *Acta Astronautica*, vol. 82, no. 2, pp. 183–188, 2013.

[49] J. A. Borja and D. Tun, "Deorbit process using solar radiation force," *Journal of Spacecraft and Rockets*, vol. 43, no. 3, pp. 685–687, 2006.

[50] C. Colombo, N. Miguel Banos, and I. Gkolias, "Modulating solar sail control for end-of-life disposal with solar sails," in *5th International Symposium on Solar Sailing*, 2019, pp. 1–13.

[51] The Planetary Society, *The planetary society*, 2023. [Online]. Available: https://www.planetary.org/.

[52] D. A. Spencer, B. Betts, J. M. Bellardo, A. Diaz, B. Plante, and J. R. Mansell, "The LightSail 2 solar sailing technology demonstration," *Advances in Space Research*, vol. 67, no. 9, pp. 2878–2889, 2021.

[53] The Planetary Society, *Lightsail, a Planetary Society solar sail spacecraft*, https://www.planetary.org/sci-tech/lightsail, 2023.

[54] M. Ceriotti, P. Harkness, and M. McRobb, "Variable-geometry solar sailing: The possibilities of the quasi-rhombic pyramid," *Advances in solar sailing*, pp. 899–919, 2014.

[55] N. Miguel and C. Colombo, "Deorbiting spacecraft with passively stabilised attitude using a simplified quasi-rhombic-pyramid sail," *Advances in Space Research*, vol. 67, no. 9, pp. 2561–2576, 2021.

[56] COMPASS team, *Control for orbit manoeuvring through perturbations for application to space systems*, 2023. [Online]. Available: https://www.compass.polimi.it/.

[57] G. Cook, "The use of simplified orbital theory for satellites of large area-to-mass ratio," *Planetary and Space Science*, vol. 11, no. 11, pp. 1289–1295, 1963.

[58] D. A. Vallado and D. Finkleman, "A critical assessment of satellite drag and atmospheric density modeling," *Acta Astronautica*, vol. 95, pp. 141–165, 2014.

[59] M. Möckel, *High performance propagation of large object populations in earth orbits*. Logos Verlag Berlin GmbH, 2015.

[60] J. C. Van der Ha, "Long-term evolution of near-geostationary orbits," *Journal of Guidance, Control, and Dynamics*, vol. 9, no. 3, pp. 363–370, 1986.

[61] A. Rossi, L. Anselmo, C. Pardini, R. Jehn, and G. Valsecchi, "The new space debris mitigation (SDM 4.0) long term evolution code," in *Fifth European Conference on Space Debris*, vol. 672, 2009.

[62] H. Fraysse, V. Morand, C. Le Fevre, *et al.*, "Long term orbit propagation techniques developed in the frame of the French Space Act," in *22nd International Symposium on Space Flight Dynamics*, vol. 28, 2011.

[63] D. Amato, A. J. Rosengren, and C. Bombardelli, "Thalassa: A fast orbit propagator for near-earth and cislunar space," in *2018 Space Flight Mechanics Meeting*, 2018, p. 1970.

[64] R. Lucken and D. Giolito, "Collision risk prediction for constellation design," *Acta Astronautica*, 2019.

[65] L. Sagnières, "Modeling and simulation of long-term rotational dynamics of large space debris," Ph.D. dissertation, McGill University, Feb. 2019.

[66] L. B. Sagnières and I. Sharf, "Long-term rotational motion analysis and comparison to observations of the inoperative Envisat," *Journal of Guidance, Control, and Dynamics*, vol. 42, no. 2, pp. 364–376, 2019.

[67] L. B. Sagnières, I. Sharf, and F. Deleflie, "Simulation of long-term rotational dynamics of large space debris: A TOPEX/Poseidon case study," *Advances in Space Research*, vol. 65, no. 4, pp. 1182–1195, 2020.

[68] L. B. Sagnières and I. Sharf, "Stochastic modeling of hypervelocity impacts in attitude propagation of space debris," *Advances in Space Research*, vol. 59, no. 4, pp. 1128–1143, 2017.

[69] H. D. Curtis, *Orbital mechanics for engineering students*. Butterworth-Heinemann, 2013.

[70] C. R. McInnes, *Solar sailing: technology, dynamics and mission applications*. Springer Science & Business Media, 2013, ch. 2, pp. 47–49.

[71] J. Daquin, A. J. Rosengren, E. M. Alessi, F. Deleflie, G. B. Valsecchi, and A. Rossi, "The dynamical structure of the MEO region: Long-term stability, chaos, and transport," *Celestial Mechanics and Dynamical Astronomy*, vol. 124, no. 4, pp. 335–366, 2016.

[72] R. Jastrow and R. Bryant, "Variations in the orbit of the Echo satellite," *Publications of Goddard Space Flight Center*, vol. 65, no. 10, p. 386, 1960.

[73] I. I. Shapiro and H. M. Jones, "Perturbations of the orbit of the Echo balloon," *Science*, vol. 132, no. 3438, pp. 1484–1486, 1960.

[74] R. J. Mackey, *Echo 1*, 2022. [Online]. Available: https://nssdc.gsfc.nasa.gov/nmc/spacecraft/display.action?id=1960-009A.

[75] A. Wilson, "A history of balloon satellites," *Journal of the British Interplanetary Society*, vol. 34, p. 10, 1981.

[76] G. L. Davis and R. L. Tanimoto, "Mechanical development of antenna systems," *Spaceborne Antennas for Planetary Exploration*, pp. 425–454, 2006.

[77] P. E. Zadunaisky, I. I. Shapiro, and H. M. Jones, "Experimental and theoretical results on the orbit of Echo 1," *SAO Special Report*, vol. 61, 1961.

[78] T. Kubo-oka and A. Sengoku, "Solar radiation pressure model for the relay satellite of selene," *Earth, planets and space*, vol. 51, no. 9, pp. 979–986, 1999.

[79] A. F. Heaton and A. Artusio-Glimpse, "An update to the NASA reference solar sail thrust model," in *AIAA SPACE 2015 Conference and Exposition*, 2015, p. 4506.

[80] G. Cook, "Satellite drag coefficients," *Planetary and Space Science*, vol. 13, no. 10, pp. 929–946, 1965.

[81] F. Goodarzi, D. Lee, and T. Lee, "Geometric nonlinear PID control of a quadrotor UAV on SE (3)," in *2013 European control conference (ECC)*, IEEE, 2013, pp. 3845–3850.

[82] D. A. Danielson, C. P. Sagovac, B. Neta, and L. W. Early, "Semianalytic satellite theory," Department of Mathematics, Naval Postgraduate School, Tech. Rep., 1995.

[83] A. A. Albuja, D. J. Scheeres, R. L. Cognion, W. Ryan, and E. V. Ryan, "The YORP effect on the GOES 8 and GOES 10 satellites: A case study," *Advances in Space Research*, vol. 61, no. 1, pp. 122–144, 2018.

[84] L. Cerri, A. Couhert, P. Ferrage, and P. Perrachon, "DORIS satellites models implemented in POE processing," CNES, Tech. Rep. SALP-NT-BORD-OP-16137-CN, Feb. 2021, p. 38. [Online]. Available: https://ids-doris.org/documents/BC/satellites/DORISSatelliteModels.pdf.

[85] M. A. Swartwout, “Earth escape using a slowly rotating, doubly reflective solar sail,” *Journal of guidance, control, and dynamics*, vol. 28, no. 2, pp. 374–377, 2005.

[86] P. Kelly and R. Bevilacqua, “An optimized analytical solution for geostationary debris removal using solar sails,” *Acta Astronautica*, vol. 162, pp. 72–86, 2019.

[87] S. Caldwell, *State-of-the-art of small spacecraft technology*, Oct. 2021. [Online]. Available: https://www.nasa.gov/smallsat-institute/sst-soa.